

# **Three-Dimensional Nonlinear Waves Under Spatial Confinement**

vorgelegt von  
Dipl.-Phys.  
Arash Azhand  
geb. in Kabul

Von der Fakultät II - Mathematik und Naturwissenschaften  
der Technischen Universität Berlin  
zur Erlangung des akademischen Grades  
Doktor der Naturwissenschaften  
– Dr. rer. nat –  
genehmigte Dissertation

Promotionsausschuss:

Vorsitzende: Prof. Dr. Ulrike Woggon  
Gutachter: Prof. Dr. Harald Engel  
Gutachter: Prof. Dr. Markus Bär  
Gutachter: Prof. Dr. Oliver Steinbock

Tag der wissenschaftlichen Aussprache: 12. Oktober 2015

Berlin 2016



## ABSTRACT

---

The aim of my thesis is to study the evolution of scroll waves under spatial confinement both experimentally as well as numerically. Scroll waves represent three-dimensional (3D) analogs of spiral waves. In the simplest case, the central axis around which a scroll wave rotates is a straight line. The line is named the filament of the scroll wave, and each infinitesimal cross-section represents the core of a spiral wave. Two specific types of scroll waves are considered: (1) Straight scroll waves whose filaments can also be bent and (2) scroll rings whose filaments are bent such that the two end points of the filament attach to form a ring. Depending on the sign of the filament tension, two modes of time evolution arise in unbounded media: (1) Contraction for positive filament tension or (2) expansion for negative filament tension.

The experimental studies in my thesis are achieved in thin layers of the photosensitive Belousov-Zhabotinsky reaction (PBZR). The usage of a continuously stirred tank reactor allows us to maintain the layers at non-equilibrium conditions. A novel experimental setup is developed that enables the initiation of any type of scroll wave in a reliable and reproducible manner through the application of variable spatio-temporal illumination. A numerical reaction-diffusion simulation program is developed, and accompanies the PBZR experimental results. The program is termed Virtual Lab and is constructed such that it mimics parameter variation strategies that already enabled to initiate various types of scroll waves in our experimental laboratory.

I will highlight and report on the first successful boundary-mediated stabilization of an expanding scroll ring at a planar no-flux boundary in the PBZR. This behavior represents a novel type of a 3D autonomous pacemaker (APM). Numerical simulations in the modified complete Oregonator (MCO) model confirm the existence of APMs in a broad parameter regime, and predict existence of “breathing” APMs. A breathing APM is a scroll ring that exhibits periodical oscillations both in the filament radius  $R$  and the  $z$  axis position of the filament plane. More results include: the numerical observation of travelling deformation waves along straight scroll wave filaments; the observation of highly writhed filaments in the PBZR and MCO model; and the formation of modulated scroll ring filaments with distinct geometric shapes (ellipsis, triangles, and squares) both in the PBZR and MCO model. Finally, modulated scroll wave filaments are explained to emerge within the dynamical Kirchhoff theory for elastic ribbons.

## ZUSAMMENFASSUNG

---

Das Thema der vorliegenden Arbeit ist, die Dynamik von *scroll waves* unter räumlichen Einschränkungen sowohl experimentell als auch anhand von numerischen Simulationen zu untersuchen. Scroll waves repräsentieren dabei das dreidimensionale Analogon zu Spiralwellen. Im einfachsten Fall ist die zentrale Achse, um die ein scroll wave rotiert, eine Linie. Diese Linie bezeichnen wir als das Filament der scroll wave, wobei jeder Querschnitt des Filaments den Kern einer Spirale darstellt. Zwei Arten von scroll waves werden hier behandelt: (1) Scroll waves, dessen Filamente gerade oder auch gekrümmmt sein können und (2) scroll waves mit ringförmigem Filament. Die letztere Struktur bezeichnen wir als *scroll ring*. Abhängig vom Vorzeichen der Filamentspannung, unterscheiden wir zwei Arten der Zeitentwicklung für scroll waves: (1) Kontraktion für positive Filamentspannung oder (2) Expansion bei negativer Filamentspannung.

Die experimentellen Untersuchungen in meiner Arbeit wurden in dünnen Schichten von photosensitiven Belousov-Zhabotinsky-Medien (PBZM) durchgeführt. Diese wurden durch die Verwendung von Durchflussreaktoren ständig im Zustand des stationären Nichtgleichgewichts gehalten. Ein neuer Aufbau wurde entwickelt und erlaubt die verlässliche und wiederholbare Initiierung von scroll waves durch die Anwendung variabler raum-zeitlicher Beleuchtung. Zur Interpretation und Vorhersage experimenteller Ergebnisse wurden auch numerische Simulationen durchgeführt. Dazu wurde ein allgemeiner Reaktions-Diffusions-Simulator entwickelt. Das Projekt *Virtual Lab* ist so konstruiert, dass es die zahlreichen im Labor vorhandenen Strategien zur Parametervariation nachahmt.

Es war mir möglich, zum allerersten Mal im Rahmen der PBZM einen expandierenden scroll ring durch Wechselwirkung mit einem Neumann-Rand zu stabilisieren. Diese stabilen Ringe stellen einen neuen Typus dreidimensionaler autonomer Schrittmacher dar. Numerische Simulationen im Rahmen des Oregonator-Modells bestätigen die Existenz dieser Schrittmacher, und sagen darüber hinaus auch die Existenz von "atmenden" Schrittmachern voraus. Letztere sind scroll rings, dessen Filamente sowohl im Radius  $R$  als auch in der axialen Position der Filamentebene  $z$  bezüglich des stabilisierenden Randes periodisch oszillieren. Des Weiteren zeigen numerische Simulationen propagierende Krümmungswellen entlang der geraden scroll waves. Weitere hervorzuhebende Ergebnisse, die sowohl im Experiment als auch in der Simulation erhalten wurden, beinhalten das Auftreten von in hohem Maße gekrümmten Filamenten und die Ausbildung von scroll ring-Filamenten mit verschiedenen Geometrien (Ellipse, Dreieck, und Quadrat). Schließlich war es möglich, die Entstehung modulierter scroll wave-Filamente im Rahmen der dynamischen Kirchhoff-Theorie für elastische Bänder zu erklären.

## PUBLICATIONS

---

Some ideas and figures have appeared previously in the following publications:

1. A. Azhand, R. Buchholz, F. Buchholz, J. Totz and H. Engel, "No-flux boundaries stabilize scroll rings in excitable media with negative filament tension", arXiv:1401.8119.
2. A. Azhand, J. F. Totz and H. Engel, "Three-dimensional autonomous pacemaker in the photosensitive Belousov-Zhabotinsky medium", *Europhysics Letters* **108**, 10004 (2014).
3. D. Kulawiak, A. Azhand, J. Totz, S. Martens and H. Engel, "Suppression of scroll wave filament instabilities in confined excitable media", in preparation.
4. A. Azhand and H. Engel, "Boundary-induced modulation of scroll wave and scroll ring filaments in the photosensitive Belousov-Zhabotinsky medium", in preparation.



## CONTENTS

---

<b>1</b>	<b>INTRODUCTION</b>	<b>1</b>
1.1	The influence of confinement on spiral waves . . . . .	8
1.2	Scroll waves and scroll rings . . . . .	10
1.3	Purpose and highlights of the thesis . . . . .	15
<b>I</b>	<b>THEORY</b>	<b>19</b>
<b>2</b>	<b>THEORETICAL CONCEPTS ON SPIRAL WAVES</b>	<b>21</b>
2.1	Introduction . . . . .	21
2.2	Stability of unperturbed spirals . . . . .	22
2.3	Stability of perturbed spirals under generic perturbations . . . . .	24
2.4	Specific types of perturbations . . . . .	28
2.5	Numerical computation of response functions . . . . .	30
<b>3</b>	<b>THEORETICAL APPROACHES ON SCROLL WAVE FILAMENTS</b>	<b>35</b>
3.1	Introduction . . . . .	35
3.2	Approach by Keener . . . . .	36
3.2.1	Untwisted scroll ring . . . . .	39
3.2.2	Twisted scroll ring . . . . .	40
3.3	Approach by Biktashev . . . . .	41
3.4	Approach by Henry and Hakim . . . . .	43
<b>II</b>	<b>METHODS</b>	<b>53</b>
<b>4</b>	<b>A NOVEL SETUP FOR EXPERIMENTS IN THE PBZ MEDIUM</b>	<b>55</b>
4.1	Introduction . . . . .	55
4.2	Self-completion of three-dimensional waves . . . . .	56
4.3	The Continuously stirred tank reactor (CSTR) . . . . .	58
4.4	Experimental setup . . . . .	59
4.5	Initiation of straight scroll waves and scroll rings . . . . .	64
4.6	Used BZ recipes . . . . .	65
<b>5</b>	<b>THE VIRTUAL LAB PROJECT</b>	<b>67</b>
5.1	The purpose of the Virtual Lab project . . . . .	67
5.2	Exhibition of the Virtual Lab capabilities . . . . .	73
<b>III</b>	<b>STRAIGHT SCROLL WAVES UNDER SPATIAL CONFINEMENT</b>	<b>79</b>
<b>6</b>	<b>STRAIGHT SCROLL WAVES UNDER CONFINEMENT - NUMERICAL STUDY</b>	<b>81</b>
6.1	Introduction . . . . .	81
6.2	Three-dimensional meander instability . . . . .	83
6.3	Negative line tension instability . . . . .	88
<b>7</b>	<b>STRAIGHT SCROLL WAVES WITH THE MEANDER INSTABILITY IN THIN PBZ LAYERS</b>	<b>93</b>
7.1	Introduction . . . . .	93
7.2	Results . . . . .	95

<b>IV SCROLL RINGS UNDER SPATIAL CONFINEMENT</b>	<b>101</b>
<b>8 NUMERICAL STUDY OF SCROLL RINGS UNDER VARIATION OF EXCITABILITY</b>	<b>103</b>
8.1 Introduction . . . . .	103
8.2 Free scroll rings . . . . .	106
8.3 Motivation for studying confined scroll rings . . . . .	109
8.4 Contracting scroll rings . . . . .	110
8.5 Expanding scroll rings . . . . .	115
8.6 Numerical tests for observing an APM in the PBZR . . . . .	119
<b>9 A THREE-DIMENSIONAL APM IN THE PBZ MEDIUM</b>	<b>123</b>
<b>10 MODULATED RING FILAMENTS IN THE PBZR</b>	<b>127</b>
<b>11 CONCLUSIONS</b>	<b>133</b>
<b>V DYNAMICS OF FILAMENTS WITHIN A NONLINEAR ELASTICITY THEORY</b>	<b>135</b>
<b>12 DYNAMICS OF FILAMENTS WITHIN A NONLINEAR ELASTICITY THEORY</b>	<b>137</b>
12.1 The basic elements of the approach by Goriely and colleagues .	138
12.2 The straight Filament . . . . .	140
12.3 The ring-shaped Filament . . . . .	144
<b>VI CONCLUSIONS AND OUTLOOK</b>	<b>147</b>
<b>VII BIBLIOGRAPHY</b>	<b>153</b>

## LIST OF FIGURES

---

Figure 1	Examples of snow crystal patterns. . . . .	1
Figure 2	Examples for Turing patterns in the animal world. . . . .	2
Figure 3	Rayleigh-Bénard convection cells. . . . .	3
Figure 4	Phase- and trigger waves in the BZ reaction. . . . .	4
Figure 5	Sketch to illustrate emergence of a trigger wave at the boundary of an excitable medium. . . . .	5
Figure 6	Scheme of spiral wave initiation by Winfree. . . . .	6
Figure 7	Spirals in various excitable media. . . . .	7
Figure 8	Sketch of straight and curved scroll waves. . . . .	10
Figure 9	Anatomy of a scroll ring. . . . .	11
Figure 10	The visualized structure of the thesis - part ii: the methods. . . . .	16
Figure 11	The visualized structure of the thesis - part iii: straight scroll waves under spatial confinement. . . . .	17
Figure 12	The visualized structure of the thesis - part iv: scroll rings under spatial confinement. . . . .	18
Figure 13	Goldstone modes and response functions numerically calculated in the Barkley model. . . . .	32
Figure 14	Spiral bifurcation diagram for the Barkley reaction-diffusion model. . . . .	44
Figure 15	Schematic for scroll wave initial states investigated by H. Henry and V. Hakim. . . . .	46
Figure 16	Eigenvalue spectrum for a straight scroll wave with translation band instability. . . . .	47
Figure 17	Instantaneous filament evolution for a straight scroll wave with translation band instability. . . . .	48
Figure 18	Winfree's self-completion method for straight scroll waves. . . . .	56
Figure 19	Winfree's self-completion method for scroll rings. . . .	57
Figure 20	The continuously stirred tank reactor (CSTR). . . . .	59
Figure 21	Spectrophotometric measurement of spiral waves in the BZR. . . . .	60
Figure 22	Schematic illustration of our experimental setup. . . . .	61
Figure 23	Schematic illustration of straight scroll wave initiation in the PBZR. . . . .	63
Figure 24	Schematic illustration of scroll ring initiation in the PBZR. . . . .	65
Figure 25	Proposed architecture of the VirtualLab project. . . . .	68
Figure 26	Spiral wave initiation in Virtual Lab. . . . .	73
Figure 27	Spiral wave analysis in the Virtual Lab project. . . . .	75
Figure 28	Visualization of straight scroll waves and scroll rings in the Virtual Lab project. . . . .	76

Figure 29	Analysis of scroll ring filaments. . . . .	77
Figure 30	Spiral bifurcation diagram for the Barkley model with four chosen parameters. . . . .	81
Figure 31	Simulation setups for straight scroll waves under spatial confinement. . . . .	83
Figure 32	Secondary 3D meander instability. . . . .	84
Figure 33	FFT analysis elucidating emergence of a secondary 3D meander instability. . . . .	85
Figure 34	Suppression of the secondary meander instability. . . . .	86
Figure 35	Propagating deformation waves. . . . .	87
Figure 36	Development of the NLTI. . . . .	88
Figure 37	Delayed development of the NLTI. . . . .	89
Figure 38	FFT analysis explaining delayed development of the NLTI. . . . .	90
Figure 39	Simulation setups for straight scroll waves in the MCO model . . . . .	94
Figure 40	Straight scroll waves at one no-flux boundary: experiment compared with numerical simulation. . . . .	95
Figure 41	Evolution of a free straight scroll wave. . . . .	96
Figure 42	Evolution of a confined straight scroll wave. . . . .	97
Figure 43	Spiral wave characteristica for two parameter sets of the MCO model. . . . .	104
Figure 44	Initial placement of scroll ring filaments. . . . .	105
Figure 45	Filament length evolution in unbounded media. . . . .	106
Figure 46	Modulated filaments of contracting free scroll rings. . . . .	107
Figure 47	First stages of an expanding free scroll ring. . . . .	108
Figure 48	Development of scroll wave turbulence. . . . .	109
Figure 49	Cooperative and antagonistic boundary interactions. . . . .	110
Figure 50	Relative life time enhancement of contracting scroll rings at one boundary. . . . .	111
Figure 51	Free versus confined scroll rings for parameter set (2) and $\phi = 0.022$ . . . . .	111
Figure 52	Time evolution of the filament shape for $\phi = 0.021$ in set (2). . . . .	112
Figure 53	Time evolution of filament shapes for $\phi = 0.022$ and $\phi = 0.023$ in set (2). . . . .	114
Figure 54	Delayed development of the NLTI for $\phi = 0.028$ in set (2). . . . .	115
Figure 55	Complete stabilization of scroll ring for $\phi = 0.014$ in set (1). . . . .	116
Figure 56	Complete stabilization of scroll ring for $\phi = 0.014$ in set (1) - two viewing modes. . . . .	116
Figure 57	Breathing APM in parameter set (1) with $\phi = 0.0125$ . . . . .	118
Figure 58	Breathing APM in parameter set (1) with $\phi = 0.012$ . . . . .	119
Figure 59	Investigation for layer thickness versus intensity of photoinhibition. . . . .	120
Figure 60	Inclined initiation of a scroll ring. . . . .	121

Figure 61	Primary experimental observation of a stationary APM in the PBZR. . . . .	124
Figure 62	Experimental verification of a scroll ring with square- shaped filament in the PBZR. . . . .	128
Figure 63	Examples for triangle- and oval-shaped filaments in the PBZR. . . . .	129
Figure 64	Complex filament structures in the PBZR. . . . .	130
Figure 65	Sketch of a filament described by the director basis. . .	138
Figure 66	Travelling pulselike deformation wave. . . . .	142
Figure 67	Travelling frontlike deformation wave. . . . .	143
Figure 68	Dispersion relation for a ring filament. . . . .	144
Figure 69	Evolution of the mode $n = 2$ . . . . .	145

---

## LIST OF TABLES

---

Table 1	Table of the used BZ recipes in this thesis. . . . .	64
Table 2	Wave lengths and periods of spiral waves at four cho- sen parameters of the Barkley model. . . . .	82

---

## LISTINGS

---

Listing 1	An example ini file. . . . .	71
-----------	------------------------------	----

---

## ACRONYMS

---



## INTRODUCTION

---

*Ignis Mutat Res*  
(engl.: Heat transforms matter)

Self-organization is an ubiquitous mechanism that leads itself to the emergence of macroscopic patterns in complex physical, chemical, biological, social, and economical systems.

The macroscopic patterns which emerge in complex systems under non-equilibrium conditions, are contrasted from those which arise in classical thermodynamical systems under equilibrium. The latter are well understood through the “Boltzmann order principle” [1]. This principle assigns the highest probability to the least ordered state of a thermodynamical system, which is the equilibrium state. Isolated and closed systems evolve irreversibly into this equilibrium state within time. Therefore, the equilibrium state of a particular thermodynamic system possesses the character of an attractor for all possible non-equilibrium states of the corresponding system. One example for these equilibrium patterns is represented by low temperature crystallization, which leads to such mesmerizing snow crystal patterns presented in figure 1.

In contrast, pattern formation in non-equilibrium systems is a visually defining feature of living systems, a fact exposed by the individual paintings on the skin of numerous animals (see figure 2). These are Turing patterns, named after famous British mathematician Alan Turing who first made the attempt to describe them theoretically by the joint interaction of chemical reactions and molecular diffusion [2].

In order to affirm the role of energy dissipation for sustaining these non-equilibrium open systems, Prigogine et. al. denoted them as dissipative patterns [1, 3, 4, 5, 6]. Theoretical investigation of dissipative patterns led to a new order principle which, in contrast to the Boltzmann order principle, is



**Figure 1:** Three distinct examples (A, B and C) by Wellcome Images, licensed under CC BY 2.0 of snow crystal patterns are shown.

applicable to open systems far from equilibrium. Prigogine and colleagues named it the “dissipative order principle” and emphasized its importance for biological systems:

“... the biosphere as a whole is a non-equilibrium system, as it is subject to the flow of solar energy. In the cellular level, cell membranes or the various biochemical reaction chains are subject to concentration gradients of chemical constituents ...” (cited from [1, page 25]).

Lars Onsager bridged both worlds - one described by the Boltzmann order principle and the other by the Prigogine dissipative order principle - with the reciprocity relations [7]. These relations, which link forces (e.g. temperature gradient, concentration gradient, etc.) with fluxes (e.g. diffusional motion, heat flux, etc.), describe systems in the vicinity of the equilibrium state.

As we get further away from equilibrium, the system achieves a state where the fluxes resemble nonlinear relations to the forces. In-depth investigations for far from equilibrium situations have shown that coherent macroscopic states appear even when the corresponding microscopic state may be characterized by a chaotic turbulent dynamics.

For example in the hydrodynamics, the most prominent example for spontaneous self-organization in a non-equilibrium open system might be the Rayleigh-Bénard convection (see figure 3 for some examples). Within the scope of the Rayleigh-Bénard convection, microscopic fluctuations are amplified by the constant influx of energy from the environment, which takes control over the macroscopic evolution of the system.

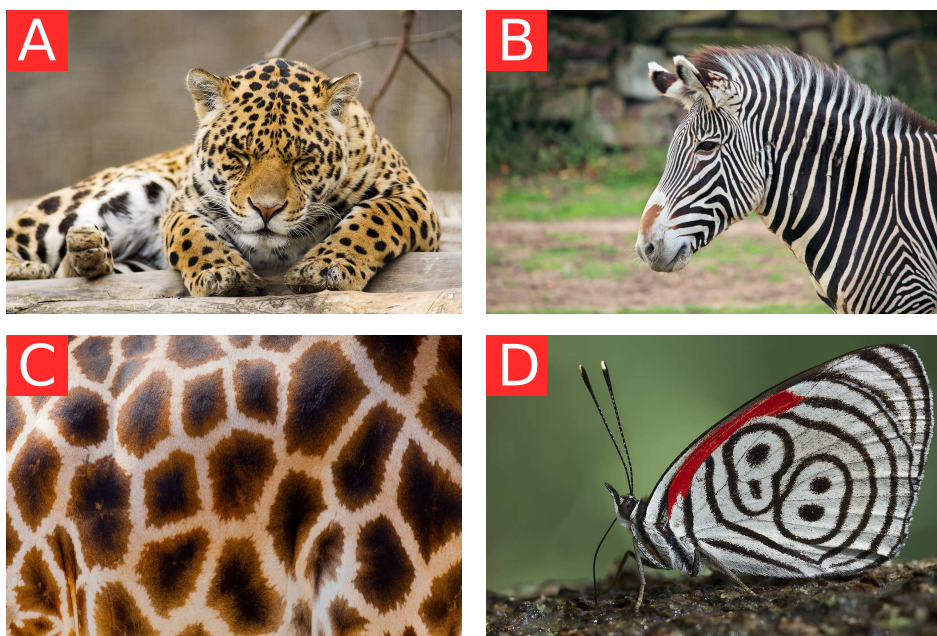


**Figure 2:** Turing patterns on the skin of (A) a panther (by Jean Pierre Turpault licensed under [CC0 1.0 Universal](#)), (B) a zebra (by Petr Kratochvil licensed under [CC0 1.0 Universal](#)), (C) a giraffe (by Petr Kratochvil licensed under [CC0 1.0 Universal](#)), and (D) the butterfly “*Diaethria eluina*” (by José Roberto Peruca licensed under [CC BY 2.0](#)).

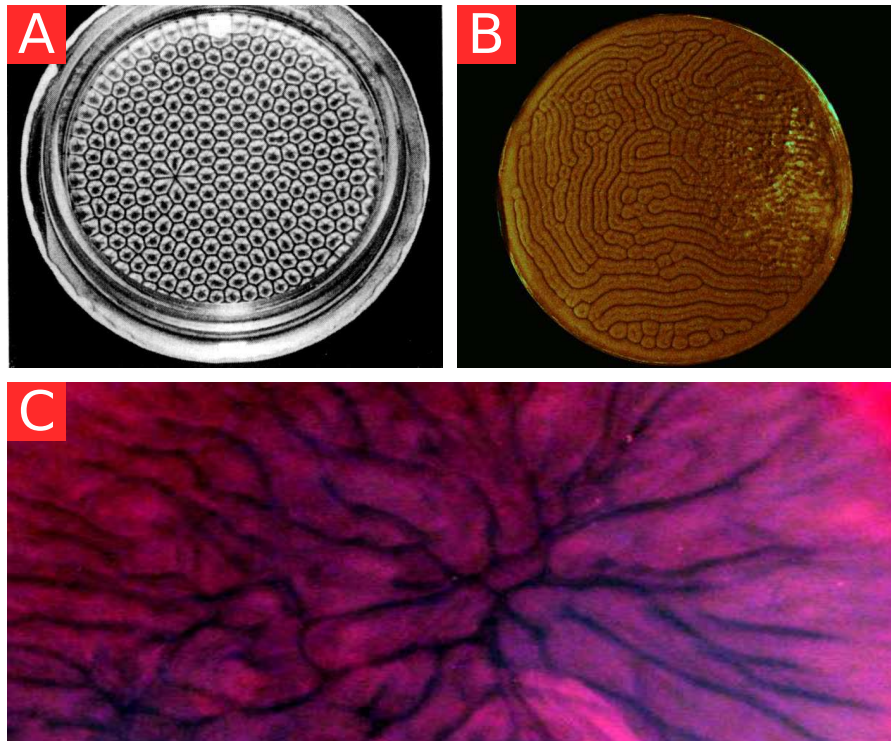


**Figure 3:** Rayleigh-Bénard convection cells in (A) a pan of oil (reprinted with permission from [8], copyright by John Wiley and Sons), (B) in a mixture of olive oil and canola oil with aluminum and magnesium fillings by Ilya Lisenker and Terese Decker (from [http://www.colorado.edu/MCEN/flowvis/galleries/2010/Team-3/FV\\_popup1-11.htm](http://www.colorado.edu/MCEN/flowvis/galleries/2010/Team-3/FV_popup1-11.htm)), and (C) in water with shampoo by Terese Decker and Ilya Lisenker (from [http://www.colorado.edu/MCEN/flowvis/galleries/2010/Team-3/FV\\_popup1-10.htm](http://www.colorado.edu/MCEN/flowvis/galleries/2010/Team-3/FV_popup1-10.htm)).

The constant influx of energy is achieved through a vertical temperature gradient in a horizontal fluid [9]. The lower interface of the fluid is maintained at a higher temperature than that of the upper interface ( $T_{\text{lower}} > T_{\text{upper}}$ ). At low temperature differences,  $\Delta T = T_{\text{lower}} - T_{\text{upper}}$ , the heat is transported through diffusion. Further increasing the value for  $\Delta T$  drives the system farther away from the linear non-equilibrium regime, until the Rayleigh-Bénard instability occurs at a critical temperature difference  $\Delta T_{\text{crit}}$ . Spontaneously, convection cells appear at the instability point as the visual indication for a highly ordered state. This spontaneous self-organizing pattern incorporates the coherent motion of molecular ensembles, leading to an amplified heat transport from the bottom to the top of the fluid layer. Increasing the gradient of temperature even further, may lead to a turbulent state.

Other examples for dissipative pattern formation far from equilibrium involve chemical reaction systems [1, 3]. One important example is given by the autocatalytic chemical system that was discovered by B. P. Belousov [10, 11]. In general, the Belousov reaction system can be described as a chemical system in which the oxidative decarboxylation of an organic substrate is achieved in the presence of a redox catalyst [12]. While dicarboxylic acids like malonic acids or malic acids serve as organic substrates, redox systems

like cerium, ferroin, and ruthenium are used as catalysts for the reaction. Some years later, A. M. Zhabotinsky investigated the chemical system by Belousov within the scope of his Ph.D. thesis [13]. Hence, this autocatalytic chemical system is denoted as the Belousov-Zhabotinsky (BZ) reaction. In succession, A. N. Zaikin together with Zhabotinsky was able to examine propagating wave patterns in thin layers of unstirred BZ solutions [14].

What Zaikin and Zhabotinsky observed in a ferroin-catalyzed BZ reaction system [14], is shown schematically in figure 4. In panel A, a later stage of their experiment is illustrated. The background is drawn in red indicating the catalyst ferroin in its reduced form. We see further that already some of the propagating circular wave patterns are formed, coming from “leading centers”, and resembling fronts of oxidized ferroin. Today, these wave patterns are termed “target patterns”.

At some specified moment of time a spontaneous oscillation of the bulk medium occurs, shown in panel B. The blue background is indicating ferroin in its oxidized form. The period  $T_b$  of this bulk oscillation is larger than the periods of wave propagation originating from the targets. After the appearance of the bulk oscillation, one observes that the leading front of each target pattern is vanishing (panel C). Finally, Panels D to F illustrate interaction of two chosen target patterns in the course of time. We see that the target pattern with the lower period  $T$  (higher frequency  $\nu$ ) pushes continuously the collision line between the two targets (white dashed line) into the region of the second target.

Zaikin and Zhabotinsky concluded that eventually one target pattern, namely the fastest in an ensemble of targets, may win and take the control over the whole medium. However, waves emitted by the leading centers might break in the most cases, and a more complex and chaotic state will be attained.

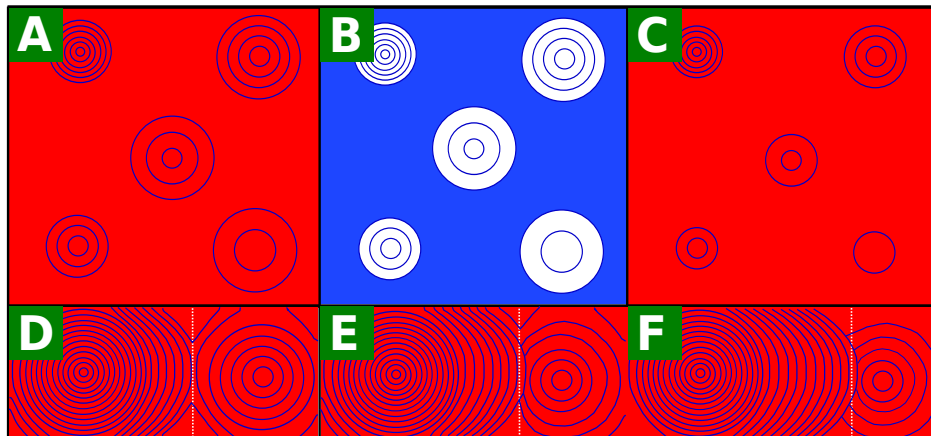


**Figure 4:** A sketch to illustrate phase and trigger waves in the BZ reaction as it was observed by Zaikin and Zhabotinsky (see [14]). Panels (A) - (C) show a specific time interval of the experiments resembling evolution of target patterns (blue circular shaped waves triggered by heterogeneities as leading centers) and the spontaneous occurrence of the bulk oscillation (blue background in B). Panels (E) - (F) display the interaction of two chosen target patterns in the course of time.

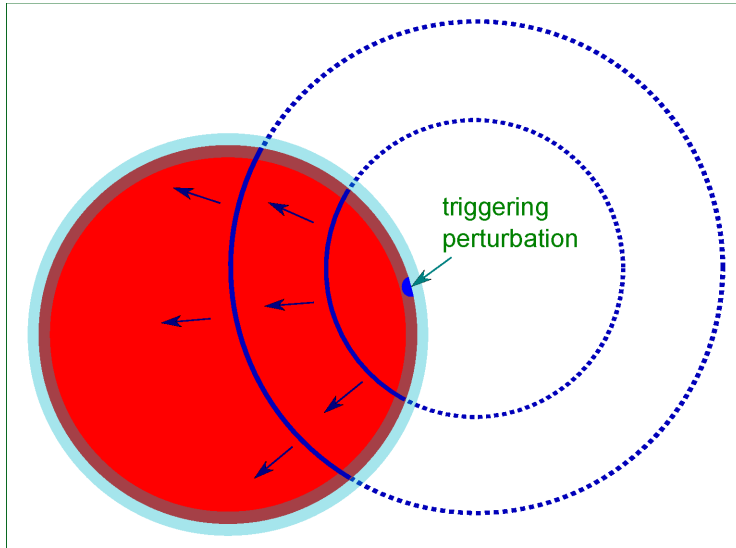


**Figure 5:** A schematic illustration of propagating trigger waves (blue curved segments) which initially were triggered at a specified point on the boundary of the medium. The blue arrows indicate the propagation direction of these wave segments, while the dashed circles are drawn to depict the trigger waves as segments of closed rings. Finally, the green arrow directs to this specific point on the boundary where the perturbing pacemaker is located.

In summary, they observed a simultaneous appearance of two wave types in their experiment [15]: phase waves (bulk oscillation) and trigger waves (triggered by a finite perturbation). The transition from phase to trigger waves and back again has been studied by Bordyugov and Engel [16].

Theoretical investigations of phase waves were accomplished by Smoes and Dreitlein [17], Thoenes [18], and by Ortoleva and Ross [19, 20]. Some intriguing properties of phase waves are [21]: no existence of an upper bound limit for their propagation velocity, they can not be blocked by impermeable barriers [22, 23], and a distinct phase wave front does not exist either.

Trigger waves are contrasted from phase waves by several properties [15]. Particularly, the media in which they arise are not purely oscillatory, while a *finite* disturbance is needed to trigger a wave. In contrast to phase waves, an upper bound limit for the velocity of wave propagation exists for trigger waves, which is an intrinsic property of the underlying medium. The leading edge of the waves is a thin interface, independent of the distance between consecutive wave fronts, and trigger waves are blocked by any barrier to molecular diffusion [22, 24] or a temporary chemical blockade [25].

Target patterns are intermediates of phase and trigger waves, and they are related to periodic trains of trigger waves. Their periods are located in a continuous interval between the period of a trigger wave  $T_0$  and the period of the bulk oscillations  $T_b$ , while they arise due to local heterogeneities (e.g. dust particles in unfiltered BZ media, [26]). After target patterns were observed and described by Zaikin and Zhabotinsky in the BZ reaction, they

were also specified in various systems of chemical, physical and biological origin [27, 28, 29, 30].

Since target patterns are circular shaped waves periodically emitted by heterogeneities as leading centers, we may denote the latter as pacemakers and the emitted waves as trigger waves without the property of a unique propagation velocity. Contrary to defect-induced pacemakers, spontaneous pacemakers may also emerge due to intrinsic dynamical processes in otherwise spatially uniform media. Such induced pacemakers are named autonomous pacemakers [31, 32, 33, 34, 35].

Additionally, one can imagine trigger waves to arise from an inhomogeneity at the boundary of the medium (see figure 5). Note that generally a spontaneous wave nucleation is amplified at the boundaries. The shape of the emerging wave will be a segment whose two endings always be pinned at the boundary, thus being influenced by the shape of the boundary. For a medium which is circular (like illustrated in the schematic figure 5), the corresponding waves which arise at the boundaries will be segments of a closed ring.

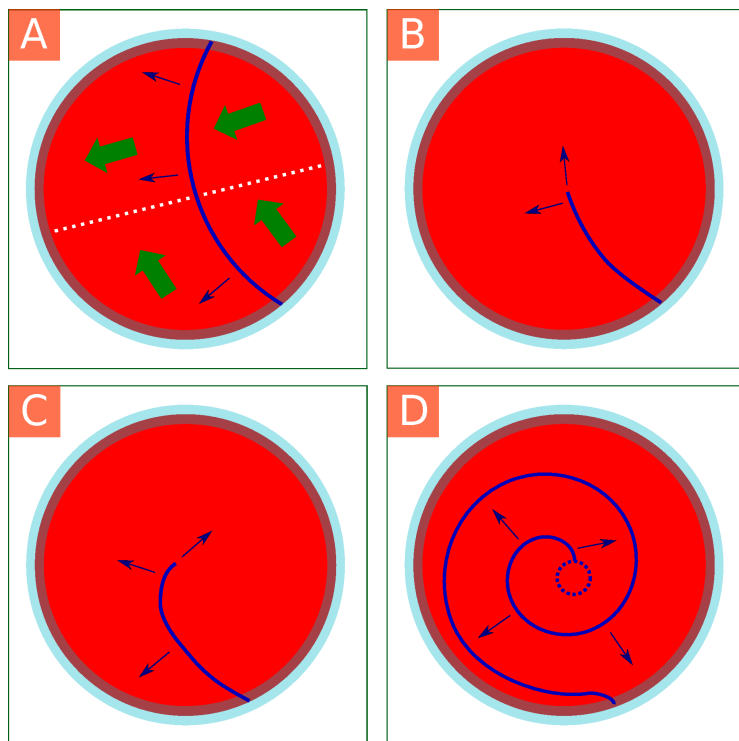


**Figure 6:** Scheme of spiral wave initiation by Winfree [22]. The panels (A) to (D) show subsequent stages of spiral initiation and evolution from a trigger wave (blue curves). The blue arrows indicate the direction of propagation for wave segments, the thick green arrows show the direction of flow which is applied on the medium, and the white dashed line in panel (A) indicates the border between the region of the medium where flows are in parallel to the wave front (lower region) and that region where the flows are in direction of wave propagation (upper region).

An interesting example of a trigger wave would be a spiral wave. Although Zhabotinsky already has mentioned spiral waves in the oscillating BZ reagent within the scope of his PhD thesis [13], it was Winfree who primarily discussed a procedure for spiral wave initiation in the excitable version of the BZ reaction by the year 1972 [22]. This procedure for initiation of spiral waves is illustrated in the schematic figure 6. In panel A, a fully evolved wave segment initiated by a perturbing inhomogeneity at the boundary (see figure 5) is shown. Now, the idea of Winfree is as follows: Inclination of the beaker induces flows in the medium, such that in the lower region of the beaker (below the white dashed line) flows are parallel to the wave segment, while in the upper region the flows are in direction of the wave propagation (in the figure indicated by the thick green arrows). Through this procedure the upper half of the wave segment may be extinguished (panel B). Hence, the remaining half wave evolves into a spiral (panels C and D).

Winfree also emphasized the importance of the BZ reagent as a model system for investigation of chemical waves in living organisms (see in [22, and references therein]). Discovery and investigation of spiral waves, both in the BZ reagent and several other complex media have since advanced enormously, particularly for pattern formation in embryos, for cellular networks, neural networks, and the fibrillating heart muscle. A selection is presented in figure 7.

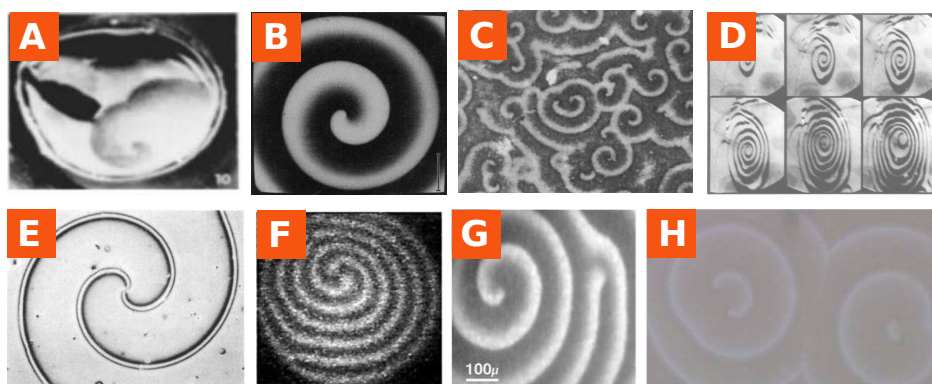


**Figure 7:** Spiral waves (A) of spreading depression in the isolated chicken retina (reprinted with permission from [36], copyright by John Wiley and Sons), (B) in the Belousov-Zhabotinsky reaction (reprinted with permission from [37], copyright by the American Association for the Advancement of Science), (C) in *Dictyostelium discoideum* (reprinted with permission from [38], copyright by the Company of Biologists, Inc.), (D) forming due to the oxidation of carbon monoxide,  $\text{CO}$ , on a platinum,  $\text{Pt}(110)$ , surface (reprinted with permission from [27], copyright by the American Physical Society), (E) in a liquid crystal (reprinted with permission from [39], copyright by the American Physical Society), (F) in a planar dc driven semiconductor-gas discharge system (reprinted with permission from [29], copyright by the American Physical Society), (G) of calcium,  $\text{Ca}^{2+}$ , in *Xenopus* oocytes (reprinted with permission from [40], copyright by Elsevier), and (H) of precipitation in a reaction of  $\text{AlCl}_3$  with  $\text{NaOH}$  (reprinted with permission from [41], copyright by the American Chemical Society).

### 1.1 THE INFLUENCE OF CONFINEMENT ON SPIRAL WAVES

In 1996, Hartmann et al. investigated the influence of the medium size on evolution of spiral waves in the  $\text{NO} + \text{CO}$  reaction on a microstructured  $Pt(100)$  surface [42] (see also reference [43]). These studies revealed a strong influence of the circular no-flux boundary on the frequency of the rotating waves. The authors reported a substantial growth of the frequency due to interaction of spiral tips with the boundary. Simulations in the framework of a reaction-diffusion model reproduced the observations qualitatively.

Later, influence of no-flux boundaries together with interaction of counter-rotating spiral waves were also investigated in experiments with the photo-sensitive variant of the BZ reaction [44]. The authors of the latter publication reported on boundary-induced drift of spirals while the drift was measured as a function of applied light intensity. Previously obtained experimental results also revealed boundary-induced spiral drift in the ferroin catalyzed BZ reaction [45]. Additionally, experiments regarding the interaction between two spiral waves respectively two scroll waves (bound states) revealed interaction distances at the scale of the core diameters [46, 47].

The experimental findings strongly suggest that there is some kind of particle-like interaction [48] between the spiral core and the no-flux boundaries, and interactions between two separate spiral cores. Some early work in the framework of the complex Ginzburg-Landau equation - which describes oscillatory media - implied a  $1/r$  decay for the interaction distance [49, 50]. However, other studies in the same model suggested exponential decay [51]. Extensive theoretical and numerical work on the basis of the two-component FitzHugh-Nagumo model - which describes excitable media - suggested a super-exponential decay [52].

In 2003, Bär et al. published their numerical bifurcation and stability analysis for spiral waves in the FitzHugh-Nagumo model [53]. By means of this approach, the authors were able to show significant effects of domain size on the dynamics of the spiral core. In particular, they found out that rigidly rotating spirals start to perform meandering motion in small domains. They denoted this effect as "boundary-induced meandering". They also observed suppression of meandering at intermediate sizes of the medium. We may summarize the approach by Bär et al. in the following way: a spiral wave in a reaction-diffusion model with simple rotation serves as steady state solution. Subsequently, the corresponding reaction-diffusion equations in the co-rotating frame are linearized in the vicinity of the steady state solution. The linear stability analysis in unbounded media then yields three eigenvalues with the real parts being practically zero - otherwise known as Goldstone modes [54, 55, 56]. These include one eigenvalue which stems from rotation symmetry, and one complex-conjugate pair of eigenvalues originating from the translational symmetry on the plane. Whilst decreasing the size of the domain, the real part of the complex-conjugate pair becomes negative due to repulsive interaction with the no-flux boundary. Further decreasing the

medium size leads to growth of the real part to become positive, yielding boundary-induced meandering.

In the last ten to fifteen years, Biktasheva and co-workers achieved much work on theoretical investigation and numerical calculation of the response functions [48, 57, 58]. I will provide an extensive summary of the response functions on the basis of the asymptotic theory of spirals later (in chapter 2). For the time being, it is solely important to emphasize that response functions are always localized in the core region of spirals while decreasing exponentially outside of the core. Additionally, responses of the spiral wave to any kind of perturbation are given by convolutions of the perturbation with the response functions in the framework of spiral wave asymptotic theory. Hence, perturbations far away from the core do not contribute to a change in spiral wave evolution.

### 1.2 SCROLL WAVES AND SCROLL RINGS

Back in 1973, it was Arthur Winfree who described a spiral wave as an infinitesimal slice through a three-dimensional structure [59]. Winfree called them scroll waves [60]. Since then, one considers a scroll wave in its simplest form as a straight continuous stack of spiral waves. A schematic of this simple three-dimensional pattern is displayed by figure 8, panel A. Here, the organizing center of the scroll wave is drawn in red. We shall denote this organizing center as the filament of the scroll wave. Within this thesis, the filament will be defined as the line containing the instantaneous positions of each spiral wave. It is not mandatory to consider solely existence of such simple straight scroll wave filaments, but also a filament structure that might be curved in some way. The latter is illustrated by panel B of the figure. Particularly, the normal vectors  $\mathbf{N}(s)$  are depicted in both cases by black arrows and parametrized by the arc length  $s$  along the filaments to illustrate the presence and absence of curvature.

Winfree suggested scroll waves as portions of a bigger ring-shaped structure. In 1974, he discussed initiation and evolution of scroll rings in BZ soaked millipore filter papers [15, 61]. To capture, what he denoted as the anatomy of the scroll ring [15], Winfree had to quickly unstack the millipore filters and insert them into a chemical fixative. This stopped the reactions. Henceforth, he could investigate the form of the ring in its entirety. Let us now study the anatomy of a scroll ring with the aid of figure 9. We see three different views of the scroll ring: The one which Winfree observed via his method, is shown by panel C of the figure. Each filter that was treated with the fixative displayed concentric circles of different sizes. Each vertical cross section through the medium containing the symmetry axis shows a pair of counter-rotating spirals. This is displayed by panel B. Finally, when we put together all observations, the three-dimensional structure of a ring-shaped filament appears, which continuously emits waves of activity in all directions of the medium (panel A of figure 9).

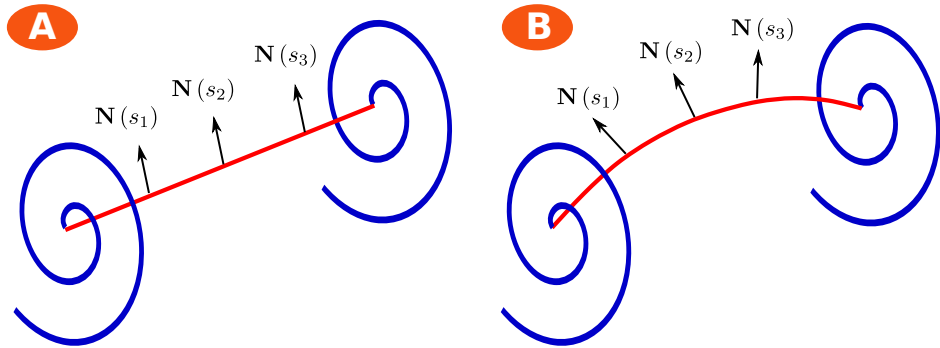


**Figure 8:** Schematic for scroll waves. The filament is shown in red, and in blue are drawn single spiral waves in order to emphasize the scroll wave as a continuous stack of spirals. The black arrows indicate direction of the normal vectors  $\mathbf{N}(s)$  along the arc length  $s$ . (A) Straight scroll wave. (B) Curved scroll wave.

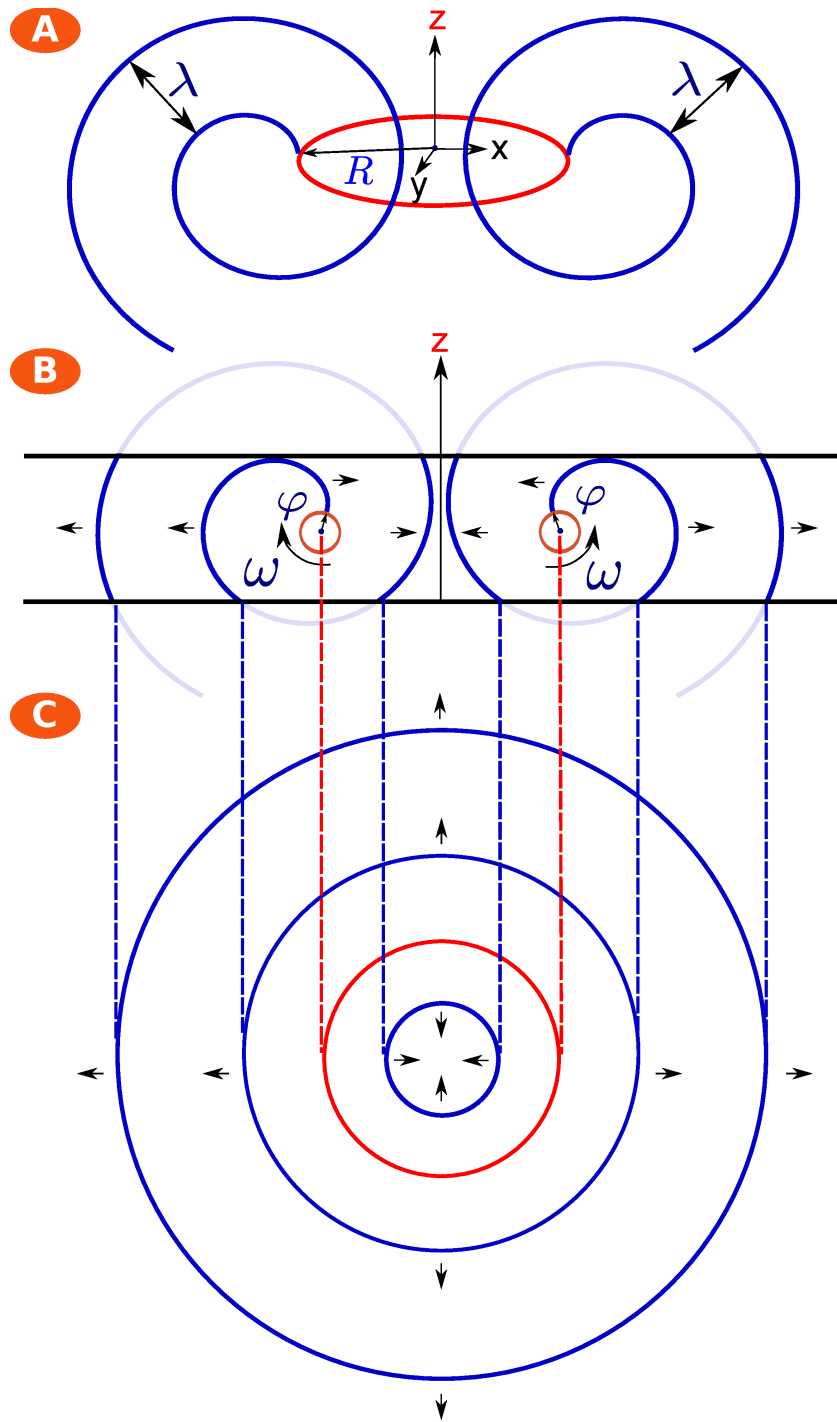


**Figure 9:** Anatomy of a scroll ring, inspired by a figure in [61]. (A) perspective view of scroll ring filament (in red) around which in each cross section an involute pair of spirals rotate. (B) A cross section of the ring in a confined medium containing not one complete spiral wave length in the height direction. Small arrows indicate direction of wave propagation. (C) View of one horizontal slice through the scroll ring showing a series of concentric rings in blue. Once again, direction of wave propagation is displayed via small arrows. The anticipated location of the filament is denoted by the red circle. The figure illustrates characteristic parameters such as the rotation frequency  $\omega$  of each spiral, the phase of rotation  $\varphi$ , wavelength  $\lambda$  measuring the distance between subsequent wave fronts, the radius  $R$  of the ring filament, and its axial position  $z$ .

The evolution of the ring filament can be described by its radius  $R$  and its axial position  $z$ . The anatomy of the emitted waves can be described by the wave length  $\lambda$ , frequency of rotation  $\omega$ , and the phase of rotation  $\varphi$ . Whereas, the phase and frequency of rotation are correlated with each other, since  $\omega = \partial_t \varphi$ . A natural way to parametrize the filaments of scroll waves and scroll rings, is achieved by the choice of the arc length coordinate  $s$ . Specifically, I illustrated this for the case of the scroll wave filament in figure 8. Given this parametrization, one shall be able to investigate the shape of the filaments in three-dimensional space by the curvature distribution  $\kappa(s)$  along the filament, meaning that  $\partial_s \kappa \neq 0$  points out a curved filament structure. Analogously, one can examine twist along the filament by introducing it as the distribution of phase  $\varphi(s)$  along the filament, meaning that  $\partial_s \varphi \neq 0$  will demonstrate twisted filament structures.

In the years after Winfree's primary discussion of scroll waves and scroll rings, further experimental and numerical studies were achieved. Welsh et al. investigated time evolution of scroll rings in the BZ reaction [62]. Numerical studies were reported in a reaction diffusion model [63], and in a cellular automaton model [64]. Meanwhile, Winfree and Strogatz published a series of four papers in which they proposed the possible observation of scroll waves with a multitude of geometrical and topological shapes [65, 66, 67, 68] (see also the nature review article from 1984 [69]), including twisted scroll waves, multiply knotted scroll rings, etc. This was followed by numerical and experimental investigations on the contraction of untwisted and twisted scroll rings [63, 70, 71]. The latter studies revealed a slower contraction of twisted rings in comparison with the untwisted rings. Additionally, the corresponding spirals of the twisted ring possess a shorter period compared to the simple ring spirals, and the ring filament appeared to vertically drift along the axle of the filament plane.

Scroll ring filaments expanding within time, were observed in numerical simulations primarily by Panfilov and Rudenko in 1987 [72]. Later, Nandapurkar and Winfree reported on the stabilization of intrinsically expanding scroll rings near a no-flux boundary [73]. In numerical simulations, they observed that the ring starts to contract as it approaches a nearby no-flux boundary, and reaches a stable radius which it holds provided that the ring remains in the vicinity of interaction distance to the boundary. This was the first hint that interaction with a no-flux boundary might play a big role in the evolution of scroll waves and scroll rings. Furthermore, Nandapurkar and Winfree observed also the emergence of "aperiodic or meandering" motion of the filament near the boundary.

The evolution of untwisted scroll waves were primarily considered by Keener and Tyson in the BZ reaction [74], while dynamics of twisted and linked scroll waves were studied numerically by Nandapurkar and Winfree [75]. In succession, the role of twist in the evolution of scroll waves received much more interest. For instance, Biktashev derived an equation of motion describing time-evolution of a scroll wave with non-homogeneous twist in a general reaction-diffusion system [76].

This was followed by a combined numerical and differential geometry approach by Henze et al. in 1990 [77]. The authors reported on the numerical observation of a twist-induced helical instability for scroll waves. Therein, twist enters as an order parameter, inducing a spontaneous bifurcation to the helical state of the filament. They denoted the emergence of this instability as the “sproing” bifurcation. Keener and Tyson proposed a simple theoretical model in order to describe evolution of helical filaments [78]. Their model grounds on a nonlinear function for the principal normal component of the filament’s velocity vector, and was reported to account qualitatively well with numerical observations. Another analytical approach for the study of helical scroll wave filaments was delivered by Aranson and Mitkov in 1998 [79]. In this work, the authors proposed that an intrinsic three-dimensional instability of a straight scroll wave leads to the helical state, and persists even beyond the meander core instability of the spiral waves. Margerit and Barkley provided a theoretical approach in which they investigated selection of shape and rotation frequency for twisted scroll waves in reaction-diffusion systems [80]. Finally, Pertsov and co-workers were able to study evolution of scroll waves under twist [81], and appearance of the sproing instability in experiments with the BZ reaction system [82]. They used a vertical temperature gradient in the BZ medium as the experimental control parameter in these studies. The gradient was applied parallel to the initially straight scroll wave filament. In succession, the instability emerged above a certain critical value for the temperature gradient.

Pertsov and colleagues also investigated evolution of scroll rings under the application of temperature gradients [83, 84], being able to control spatial orientation and lifetime of scroll rings. Amemiya et al. have used the photo-sensitive variant of the BZ reaction in order to investigate evolution of scroll rings under a gradient in the applied light intensity [85]. It was shown that this leads to contraction and expansion of the ring filaments depending on the gradient strength and direction.

To consider evolution of straight scroll waves in unbounded media, one has to mention the profound work by Henry and Hakim [86, 87]. In these publications, Henry and Hakim report on their thorough linear stability approach for scroll waves in the framework of the Barkley model [88]. These studies delivered clear understanding for three important instabilities observed earlier in numerical simulations and experiments. The first instability deals with the translation bands. The appearing instability in that case is equivalent to the negative line tension instability [89, 90, 91, 92] leading to expansion of the filament, and in the long run to scroll wave turbulence [93, 94]. The second instability type deals with the meander bands, which yields re-stabilized helical filaments in the nonlinear evolution. Finally, they considered twist as an instability source, explaining the emergence of the “sproing” bifurcation as a supercritical Hopf bifurcation (respectively the Andronov-Hopf bifurcation<sup>1</sup>, [95]).

---

<sup>1</sup> See also the scholarpedia article on the Adronov-Hopf bifurcation by Prof. Yuri A. Kuznetsov ([http://www.scholarpedia.org/article/Andronov-Hopf\\_bifurcation](http://www.scholarpedia.org/article/Andronov-Hopf_bifurcation)).

With regard to the first two instabilities, negative line tension and three-dimensional meander, recently experimental evidence was delivered. Bán-sági Jr. and Steinbock reported on the primary observation of the negative line tension instability [96], and Luengviriya et al. on the observation of both instabilities [97], in experiments with a BZ reaction system.

The primary theoretical attempt to describe the time evolution of scroll ring filaments was delivered by Yakushevich. He could show contraction of scroll ring filaments within time by basic elasticity considerations in the framework of the complex Ginzburg-Landau model [98]. Later, Keener derived generic equations of motion for the radius  $R(t)$  and the axial position  $z(t)$  of planar untwisted scroll ring filaments in the framework of an asymptotic theory for scroll wave filaments [99]. An extension to Keener's theory of filaments was provided by Biktashev and colleagues in 1994 [89]. They denoted one coefficient, which was introduced in Keener's theory, as the filament tension  $\alpha$ . The latter coefficient was shown to determine whether the ring-shaped filament contracts (positive filament tension,  $\alpha > 0$ ) or expands (negative filament tension,  $\alpha < 0$ ) in time. Just recently, Dierckx and Verschelde achieved derivation of much more generic equations of motion for filaments, both for scroll waves and scroll rings [100]. This approach yields, among other important results, an equation for the effective tension of the filament adding more terms to the basic filament tension  $\alpha$ .

Another theoretical approach that explains evolution of scroll rings, is based upon the kinematical theory for spiral waves. The latter kinematical theory was proposed by Brazhnik, Davydov, and Mikhailov in 1986 [101]. Details of the two-dimensional kinematical theory can also be found in review papers by Mikhailov et al. [102, 103]. The first attempt to extend the two-dimensional kinematic theory, such that it would describe evolution of scroll rings, was also achieved by Brazhnik et al. in the late 1980s [104]. This three-dimensional kinematic theory particularly predicts and explains collapse or expansion of scroll rings through resonant interactions between individual waves in the scroll ring pattern [105].

Some more very interesting experimental, numerical, and theoretical work were achieved in recent years. For instance, control and suppression of scroll wave (Winfree) turbulence by global periodic forcing [106, 107], and by local periodic forcing [108, 109]. Additionally, lifetime enhancement of scroll rings by space-time fluctuations [110], chemical turbulence and line defects induced by gradient effects [111], and control of this chemical turbulence [112] were achieved. Echebarria et al. proposed a non-equilibrium ribbon model for twisted scroll waves [113], evidence for Burger's equation in the untwisting dynamics of twisted scroll rings with positive filament tension was illustrated by Marts et al. [114], pinning of scroll filaments to different types of obstacles [115, 116, 117], motion of hairpin-shaped filaments [118], studies on scroll rings in advective fields [119, 120], and twists of opposite handedness on a scroll wave [121].

### 1.3 PURPOSE AND HIGHLIGHTS OF THE THESIS

My thesis is a report on the study of scroll waves and scroll rings under spatial confinement. I worked both experimentally as well as numerically.

Up to now, it was the purpose of this introductory chapter to visualize the background of these three-dimensional nonlinear wave patterns. It was shown that such wave patterns emerge in media necessarily being maintained at conditions far from thermodynamic equilibrium. The latter waves are contrasted from linear waves, such as light waves. The linear waves show such phenomena like interference, while nonlinear waves both in conservative as well as in dissipative systems do not.

The study of these nonlinear three-dimensional waves like straight scroll waves, being a continuous stack of spiral waves rotating along a linear axis, and scroll rings which are considered as continuous ring-shaped arrangement of spiral waves, was conducted in the Belousov-Zhabotinsky reaction system extensively. However, this was achieved not only in the latter experimental system, but in other dissipative active media too, certainly also theoretically, and numerically within a multitude of reaction-diffusion models. For that the reader would have a glimpse of this in-depth study being accomplished with regard to the straight scroll waves and scroll rings in the last three to four decades, I wrote the previous section.

If the scroll waves and scroll rings have been investigated in such an extensive way, you may pose the question for the reason of yet another study on these three-dimensional wave patterns. In order to prepare my answer on this question, I took one step behind and reported first on the most prominent studies being achieved with regard to the influence of confinement on the evolution of spiral waves (in section 1.1). Since spiral waves are the building-blocks of scroll waves, the presented significant influence of spatial confinement on the time-evolution of the former (spiral waves) might give us an intuition for the influence of spatial confinement on the evolution of the latter (scroll waves).

Intuition might be a motivation for taking the next steps towards an extensive scientific study. With this in mind, P. Kolski was able to explain previously obtained experimental results within the photosensitive Belousov-Zhabotinsky reaction (PBZR), which were unexpected if one is viewing them from a purely two-dimensional perspective [122]. His numerical investigations depicted the latter observations as three-dimensional phenomena which arise under spatial confinement. Until that time, the influence of spatial confinement on the evolution of scroll waves was not studied systematically.

This lack of a systematic study in direction of one or more no-flux boundaries on the dynamics of scroll waves was the motivation for my thesis. It is now my purpose to report on the results which I have obtained during that systematic study.

The upcoming part of my thesis will be devoted to a summary of some theoretical concepts which I consider important for the understanding of my results. At first, I will explain theoretical approaches for spiral waves in chapter 2. Afterwards, I will present some important theoretical considerations on the time evolution of scroll waves, scroll rings, and their filaments in chapter 3.

Part two of my thesis is devoted to the experimental and numerical methods I used for investigation of scroll waves under confined conditions. The first chapter presents a novel experimental setup for the study of these three-dimensional waves in the PBZR under stationary non-equilibrium conditions (see chapter 4). The continuously stirred tank reactor (CSTR), which allows the maintenance of stationary non-equilibrium conditions, is shown in figure 10, top panel. Inspired by the experimental setup and its capabilities, we devised a reaction-diffusion simulator which we termed as the Virtual Lab project. The purpose, design, and capabilities of the Virtual Lab project will be illustrated and discussed in chapter 5. Spiral waves, straight scroll waves, and scroll rings can be visualized with the aid of this project (see panel VLab in figure 10).

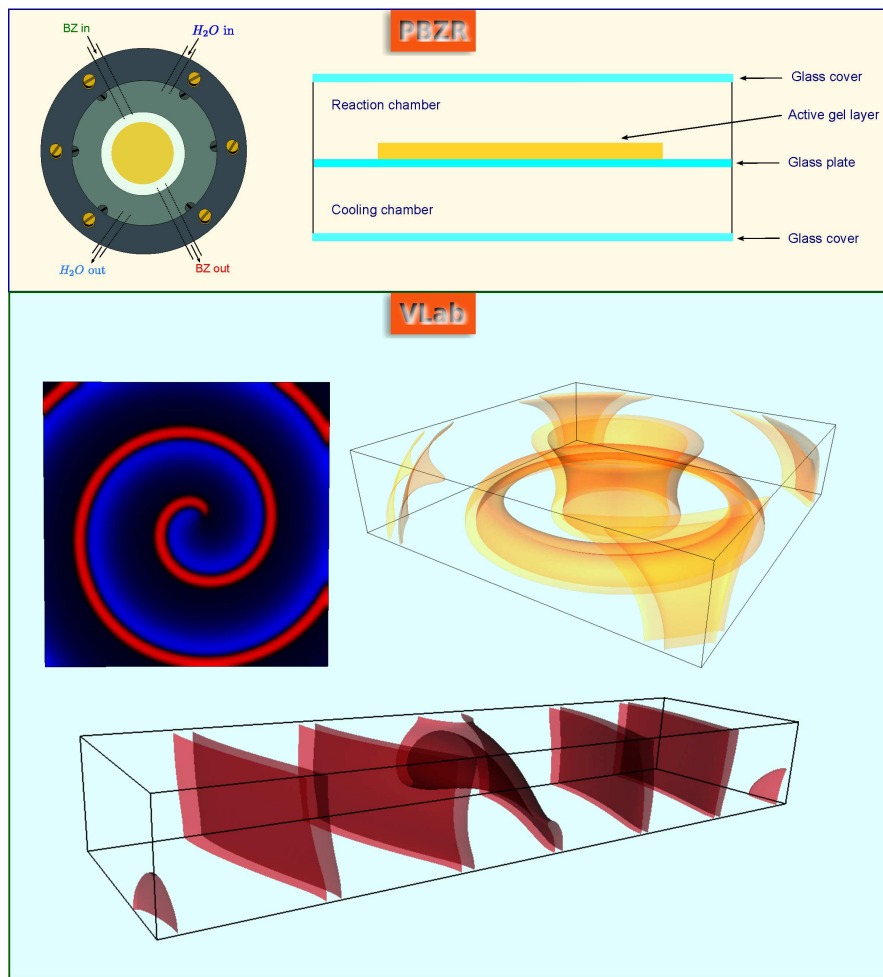


**Figure 10:** The visualized structure of the thesis - part ii: the methods.

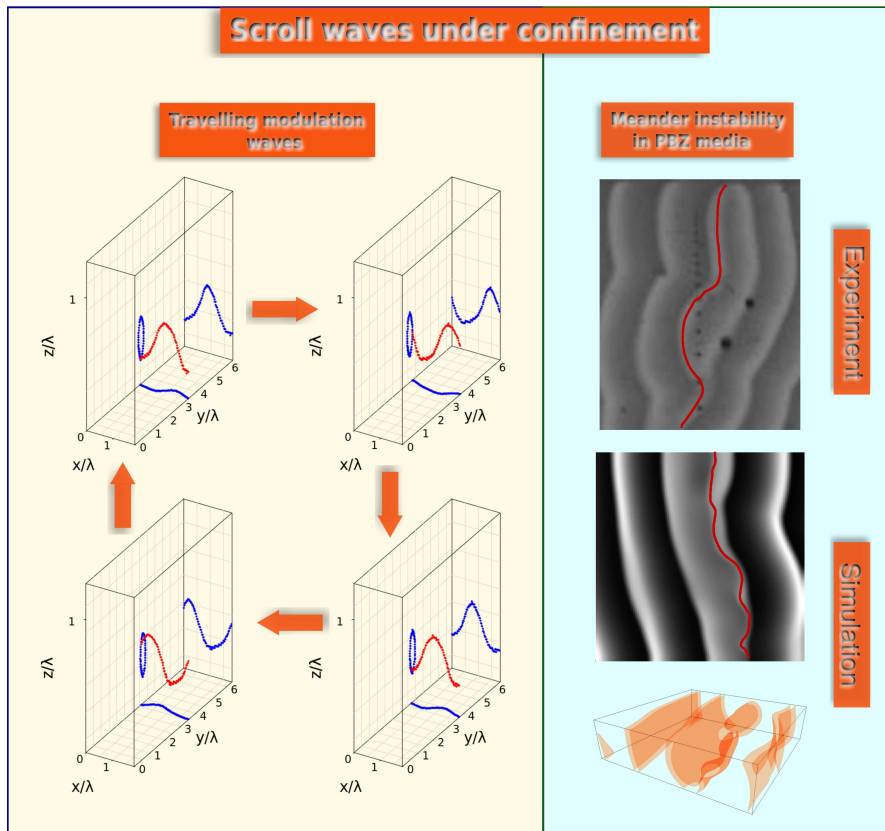


**Figure 11:** The visualized structure of the thesis - part iii: straight scroll waves under spatial confinement.

Part three considers straight scroll waves under confinement. The first chapter examines potential influences of confinement on known scroll wave instabilities (chapter 6). Particularly, we will observe travelling pulselike deformation waves along filaments (see figure 11, left). More complex restabilization phenomena, observed in the PBZR and compared to numerical simulations, will be discussed in chapter 7 (see for example the one time snapshot comparison between experiment and simulation presented in figure 11, right).

The first chapter of part four in my thesis is devoted to a numerical survey which will compare evolution of free scroll rings with their confined counter-parts (see chapter 8). Particularly, we will observe novel types of autonomous pacemakers (APMs) in three-dimensional media. These are the stationary and breathing APMs that are illustrated in figure 12 (top left and top right panels, respectively). The next chapter presents the primary experimental observation of a stationary APM in the PBZR (see chapter 9). The third chapter of part four reports on the novel experimental observation of different filament structures in the PBZR, including the square-shaped filament shown in figure 12, bottom panel. However, triangle-, ellipse-, and much more complex-shaped filaments are observed too, both in the experiment as well as in the numerical simulations (see chapter 10).

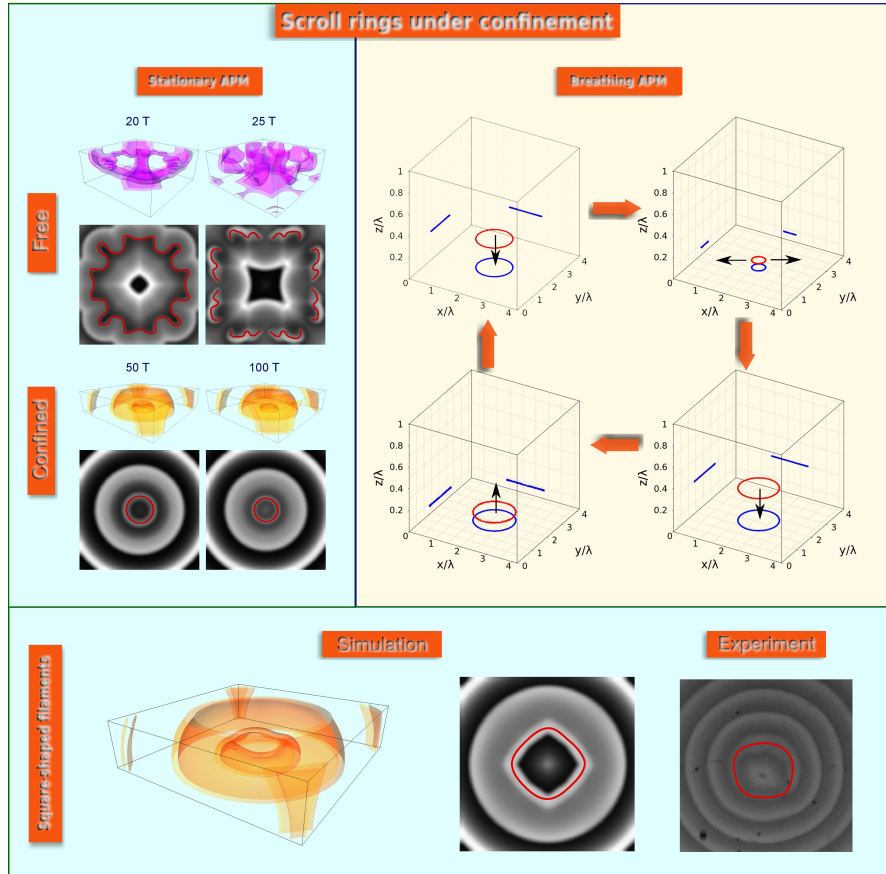


**Figure 12:** The visualized structure of the thesis - part iv: scroll rings under spatial confinement.

Part I

THEORY



# 2

## THEORETICAL CONCEPTS ON SPIRAL WAVES

---

### 2.1 INTRODUCTION

In this chapter, I will consider exclusively generic reaction-diffusion (RD) systems under the application of arbitrary perturbations on the plane  $\mathbf{r} = (x, y) \in \mathbb{R}^2$  [56]. This system can be written in the following form:

$$\partial_t \mathbf{u} = \mathbf{f}(\mathbf{u}) + \mathbb{D}\Delta\mathbf{u} + \epsilon\mathbf{h}(\mathbf{u}, \mathbf{r}, t), \quad (1)$$

with  $\mathbf{u}, \mathbf{f}, \mathbf{h} \in \mathbb{R}^m$ ,  $\mathbb{D} \in \mathbb{R}^{m \times m}$ ,  $m \geq 2$ . Herein,  $\mathbf{u}(\mathbf{r}, t)$  can be viewed as a column-vector containing concentrations of chemical reagents, and  $\mathbf{f}(\mathbf{u})$  as a column-vector containing (nonlinear) reaction rates. The  $m \times m$  matrix  $\mathbb{D}$  is containing the diffusion coefficients and the term  $\epsilon\mathbf{h}(\mathbf{u}, \mathbf{r}, t)$  is a small perturbation (e.g.,  $\epsilon \ll 1$ ).

While spiral waves have been investigated extensively until today in experiments with the BZ reaction, numerical studies on spiral waves are based upon RD systems like the one given by equation (1). In the case of  $\epsilon = 0$ , system (1) allows the computational study of a huge family of spiral wave behavior. But, for  $\epsilon \neq 0$  the perturbation term  $\epsilon\mathbf{h}(\mathbf{u}, \mathbf{r}, t)$  may introduce changes to the rotational frequency and core position of spirals, leading to drift of the whole spiral pattern in space.

A first attempt to describe drift of spirals in response to any kind of perturbation theoretically, was made by Biktashev and Holden in 1995 (see in [56]). Later, Zykov and Engel developed a theory to describe feedback-mediated drift of spiral waves [123]. The asymptotic theory of spiral waves presented by Biktashev and Holden is “based on the idea of summation of elementary responses of the spiral wave core position and rotation phase to elementary perturbations of different modalities and at different times and places” (cited from [48, p. 1, right column]).

In succession, Biktashev and colleagues introduced and developed the mathematical concept of response functions (RF) [48, 57, 58, 124]. Both experimental as well numerical investigations pointed out the significant insensitivity of spiral waves to perturbations that are spatially distant from the core (see also section 1.1 in the introduction part). Biktashev has been presuming a fast decay of the RFs with distance from the core already in his thesis [125]. This behavior of spiral waves reflects some kind of wave-particle dualism [48]. This is the case, since on the one hand spirals are non-localized objects characterized by rotating waves of activity propagating into the whole medium, but on the other hand they behave like localized (particle-like) objects represented by the central core of the spiral wave.

In the next section, I will cover linear stability of unperturbed spiral waves based upon the system (1) with  $\epsilon = 0$ . This will lead to formulation of the Goldstone modes and the response functions for unperturbed spiral waves. Henceforth, linear stability analysis for spiral waves under generic perturbations ( $\epsilon \neq 0$ ) will be considered in section 2.3. This approach will help us derive generic equations of motion for the phase  $\Phi$  and the position of the core center  $\mathbf{R}$  of rigidly rotating spiral waves under the influence of perturbations. In order to illustrate the power of thus derived equations of motion, some example perturbations will be considered (see in section 2.4). These examples include time-periodic stimulations, inhomogeneous media, and the influence of boundaries. The general asymptotic theory for spiral waves under perturbation was primarily elaborated by Biktashev and Holden [56]. In this publication further details can be found on what I shall discuss more briefly in sections 2.2 - 2.4. A short summary of numerical methods for computation of RFs will be delivered in section 2.5, the details of which have been worked out by Biktasheva and colleagues in references [57, 58].

## 2.2 STABILITY OF UNPERTURBED SPIRALS

A solution to system (1) with  $\epsilon = 0$  can be given by rigidly rotating spiral waves, mathematically represented in the form

$$\mathbf{u}(\mathbf{r}, t) = \mathbf{U}(\mathbf{r}, t) = \mathbf{U}(\rho, \vartheta + \omega t). \quad (2)$$

Here,  $\rho = \rho(\mathbf{r})$  and  $\vartheta = \vartheta(\mathbf{r})$  are polar coordinates in the  $(x, y)$ -plane. The vector function  $\mathbf{U}$  is  $2\pi$ -periodic with respect to the angular argument. In a next step, Biktashev and Holden formulated a stability postulate [56]: Any solution to (1) at  $\epsilon = 0$  with initial conditions sufficiently close to (2) tends in the limit of  $t \rightarrow \infty$  to a solution that is an element of the manifold

$$\mathbf{U}_{\delta\mathbf{r}, \delta t}(\mathbf{r}, t) = \mathbf{U}(\mathbf{r} - \delta\mathbf{r}, t - \delta t), \quad (3)$$

with arbitrary constant variations in space  $\delta\mathbf{r}$  and time  $\delta t$ . The now following analysis grounds on this stability postulate and treats the behavior of the solutions to (1) at  $\epsilon = 0$  from initial conditions given by

$$\mathbf{u}(\mathbf{r}, 0) = \mathbf{U}(\mathbf{r}, 0) + \mathbf{v}_0(\mathbf{r}). \quad (4)$$

A linear approximation in the small variable  $\mathbf{v}_0$  is now leading to solutions of the system (1) represented by

$$\mathbf{u} = \mathbf{U}(\rho, \vartheta + \omega t) + \mathbf{v}(\mathbf{r}, t). \quad (5)$$

This yields a linear evolution equation for the perturbation  $\mathbf{v}(\mathbf{r}, t)$ ,

$$\partial_t \mathbf{v} = \mathcal{L} \cdot \mathbf{v}, \quad (6)$$

with the linear operator  $\mathcal{L}$  that is given by

$$\mathcal{L} = \mathbb{D}\Delta \mathbf{v} + \mathbb{F}[\mathbf{U}(\rho, \vartheta + \omega t)] \cdot \mathbf{v}. \quad (7)$$

Here,  $\mathbb{F}[\mathbf{U}] \equiv \partial_{\mathbf{u}} \mathbf{f}(\mathbf{u})|_{\mathbf{u}=\mathbf{U}}$  depicts the Jacobian matrix containing partial derivatives of the reaction terms evaluated at the rigidly rotating spiral solution (2).

Next, the stability analysis for the solution (2) is transformed to the analysis of the linear system (6) and (7). The linear stability problem is at best performed after a transition to a rotating coordinate system that can be written in the following form

$$\begin{aligned} t &\rightarrow \tilde{t}: & \tilde{t} &= t, \\ \mathbf{r} &\rightarrow \tilde{\mathbf{r}}: & \tilde{\rho}(\tilde{r}) &= \rho(\mathbf{r}), \\ && \tilde{\vartheta}(\tilde{\mathbf{r}}) &= \vartheta(\mathbf{r}) + \omega t. \end{aligned} \quad (8)$$

Performing this coordinate transformation, and for convenience omitting the  $\sim$ -symbols, yields the linearized equation

$$\partial_t \mathbf{v} = \mathcal{L} \cdot \mathbf{v}, \quad (9)$$

with the linear operator in the rotating coordinate frame,

$$\mathcal{L} = \mathbb{D}\Delta \mathbf{v} - \omega \partial_\vartheta \mathbf{v} + \mathbb{F}[\mathbf{U}] \cdot \mathbf{v}. \quad (10)$$

Since the linear operator  $\mathcal{L}$  in (10) is independent of time  $t$ , it is sufficient to seek for the spectrum of the operator in order to solve the linear stability problem. The stability postulate which was defined above demands that the operator  $\mathcal{L}$  does not possess any eigenvalue with a positive real part. The symmetry of the problem then leads to three non-decaying eigenfunctions and their corresponding eigenvalues (both in the Cartesian as well in the rotating coordinate frame):

$$\begin{aligned} \mathbf{V}_0 &= -\frac{1}{\omega} \partial_t \mathbf{U}(\mathbf{r}, t) \\ &= -\partial_\vartheta \mathbf{U}(\rho, \vartheta)|_{t=0}, & \lambda &= 0, \\ \mathbf{V}_{+1} &= -\frac{1}{2} e^{-i\omega t} (\partial_x - i\partial_y) \mathbf{U}(\mathbf{r}, t) \\ &= -\frac{1}{2} e^{-i\vartheta} \left( \partial_\rho - \frac{i}{\rho} \partial_\vartheta \right) \mathbf{U}(\rho, \vartheta)|_{t=0}, & \lambda &= +1, \\ \mathbf{V}_{-1} &= -\frac{1}{2} e^{+i\omega t} (\partial_x + i\partial_y) \mathbf{U}(\mathbf{r}, t) \\ &= -\frac{1}{2} e^{+i\vartheta} \left( \partial_\rho + \frac{i}{\rho} \partial_\vartheta \right) \mathbf{U}(\rho, \vartheta)|_{t=0}, & \lambda &= -1. \end{aligned} \quad (11)$$

These functions are also called the Goldstone modes which are the critical eigenfunctions of the linearized operator  $\mathcal{L}$ , that is

$$\mathcal{L} \cdot \mathbf{V}_\lambda = i\omega \lambda \mathbf{V}_\lambda, \quad \lambda = 0, \pm 1. \quad (12)$$

Here, we have the rotational Goldstone mode  $\mathbf{V}_0$  and the two translational Goldstone modes  $\mathbf{V}_{\pm 1}$ .

Analogously, one can formulate the eigenvalue problem for the adjoint linearized operator which is given by

$$\mathcal{L}^\dagger = \mathbb{D}\Delta + \omega\partial_\vartheta + \mathbb{F}^\dagger [\mathbf{U}]. \quad (13)$$

The critical eigenfunctions  $\mathbf{W}_\lambda$  with their corresponding critical eigenvalues  $\lambda = 0, \pm 1$  which are solving the eigenvalue problem

$$\mathcal{L}^\dagger \cdot \mathbf{W}_\lambda = -i\omega\lambda \mathbf{W}_\lambda \quad (14)$$

are denoted as the “response functions” (RF) of spiral waves [48]. The RFs yet have to be chosen such that they are bi-orthogonal to the previously introduced Goldstone modes,

$$(\mathbf{W}_\lambda, \mathbf{V}_\mu) = \delta_{\lambda\mu}, \quad \lambda, \mu \in \{0, +1, -1\}. \quad (15)$$

At the moment, these RFs are unknown and will be calculated numerically later. However, we may write the functional  $(\bullet, \bullet)$  in an integral form with some regular functions  $\mathbf{Y}_\lambda$  representing the RFs. Thus we get

$$(\mathbf{W}_\lambda, \bullet) = \int \langle \mathbf{Y}_\lambda, \bullet \rangle d^2\mathbf{r}. \quad (16)$$

Here,  $\langle \bullet, \bullet \rangle$  denotes the inner product in  $\mathbb{C}^m$ , with  $m \geq 2$ . The regular functions  $\mathbf{Y}_\lambda$  must obey to an analogous eigenvalue equation like the one defining the RFs (14),

$$\mathcal{L}^\dagger \cdot \mathbf{Y}_\lambda = \lambda^* \mathbf{Y}_\lambda. \quad (17)$$

Contrary to the Goldstone modes, both the RFs  $\mathbf{W}_\lambda$  and the regular functions  $\mathbf{Y}_\lambda$  representing the RFs are decaying rapidly and are vanishing as  $\rho \rightarrow \infty$ . The characteristic distance at which these functions decay are denoted as the sensitivity distance [56]. This characteristic decay of the RFs is reinforced by the experimental observation [44, 47] that spiral waves, respectively scroll waves, are only sensitive to such perturbations which are not farther away from the core than the sensitivity distance. Later, we will see that RFs for spirals are centered at the spiral wave core.

### 2.3 STABILITY OF PERTURBED SPIRALS UNDER GENERIC PERTURBATIONS

In the last section, I introduced the asymptotic theory for spirals in the framework of an RD system (1) with vanishing perturbation term ( $\epsilon = 0$ ), as it was evolved by Biktashev and Holden (see in [56]). The purpose of the now following section is to derive equations of motion for the phase  $\Phi$  and position vector  $\mathbf{R}$  of the spiral core when the parameter  $\epsilon$  is not vanishing but small. The perturbative derivation of these motion equations was once again introduced primarily by Biktashev and Holden in [56].

Before discussing derivation of such equations of motion, let us prepend some important notions. In the previous section we became acquainted with the Goldstone modes of rigidly rotating spiral waves. These are given by the equations (11), as the critical eigenfunctions of the linearized operator  $\mathcal{L}$ . Any solution on the plane  $(x, y)$  then shall be generated by the two translational Goldstone modes  $\mathbf{V}_{\pm 1}$ , yielding

$$\begin{aligned}\mathbf{V}_x &= \mathbf{V}_{+1}e^{i\omega t} + \mathbf{V}_{-1}e^{-i\omega t}, \\ \mathbf{V}_y &= i\mathbf{V}_{+1}e^{i\omega t} - i\mathbf{V}_{-1}e^{-i\omega t}.\end{aligned}$$

Moreover, the linear approximation  $\mathbf{v}(\mathbf{r}, t)$  that was introduced in the slightly perturbed spiral solution (5) shall be generated by all three Goldstone modes as follows (at order zero):

$$\mathbf{v}(\mathbf{r}, t) = c_0 \mathbf{V}_0(\mathbf{r}) + c_{+1} e^{i\omega t} \mathbf{V}_{+1}(\mathbf{r}) + c_{-1} e^{-i\omega t} \mathbf{V}_{-1}(\mathbf{r}) + o(1). \quad (18)$$

The above relation holds for  $t \rightarrow \infty$ , and the coefficients  $c_{0,\pm 1}$  have to be determined as the convolution of the RFs  $\mathbf{W}_{0,\pm 1}$  with the initial conditions  $\mathbf{v}_0 = \mathbf{v}(\mathbf{r}, 0)$ , that is

$$c_{0,\pm 1} = (\mathbf{W}_{0,\pm 1}, \mathbf{v}_0). \quad (19)$$

Additionally, we have seen that the RFs  $\mathbf{W}_\lambda$  ( $\lambda = 0, \pm 1$ ) are eigenfunctions to the adjoint operator  $\mathcal{L}^\dagger$ . Thus:

$$(\mathbf{W}_\lambda, \mathcal{L} \cdot \mathbf{v}) = (\mathbf{W}_\lambda, \partial_t \mathbf{v}) = \partial_t (\mathbf{W}_\lambda, \mathbf{v}) = \lambda (\mathbf{W}_\lambda, \mathbf{v}). \quad (20)$$

Now let us proceed with the perturbed problem (1) with  $\epsilon \neq 0$ . Notice that the regular perturbation technique will not be successful in this case since the perturbed solutions will be growing infinitely (“secular growth problem”) [126, 127]<sup>1</sup>. Hereafter, the singular perturbation technique will be introduced and will lead to the equations of motion that we seek.

Let us consider the unperturbed spiral core center to be located initially at the origin of the coordinate frame  $\mathbf{u}(\mathbf{r}, 0) = \mathbf{U}(\mathbf{r}, 0)$ . Hence, taking into account the linearization at this core position,

$$\mathbf{u}(\mathbf{r}, t) = \mathbf{U}(\mathbf{r}, t) + \epsilon \mathbf{v}(\mathbf{r}, t), \quad (21)$$

leads in the rotating coordinate frame to the problem

$$\partial_t \mathbf{v} = \mathcal{L} \cdot \mathbf{v} + \mathbf{h}[\mathbf{U}(\mathbf{r}), \mathbf{r}, t]. \quad (22)$$

Therefore, with the aid of the identities (20), we get

$$\partial_t (\mathbf{W}_\lambda, \mathbf{v}) = \lambda (\mathbf{W}_\lambda, \mathbf{v}) + (\mathbf{W}_\lambda, \mathbf{h}). \quad (23)$$

We now are able to solve this equation explicitly. Provided that the sets  $\{\mathbf{W}_\lambda | \lambda = 0, \pm 1\}$  and  $\{\mathbf{V}_\lambda | \lambda = 0, \pm 1\}$  constitute bases of the corresponding

---

<sup>1</sup> See also the scholarpedia article on multiple scale analysis by Carson C. Chow ([http://www.scholarpedia.org/article/Multiple\\_scale\\_analysis](http://www.scholarpedia.org/article/Multiple_scale_analysis)).

spaces, the general solution to the linear perturbation problem (22) is given by

$$\mathbf{v}(t) = \sum_{\lambda} \mathbf{V}_{\lambda} e^{i\omega\lambda t} \int_0^t e^{-i\omega\lambda\tau} (\mathbf{W}_{\lambda}, \mathbf{h}(\tau)) d\tau. \quad (24)$$

The problem that renders the regular perturbation technique unsuccessful appears now. As  $t \rightarrow \infty$ , the solution (24) grows infinitely, even if the perturbation  $\mathbf{h}$  remains uniformly bounded in time. We see the secular growth exemplarily by projecting the above solution into  $\mathbf{W}_0$ , that is

$$(\mathbf{W}_0, \mathbf{v}(t)) = \int_0^t (\mathbf{W}_0, \mathbf{h}(\tau)) d\tau. \quad (25)$$

The above projection goes to infinity as time goes to infinity, provided that  $(\mathbf{W}_0, \mathbf{h}(\tau))$  is a non-zero constant.

To solve this issue, let us consider now the singular perturbation technique. What follows was presented by Biktashev and Holden in [56] and was also used by them in order to derive equations of motion for scroll wave filaments [89].

The initial idea is to expand the solutions to the system (1) in the vicinity of the solution manifold (3) in the following form:

$$\begin{aligned} \mathbf{u}(\mathbf{r}, t) &= \mathbf{U} \left[ \mathbf{r} - \mathbf{R}(t), t - \frac{\Phi(t)}{\omega} \right] + \epsilon \mathbf{v}(\mathbf{r}, t) \\ &= \mathbf{U} [\rho(\mathbf{r} - \mathbf{R}(t)), \vartheta(\mathbf{r} - \mathbf{R}(t)) + \omega t - \Phi(t)] + \epsilon \mathbf{v}(\mathbf{r}, t). \end{aligned} \quad (26)$$

In this expansion, the new coordinates  $\mathbf{R}(t)$  and  $\Phi$  appear. While  $\mathbf{R} = (X, Y)$  gives the momentary center coordinate of the spiral core,  $\Phi$  denotes the current rotation phase of the spiral. The approximation vector  $\mathbf{v}$  is chosen to be orthogonal to the RFs,

$$(\mathbf{W}_{0,\pm 1}, \mathbf{v}) = 0. \quad (27)$$

In addition, we will represent the RFs  $\mathbf{W}_{\lambda}$  by regular functions  $\mathbf{Y}_{\lambda}$  ( $\lambda = 0, \pm 1$ ) as follows

$$(\mathbf{W}_{\lambda}, \bullet) = \int \langle \mathbf{Y}_{\lambda} [\rho(\mathbf{r} - \mathbf{R}), \vartheta(\mathbf{r} - \mathbf{R}) + \omega t - \Phi], \bullet \rangle d^2 \mathbf{r}. \quad (28)$$

Equation (28) indicates that the RFs, which were constant in the co-rotating frame, now become rotating in the original frame. Under the assumption that the drifting spiral core does not leave the  $\epsilon$ -vicinity of the manifold (5), we shall insert (26) into the RD system (1), just keep terms at the order  $\epsilon$ , and hence get

$$\begin{aligned} \epsilon \partial_t \mathbf{v} &= \epsilon \left\{ \mathcal{L} \cdot \mathbf{v} + \mathbf{h} \left[ \mathbf{U} \left( \mathbf{r} - \mathbf{R}, t - \frac{\Phi}{\omega} \right), \mathbf{r}, t \right] + \partial_{\vartheta} \mathbf{U} \left( \mathbf{r} - \mathbf{R}, t - \frac{\Phi}{\omega} \right) \partial_t \Phi(t) + \right. \right. \\ &\quad \left. \left. \partial_x \mathbf{U} \left( \mathbf{r} - \mathbf{R}, t - \frac{\Phi}{\omega} \right) \partial_t X(t) + \partial_y \mathbf{U} \left( \mathbf{r} - \mathbf{R}, t - \frac{\Phi}{\omega} \right) \partial_t Y(t) \right\} + \mathcal{O}(\epsilon^2). \end{aligned} \quad (29)$$

By transforming the above equation to the coordinate frame of reference associated with the spiral core,

$$\begin{aligned}\tilde{t} &= t, \\ \rho(\tilde{\mathbf{r}}) &= \rho(\mathbf{r} - \mathbf{R}), \\ \vartheta(\tilde{\mathbf{r}}) &= \vartheta(\mathbf{r} - \mathbf{R}) + \omega t - \Phi,\end{aligned}$$

and reminding ourselves to the definitions for the Goldstone modes (11), we arrive at

$$\begin{aligned}\epsilon \partial_{\tilde{t}} \mathbf{v} = & \epsilon \left\{ \tilde{\mathcal{L}} \cdot \mathbf{v} + \mathbf{h}(\mathbf{U}(\tilde{\mathbf{r}}), \mathbf{r}, t) - \omega^{-1} \tilde{\mathbf{V}}_0(\tilde{\mathbf{r}}) \partial_t \Phi(t) \right. \\ & - \left[ \tilde{\mathbf{V}}_{+1}(\tilde{\mathbf{r}}) e^{i(\omega t - \Phi)} + \tilde{\mathbf{V}}_{-1}(\tilde{\mathbf{r}}) e^{-i(\omega t - \Phi)} \right] \partial_t X(t) \\ & - i \left[ \tilde{\mathbf{V}}_{+1}(\tilde{\mathbf{r}}) e^{i(\omega t - \Phi)} - \tilde{\mathbf{V}}_{-1}(\tilde{\mathbf{r}}) e^{-i(\omega t - \Phi)} \right] \partial_t Y(t) \Big\} \\ & + \mathcal{O}(\epsilon^2).\end{aligned}\quad (30)$$

We approach to the equations of motion for the spiral core position  $\mathbf{R}$  and rotation phase  $\Phi$ , if we multiply both sides of equation (30) with the RFs  $\tilde{\mathbf{W}}_{0,\pm 1}$  in the sense of an inner product  $(\tilde{\mathbf{W}}_{0,\pm 1}, \bullet)$ , apply the conditions (20) and (27), and use the bi-orthogonality relation of eigenfunctions and adjoint eigenfunctions:

$$\begin{aligned}\partial_t \Phi &= \epsilon \omega (\tilde{\mathbf{W}}_0, \mathbf{h}) + \mathcal{O}(\epsilon^2), \\ \partial_t X &= \epsilon \Re \left\{ e^{-i(\omega t - \Phi)} (\tilde{\mathbf{W}}_1, \mathbf{h}) \right\} + \mathcal{O}(\epsilon^2), \\ \partial_t Y &= \epsilon \Im \left\{ e^{-i(\omega t - \Phi)} (\tilde{\mathbf{W}}_1, \mathbf{h}) \right\} + \mathcal{O}(\epsilon^2).\end{aligned}\quad (31)$$

Here, we have the real and imaginary parts,  $\Re \{ \bullet \}$  and  $\Im \{ \bullet \}$  respectively. A transformation back to the original coordinate frame and using the integral expression for the adjoint eigenvectors, given by (28), yields

$$\begin{aligned}\partial_t \Phi &= \epsilon \int \langle \tilde{\mathbf{Y}}_0 [\rho(\mathbf{r} - \mathbf{R}), \vartheta(\mathbf{r} - \mathbf{R}) + \omega t - \Phi], \mathbf{h} \rangle d^2 \mathbf{r} + \mathcal{O}(\epsilon^2), \\ \partial_t X &= \epsilon \Re \left\{ e^{-i(\omega t - \Phi)} \int \langle \tilde{\mathbf{Y}}_1 [\rho(\mathbf{r} - \mathbf{R}), \vartheta(\mathbf{r} - \mathbf{R}) + \omega t - \Phi], \mathbf{h} \rangle d^2 \mathbf{r} \right\} \\ &\quad + \mathcal{O}(\epsilon^2), \\ \partial_t Y &= \epsilon \Im \left\{ e^{-i(\omega t - \Phi)} \int \langle \tilde{\mathbf{Y}}_1 [\rho(\mathbf{r} - \mathbf{R}), \vartheta(\mathbf{r} - \mathbf{R}) + \omega t - \Phi], \mathbf{h} \rangle d^2 \mathbf{r} \right\} \\ &\quad + \mathcal{O}(\epsilon^2),\end{aligned}\quad (32)$$

These equations of motion under the generic perturbation  $\mathbf{h}(\mathbf{u}, \mathbf{r}, t)$  can also be written as a generic vectorial system of ordinary differential equations as follows [48, 57, 58]:

$$\begin{aligned}\partial_t \Phi &= \epsilon F_0(\mathbf{R}, \Phi), \\ \partial_t \mathbf{R} &= \epsilon \mathbf{F}_1(\mathbf{R}, \Phi),\end{aligned}\quad (33)$$

where the “forces”  $F_0$  and  $\mathbf{F}_1 = (\Re\{\mathbf{F}_1\}, \Im\{\mathbf{F}_1\})^T$  can be determined using the central moving average over the spiral wave rotation period. The latter procedure yields the formulation of the forces as convolution integrals of the RFs  $\mathbf{W}_n(\rho, \theta)$  in the co-rotating frame of reference with the generic perturbations  $\mathbf{h}(\mathbf{r}, t)$  [48, 57]:

$$\begin{aligned} F_n(\mathbf{R}, t) &= e^{in\Phi} \oint_{t-\pi/\omega}^{t+\pi/\omega} \frac{\omega d\tau}{2\pi} \int \int_{\mathcal{R}^2} d^2\mathbf{r} \\ &\times e^{-in\omega\tau} \left\langle \mathbf{W}_n(\rho(\mathbf{r} - \mathbf{R}), \theta(\mathbf{r} - \mathbf{R}) + \omega\tau - \Phi), \mathbf{h}(\mathbf{r}, \tau) \right\rangle, \end{aligned}$$

$n = 0, \pm 1.$  (34)

#### 2.4 SPECIFIC TYPES OF PERTURBATIONS

The asymptotic theory for spirals under generic perturbations shall now be illustrated by the effect of specific perturbations in time and space. Let us consider a medium which depends on space and time parametrically, mathematically formulated through

$$\partial_t \mathbf{u} = \mathbf{f}(\mathbf{u}, \alpha(t), \beta(\mathbf{r})) + \mathbb{D}\Delta \mathbf{u}. \quad (35)$$

In this equation a time-periodic stimulation is given by the function  $\alpha(t) = \epsilon A(\Omega t - \varphi)$  possessing the property of periodicity,  $A(\varphi + 2\pi) \equiv A(\varphi)$ . The spatial inhomogeneity is formalized by the parameter  $\beta(\mathbf{r}) = \epsilon B(\mathbf{r})$ . Both parametric perturbations are assumed to be small, meaning that  $\epsilon \neq 0$  holds with  $\epsilon \ll 1$ .

Let us first treat the simple case of a time-periodic stimulation in a homogeneous medium, meaning that we will assume  $\beta(\mathbf{r}) = 0$ . In this case our additive perturbation term in the RD system (1) gets

$$\mathbf{h}(\mathbf{u}, \mathbf{r}, t) = \partial_\alpha \mathbf{f}(\mathbf{u}, 0) A(\Omega t - \varphi). \quad (36)$$

Thus, if we set the current phase difference between the spiral rotation and stimulation equal to  $\phi$ , we get averaged motion equations

$$\begin{aligned} \partial_t \phi &= \omega + \epsilon F_0 - \Omega + \mathcal{O}(\epsilon^2), \\ \partial_t \bar{X} &= \epsilon |F_1| \cos \phi + \mathcal{O}(\epsilon^2), \\ \partial_t \bar{Y} &= \epsilon |F_1| \sin \phi + \mathcal{O}(\epsilon^2), \end{aligned}$$

where the parameters  $F_n$  with  $n = 0, 1$  are given by

$$F_n\{\alpha\} = \oint \int \oint \left\langle \tilde{\mathbf{Y}}_n(\rho, \xi), \partial_\alpha \mathbf{f}[\mathbf{U}(\rho, \xi), 0] \right\rangle d\xi \rho d\rho A(\eta) e^{-in\eta} d\eta. \quad (37)$$

Now, let us proceed further and consider a perturbation approach in which the time-periodic stimulation is accompanied by a spatial inhomogeneity. In

this case the parametric perturbation term  $\beta(\mathbf{r})$  is non-zero. Therefore, we get

$$\mathbf{h}(\mathbf{u}, \mathbf{r}, t) = \partial_\alpha \mathbf{f}(\mathbf{u}, 0, 0) A(t) + \partial_\beta \mathbf{f}(\mathbf{u}, 0, 0) B(\mathbf{r}) \quad (38)$$

for the additive perturbation term of the RD system (1). Once this relation is determined, we are able to calculate the forces acting on the spiral core via the equations (32). The calculation then leads to a superposition of the forces in the following form:

$$F_n\{\alpha, \beta\} = F_n\{\alpha\} + F_n(\beta), \quad n = 0, 1. \quad (39)$$

While the term for the time-periodic stimulation  $F_n\{\alpha\}$  is defined by equation (37), the term for perturbation through spatial inhomogeneity  $F_n\{\beta\}$  is defined as

$$\begin{aligned} F_n\{\beta\} &= \oint \int \oint \left\langle \tilde{\mathbf{Y}}_n(\rho, \xi), \partial_\alpha \mathbf{f}[\mathbf{U}(\rho, \xi), 0] \right\rangle \\ &\quad \times B[X + \rho \cos(\xi - \eta), Y + \rho \sin(\xi - \eta)] \\ &\quad \times d\xi \rho d\rho A(\eta) e^{-in\eta} d\eta. \end{aligned} \quad (40)$$

The resulting equations of motion then can be formulated as follows (omitting dash signs over  $\mathbf{R}$ ,  $X$ , and  $Y$ ):

$$\begin{aligned} \partial_t \phi &= \Omega_0(\mathbf{R}) - \Omega + (\partial_t \mathbf{R} \cdot \nabla) \arg[F_1\{\alpha\}], \\ \partial_t X &= C_x(\mathbf{R}) + c(\mathbf{R}) \cos \phi, \\ \partial_t Y &= C_y(\mathbf{R}) + c(\mathbf{R}) \sin \phi. \end{aligned} \quad (41)$$

In these equations the term  $\Omega_0(\mathbf{R})$  is the local resonance frequency,

$$\Omega_0(\mathbf{R}) = \omega_\beta(\mathbf{R}) + \epsilon F_0\{\alpha\} = \omega + \epsilon F_0\{\alpha\} + \epsilon F_0\{\beta\}(\mathbf{R}), \quad (42)$$

where  $c(\mathbf{R})$  denotes the resonance-induced drift velocity,

$$c(\mathbf{R}) = \epsilon |F_1\{\alpha\}(\mathbf{R})|, \quad (43)$$

and  $C_x$  and  $C_y$  are the velocities for the drift caused by inhomogeneities,

$$C_x(\mathbf{R}) + iC_y(\mathbf{R}) = \epsilon F_1\{\beta\}(\mathbf{R}). \quad (44)$$

Last but not least,  $(\partial_t \mathbf{R} \cdot \nabla) \arg[F_1\{\alpha\}]$  is an “anisotropic” term.

The set of motion equations (41) displays a superposition principle for drift forces acting on the spiral core [56]. These drift forces can stem from different kinds of sources. Nevertheless, the superposition principle holds its validity. Furthermore, it has been observed in numerical simulations that the dynamics of vortices close to the boundaries are analogous to those in media with inhomogeneities (see in [128]). Since the direction and velocity of drift for the spiral core and the deviation of its rotation frequency are determined by the position of the core with respect to boundaries, they can be described by the same terms  $\Omega_0(\mathbf{R})$ ,  $C_x(\mathbf{R})$ , and  $C_y(\mathbf{R})$  in equations (41).

In the reference [58], the authors considered special perturbations that are  $2\pi/\omega$ -periodic in time. Subsequently, they investigated such different spiral drift phenomena induced by resonance, electrophoresis, and inhomogeneity. Moreover, a quantitatively good agreement with numerical simulations in the framework of both the FitzHugh-Nagumo and the Barkley models was demonstrated.

In the following section, I will provide a short summary on the numerical calculation of the RFs as it was illustrated by Biktasheva et al. in several publications [48, 57, 58].

## 2.5 NUMERICAL COMPUTATION OF RESPONSE FUNCTIONS

Primarily, I. V. Biktasheva and V. N. Biktashev provided a method to compute RFs for the complex Ginzburg-Landau equation (CGLE) in 2003 (see [48]). In this paper, they also introduced and discussed for the first time the “wave-particle duality” which is connected to the behavior of spiral waves in generic excitable media. Then, a more thorough description of a numerical computation method for RFs, being valid for a generic class of RD models, was delivered by them in 2009 [57]. Later, Biktasheva et al. also illustrated computation of spiral wave drift velocities induced by a variety of perturbations. These drift velocities were determined with the help of numerically computed RFs in the FitzHugh-Nagumo and the Barkley models.

In this section, I shall provide a short summary of the numerical computation method for the RFs in generic RD models, as it was proposed in [57]. The interested reader seeking for further details of the procedure is referred to the literature by Biktasheva and colleagues [48, 57, 58].

Let us now introduce the ingredients needed in order to compute the RFs. These are:

### (1) Spiral wave problem in the co-rotating frame

In the coordinate system that is co-rotating with the initial phase and angular velocity  $\omega$  of the spiral, the polar angle is given by  $\theta = \vartheta + \omega t$ . The corresponding spiral wave solution in this frame gets time-independent and satisfies the equation

$$\mathbf{f}(\mathbf{U}) - \omega \partial_\theta \mathbf{U} + \mathbb{D}\Delta \mathbf{U} = 0. \quad (45)$$

The unknowns in this equation are the field  $\mathbf{U}(\rho, \theta)$  and the scalar angular velocity  $\omega$ .

### (2) Eigenvalue problem for the linearized operator

The linear stability spectrum of a steadily rotating spiral is defined by the eigenvalue equation

$$\mathcal{L} \cdot \mathbf{V} = \lambda_n \mathbf{V}, \quad (46)$$

with the linearized operator given by

$$\mathcal{L} = \mathbb{D}\Delta - \omega\partial_\theta + \partial_u \mathbf{f}(\mathbf{U}). \quad (47)$$

The eigenvectors solving the problem are the Goldstone modes (GMs)  $\{\mathbf{V}_n, n = 0, \pm 1\}$ , with their corresponding eigenvalues  $\lambda_n = in\omega$ . (see equations (11)).

(3) *Eigenvalue problem for the adjoint linearized operator:*

Analogously to the previous paragraph, one can formulate an eigenvalue problem

$$\mathcal{L}^\dagger \cdot \mathbf{W}_n = \mu_n \mathbf{W}_n \quad (48)$$

for the adjoint linearized operator

$$\mathcal{L}^\dagger = \mathbb{D}\Delta + \omega\partial_\theta + (\partial_u \mathbf{f}(\mathbf{U}))^T. \quad (49)$$

The vectors solving this eigenvalue problem are the response functions (RFs)  $\{\mathbf{W}_n, n = 0, \pm 1\}$  with their corresponding eigenvalues  $\mu_n = -in\omega$ .

The complete system containing the three equations (45), (46), and (48) are now discretized and numerically solved on the same polar grid  $(\rho_j, \theta_k) = (j\Delta k, k\Delta\theta)$  where  $0 < j \leq N_\rho$  and  $0 \leq k < N_\theta$  plus the center point  $\rho = 0$ . The nonlinear problem (45) is considered on a disk  $\rho \leq \rho_{\max}$ , with homogeneous no-flux boundary conditions,  $\partial_\rho \mathbf{U}(\rho_{\max}, \theta) = 0$ . The linearized problems (46) and (48) are solved in the same domain with similar boundary conditions, while the critical eigenvalues and eigenvectors of the discretized operators  $\mathcal{L}$  and  $\mathcal{L}^\dagger$  are determined by using a complex shift and Caylay transform. Let the matrix  $\mathbb{L}$  be either the discretization of  $\mathcal{L}$  or  $\mathcal{L}^\dagger$ , then the complex shift is defined as

$$\mathbb{A} = \mathbb{L} + i\kappa\mathbb{I}, \quad (50)$$

and the subsequent Caylay transform as

$$\mathbb{B} = \frac{\eta\mathbb{I} + \mathbb{A}}{\xi\mathbb{I} + \mathbb{A}}. \quad (51)$$

In these two equations,  $\kappa$ ,  $\xi$ , and  $\eta$  are real-valued parameters and  $\mathbb{I}$  the identity matrix. Let us consider  $\lambda$ ,  $\alpha$ , and  $\beta$  as eigenvalues of  $\mathbb{L}$ ,  $\mathbb{A}$ , and  $\mathbb{B}$ , respectively. Then

$$\begin{aligned} \alpha &= \lambda + i\kappa, \\ \beta &= \frac{\eta + \alpha}{\xi + \alpha} \end{aligned}$$

holds. Then, the selected eigenvalues and eigenvectors of the such constructed matrices  $\mathbb{B}$  are calculated by the Arnoldi method, using ARPACK [129].

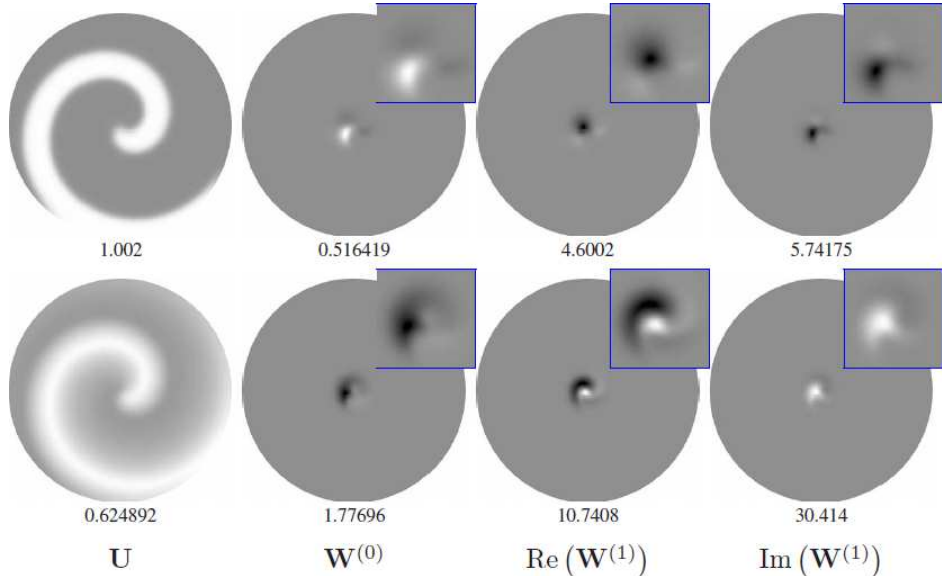


**Figure 13:** Solution of the nonlinear problem (45), and the adjoint linearized problem (48) for calculation of the response functions. Achieved in the Barkley system for  $\rho_{\max} = 12.8$ ,  $N_\rho = 1280$ ,  $N_\theta = 64$  and shown as density plots. Numbers under the density plots are their amplitudes  $A$ : white color in the plots correspond to the value  $A$  and black corresponds to the value  $-A$  of the designated field. Upper row: first components ( $u$ ); lower row: second components ( $v$ ). The central areas of RFs  $W_n$ ,  $n = 0, 1$ , are also shown magnified in the small corner panels. Figure is reprinted from [58] and licensed under CC BY 3.0.

Now, the Goldstone modes are analytically obtained by numerical differentiation of the numerical spiral wave solution  $\hat{U}$ , that is

$$\begin{aligned}\check{V}_0 &= -\partial_\theta \hat{U}(\rho, \theta), \\ \check{V}_{\pm 1} &= -\frac{1}{2} e^{\mp i\theta} \left( \partial_\rho \mp \frac{i}{\rho} \partial_\theta \right) \hat{U}(\rho, \theta),\end{aligned}$$

with the differentiation implemented using the same discretization schemes as in the calculations. The response functions  $\hat{W}_k$ , calculated by ARPACK, are normalized with respect to the analytically obtained Goldstone modes  $\check{V}_k$ , such that

$$\langle \hat{W}_k, \check{V}_k \rangle = 1, \quad k = 0, \pm 1$$

holds. Finally, the Goldstone modes  $\hat{V}_k$ , computed by ARPACK, are normalized with respect to the normalized response functions, such that

$$\langle \hat{W}_k, \hat{V}_k \rangle = 1, \quad k = 0, \pm 1$$

holds.

In summary, the following points are achieved by the above procedure: (1) a numerical solution for the spiral wave problem (45) together with the angular velocity  $\omega$ , (2) analytical determination of the Goldstone modes  $\check{V}_k$ ,

(3) numerical determination of normalized Goldstone modes  $\hat{\mathbf{V}}_k$ , and (4) determination of normalized response functions  $\hat{\mathbf{W}}_k$ .

Without going too much into detail with the numerical tests performed by Biktaşheva et al., I solely present here one typical result of the numerically calculated RFs originally published in [57, 58]. Figure 13, taken from [58], displays spiral wave solutions together with the RFs in a spatial domain defined by  $\rho_{\max} = 25$ ,  $N_\rho = 1280$ , and  $N_\theta = 64$ . The RFs  $\hat{\mathbf{W}}$  are localized in a small area at the spiral core while tending to zero outside of that region. These results were achieved for the Barkley model.



# 3

## THEORETICAL APPROACHES ON SCROLL WAVE FILAMENTS

---

### 3.1 INTRODUCTION

Primarily, Yakushevich investigated some basic elastic properties of scroll wave filaments in excitable media [98]. He did these investigations in the framework of the complex Ginzburg-Landau equation (CGLE). Under the assumption that the waves near the filaments behave like vortices (spiral waves), he showed that the relaxation velocity of the filament will be proportional to the medium diffusion coefficient and to the filament curvature. Yakushevich's approach for the case of a scroll ring filament, which is assumed to be relatively large ( $R \gg 1$ ) and planar, yields the radial relaxation velocity

$$v_R = \frac{dR}{dt} = \frac{D_0}{R}. \quad (52)$$

Since the real part of the complex-valued diffusion coefficient in the CGLE is positive,  $D_0 > 0$ , this result implies that the corresponding scroll ring filament will continuously contract in time. For the complete derivation see in [98].

In 1988, Keener presented derivation of motion equations for scroll ring filaments [99]. His derivation is based upon multiscale or averaging methods valid in the asymptotic limit of small curvature and torsion of corresponding filaments. As an example, the generic equations of motion by Keener led to specific evolution equations for the radius  $R(t)$  and the axial position  $z(t)$  of planar untwisted scroll ring filaments,

$$\begin{aligned} \frac{dR}{dt} &= -\frac{\alpha}{R}, \\ \frac{dz}{dt} &= \frac{\beta}{R}. \end{aligned} \quad (53)$$

A summary of Keener's approach together with the specific form of the coefficients  $\alpha$  and  $\beta$  will be delivered in the next section.

An extension to the asymptotic theory of scroll filaments was provided by Biktashev and colleagues in 1994 [89]. In this work, the authors proposed a monotonic change of the total filament length, independently of initial conditions. Furthermore, they denoted the coefficient  $\alpha$  as the filament tension governing the rate of shrinking (positive filament tension,  $\alpha > 0$ ) or expansion (negative filament tension,  $\alpha < 0$ ) for the filament. A summary of the approach by Biktashev and co-workers will be delivered in the second section of this chapter (section 3.3).

Later, H. Henry and V. Hakim delivered a thorough approach on the linear stability of straight scroll waves in the framework of the Barkley reaction-diffusion model [86, 87]. In these publications, they considered three types of instabilities emerging for perturbed straight scroll waves. In case of the translation bands, the emerging instability is equivalent to the negative line tension instability [89, 90, 91, 92], which eventually leads to scroll wave turbulence [93, 94]. In case of the meander bands, the scroll waves re-stabilize and their filaments maintain helical morphologies after the appearance of the instability. Thirdly, they also considered the twisting of filaments and have shown that twist-induced instability emerges in the form of a super-critical bifurcation, which is termed as the “sproing” bifurcation [77]. A summary of the approach by Henry and Hakim will be provided in section 3.4.

Recently, H. Dierckx and H. Verschelde delivered a much more generic derivation of motion equations for filaments of scroll waves and scroll rings [100]. I will not discuss the approach by them in my thesis. The interested reader is referred to the latter citation.

### 3.2 APPROACH BY KEENER

Derivation of motion equations for planar scroll ring filaments were achieved primarily by Keener in the asymptotic limit of small curvature and torsion [99]. Keener’s approach is based upon behavior of solutions to generic reaction-diffusion (RD) systems, given by

$$\partial_t \mathbf{u}(\mathbf{r}, t) = \mathbb{D} \Delta \mathbf{u}(\mathbf{r}, t) + \mathbf{f}[\mathbf{u}(\mathbf{r}, t)]. \quad (54)$$

In this RD system we have the vector  $\mathbf{u}(\mathbf{r}, t) \in \mathbb{R}^m$  (e.g. the vector of some chemical concentrations), the vector of functions  $\mathbf{f}[\mathbf{u}(\mathbf{r}, t)] \in \mathbb{R}^m$  (e. g. non-linear reaction rates), the  $m \times m$  diagonal matrix,  $\mathbb{D} \in \mathbb{R}^{m \times m}$ , of diffusion coefficients (e.g. of the corresponding chemical species), while dimension of the RD system is  $m \geq 2$ . The spatial coordinate system is two- or three-dimensional, that is  $\mathbf{r} \in \mathbb{R}^n$  with  $n = 2$  or  $n = 3$ . Hence, the Laplace operator  $\Delta$  is defined in two or three spatial dimensions.

This RD system is equivalent to the one which was introduced in the previous chapter, except for the perturbation term  $\epsilon \mathbf{h}(\mathbf{u}, \mathbf{r}, t)$  (see chapter 2, specifically equation (1)). Therefore, the linear stability for unperturbed spiral solutions presented in section (2.2) will be helpful for the now following summary of the approach by Keener.

On our way to the sought filament motion equations, we have to introduce some assumptions. The first assumption is to consider a three-dimensional solution of the system (54) as a spiralling scroll wave which is rotating about an axis represented by a slowly moving curve in three-dimensional space. Secondly, curvature and torsion of the curve are assumed to be small. This curve now defines the filament of the scroll wave.

Let us now consider the filament to be defined by the position vector  $\mathbf{R}(s, t)$ . Here, we have the parametrization of the filament curve, in space and time, given by the arc length  $s$  and time  $t$ , respectively. The curvature of the filament will be denoted by  $\kappa$  and the torsion by  $\tau$ . In the following, the coordinate representation

$$\mathbf{X} = \mathbf{R} + p\mathbf{N} + q\mathbf{B},$$

with  $\mathbf{N}$  being the normal vector and  $\mathbf{B}$  the bi-normal vector to the curve, will be taken into account. Parameterizations  $p$  and  $q$  are characterizing the plane which is normal to the curve at any given arc length  $s$ . Note that this coordinate representation is orthogonal only in the vicinity of the curve, but possesses singularities at distances more than one curvature radius away from the curve  $\mathbf{X} = \mathbf{R}$ .

Now, we take into account the introduced coordinate frame and the Frenet-Serret equations,

$$\begin{aligned}\frac{d\mathbf{R}}{ds} &= \mathbf{T}, \\ \frac{d\mathbf{T}}{ds} &= \kappa\mathbf{N}, \\ \frac{d\mathbf{N}}{ds} &= -\kappa\mathbf{T} + \tau\mathbf{B}, \\ \frac{d\mathbf{B}}{ds} &= -\tau\mathbf{N},\end{aligned}\tag{55}$$

for the position vector  $\mathbf{R}$ , the tangent vector  $\mathbf{T}$ , the normal vector  $\mathbf{N}$ , and the bi-normal vector  $\mathbf{B}$ . By all the above assumptions, Keener was able to express both the gradient operator as well the Laplace operator with respect to the coordinates  $s$ ,  $p$ , and  $q$ . In particular, the gradient operator becomes

$$\nabla \cdot \mathbf{u} = H\mathbf{u} \cdot \mathbf{T} + \frac{\partial \mathbf{u}}{\partial p} \cdot \mathbf{N} + \frac{\partial \mathbf{u}}{\partial q} \cdot \mathbf{B}.\tag{56}$$

Here, we have the first order differential operator  $H\mathbf{u}$ , represented by

$$H\mathbf{u} = \frac{1}{1 - \kappa p} \left( \frac{\partial \mathbf{u}}{\partial s} - \tau \frac{\partial \mathbf{u}}{\partial \theta} \right),\tag{57}$$

where  $\theta$  is the angular variable in the polar coordinate frame of the  $p$ - $q$ -plane,  $p = \rho \cos \theta$ ,  $q = \rho \sin \theta$ . Consequently,  $\rho$  is the radial variable in this frame. Next, the three-dimensional Laplace operator is expressed by the relation

$$\Delta \mathbf{u} = H(H\mathbf{u}) - \frac{\kappa}{1 - \kappa p} \frac{\partial \mathbf{u}}{\partial p} + \frac{\partial^2 \mathbf{u}}{\partial p^2} + \frac{\partial^2 \mathbf{u}}{\partial q^2},\tag{58}$$

where the last two terms represent the two-dimensional Laplace operator in the  $p$ - $q$ -plane. In addition, the assumption of slowly moving filament curves leads to transformation of the time derivative,

$$\frac{\partial \mathbf{u}}{\partial t} \rightarrow \frac{\partial \mathbf{u}}{\partial t} - (\mathbf{T} \cdot H\mathbf{u}) \frac{\partial \mathbf{X}}{\partial t} - \left( \mathbf{N} \cdot \frac{\partial \mathbf{u}}{\partial p} + \mathbf{B} \cdot \frac{\partial \mathbf{u}}{\partial q} \right) \frac{\partial \mathbf{R}}{\partial t} - \left( \mathbf{B} \cdot \frac{\partial \mathbf{u}}{\partial \theta} \right) \frac{\partial \mathbf{N}}{\partial t},\tag{59}$$

where  $\partial_t \mathbf{X} = \partial_t \mathbf{R} + p\partial_t \mathbf{N} + q\partial_t \mathbf{B}$ .

Now, we seek approximate solutions of the RD system (54) of the form

$$\mathbf{u}(s, p, q, t) = \mathbf{V}(\mathbf{r}, \theta + \phi(s, t) - \omega t) + \mathbf{u}_1. \quad (60)$$

In this approximate solution, the term  $\mathbf{V}(\mathbf{r}, \theta + \phi(s, t) - \omega t)$  is a vortex solution for a  $p$ - $q$ -plane that is normal to the filament curve at arc length  $s$ , and  $\mathbf{u}_1$  represents the approximation. Keener now introduces a small parameter  $\epsilon$ . He then considers  $\tau$  and  $\partial_s \phi$  of order  $\epsilon$ , while he regards  $\mathbf{u}_1$ ,  $\partial_t \mathbf{X}$ ,  $\partial_s^2 \phi$ ,  $\partial_s \tau$ , and  $\kappa$  of order  $\epsilon^2$ . Next, the approximate solution (60) is inserted into (54). By using the substitutions for the Laplace operator (58), for the time derivative (59), and keeping only terms of order  $\epsilon$  and  $\epsilon^2$ , one arrives at

$$\mathcal{L} \cdot \mathbf{u}_1 = \mathcal{F}[\mathbf{V}, \mathbf{R}, \mathbf{T}, \mathbf{N}, \mathbf{B}], \quad (61)$$

where the function  $\mathcal{F}$  is defined as

$$\begin{aligned} \mathcal{F}[\mathbf{V}, \mathbf{R}, \mathbf{T}, \mathbf{N}, \mathbf{B}] &= \frac{\partial}{\partial s} \left( \frac{\partial \phi}{\partial s} - \tau \right) \mathbb{D} \cdot \frac{\partial \mathbf{V}}{\partial \theta} + \left( \frac{\partial \phi}{\partial s} - \tau \right)^2 \mathbb{D} \cdot \frac{\partial^2 \mathbf{V}}{\partial \theta^2} - \kappa \mathbb{D} \cdot \frac{\partial \mathbf{V}}{\partial p} \\ &\quad + \mathbf{T} \cdot \frac{\partial \mathbf{R}}{\partial t} \left( \frac{\partial \phi}{\partial s} - \tau \right) \frac{\partial \mathbf{V}}{\partial \theta} + \left( \mathbf{N} \cdot \frac{\partial \mathbf{R}}{\partial t} \right) \frac{\partial \mathbf{V}}{\partial p} + \left( \mathbf{B} \cdot \frac{\partial \mathbf{R}}{\partial t} \right) \frac{\partial \mathbf{V}}{\partial q} \\ &\quad + \left( \mathbf{B} \cdot \frac{\partial \mathbf{N}}{\partial t} - \frac{\partial \phi}{\partial t} \right) \frac{\partial \mathbf{V}}{\partial \theta}, \end{aligned} \quad (62)$$

and the linear stability operator  $\mathcal{L}$  is given by

$$\mathcal{L} \equiv \frac{\partial}{\partial t} - \mathbb{D} \Delta_{2D} - \mathbb{F}[\mathbf{U}], \quad (63)$$

with  $\mathbb{F}[\mathbf{U}] = \partial_u \mathbf{f}(\mathbf{U})$  and the two-dimensional Laplace operator  $\Delta_{2D}$  (the last two terms in equation (58)).

Through the discussion of the asymptotic theory for unperturbed spiral waves (see section 2.2 on page 22), we found the eigenvectors of the linear operator (63), the Goldstone modes (GMs). In the case treated here, we may define the GMs by  $\mathbf{V}_\theta = \partial_\theta \mathbf{V}$ ,  $\mathbf{V}_p = \partial_p \mathbf{V}$ , and  $\mathbf{V}_q = \partial_q \mathbf{V}$ . Moreover, we also discovered the adjoint linearized operator,

$$\mathcal{L}^\dagger \equiv \frac{\partial}{\partial t} + \mathbb{D} \Delta_{2D} + \mathbb{F}^\dagger[\mathbf{U}], \quad (64)$$

with their corresponding eigenvectors, the response functions (RFs), which we shall represent here by  $\mathbf{W}_\theta$ ,  $\mathbf{W}_p$ , and  $\mathbf{W}_q$ . The GMs and the RFs form a normalized bi-orthogonal set with respect to the natural product of two complex functions  $\mathbf{u}, \mathbf{v} \in \mathbb{C}^m$  ( $m \in \mathcal{N}^+$ ). This inner product is defined by

$$(\mathbf{u}, \mathbf{v}) = \int_0^P dt \iiint dp dq d\theta \mathbf{u}(p, q, \theta, t) \cdot \mathbf{v}(p, q, \theta, t), \quad (65)$$

In this relation,  $P = 2\pi/\omega$  is the period of the corresponding spiral and the dot denotes usual scalar product in  $\mathbb{C}^m$ . Accordingly, in the case treated here we have

$$(\mathbf{V}_\lambda, \mathbf{W}_\mu) = \delta_{\lambda\mu}, \quad \lambda, \mu \in \{p, q, \theta\}. \quad (66)$$

In order to solve equation (61) for the motion equations of the filament curve, it is required that the right-hand side of (61), namely the function  $\mathcal{F}[\mathbf{V}, \mathbf{R}, \mathbf{T}, \mathbf{N}, \mathbf{B}]$ , be orthogonal to the RFs. The resulting solubility conditions yield equations of motion for the filament curve  $\mathbf{R}(t)$  and for the rotation phase distribution  $\phi(t)$  along the scroll wave filament:

$$\begin{aligned}\frac{\partial\phi}{\partial t} &= \frac{\partial\mathbf{N}}{\partial t} \cdot \mathbf{B} + \left( \frac{\partial\phi}{\partial s} - \tau \right) \frac{\partial\mathbf{R}}{\partial t} \cdot \mathbf{T} + a_1 \left( \frac{\partial\phi}{\partial s} - \tau \right)^2 + b_1 \left( \frac{\partial^2\phi}{\partial s^2} - \frac{\partial\tau}{\partial s} \right) - c_1\kappa, \\ \frac{\partial\mathbf{R}}{\partial t} \cdot \mathbf{N} &= -a_2 \left( \frac{\partial\phi}{\partial s} - \tau \right)^2 + b_2\kappa - c_2 \left( \frac{\partial^2\phi}{\partial s^2} - \frac{\partial\tau}{\partial s} \right), \\ \frac{\partial\mathbf{R}}{\partial t} \cdot \mathbf{B} &= -a_3 \left( \frac{\partial\phi}{\partial s} - \tau \right)^2 + c_3\kappa - c_4 \left( \frac{\partial^2\phi}{\partial s^2} - \frac{\partial\tau}{\partial s} \right).\end{aligned}\quad (67)$$

The coefficients  $a_i$  with  $i \in \{1, 2, 3\}$ ,  $b_j$  with  $j \in \{1, 2\}$ , and  $c_k$  with  $k \in \{1, 2, 3, 4\}$  are given by

$$\begin{aligned}a_1 &= (\mathbb{D}\partial_\theta^2 \mathbf{V}, \mathbf{W}_\theta), & a_2 &= (\mathbb{D}\partial_\theta^2 \mathbf{V}, \mathbf{W}_p), & a_3 &= (\mathbb{D}\partial_\theta^2 \mathbf{V}, \mathbf{W}_q), \\ b_1 &= (\mathbb{D}\partial_\theta \mathbf{V}, \mathbf{W}_\theta), & b_2 &= (\mathbb{D}\partial_p \mathbf{V}, \mathbf{W}_p), & c_1 &= (\mathbb{D}\partial_p \mathbf{V}, \mathbf{W}_\theta), \\ c_2 &= (\mathbb{D}\partial_\theta \mathbf{V}, \mathbf{W}_p), & c_3 &= (\mathbb{D}\partial_p \mathbf{V}, \mathbf{W}_q), & c_4 &= (\mathbb{D}\partial_\theta \mathbf{V}, \mathbf{W}_q),\end{aligned}\quad (68)$$

An additional equation must be considered with respect to the tangential component of the filament velocity,  $\partial_t \mathbf{R} \cdot \mathbf{T}$ , since equations (67) are expressed in arc length coordinates. Therefore, the tangential component is required to satisfy

$$\partial_s(\partial_t \mathbf{R} \cdot \mathbf{T}) = \kappa(\partial_t \mathbf{R} \cdot \mathbf{N}),$$

in order that flow maintains the arc length coordinate system. When another coordinate frame is chosen to describe evolution of the filament curve  $\mathbf{R}$ , this last relation may be dropped.

For illustrating the power of the motion equations (67), Keener discussed some example cases. Here, I will not provide these examples completely. Instead, I will illustrate shortly the two cases for planar scroll rings with and without twist, while skipping Keener's considerations on the evolution of helical scroll waves. The interested reader is referred to Keener's paper from 1988 [99].

### 3.2.1 Untwisted scroll ring

We shall assume that the scroll ring considered here is planar and the twist  $\partial_s\phi$  is the same at any point of the filament. Hence, torsion of the filament  $\tau$  is zero everywhere, and equations (67) are reduced to

$$\begin{aligned}\frac{\partial\phi}{\partial t} &= -c_1\kappa, \\ \frac{\partial\mathbf{R}}{\partial t} \cdot \mathbf{N} &= b_2\kappa, \\ \frac{\partial\mathbf{R}}{\partial t} \cdot \mathbf{B} &= c_3\kappa.\end{aligned}\quad (69)$$

Additionally, when we assume that the diffusion matrix is  $\mathbb{D} = d \cdot \mathbb{I}$  for a constant value of  $d$  and  $\mathbb{I}$  being the identity matrix, then we have  $b_2 = d$  and  $c_1 = c_3 = 0$ . Therefore, the above equations are reduced further and the considering scroll ring filament holds its plane form for all times while vertically drifting with a velocity proportional to the diffusion coefficient times the curvature of the filament. This remaining last equation, namely  $\partial_t \mathbf{R} \cdot \mathbf{N} = d\kappa$ , was also derived by Panfilov et al. in 1986 in the special case of exactly circular filaments [130]. Keener and Tyson studied this case experimentally in the framework of the BZ reaction [74]. If the two coefficients  $c_1$  and  $c_3$  are nonzero, then more complex phenomena may arise. For a nonzero  $c_1$ , the equations forecast development of twist in the course of time while for nonzero  $c_3$ , an initially planar scroll ring will not remain planar. But in both of these two cases, it is desired that the scroll ring is not exactly circular initially.

For a scroll ring we may write equations (69) in terms of the radius  $R(t)$  and the height  $z(t)$  of the filament,

$$\begin{aligned}\frac{dR}{dt} &= -\frac{b_2}{R}, \\ \frac{dz}{dt} &= \frac{c_3}{R},\end{aligned}\tag{70}$$

with the solutions given by

$$\begin{aligned}R(t) &= \sqrt{R_0^2 - 2b_2 t}, \\ z(t) &= z_0 - \frac{c_3 R(t)}{b_2}.\end{aligned}\tag{71}$$

The first of the two equations (70) attributes a physical quality to the coefficient  $b_2$ . This is getting apparent when we consider the sign of it. If  $b_2$  is positive, then the scroll ring is contracting and has a finite lifetime, the latter given by  $T = R_0^2/2b_2$ . In contrast, the ring expands in case of negative  $b_2$ . Later, Biktashev et al. considered the coefficient  $b_2$  as an elastic property of the scroll wave filament, and denoted it as the filament tension [89].

### 3.2.2 Twisted scroll ring

The assumptions of uniform initial twist and zero torsion lead to the following reduced motion equations for the ring filament:

$$\begin{aligned}\frac{\partial\phi}{\partial t} &= a_1 \left( \frac{\partial\phi}{\partial s} \right)^2, \\ \frac{\partial\mathbf{R}}{\partial t} \cdot \mathbf{N} &= b_2 \kappa - a_2 \left( \frac{\partial\phi}{\partial s} \right)^2, \\ \frac{\partial\mathbf{R}}{\partial t} \cdot \mathbf{B} &= c_3 \kappa - a_3 \left( \frac{\partial\phi}{\partial s} \right)^2.\end{aligned}\tag{72}$$

Analogously to the previous case of untwisted scroll rings, we may consider equal diffusion coefficients by  $\mathbb{D} = d \cdot \mathbb{I}$ . This leads again to  $b_2 = d$  and  $c_1 = c_3 = 0$ , but nevertheless the coefficients  $a_1$ ,  $a_2$ , and  $a_3$  remain. The reduced motion equations (72) indicate that a planar scroll ring with uniform twist holds both its planar structure as well its uniform twist with the passing of time.

Now, under the assumption that the ring filament is exactly circular, one can consider the total twist as an integer multiple of  $2\pi$  and write  $\partial_s \phi = j/R$ . Hence, we reduce the equations of motion for the filament's curve  $\mathbf{R}$  in normal and bi-normal directions to equations for the radius  $R$  and height  $z$ . These and the one for the twist  $\phi$  get

$$\begin{aligned}\frac{\partial R}{\partial t} &= \frac{a_2 j}{R} - \frac{b_2}{R}, \\ \frac{\partial z}{\partial t} &= \frac{c_3}{R} - \frac{a_3 j^2}{R^2}, \\ \frac{\partial \phi}{\partial t} &= \frac{a_1 j^2}{R^2} - \frac{c_1}{R}.\end{aligned}\tag{73}$$

Both the effective evolutions for the radius as well the height of the scroll ring are now affected by additional terms, in comparison to the equations for initially untwisted rings (70). The radius evolution equation indicates the existence of a stationary scroll ring for positive filament tension coefficient ( $b_1 > 0$ ) with a stationary radius  $R_1 = a_2 j^2 / b_2$ . The vertical drift of the ring reverses its direction as the radius passes through the second critical radius  $R_2 = a_3 j^2 / c_3$ .

### 3.3 APPROACH BY BIKTASHEV

In 1994, Biktashev et al. showed that some of the coefficients (68) in Keener's filament motion equations (67) will always vanish [89], by using the rotation symmetry of the unperturbed vortex solution  $\mathbf{u} = \mathbf{U}(r, \theta - \omega t)$  for a generic reaction diffusion system (54). Additionally, their approach predicts that the overall filament length will change monotonically with time, independently from initial conditions, and just governed by one single coefficient which is dependent on medium parameters. I will provide a summary of this approach in this section, and we will see that this coefficient is the filament tension, meaning that  $\alpha \equiv b_2$ .

A change to a rotating coordinate frame  $t \rightarrow \tilde{t}$ ,  $r \rightarrow \rho$ ,  $\theta = \xi$  with

$$\begin{aligned}\tilde{t} &= t, \\ \xi &= \theta - \omega t, \\ \rho &= r\end{aligned}$$

leads to the following rotation-symmetric equations for the linear operators  $\tilde{\mathcal{L}}$  and  $\tilde{\mathcal{L}}^\dagger$ :

$$\tilde{\mathcal{L}} \cdot \tilde{\mathbf{u}} = \partial_t \tilde{\mathbf{u}} - \omega \partial_\xi \tilde{\mathbf{u}} - \tilde{\Delta}_{2D} \tilde{\mathbf{u}} - \mathbb{F}[\mathbf{U}(\rho, \xi)] \cdot \tilde{\mathbf{u}} = 0, \quad (74)$$

$$\tilde{\mathcal{L}}^\dagger \cdot \tilde{\mathbf{v}} = \partial_t \tilde{\mathbf{v}} - \omega \partial_\xi \tilde{\mathbf{v}} + \tilde{\Delta}_{2D} \tilde{\mathbf{v}} + \mathbb{F}^\dagger[\mathbf{U}(\rho, \xi)] \cdot \tilde{\mathbf{v}} = 0. \quad (75)$$

Under the consideration of the inner product  $(\tilde{\mathbf{u}}(\rho, \xi, t), \tilde{\mathbf{v}}(\rho, \xi, t))$  for the functions  $\tilde{\mathbf{u}}, \tilde{\mathbf{v}}$  (65) in the co-rotating frame, together with the eigenfunctions for the linear operator  $\mathcal{L}$  (Goldstone modes  $\mathbf{V}_\mu$  with  $\mu \in \{0, \pm 1\}$ ) and the adjoint operator  $\mathcal{L}^\dagger$  (response functions  $\mathbf{W}_\lambda$  with  $\lambda \in \{0, \pm 1\}$ ), Biktashev and colleagues were able to show that the conditions

$$\begin{aligned} (\mathbf{V}_x, \mathbf{W}_x) &= 1, \\ (\mathbf{V}_y, \mathbf{W}_x) &= 0, \\ (\mathbf{V}_x, \mathbf{W}_\theta) &= 0, \end{aligned}$$

are fulfilled. In accordance, all inner products in (68) including rotational eigenfunctions on the one side and shift eigenfunctions on the other side will also vanish [89]. Hence, we get

$$a_2 = a_3 = c_1 = c_2 = c_4 = 0.$$

With these arguments, the resulting equations of motion for the filament reduce to

$$\begin{aligned} \frac{\partial \phi}{\partial t} &= \frac{\partial \mathbf{N}}{\partial t} \cdot \mathbf{B} + \left( \frac{\partial \phi}{\partial s} - \tau \right) \frac{\partial \mathbf{R}}{\partial t} \cdot \mathbf{T} \\ &\quad + b_1 \left( \frac{\partial^2 \phi}{\partial s^2} - \frac{\partial \tau}{\partial s} \right) + a_1 \left( \frac{\partial \phi}{\partial s} - \tau \right)^2, \\ \frac{\partial \mathbf{R}}{\partial t} \cdot \mathbf{N} &= b_2 \kappa, \\ \frac{\partial \mathbf{R}}{\partial t} \cdot \mathbf{B} &= c_3 \kappa. \end{aligned} \quad (76)$$

In comparison to the motion equations that were derived by Keener (equations (67)), the reduced equations for the filament curve  $\mathbf{R}$  are independent of the rotation phase distribution  $\phi$  in here. One may combine the last two equations in (76) with the help of the Frenet-Serret equations (55) to get

$$\frac{\partial \mathbf{R}}{\partial t} = b_2 \mathcal{D}_s^2 \mathbf{R} + c_3 [\mathcal{D}_s \mathbf{R} \times \mathcal{D}_s^2 \mathbf{R}]. \quad (77)$$

In this equation the arc length differentiation operator with respect to a function  $f(\sigma, t)$  is defined as

$$\mathcal{D}_s f(\sigma, t) \equiv \frac{\partial_\sigma f(\sigma, t)}{|\partial_\sigma r(\sigma, t)|}, \quad (78)$$

and the filament curve vector function  $\mathbf{R}(\sigma, t)$  is described by the parameter  $\sigma$  such that points with equal  $\sigma$  move orthogonally to the filament, while arbitrary in other respects.

Let us now write down the total length of the filament at each time  $t$ :

$$S(t) = \int ds = \int |\partial_\sigma \mathbf{R}(\sigma, t)| d\sigma, \quad (79)$$

Here, the integration is achieved over the whole filament. Time derivation of this function under the assumption that the boundaries of the medium are smooth and impermeable (assumption that the filament is closed to a ring) yields

$$\frac{\partial S}{\partial t} = -b_2 \int |\mathcal{D}_s^2 \mathbf{R}|^2 ds = -b_2 \int \kappa^2(s) ds. \quad (80)$$

This equation displays time evolution of the filament subject to the coefficient  $b_2$ , independent of initial conditions and other coefficients of the equations (76). If  $b_2 > 0$ , the filament contracts continuously until it diminishes. Contrary to this, the total filament length increases in time for  $b_2 < 0$ . Accordingly, Biktashev et al. attributed a key role to the coefficient  $b_2$  and denoted it as the filament tension parameter.

### 3.4 APPROACH BY HENRY AND HAKIM

The purpose of this section is to summarize the linear stability analysis for straight scroll waves which was achieved by H. Henry and V. Hakim [86, 87]. Henry and Hakim performed their investigations in the framework of the Barkley model. This model was proposed by D. Barkley in 1991 [88] and can be written in the following form:

$$\frac{\partial u}{\partial t} = D_u \Delta u + \frac{1}{\epsilon} f(u, v), \quad (81)$$

$$\frac{\partial v}{\partial t} = g(u, v), \quad (82)$$

with

$$f(u, v) = u(1-u) \left( u - \frac{v+b}{a} \right), \quad (83)$$

$$g(u, v) = u - v. \quad (84)$$

The model parameters are  $a, b, \epsilon$ , and solely the first component  $u$  diffuses with a coefficient  $D_u = 1$ . Henry and Hakim used throughout of their work a fixed value for  $\epsilon$  ( $\epsilon = 0.025$ ), while presenting investigation of scroll wave stability for distinct  $a$ -values along the line  $b = 0.01$ . This is shown in figure 14.

In the following, I will present their approach in several steps. The first step is to transform equations (81) and (82) to a co-rotating cylindric coordinate frame described by  $r, \phi = \theta - \omega t - \tau_\omega z$ ,  $z$ , and  $t$ . Here, we have the rotation frequency  $\omega$  and the imposed twist along the scroll wave filament  $\tau_\omega$ . Transformation then yields

$$\left( \partial_t + 2\tau_\omega \partial_{\phi z}^2 - \partial_{zz}^2 \right) u = \left( \omega \partial_\phi + \tau_\omega^2 \partial_{\phi\phi}^2 + \Delta_{2D} \right) u + \frac{1}{\epsilon} f(u, v), \quad (85)$$

$$\partial_t v = \omega \partial_\phi v + g(u, v). \quad (86)$$

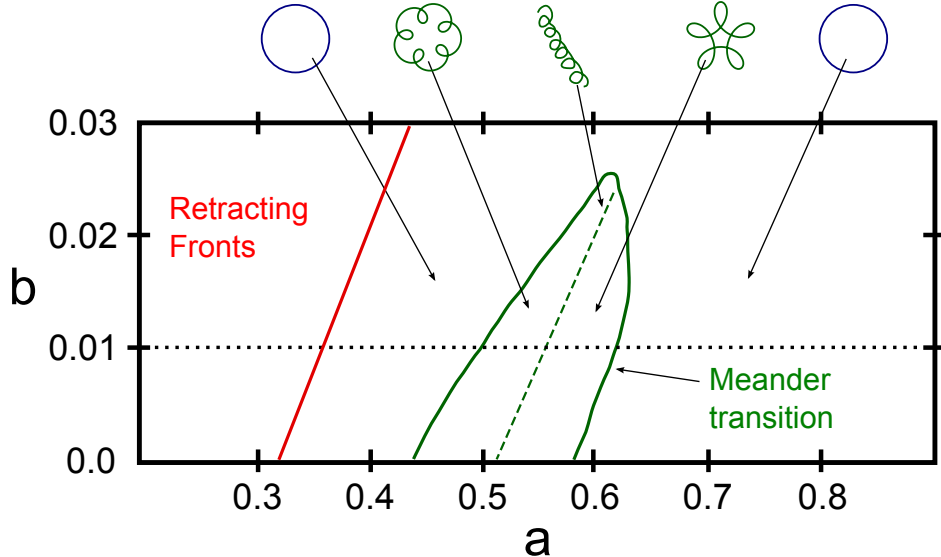


**Figure 14:** Schematic bifurcation diagram for spiral waves simulated in the Barkley model. The bold green line depicts the meander transition line which separates spirals with rigidly rotating tips from spirals with meandering tip motion. Spirals retract left of the thick red line [131]. Along the dotted line through  $b = 0.01$  different parameters were chosen by Henry and Hakim to investigate scroll wave evolution.

Next, one gets the stationary equations by setting solutions of equations (81) and (82) at each  $z$ -slice of the medium equal to those of steadily rotating spiral waves, meaning that  $u(r, \phi, z, t) = u_0(r, \phi)$  and  $v(r, \phi, z, t) = v_0(r, \phi)$  for the rotation frequency  $\omega = \omega_1$ . Hence, we arrive at

$$\left( \Delta_{2D} + \omega_1 \partial_\phi + \tau_\omega^2 \partial_{\phi\phi}^2 \right) u_0 + \frac{1}{\epsilon} f(u_0, v_0) = 0, \quad (87)$$

$$\omega_1 \partial_\phi v_0 + g(u_0, v_0) = 0. \quad (88)$$

These equations are purely two-dimensional due to the translation-invariance of the corresponding scroll wave in  $z$ -direction.

Yet, in order to linearize equations (85) and (86) around the stationary solutions  $u_0$  and  $v_0$ , perturbations of the form

$$u(r, \phi) = u_0(r, \phi) + \exp[\sigma(k_z)t - ik_z z] u_1(r, \phi), \quad (89)$$

$$v(r, \phi) = v_0(r, \phi) + \exp[\sigma(k_z)t - ik_z z] v_1(r, \phi) \quad (90)$$

are introduced and after insertion in (85) and (86) yield

$$\sigma(k_z) \begin{pmatrix} u_1 \\ v_1 \end{pmatrix} = \mathcal{L}_{k_z} \begin{pmatrix} u_1 \\ v_1 \end{pmatrix}, \quad (91)$$

with the linearized operator

$$\mathcal{L}_{k_z} = \begin{pmatrix} A & B \\ C & D \end{pmatrix}, \quad (92)$$

and the abbreviations

$$\begin{aligned} A &= \Delta_{2D} + \tau_\omega^2 \partial_{\phi\phi}^2 + (\omega_1 + 2ik_z \tau_\omega) \partial_\phi - k_z^2 + \frac{1}{\epsilon} \partial_u f(u_0, v_0), \\ B &= \frac{1}{\epsilon} \partial_v f(u_0, v_0), \\ C &= \partial_u g(u_0, v_0), \\ D &= \omega_1 \partial_\phi + \partial_v g(u_0, v_0). \end{aligned}$$

In the next step, the eigenvalues corresponding to this linear system are calculated by usage of an iterative algorithm numerically. The algorithm is described in reference [132], while the numerical procedure is analogous to linear stability analysis for spiral waves discussed in [55, 133]. The main ideas of that procedure are:

1. There exists a subspace spanned by  $m$  eigenvectors  $\mathbf{e}_1, \mathbf{e}_2, \dots, \mathbf{e}_m$  of the largest real part of  $\mathcal{L}_{k_z}$ .
2. Projection of  $\mathcal{L}_{k_z}$  onto this subspace.
3. Diagonalization of  $\mathcal{L}_{k_z}$ .

Two cases have to be considered corresponding to the spectrum of  $\mathcal{L}_{k_z}$ : **(a)** For the case of zero twist ( $\tau_\omega = 0$ ), the linear system (91) and (92) depends only on  $k_z^2$  and the spectral bands are linear functions of the wave number  $k_z$ . Furthermore, the linear operator  $\mathcal{L}_{k_z}$  is real-valued, such that the complex eigenvalues are complex-conjugated pairs. **(b)** There are no symmetries for the case of non-vanishing twist ( $\tau_\omega \neq 0$ ). Hence, we have  $\mathcal{L}_{k_z} = \mathcal{L}_{-k_z}^*$  and the bands of the complex modes are grouped in pairs of  $\sigma_1(k_z), \sigma_2(k_z)$  with  $\sigma_2(k_z) = \sigma_1^*(-k_z)$ .

There are five dominant modes in the two-dimensional case: **(1)** One rotation mode with its corresponding eigenvalue  $\sigma = 0$  following from the rotation-invariance of equations (85) and (86), **(2)** two translation modes follow from the translation-invariance of equations (81) and (82) with purely imaginary eigenvalues  $\sigma = \pm i\omega_1$ , and **(3)** two complex-conjugated modes with their corresponding eigenvalues  $\sigma = \omega_1 \pm i\omega_2$  emerge and are denoted as the meander modes (real parts of these modes cut the meander instability line depicted by the green dashed line in figure 14).

First, Henry and Hakim investigated the linear stability of these three modes. Afterwards, they presented the nonlinear evolution of the corresponding scroll waves by direct numerical simulations of the model equations (81) and (82) in three spatial dimensions. Investigations were accomplished for straight scroll waves with and without twist as initial states. The setups for the numerical simulations are shown in the schematic figure 15. Vertically placed scroll waves are drawn in the middle of the boxes. Panel A displays a scroll with zero twist ( $\tau_\omega = 0$ ), while in panel B a scroll with non-zero twist ( $\tau_\omega \neq 0$ ) is presented.

Henry and Hakim have chosen the simulation boxes to possess either periodic or no-flux boundary conditions at the top and bottom faces, while the

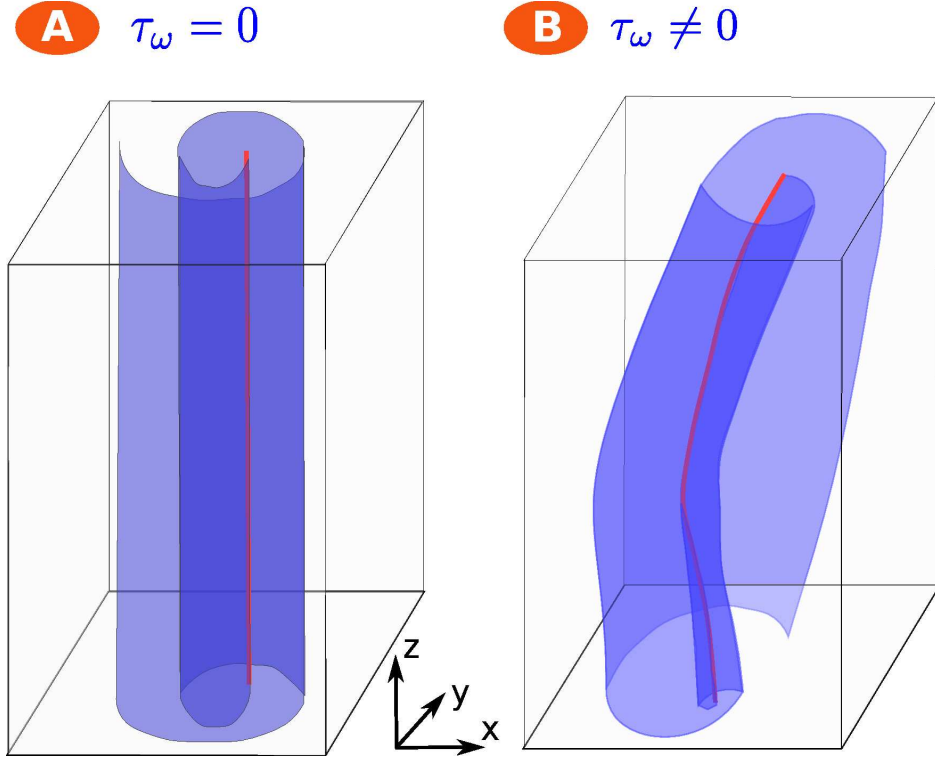


**Figure 15:** Schematic for scroll wave initial states investigated by H. Henry and V. Hakim. (A) Scroll wave with zero twist ( $\tau_\omega = 0$ ). (B) Scroll wave with nonzero twist ( $\tau_\omega \neq 0$ ).

other medium walls were always chosen to be periodic. Simulations were then performed for different parameter sets of the Barkley model showing instability of either the translation modes or the meander modes. Spiral tips were defined as the intersection of two iso-concentration lines  $u = u_{\text{tip}}$  and  $v = v_{\text{tip}}$ . Analogously, filaments were detected as intersection of iso-concentration planes  $u = u_{\text{tip}} = 0.5$  and  $v = v_{\text{tip}} = 0.75$  ( $0.5a - b$ ). The latter is the instantaneous filament definition. In the following, I will provide a summary of the results by Henry and Hakim. I will begin with their investigation for scroll waves without initially induced twist and conclude this section with their findings for twist-induced instabilities.

As an example for the translation band instability, the parameter set  $a = 0.44$ ,  $b = 0.01$ , and  $\epsilon = 0.025$  was selected. In this case, Henry and Hakim observe the instability appearing for  $k_z \neq 0$  while in two spatial dimensions spirals are stable. The results for the spectrum of the linearized system (91) in this case is shown by figure 16. Clearly, the maximum of  $\text{Re}(\sigma)$  is at  $k_z \approx 0.5$ . Since the instability occurs at very small wave numbers, as soon as  $k_z \neq 0$ , this corresponds to the negative line tension instability (see reference [89]).

Hereafter, Henry and Hakim show that the translation band instability is a long-wavelength instability which can be explained by drift of spirals in an

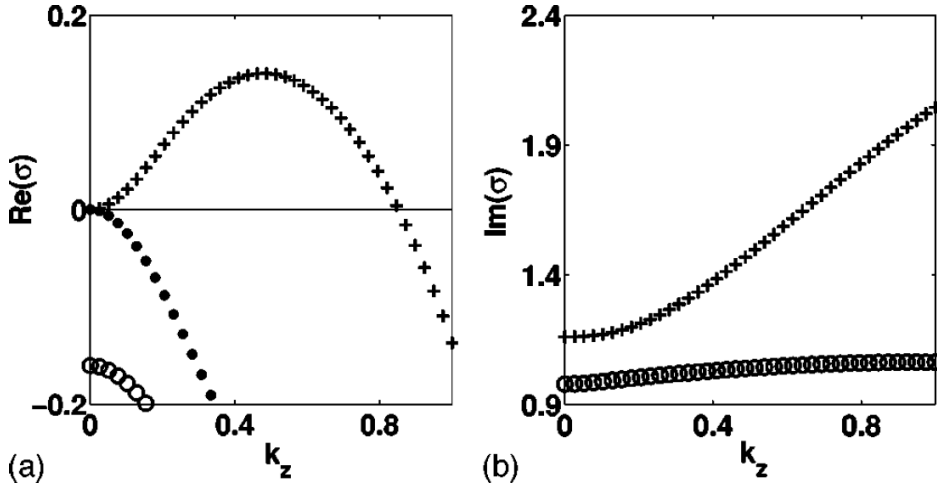


**Figure 16:** Eigenvalue spectrum for a straight scroll wave with translation band instability. (a) Real and (b) imaginary part of the growth rate  $\sigma(k_z)$  as a function of the wave number  $k_z$  for the values of parameters  $a = 0.44$ ,  $b = 0.01$ , and  $\epsilon = 0.025$  are displayed. Figure reprinted with permission from [87], copyright by the American Physical Society.

external field. Let us consider an external field  $\mathbf{E}$  that leads to a drift of the spiral core center with the velocity

$$\mathbf{v} = \alpha_{\parallel} \mathbf{E} + \alpha_{\perp} \omega_1 \times \mathbf{E}, \quad (93)$$

with the rotation vector  $\omega_1$  of the spiral tip around its core. Hakim and Karma have shown (for weakly excitable media) that a slightly curved scroll wave acts as an external field [131]. This represents the main reason that a straight scroll is not stable if  $\alpha_{\parallel} < 0$ . To be more precise, one can derive an equation for the translation bands for small  $k_z$  by perturbation analysis at first order. The perturbation analysis yields

$$\sigma_{\pm}(k_z) = \pm i\omega_1 + (-\alpha_{\parallel} \pm i\alpha_{\perp}) k_z^2 + \mathcal{O}(k_z^4). \quad (94)$$

The nonlinear evolution of the instability was investigated by direct numerical simulations of equations (81) and (82), for the same parameter set ( $a = 0.44$ ,  $b = 0.01$ , and  $\epsilon = 0.025$ ), and with initial states as shown in figure 15, panel A. The results of the simulations by Henry and Hakim is presented in figure 17. In agreement with previous observations by Biktashev et al. [89], development of the negative line tension instability was observed. The slightly perturbed straight scroll deforms, the overall length is increasing, and finally it departs. Initiation and development of the instability necessitates a minimum size of the medium. In particular, for the chosen parameter set, a minimum box height corresponding to wave number  $k_z = 84$  was found. Simulations yield a minimum box height corresponding to  $k_z = 81$ . Additionally, Henry and Hakim have shown how the choice of boundary type for the bottom and top faces of the box will influence the minimum box height. This critical size was found to be larger by a factor of two for periodic boundaries than for no-flux boundaries [87].

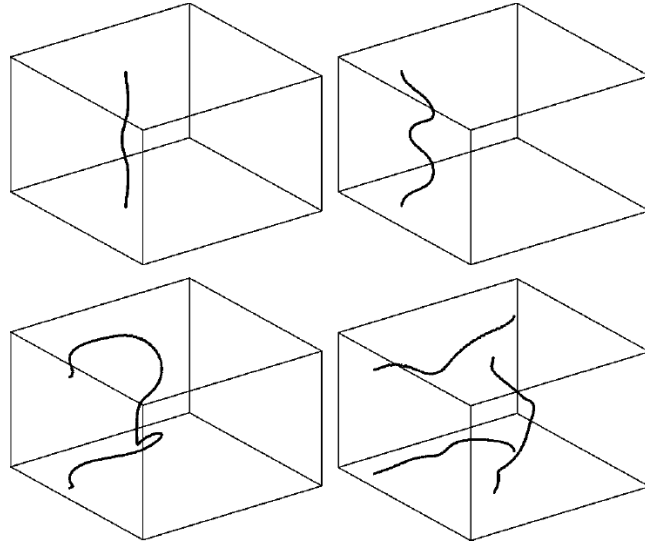


**Figure 17:** Instantaneous filament evolution starting from a slightly perturbed straight scroll for equally spaced times ( $t = 25$ ,  $t = 50$ ,  $t = 75$ , and  $t = 100$ ) during a simulation in a simulation box of size  $(128 \times 128 \times 120)$  with a space discretization step  $dx = 0.2$  using periodic boundary conditions. The parameters are  $a = 0.44$ ,  $b = 0.01$ , and  $\epsilon = 0.025$  and correspond to the linear spectrum shown in figure 16. Figure reprinted with permission from [87], copyright by the American Physical Society.

Contrary to the case of scroll waves with translation band instability, filaments of scroll waves that possess the meander band instability form re-stabilized states. These re-stabilized states strongly depend on the choice of the boundary conditions at the top and bottom faces of the media. For the choice of periodic boundary conditions on these two faces, simulations for the parameter  $a = 0.67$  were performed. This was achieved with three different initial conditions for the fields  $u(x, y, z)$  and  $v(x, y, z)$ :

(1)

$$\begin{aligned} u(x, y, z) &= u_{2D}(x, y) [1 + \alpha \cos(k_z z)], \\ v(x, y, z) &= u_{2D}(x, y) [1 + \alpha \sin(k_z z)], \end{aligned}$$

where  $\alpha \sim 10^{-2}$ , and  $u_{2D}$ ,  $v_{2D}$  are stationary spirals in two-dimensional space. Application of this initial state turns the filament into a helix with small elliptic cross-section and a pitch of  $2\pi/k_z$ . Provided that the wave number  $k_z$  is equal to an unstable mode, the helix grows until it reaches a re-stabilized state with the periodicity equal to  $k_z$ .

(2)

$$\begin{aligned} u(x, y, z) &= u_{2D}(x, y) [1 + \alpha \cos(k_z z)], \\ v(x, y, z) &= u_{2D}(x, y) [1 + \alpha \cos(k_z z)]. \end{aligned}$$

In this case, an instantaneous filament  $[x_f(z), y_f(z)]$  with a planar “zig-zag”-pattern is the consequence. Nonlinear evolution through direct numeri-

cal simulation then turns the scroll filament again into the re-stabilized helix with periodicity  $k_z$ .

(3)

$$\begin{aligned} u(x, y, z) &= u_{2D}(x, y) \left[ 1 + \alpha \exp \left\{ -\frac{(z - z_0)^2}{L_c} \right\} \right], \\ v(x, y, z) &= v_{2D}(x, y) \left[ 1 + \beta \exp \left\{ -\frac{(z - z_0)^2}{L_c} \right\} \right], \end{aligned}$$

with  $\|(\alpha, \beta)\|_2 = 0.01$  and  $L_c \sim (1/10)dx$ . This choice of initial conditions leads to a competition between various unstable modes, at least up to four distinct  $k_z$ . After a transient time, the most unstable mode which corresponds to the box height is selected. The duration of this transient depends on whether the initial perturbation of the filament is planar ( $\alpha = \beta$ ) or non-planar ( $\alpha \neq \beta$ ). In case of planar perturbation, the zig-zag filament grows before it transforms to a helix, while the latter emerges directly for non-planar perturbation.

Henry and Hakim denoted the emergence of the above described instability, in accordance with the work by Aranson and Mitkov (see reference [79]), as “three-dimensional meander bifurcation”. In order to better quantify this bifurcation, they also performed two systematic numerical investigations:

- (a) Fixing size of simulation box, while varying excitability with the aid of parameter  $a$ , and
- (b) Fixing  $a$ , while varying height of simulation box, e.g. the wavelength of initial perturbation.

In both cases, the radius of the instantaneous filament helix  $R$  appeared to be a good measure for the amplitude of the three-dimensional meander instability. They observed that this measure is proportional to the square root of the distance to the instability threshold, either  $R^2 \sim |a - a_c|$  or  $R^2 \sim |k_z - k_{\pm}(a)|$ . Hence, the three-dimensional meander bifurcation is a supercritical Hopf bifurcation, analogous to the meander bifurcation of spirals in two-dimensional space.

Additionally, Henry and Hakim investigated behavior of scroll waves in the meander-instability region for simulation boxes with no-flux boundary conditions on the top and bottom faces. The re-stabilized scroll waves that are forming in this case, display spiral tip meandering in each  $x$ - $y$ -plane. But contrary to the results of investigations with periodic boundary conditions, the amplitude of meander is now a function of the height coordinate  $z$  and can be well approximated by  $|\cos(k_z z)|$  (see reference [87, in particular Fig. 9]).

Finally, Henry and Hakim also investigated the influence of twist on the evolution of both the translation bands and the meander bands. The motivation for the study of twist-induced instabilities stems from several previous investigations [77, 81, 82, 134]. Furthermore, classical elasticity theory even proved that initially straight rods or ribbons may be destabilized if twist

beyond a certain critical threshold is imposed on them [135, 136]. In this classical sense, the rods which are forming possess helical structures. Henze et al. observed, as the analog to these classical elastic rods, the formation of helical scroll waves in numerical simulations of the Oregonator model with two components, and named this instability as “sproing” bifurcation for excitable filaments [77].

In order to better characterize the nature of the sproing instability, Henry and Hakim provided thorough numerical and analytical investigations. In particular, they have shown numerically that the frequency  $\omega_1$  for a family of twisted scroll waves at one parameter point ( $a = 0.8$ ,  $b = 0.01$ ,  $\epsilon = 0.025$ ) behaves quadratically at small twist and almost linearly for large twist (see [87, Fig. 11]). To show the quadratic behavior at small twists analytically, they performed first-order perturbation analysis for the equations 87 and 88, yielding

$$\omega_1 = \omega_1(\tau_\omega = 0) - \tau_\omega^2 \frac{(\tilde{u}_\phi, \partial_\phi^2 u_0)}{(\tilde{u}_\phi, \partial_\phi u_0) + (\tilde{v}_\phi, \partial_\phi v_0)} + \mathcal{O}(\tau_\omega^4). \quad (95)$$

Note, that the entities  $(\bullet, \bullet)$  denote scalar products between two functions, one defined on the functional space  $\mathbb{C}^m$  (with  $m \in \mathbb{N}^+$ ) and the other on the corresponding dual space. This can be interpreted in the framework of the asymptotic theory for spirals (by Biktashev et al., see chapter 2 and reference [56]). With this in mind, we can identify the rotational Goldstone mode  $\mathbf{V}_\phi = (\partial_\phi u_0, \partial_\phi v_0)^T$  and the rotational response function  $\mathbf{W}_\phi = (\tilde{u}_\phi, \tilde{v}_\phi)^T$ . Henry and Hakim introduced the latter as one of the left eigenvectors to the linearized operator  $\mathcal{L}$ . In view of the asymptotic theory for spirals, the left eigenvectors to  $\mathcal{L}$  are simply the eigenvectors to the adjoint linearized operator  $\mathcal{L}^\dagger$ , thus the response functions. Consequently, we can interpret the above equation for the rotation frequency of the scroll wave as a twist-induced perturbation equation for the phase  $\Phi$  given by

$$\partial_t \Phi = \omega_1 = \partial_t \Phi|_{\tau_\omega=0} - \frac{(\mathbf{W}_\phi^{(1)}, \partial_\phi \mathbf{V}_\phi^{(1)})}{(\mathbf{W}_\phi, \mathbf{V}_\phi)} \tau_\omega^2 + \mathcal{O}(\tau_\omega^4). \quad (96)$$

Here,  $\mathbf{V}_\phi^{(1)} = \partial_\phi u_0$  and  $\mathbf{W}_\phi^{(1)} = \tilde{u}_\phi$  denote the first components of the rotational Goldstone mode and the rotational response function, respectively. In this sense, the twist-induced perturbation coefficient (second term of the above equation) enters as a convolution integral of the perturbation  $\mathbf{h} = \partial_\phi \mathbf{V}_\phi^{(1)}$  with the first component of the rotational response function  $\mathbf{W}_\phi^{(1)}$ , normalized by the constant convolution integral  $(\mathbf{W}_\phi, \mathbf{V}_\phi)$ .

Henry and Hakim have shown that the twist also induces instability of the translation bands for a set of parameters that otherwise are stable. The instability occurs at a critical value for twist. Hence, the observed instability of the translation bands corresponds to the “sproing” instability which was first considered in reference [77], but was also observed experimentally in the framework of the Belousov-Zhabotinsky reaction [81, 82]. In recent years,

theoretical approaches have aimed at a better explanation of the sproing bifurcation [113, 100]. While the simple case of only one mode becoming unstable leads to a re-stabilized helical filament, observation of even more complex filament deformations have been reported by Henry and Hakim additionally. The latter is described as a consequence of growth for several unstable modes.



## Part II

### METHODS



# 4

## A NOVEL SETUP FOR EXPERIMENTS IN THE PHOTOSENSITIVE BELOUSOV-ZHABOTINSKY MEDIUM

---

### 4.1 INTRODUCTION

The first chemical reaction that was showing oscillating chemical reactions in time, was introduced by B. P. Belousov [10]. Then in 1961, A. M. Zhabotinsky began his studies based upon the recipe of Belousov [137]. In 1968, Zhabotinsky presented his results at a conference with the title “Biological and Biochemical Oscillators” in Prague. This conference initiated an increasing interest on the chemical reaction system that first was named Zhabotinsky reaction, and now the Belousov-Zhabotinsky (BZ) reaction.

In the early 1970s, a first attempt to clarify the underlying chemical mechanism of the BZ reaction was made by Field, Körös and Noyes [138]. The proposed mechanism, consisting on eleven reaction steps, is termed the FKN mechanism. Details of the FKN mechanism can also be found in [12, 139].

The catalyst cerium which was used in the original experiments by Belousov does not show a significant sensitivity to light application. This was shown by Gáspár et al. in 1983 [140]. The authors report on the investigation of photosensitivity on cerium-, ferroin-, and ruthenium-catalyzed BZ reaction systems. A weak effect of the illumination is observed in the ferroin-catalyzed system. In contrast to that, the catalyst rutheniumbipyridyl  $[\text{Ru}(\text{bpy})_3]^{2+}$  has been shown to be very useful in the attempt to control wave patterns in the BZ reaction system [140, 141, 142, 143, 144, 145, 146]. The metalorganic complex  $[\text{Ru}(\text{bpy})_3]^{2+}$  was investigated extensively by Schröder and Stephenson [147], and possesses an excited state  $[\text{Ru}(\text{bpy})_3]^{2+*}$ . The absorption spectrum for  $[\text{Ru}(\text{bpy})_3]^{2+}$  has its maximum at a wavelength of  $\lambda \approx 460 \text{ nm}$  (see [12]).

The ruthenium-catalyzed BZ reaction system was used to study properties of two- and three-dimensional wave patterns with respect to the applied illumination. As one of the first distinguished examples one shall entitle the work by Kuhnert and colleagues who discussed this system as a memory [142] and image processing [144] device. The primary attempt to examine variation of spiral tip meander patterns under the variation of the applied light intensity was delivered by Braune and Engel [148], followed by a work on the influence of periodically modulated illumination on the meander patterns [149]. Steinbock et al. further investigated the influence of time-periodic modulation of light on the motion of spiral waves in the photosensitive BZ reaction (PBZR) [150].

In three-dimensional PBZ media, one shall emphasize the work by Amemiya et al., who primarily discussed initiation of straight scroll waves and scroll rings in these media [151], and later examined the influence of light gradients on the life time of scroll rings [85].

#### 4.2 SELF-COMPLETION OF THREE-DIMENSIONAL WAVES

In order to study evolution of three-dimensional wave patterns in extended PBZ media, we have to discuss possibilities for initiation of these wave patterns. Arthur Winfree was the one who primarily sought for ways to initiate scroll waves in the classical BZ media in a reproducible manner [60, 15, 61]. Let Winfree speak himself:

“... A variety of newspapers, cigarette papers, filter papers and toilet tissue offered little improvement. Finally I tried Millipore filters, composed of chemically inert cellulose esters riddled with interconnected empty tunnels less than a micron in diameter [...] The mechanical binding of the fluid in the tiny tunnels prevents the liquid from moving quickly [...] then the filters are stacked like pancakes, they adhere closely and conduct waves in three dimensions...” [61, p. 92, last paragraph].

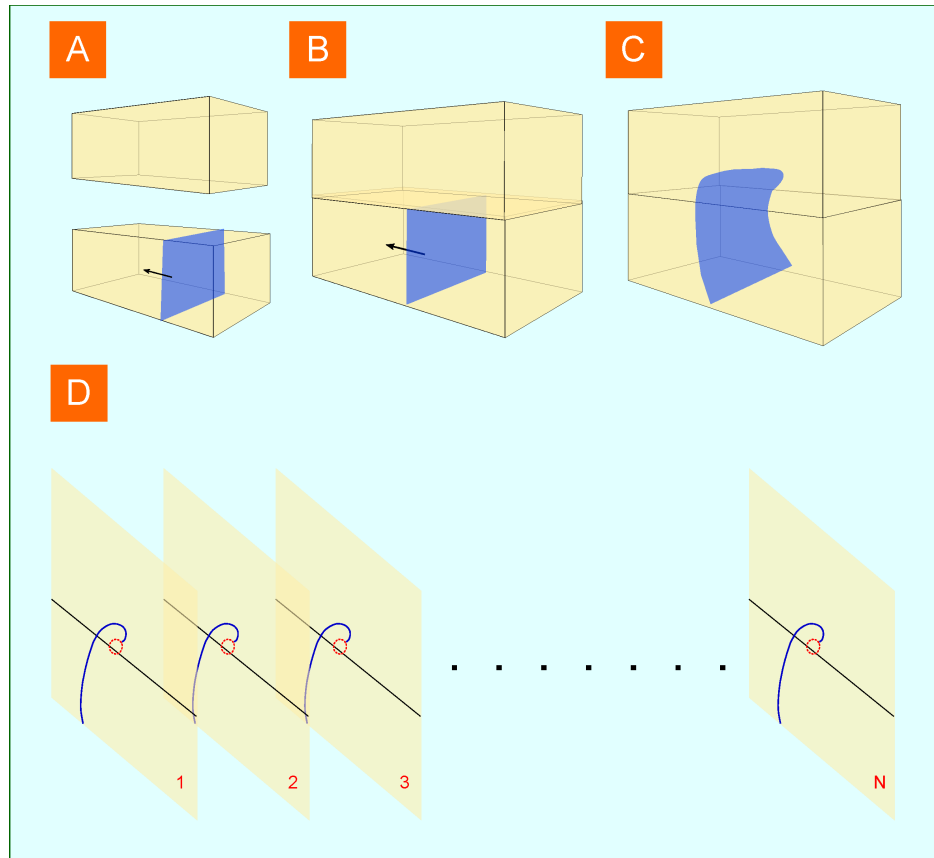


**Figure 18:** Winfree’s self-completion method for straight scroll waves.

Winfree's solution for the initiation problem of straight scroll waves and scroll rings is illustrated by the schematic figures 18 and 19. Both figures shall display his idea to initiate these three-dimensional waves in stacks of Millipore filters soaked with BZ solutions.

In panel A of figure 18 we see one such stack of filter papers in which already a plane vertical wave is propagating from right to left. Yet, a second stack of BZ-soaked filter papers is placed on top of it (panel B). This yields the self-completion of a straight scroll wave into the new stack (panel C). Panel D displays  $N$  virtual cross-sections in direction of the scroll waves's central axis (filament), illustrating the filament as a stack of spiral waves.

Analogously, initiation of a scroll ring is shown in figure 19. Here, Winfree is initiating a cylindric wave in the lower stack by placing a hot silver wire on top of the stack. Hence, a half-spherical wave forms at the top, propagates into the lower medium, and transforms to a cylindric-shaped wave (panel A). Placing the second stack on top of the first one (panel B) yields the self-completion of a scroll ring (panel C).

Panfilov and Pertsov in 1984 [63], Agladze et al. in 1989 [152], and Linde and Engel in 1991 [153] investigated the problem of self-completion for three-dimensional waves in generic excitable media thoroughly, with a special emphasis on the BZ reaction system. In particular, Agladze et al. formulated a "theorem on self-completion of 3D vortices" [152]:

"By self-completion of 3D vortices, the following process is meant. Assume a 3D medium (1) in which autowaves propagate [...] Let it make contact with a 3D autowaves medium (2) whose elements are at rest. The following statement can be formulated concerning the wave pattern generated by this 'composite' medium ((1)+(2)): self-completion results in a 3D vortex whose filament's position coincides with that of an autowave at the boundary surface of the two media at the initial instant of time" [152, pp. 38-39].

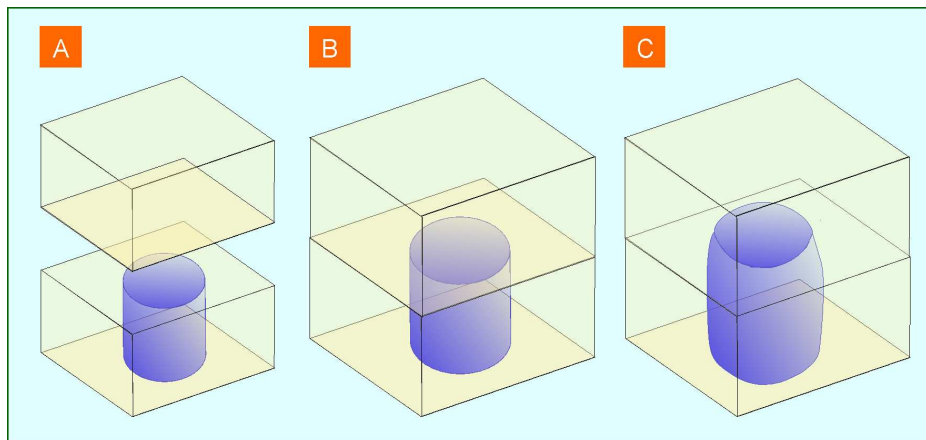


**Figure 19:** Winfree's self-completion method for scroll rings.

Agladze et al. also discussed the idea of self-completion for an arbitrary two-dimensional pattern to its three-dimensional counter-part. Particularly, they examined the self-completion of a three-dimensional wave with spiral-shaped filament. This is achieved by placing the excitable medium (2) on top of the medium (1), once a fully developed spiral wave has been initiated in medium (1).

In 1996, Amemiya et al. primarily introduced a novel initiation technique for scroll waves that is relying on the photosensitivity of the ruthenium-catalyzed BZ reaction medium [151]. In this work, the authors delivered a systematic study of the initiation under variation of illumination intensities and duration of the photoperturbation. Another novel method for initiation of scroll waves and scroll rings was proposed in the Steinbock group in the framework of the ferroin-catalyzed BZ medium [116, 118]. This approach is based upon a gel-solution mixture system, in which the lower part is an agarose gel layer while the upper part is a BZ solution. Nevertheless, both parts contain the ferroin catalyst. At the interface of the two layers, a spherical wave which will propagate equally through both parts can be initiated by a silver wire. By gently stirring the Petri dish which is containing the excitable medium, the wave part in the upper solution layer can be inhibited. Hence at the interface a scroll ring filament forms by self-completion. Recently, Totz et al. reported on life-time enhancement of intrinsically contracting scroll rings that were initiated by this method [154].

Now, a new initiation technique for the PBZR system will be described that will help us to investigate evolution of scroll waves and scroll rings in thin layers of excitable media. The experimental investigation in my thesis will be achieved in continuously stirred tank reactors (CSTR) to allow systematic studies under stationary non-equilibrium conditions. For that, I will introduce the CSTR in the next section.

#### 4.3 THE CONTINUOUSLY STIRRED TANK REACTOR (CSTR)

Achieving an experiment in a Petri dish containing the BZ medium inevitably leads to aging effects in the long run. Hence, depending on the chosen chemical recipe, the properties of the overall medium continuously change and characteristic of wave patterns vary in time. In particular, properties like wave length  $\lambda$  and rotation period  $T$  of a spiral wave initiated in such a medium do not remain constant.

In order to preclude these aging effects as good as possible, it is convenient to use a CSTR in which the active catalyst-loaded gel layer is placed in a reaction chamber. Then, the reaction chamber can be fed continuously with BZ solution. A second chamber surrounding the first one can be used to pump water with constant temperature through the chamber. A four-chamber CSTR was used in [44].

The experimental results that will be reported on in my thesis, were accomplished within a two-chamber CSTR which previously was used in [44, 155,

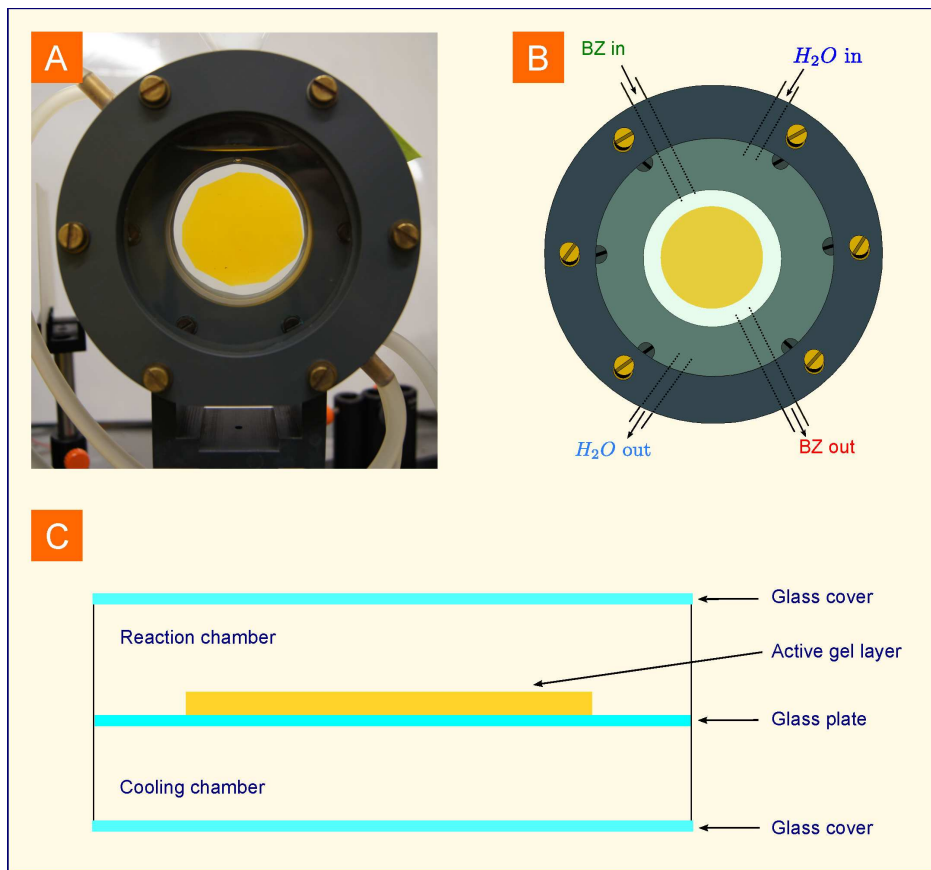


**Figure 20:** The two-chamber CSTR. (A) Actual photo of one CSTR. Schematic illustrations of the CSTR (B) in frontal view, and (C) in cross-section.

[156, 157, 158, 159, 160]. This CSTR is shown in figure 20, panel A. Schematically, the CSTR is illustrated by a frontal view in panel B and in cross-section in panel C. The reaction chamber possesses a volume of 70 ml, and the BZ solution can be fed continuously through this chamber. The active silica gel layer, which is loaded with the photosensitive catalyst  $[\text{Ru}(\text{bpy})_3]^{2+}$ , is placed on a depolished glass plate (diameter of 63 mm [160]). The details of gel preparation can be found in [44]. Water with constant temperature is pumped by a thermostat through the cooling chamber to maintain a stationary non-equilibrium condition.

#### 4.4 EXPERIMENTAL SETUP

The systematic spectrophotometric study of spiral waves in the BZ medium was pioneered by S. Müller and colleagues in the mid 1980s [37, 162, 161]. These nice experimental investigations pushed forward the understanding of spiral waves, in particular in regard to the spiral core dynamics. The structure of the core is illustrated by figure 21, both for a spiral that is rigidly rotating around a simple circular-shaped core (panel A), and for a spiral whose tip traces a “meandering” flower pattern around the central

core (panel B). These figures resemble nice examples for the power of the spectrophotometric method which was devised by Müller and colleagues.

M. Braune and H. Engel presented spectrophotometric studies of meandering spiral waves in the PBZ medium [148, 149, 163]. Since then the experimental study of spiral waves in the PBZR under various forms of external perturbations was achieved extensively in the working group of H. Engel [44, 155, 156, 157, 158, 159, 160].

At that time, the experiments mostly were carried out in thin layers of silica gels, loaded with the catalyst ruthenium, and under stationary non-equilibrium conditions maintained by the usage of the CSTR. Thin means a layer thickness ranging between  $0.2\text{ mm}$  up to  $0.6\text{ mm}$ . Some experiments that were carried out in the more thicker silica layers displayed rather peculiar results, which might have given the impression of being phenomena like reflective collision of wave bands, splitting of waves, or autonomous pacemakers in two-dimensional media. In 1999, P. Kolski investigated these results more thoroughly, with the aid of accompanying numerical simulations, and could show that these phenomena are more likely explained by three-dimensional effects showing up when scroll waves are confined in thin media [122].

The latter work strongly promoted the idea to study the influence of confinement on the evolution of scroll waves in thin layers of PBZ media more systematically. At the beginning, we decided to carry out these experiments in the framework of the experimental setup which was assembled as part of the thesis by J. Schlesner [164]. In this thesis, control of spiral wave dynamics by space- and time-modulated illumination was considered.

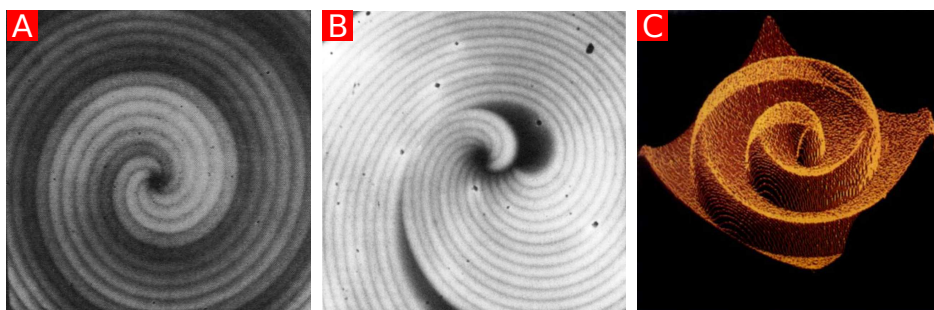


**Figure 21:** Spectrophotometric measurement of spiral waves geometric shapes and their central cores in the BZR. The first two panels, A and B, resemble digital overlays of consecutive time images, while panel C is a three-dimensional representation derived from a measurement like shown in figure 7, B (see on page 7). Panel A was constructed via additive composition of transmitted light intensities for six digital images of the propagating spiral wave. The images were measured at intervals of 3 seconds and cover almost one rotation period of the spiral. Panel B was gained by the same method as was done for the figure in panel A and shows the meandering tip motion. Panel A is reprinted with permission from [37], copyright by the American Association for the Advancement of Science. Panel B is reprinted with permission from [161], copyright by the American Chemical Society. Panel C is reprinted with permission from [162], copyright by Elsevier.

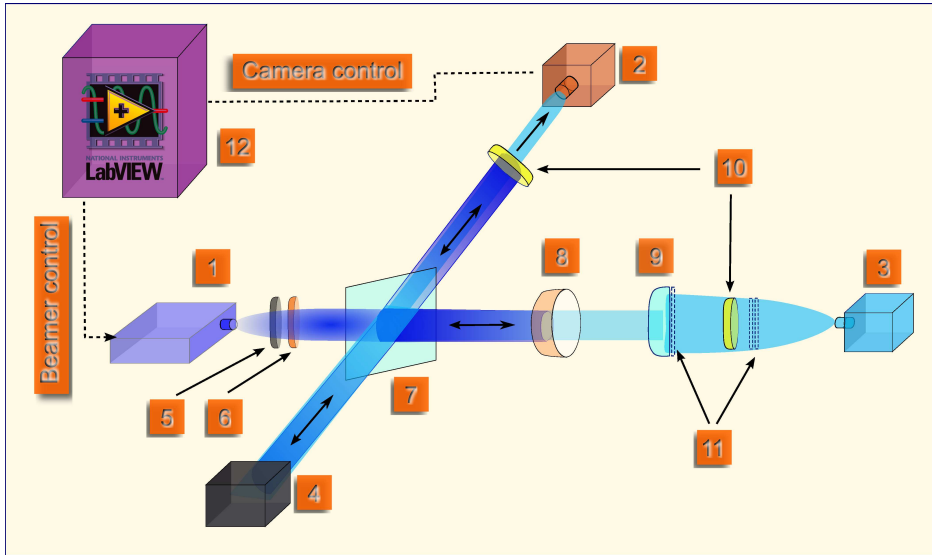


**Figure 22:** Schematic illustration of our experimental setup. (1) The projector (Casio XJ-A 140V), (2) USB CCD monochrome camera (The imaging source Europe, 1/2" Sony CCD), (3) Blue LED ( $\lambda \approx 475 \text{ nm}$ ) mounted on a cooling element, (4) black cardboard box to prevent mirroring effects, (5) blue dichroitic filter (Edmund Optics: NT-30-635; 5 cm square), (6) absorptive neutral density filter (OD 0.5 - 1.2, 5 cm square), (7) beam splitter (Edmund Optics: NT 46-632; 30% reflection, 70% transmission), (8) CSTR, (9) condenser lense (12.5 cm diameter), (10) yellow long pass filter (Edmund Optics: GG-475; 5 cm diameter), (11) diffusing foil, (12) computer with LabView-assisted control of the projector and CCD camera. For detailed explanations see in text.

Without going too much into detail, the main questions in the development of this setup were focused on the light sources (both for the observation and the control light), and how to separate these two light channels. These questions were successfully answered by a setup in which LEDs (Light emitting diodes) were used for both light sources. As the control light source a blue HighPower LED (Luminus PhlatLight PT120) was used, while a blue HighPower LED like Luxeon Rebel or K2 was taken into account as the observation light source. The issue of the optical channel separation was solved by polarization. For more details, the reader is referred to the thesis by J. Schlesner [164].

Unfortunately, experimental investigation of three-dimensional waves could not be carried out within the framework of the latter setup in a systematic manner. Although the HighPower LED (Luminus PhlatLight PT120) is the most powerful blue LED on the market to date, we were not able to initiate scroll waves in thin PBZ media reliably. The main reason for this drawback can be traced back to the following: The optical and polarization system devised to separate the two optical channels yields a significant decrease of the overall illumination intensity at the gel surface. In addition, the incident light is attenuated in the active reaction layer exponentially (Lambert-Beer law).

In summary, the incident light intensity does not suffice to inhibit wave propagation in an adequate layer section to allow formation of a three-dimensional wave such as a straight scroll waves and a scroll ring.

For that reason, we decided to develop a new setup. The main issues to solve once again involve the decision for appropriate light sources and the separation of the optical channels. There was no reason to substitute the observation light source. In contrast, the control light was too weak for our purpose, as was elaborated above. We had to seek for a light source that possesses its strongest illumination intensity at the appropriate wave length, which is at  $\lambda \approx 450\text{ nm}$  for ruthenium.

We found the projector Casio XJ-A 140 V as a good candidate. This projector possesses 24 Gallium-Nitride laser diodes with a nominal output power of  $\sim 1\text{ W}$  each. The high intensity peak of these diodes is located at a wavelength of  $\lambda = 445\text{ nm}$ . The projector additionally has a green and a red channel, the latter was blocked while the former was modified to emit also blue light. In addition, a lens with a focal distance of  $300\text{ mm}$  was mounted before the front of the projector. This was done in order to project smaller and simultaneously intenser images at shorter distances. This will allow for placement of the reactor at a much shorter distance to the projector and yield a lower loss of intensity at the gel surface. With regard to the separation of the two light channels, Schlesner already discussed three possibilities in his thesis [164]: by time, by wavelength, and by polarization. We decided to achieve a fourth separation method which is illustrated by figure 22.

The central part of the setup is the CSTR (figure 22, item 8), being illuminated by the blue LED (item 3) from right and by the projector (item 1) from left. The projector light passes through a blue dichroitic filter (item 5) and through an absorptive neutral density filter (item 6), before it reaches the beam splitter (item 7). Note that the absorptive neutral density filter solely is placed on the optical line for the purpose of calibrating the projector and camera coordinate systems before each experimental run. Otherwise the overall intensity would be too strong for the calibration procedure.

The beam splitter has a transmission value of 70 % and allows the separation of the two light channels. The observation light channel, coming from right, passes through a first diffusing foil (item 11) for homogenization. Then it passes through a yellow long pass filter (item 10) which will aid the blockade of the intense actinic light before the camera. The condenser lense (item 9), also coated with a diffusing foil, images the gel in the CSTR onto the camera (item 2). Before the camera, the second yellow long pass filter blocks the projector light while letting the observation light pass, otherwise the high intensity projector light would overdrive the observation light. A black cardboard box with a square shaped hole in its front (item 4) prevents appearance of background mirroring effects by the beam splitter.

During my primary studies of three-dimensional waves on the basis of the introduced setup, it was found that the illumination was not perfectly homogeneous. This unsatisfying situation was always leading to unwanted

twisting of scroll wave filaments. To preclude these unwanted deficiencies, we discussed passive (optical) and active (software-aided) possibilities for homogenization of both light channels. The mere optical homogenization of the observation light by the diffusing foils is sufficient for our purpose. In contrast, the homogenization of the control light was actively achieved. For that purpose, we devised a method that is coded into the LabView control software as an algorithm which can be run before each experiment. This algorithm uses the camera for measuring the outgoing light of the projector as a  $N \times N$  matrix, each of its elements assigned with a specific intensity value. For this procedure, at the position where the CSTR is placed, a flat square cardboard - coated with fluorescent color - is mounted on a sample holder. Subsequently, the measured intensity matrix is inverted and multiplied with the original intensity matrix.

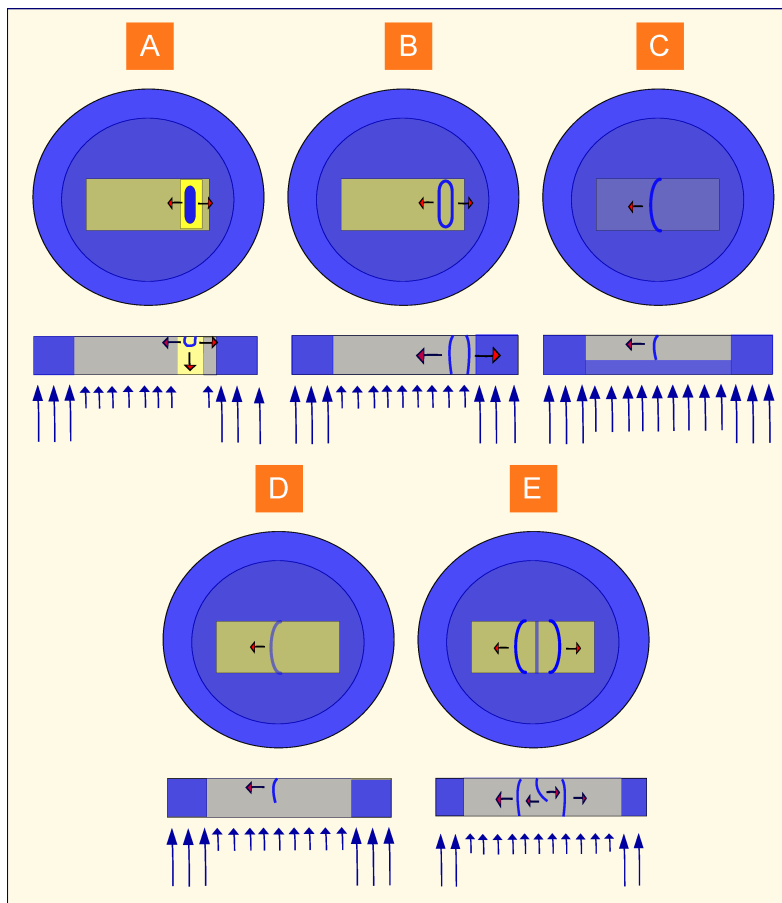


**Figure 23:** Schematic illustration of scroll wave initiation in the PBZR showing the gel layer from top and in cross-section. Blue arrows, whose lengths are proportional to the corresponding incident light intensity, indicate illumination of the catalyst-loaded gel disk from below. Red arrows indicate the direction of wave propagation. Top view shows in dark blue the unexcitable outer ring to prevent undesirable wave nucleation; light blue: partial wave annihilation; ochre: excitable domain. The yellow region in the cross-section of panel (A) corresponds to the initially dark central region with spontaneously emerging phase waves.

By that, we achieved an homogenization with a maximum intensity variation of 2 % over one diameter of the gel layer.

#### 4.5 INITIATION OF STRAIGHT SCROLL WAVES AND SCROLL RINGS

One of the advantages of the PBZ reaction is the elegant initiation of scroll waves exploiting wave inhibition in response to appropriate light application [63, 152, 153, 151]. This is illustrated for initiation of a straight scroll wave in figure 23 and for initiation of a scroll ring in figure 24.

In the following, let us explain the case for the scroll ring in more detail. At the beginning, the projector provides the illumination pattern shown in panel A. Between a strongly illuminated ( $\Phi > \Phi_2$ ) outer ring and very low light intensity in a small circular central domain (yellow in figure 24 A), the gel layer is in the excitable regime ( $\Phi_1 < \Phi < \Phi_2$ ). The strongly illuminated outer ring inhibits disturbing wave nucleation at the boundary of the gel disc. After some time, a phase wave from the dark, oscillatory central region transforms into a cylindrical trigger wave propagating outwards (figure 24 B). At a certain time moment we illuminate the gel layer (within the outer ring) uniformly with a light intensity  $\Phi > \Phi_2$  that inhibits wave propagation and therefore eliminates the lower part of the cylindrical wave front as shown in figure 24 C. After restoring the intensity back to the level applied previously (figure 24 B), the medium recovers excitability and the cut cylindrical wave curls up at its lower open end forming a circular closed filament (figure 24 D and E).

Obviously, the radius  $R$  of the emerging scroll ring and the distance of its filament plane from the layer boundaries  $z$  can be controlled varying the beginning of partial wave annihilation, and the intensity and/or the duration of illumination. Crucial for successful initiation of a planar filament plane oriented in parallel to the layer boundaries is, among other factors, a uniform illumination of the gel layer during partial annihilation of the cylindrical wave. Otherwise, scroll rings evolve with filament planes inclined with respect to the gel boundary or the filaments will be twisted.

**Table 1:** Table of the used BZ recipes in this thesis.

	[NaBrO <sub>3</sub> ]	[H <sub>2</sub> SO <sub>4</sub> ]	[CH <sub>2</sub> (COOH) <sub>2</sub> ]	[NaBr]
I	$9.33 \times 10^{-2}$	$3.07 \times 10^{-1}$	$6.25 \times 10^{-2}$	$6.67 \times 10^{-3}$
II	$2.0 \times 10^{-1}$	$2.8 \times 10^{-1}$	$1.5 \times 10^{-1}$	$6.0 \times 10^{-2}$
III	$5.0 \times 10^{-1}$	$2.8 \times 10^{-1}$	$1.5 \times 10^{-1}$	$6.0 \times 10^{-2}$
IV	$6.0 \times 10^{-1}$	$2.8 \times 10^{-1}$	$1.5 \times 10^{-1}$	$6.0 \times 10^{-2}$
V	$2.0 \times 10^{-1}$	$3.92 \times 10^{-1}$	$1.7 \times 10^{-1}$	$9.0 \times 10^{-2}$
VI	$4.5 \times 10^{-1}$	$3.0 \times 10^{-1}$	$1.9 \times 10^{-1}$	$6.0 \times 10^{-2}$

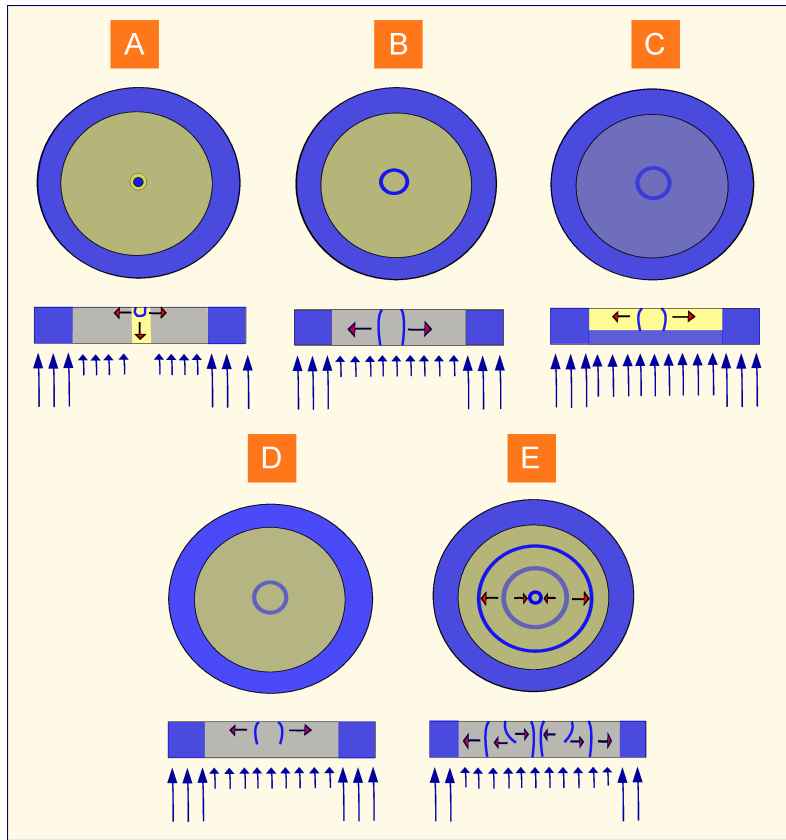


**Figure 24:** Schematic illustration of scroll ring initiation in the PBZR. Analogous to figure 18.

Analogously, we are able to initiate straight scroll waves (see figure 23). In contrast to the initiation of scroll rings, here the excitable region is always chosen to be a square-shaped area. Additionally, also the oscillatory seed wave is appearing in a larger square-shaped dark region at the right-handed exterior of the excitable area. Larger means here compared to the small circular regime that was chosen for scroll ring initiation.

#### 4.6 USED BZ RECIPES

In table 1 the six recipes that were used for the presented experimental results in this thesis are gathered. The initial and the continuously fed solutions are prepared from stock solutions containing specific molar concentrations of sodium bromate [ $\text{NaBrO}_3$ ] (Aldrich, 99 %), sulfuric acid [ $\text{H}_2\text{SO}_4$ ] (Aldrich, 95 % – 98 %), malonic acid [ $\text{CH}_2(\text{COOH})_2$ ] (Aldrich, 99 %), and sodium bromide [ $\text{NaBr}$ ] (Fluka, 99 %).



# 5

## THE VIRTUAL LAB PROJECT

---

### 5.1 THE PURPOSE OF THE VIRTUAL LAB PROJECT

The prime motivation that led to the development of the Virtual Lab project was the idea to mimic the abilities of our laboratory, where experiments of the PBZR are conducted. Primarily, we were focused on the precise spatial and temporal control of wave patterns by illumination. This puts us into the position to initiate waves of any particular form, and examine their evolution under the influence of boundaries, under external control by illumination that might be constant or periodic in time and space, and so on.

In order to interpret the experimental results, we designed a computational framework which is able to simulate the evolution of nonlinear waves by applying different reaction-diffusion models in one to three spatial dimensions, with multiple boundary conditions, and several external control strategies. For that purpose we decided to develop our reaction-diffusion simulation project within the context of an object-oriented language.

Object-orientation is a programming concept which allows development of projects with high degree of abstraction and reusability. Based upon the object-oriented philosophy one tries to subdivide the project into an optimal set of single independent units. These can be effectively interconnected. The process of finding an optimal architecture for a project is a piece of art. So-called classes represent real world objects within a object-oriented architecture. These classes define properties (attributes) and actions (methods) associated with them. One may regard to a class as a blueprint for a specific object, while the latter is referred to as an instance of the class.

There might be a good example to illustrate this concept. Let us imagine a car as an object of our everyday world. A car can be defined by a small set of properties: it has a number of doors, an accelerator pedal, a gear box, a specific number of tires, a steering wheel, and so on. A class that is defined in order to describe a car would mean to abstractly name all attributes (e.g. the color) and actions (e.g. starting the engine) which are common to all cars. Creating an instance means to provide explicit values for the attributes. The reusability of frequently used fundamental properties is additionally ensured, since the wheel must not be reinvented everytime a new car is constructed.

With the object-oriented philosophy in mind, we proposed an architecture for our reaction-diffusion simulation project referred to as the Vitual Lab. There are some object-oriented programming languages (Java, C++, Python, ...).

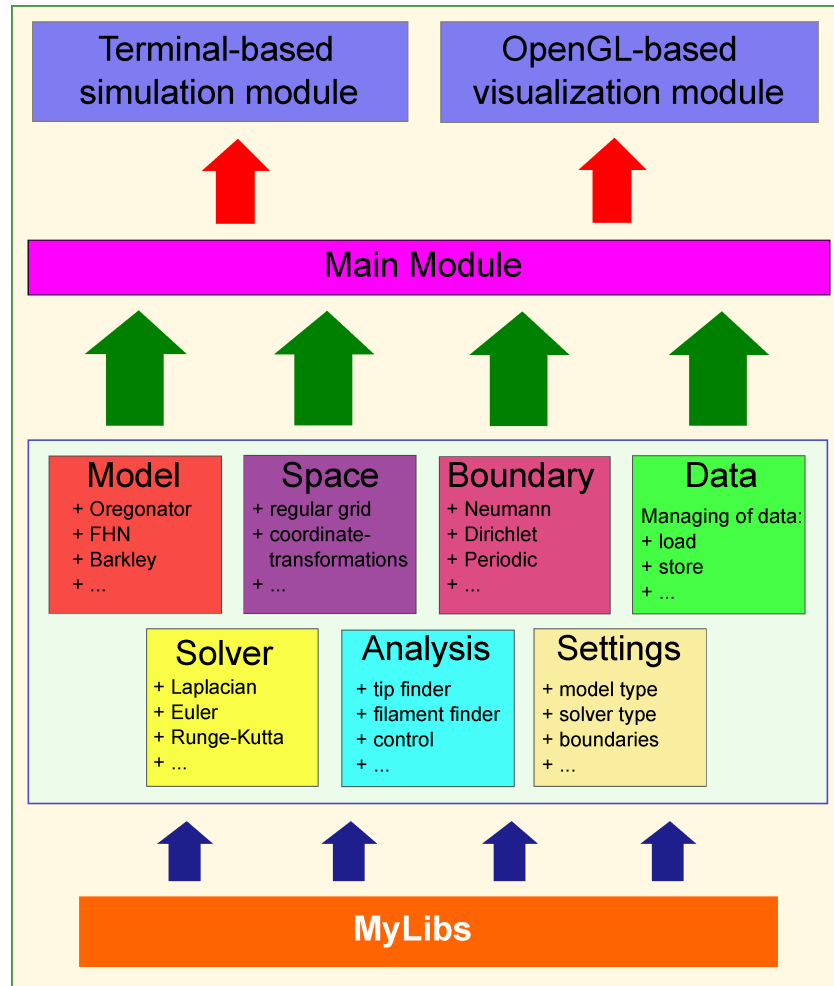


**Figure 25:** Proposed architecture of the VirtualLab project. Details are explained in the text.

We decided to take the C++ programming language as the platform for developing the project for two reasons: (1) In contrast to languages like Java and Python which possess an interpreter level that interprets the software code at run-time on the chosen hardware machine, the C++ software code primarily is compiled. The compiled binary file is directly executed on the underlying machine. This yields a speed advantage compared to the interpreted languages, in particular for solving systems of partial differential equations like those in multi-variable reaction-diffusion models in extended three-dimensional media. (2) Existing visualization software has already been developed by S. Fruhner within the scope of his doctor thesis [165]. This visualization module is written using the OpenGL library in C++. Its reuse for the VirtualLab project promised to be beneficial.

The proposed architecture for the VirtualLab project is shown in figure 25. At the center of this structure chart the subdivision into seven main modules is illustrated, each of which is represented by its title: model, space, boundary, data, solver, toolbox, control, and settings. Having defined the interfaces between the main units allows to extend the project by new models

and functions on the level of a single unit without being obliged to make changes within the other units.

The MyLibs module depicted at the bottom of the chart encapsulates all external (implemented by others) and internal libraries (implemented by us) that are frequently used in all modules. The external libraries are the window management library Fast Light Toolkit (FLTK<sup>1</sup>) and the GNU Scientific Library (GSL<sup>2</sup>).

The main module possesses two input/output interfaces: a terminal-based (unix command line) interface for compiling and running the project and a visualization module. In the following subsections, I will provide a short summary for each of the seven central modules of the project.

### *The Model Class*

The purpose of the model class is to implement a general reaction-diffusion model, characterized by a number of variables ( $m \in \mathbb{N}$ ) and a number of parameters ( $p \in \mathbb{N}$ ). The specific mathematical definition of such a reaction-diffusion model can be written in the following way (as was introduced by equation (1) on page 21 and equation (54) on page 36):

$$\partial_t \mathbf{u}(\mathbf{r}, t) = \mathbb{D} \Delta \mathbf{u}(\mathbf{r}, t) + \mathbf{f}[\mathbf{u}(\mathbf{r}, t), \mathbf{p}]. \quad (97)$$

In the above system of partial differential equations we have the vector  $\mathbf{u}(\mathbf{r}, t) \in \mathbb{R}^m$  (e.g. the vector of some chemical concentrations), the vector of parameters  $\mathbf{p} \in \mathbb{R}^p$ , the vector of (nonlinear) functions  $\mathbf{f}[\mathbf{u}(\mathbf{r}, t); \mathbf{p}] \in \mathbb{R}^m$  (e. g. nonlinear reaction rates), the  $m \times m$  diagonal matrix of diffusion coefficients  $\mathbb{D} \in \mathbb{R}^{m \times m}$  (e.g. of the corresponding chemical species), and dimension of system  $m \geq 2$ . Furthermore, the spatial coordinate system is two- or three-dimensional, that is  $\mathbf{r} \in \mathbb{R}^n$  with  $n = 2$  or  $n = 3$ . Hence, the Laplace operator  $\Delta$  is defined in two or three spatial dimensions.

A specific model can be derived (inherited) from this base parental class. Currently the implemented models are: the Barkley model, the Bueno-Orovio-Cherry-Fenton model, the FitzHugh-Nagumo model, the modified Oregonator model, the Brusselator model, the van-der-Pol oscillator model, the Ginzburg-Landau model, the Schlögl model, and the Rovinsky model.

### *The Space Class*

The geometry of the spatial grid used in the simulations is defined in the space class. Currently a cartesian grid, a radially symmetric grid, and a spherical coordinate system are supported. The base class for the space module does not deliver a specific geometry, but abstract index-coordinate

---

<sup>1</sup> <http://www.fltk.org/index.php>

<sup>2</sup> <http://www.gnu.org/software/gsl/>

conversion methods which must be implemented by the derived classes. Furthermore, conversion methods between different coordinate systems (e.g. cartesian to polar and vice versa) are defined.

### *The Boundary Conditions Class*

The boundary conditions class delivers the functionalities for specification of multiple boundary conditions in one to three spatial dimensions. In particular for three spatial dimensions, the boundary conditions for each spatial direction can be specified separately. The situations in one and two dimensions are just subsets of the three-dimensional space. In the actual version of the Virtual Lab, three boundary types are implemented: periodic, Dirichlet, and Neumann (no-flux) boundary conditions.

### *The Data Class*

The data class defines methods for storing and loading state files. The state of the simulated system at an instance of the simulation time is given by all values of the reaction-diffusion model variables at each grid point.

At run-time, the data object is created in the form of a one-dimensional array on the computer RAM (“Read Access Memory”). The length of the array is given by the product of the number of variables from the model and the number of grids in the space. This decision for choosing a one-dimensional array for the data object will speed up calculations when the solver methods operate on the data object.

Currently, the methods for loading data from files and storing data to files incorporate a simple dat-file format and the netcdf-file format<sup>3</sup>. Other file formats might be implementable in the future.

### *The Solver Module*

The solver module provides efficient solution methods for the used reaction-diffusion systems of equations. The module is subdivided into two separate abstract subclasses. The primary subclass deals with the time integration of the system which is termed the TimeEvolution class. The second submodule is the DiscretizedLaplacian class which implements variants of the Laplace operator. Basic time evolution algorithms implemented are the Euler time stepping and the Runge Kutta time integration methods (detailed explanation delivered in the textbook [166]). Examples for the Laplacian are given by several finite difference schemes [166]. For example, a scheme that takes into account only the nearest neighbors (7-points method) and a scheme

---

<sup>3</sup> For further information on the netcdf file format, see for example on the main netcdf project homepage: <http://www.unidata.ucar.edu/software/netcdf/>

which additionally takes into account the next nearest neighbors (19-points method).

### *The Analysis Module*

The analysis module incorporates tools for the analysis of the propagating nonlinear waves investigated within the simulation project. Most importantly, a parametric control scheme is provided within the module. The parametric control scheme allows control of wave patterns via any arbitrary parameter of the chosen reaction-diffusion model. As mentioned in the beginning of this chapter, the parametric control within the PBZ reaction is provided by the applied illumination, which is now provided also within the Virtual Lab. Additionally, some very essential measuring methods like the iso-surface calculation, the tip finder algorithm, and analogously the filament finder algorithm are implemented within the Analysis module.

### *The Settings Class*

The last submodule of the Virtual Lab is the settings module. The functionalities defined in the base settings class enables us to set optional and required parameters and variables of the other modules before a simulation run. This is mainly done by the so-called ini-files. The form of the ini-files with some of the various options is exemplified in listing 1. After each equal sign one can specify a numerical value or a string. In particular, one can include a path to a directory after the “path=” line at the beginning of the example ini-file and the state files will be stored there. The options of each used model, space type, tool, etc. can be specified under separated sections that start with the name inside squared brackets, e.g. [CartesianSpace], [ModelOregonator], etc.

**Listing 1:** An example ini file.

```
# Path of the files. Don't forget the '/' at the end.
path=

# Type of the grid/coordinate system
grid=CartesianSpace

# Method of time evolution
method_time_evo=Euler

# Discretized laplacian
method_diff=PointSeven

# Model to use
model=Model_Oregonator

# For selecting a starting pattern
```

```
data_start_pattern=spiral

# How often should the states be saved
auto_save_time=1

# How much steps should be at maximum calculated
max_time=20

# List of all the plugins. Simply uncomment if
# you intend to use a plugin.
{PlugIns}
TipFinder
#FilamentFinder
...

# now the sections in alphabetical order
[BoundaryConditions]
default=NEUMANN_ZERO
#~ left=PERIODIC
#~ right=PERIODIC
#~ back=
#~ front=
#~ up=
#~ down=

[CartesianSpace]
dx=0.3
dy=0.3
dz=0.3
pixels_x=200
pixels_y=200
pixels_z=0

[Model_Oregonator]
one_over_eps=8
one_over_eps_p=720
q=0.002000
f=1.80000
phi=0.002

[TipFinder]
computation_steps=100
t1=0.3
t2=0.3

[TimeEvolution]
dt=0.0005
```

## 5.2 EXHIBITION OF THE VIRTUAL LAB CAPABILITIES

In the previous section, the architecture of the Virtual Lab project was discussed in detail. In this section, the purpose is to illustrate some of the most striking abilities of the project. In particular, the reproducible initiation of a plethora of nonlinear waves in two- and three-dimensional excitable media, like we are able to achieve in the framework of the PBZ reaction, was the motivation for the development of the simulation project.

An example for initiation of spiral waves in Virtual Lab that mimics the initiation in the laboratory is shown in figure 26. The reaction-diffusion model that served as a basis for this numerical simulation is the modified complete Oregonator (MCO) model. I will introduce this model in section 7.1 on page 93, particularly represented by the equations (98) therein. In this model, the corresponding parameter  $\phi$  which is assumed to be proportional to the applied illumination intensity, serves as the control parameter for spiral wave initiation.

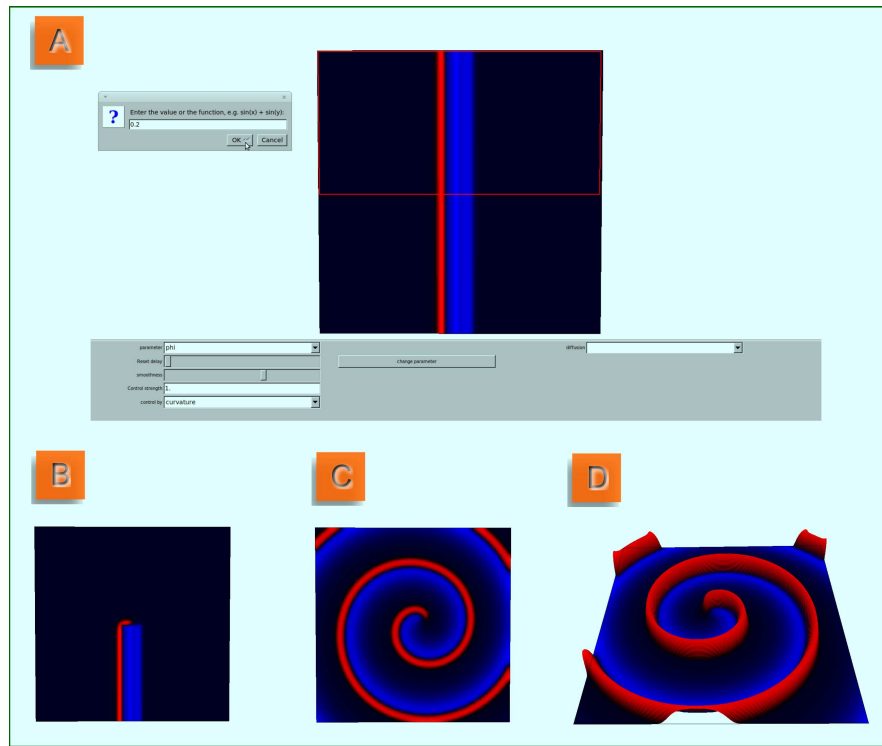


**Figure 26:** Initiation of a spiral wave in Virtual Lab. Simulation was achieved in the framework of the MCO model. MCO variable  $u$  (activator) is shown in red and variable  $w$  (inhibitor) in blue. (A) The upper half of the medium is selected (red-rimmed square area) where the photoinhibitory parameter  $\phi$  is set to a high value ( $\phi = 0.2$ ) leading to the extinction of the upper wave half. (B) After resetting the upper medium half to the homogeneous value of parameter  $\phi$ , the wave curls at its open end. (C) The fully developed spiral wave is shown from top and (D) in a pseudo-three-dimensional view, analogous to the experimental pictures constructed by Müller et al. with the aid of their spectrophotometric method (see also panel C of figure 21 on page 60).

A spiral wave in Virtual Lab is initiated analogous to the experiments conducted within the PBZ reaction. At first, a plane wave is taken as initial state for the numerical integration of the MCO equations. The initial wave is placed in the middle of the medium and propagates to the left. Subsequently, a square area in the upper half of the medium is selected (red-rimmed region in panel A of figure 26) and the parameter  $\phi$  is set directly for that chosen area ( $\phi = 0.2$ ). This sufficiently high value is assigned for each grid element of the chosen area and yields this area to be non-excitatory. Hence, the wave part located in this region will be extinguished. After resetting the chosen area to the homogeneous background  $\phi$ -value, the open end of the remained wave curls into the upper medium area and forms a spiral wave (panel B). In panel C this spiral wave is evolved completely. An additional feature of the Visualization interface is shown in panel D. This pseudo-three-dimensional visualization of the spiral wave displays the numerical analog of the spectrophotometric measurements by Müller and colleagues [37, 162, 161].

In a next step, it is essential to analyze characteristic properties of spiral waves. One of these characteristic properties is the spiral wave core structure. We can measure the pattern which is drawn by the spiral tip over the course of time and visualize it in real-time as shown by panel B of figure 27. Moreover, one can measure the time-evolution for an arbitrary set of model variables at one grid point (panel A) and space-time plots at a selected line (panel C). The latter two features can be used to determine spiral wave characteristic like the wavelength  $\lambda$  and rotation period  $T$ .

Some more features of the visualization interface include the real-time Fourier transformation of the spiral tip trajectory data and the subsequent determination of the spiral wave rotation frequency, the possibility to plot the phase-space (one model variable  $v$  plotted over another variable  $u$  for all grid points), saving and loading of state files, and exporting of the graphs to pdf- and png-files.

Regarding the parametric control, the implementation of a function parser also allows the setting of any parameter according to any arbitrary mathematical function in space and time. At the input window where the parameter  $\phi$  was set to initiate the spiral wave (see panel A of figure 26), instead of a numerical value one can just give any function that depends on space and time, e.g. functions like  $f(t) = A \sin(B \cdot t)$ ,  $f(x,y) = Ax + By + C$ ,  $f(z) = A \exp(-B \cdot z)$ , etc. In these functions  $A$ ,  $B$ , and  $C$  are some arbitrary constants.

Until now, I discussed the capabilities of the Virtual Lab project, particularly for its visualization interface, based upon the real-time initiation and analysis of spiral waves. This is due to the fact that real-time computation is still practicable in two spatial dimensions, but no more feasible in three-dimensional media. Nevertheless, the Virtual Lab can also be used for initiation and analysis of three-dimensional waves.

The whole machinery including the usage of the ini-files for the specification of all simulation parameters is achieved without the real-time visualization.

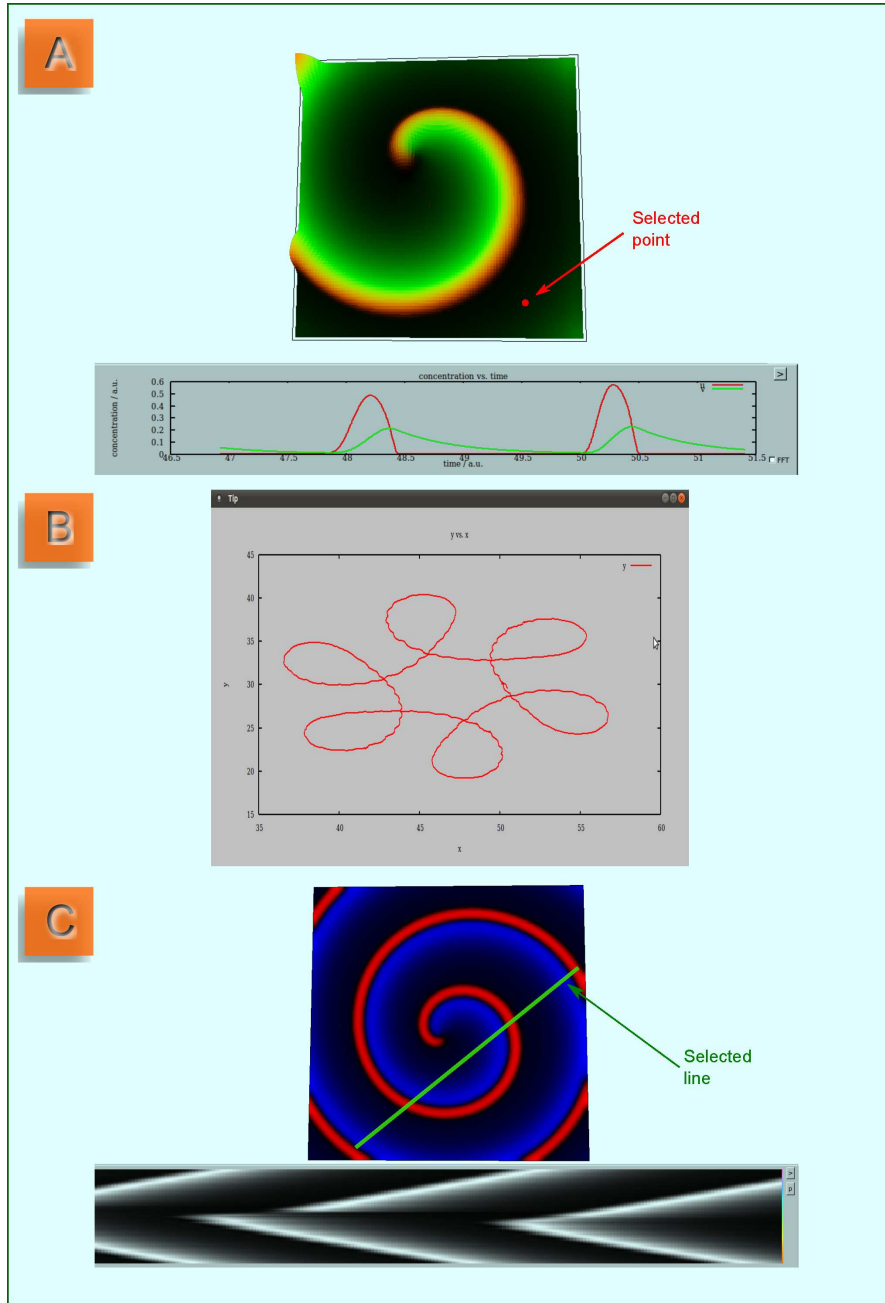


**Figure 27:** Spiral wave analysis in the Virtual Lab project. (A) Time evolution of two Oregonator variables ( $u$  and  $v$ ) measured at the selected grid point over time and illustrated in real-time by the lower graph (scaled concentrations of  $u$  and  $v$  in red and green, respectively). (B) The spiral wave tip trajectory pattern. (C) The space-time plot measured in real-time at a selected line (green line in the upper picture).

However, one can use the visualization interface at a later time for automated loading and analysis of the stored state files. In particular, these state files can be visualized from different viewing angles, and the corresponding pictures can be exported to png-files. The advantage of these features are illustrated by figure 28 showing one state of a straight scroll wave and a scroll ring, respectively. In both cases, the MCO model served as the basis

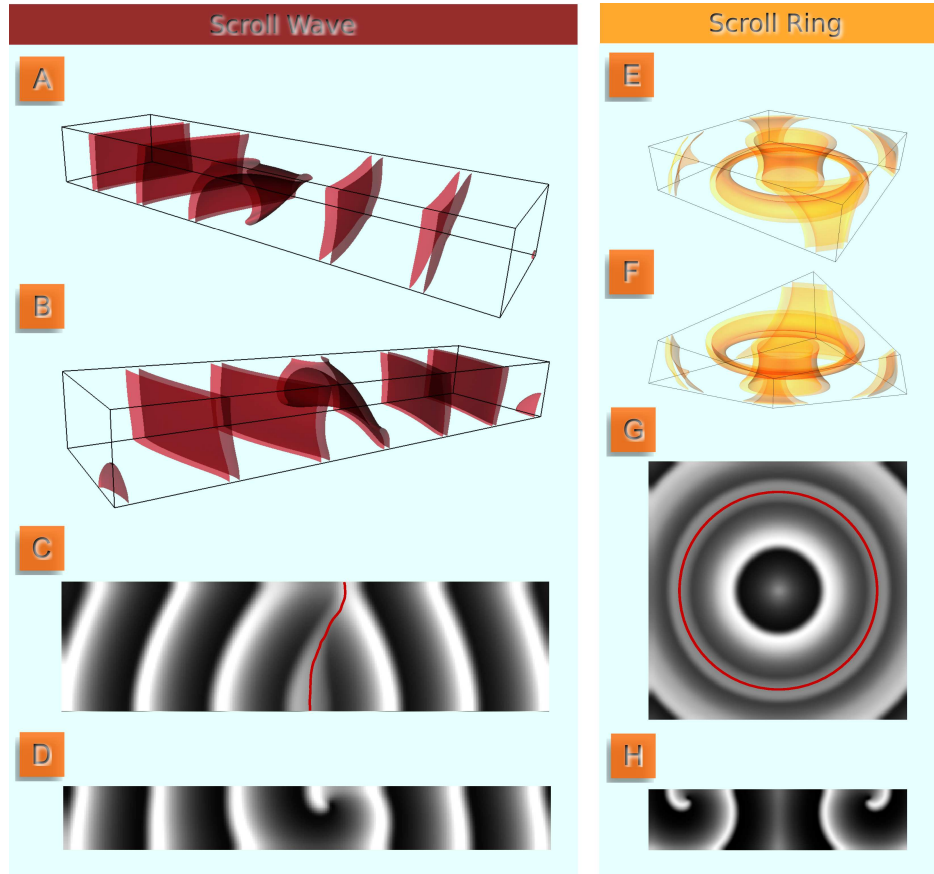


**Figure 28:** Visualization of straight scroll waves and scroll rings in the Virtual Lab project. Panels A, B, E, and F display perspective views with the iso-concentrations in dark red and orange, respectively. Panels C and D illustrate top views (analogous to the experimental measurements in our laboratory). The red curves on the top view pictures depict the corresponding filaments. Panels D and H show a cross-section through the straight scroll wave and the scroll ring, respectively.

for the numerical simulations. In case of the straight scroll wave, along the filament the parameter  $\phi$  is varying linearly, such that the appearing inhomogeneity yields a twisted filament. The perspective views are displaying iso-concentration planes for one variable of the MCO model (often for the variable  $u$ ). The top view mode is generated by the summation of one model variable (here the MCO variable  $v$ ) over the height coordinate  $z$ . This shall mimic the experimental situation where the camera is viewing the top layer of the gel. All these different viewing modes are achieved with the aid of the Virtual Lab visualization interface.

In addition, I will achieve quantitative analysis on the filaments of scroll waves. For that purpose, J. Totz has developed some scripts in Mathematica which enables us to investigate the time evolution of filaments. In particular, we can investigate the evolution of the filament for scroll rings by plotting the radius  $R$  of the ring-shaped filament, the axial position of the filament plane  $z$ , and the overall length  $l$  of the filament over time.

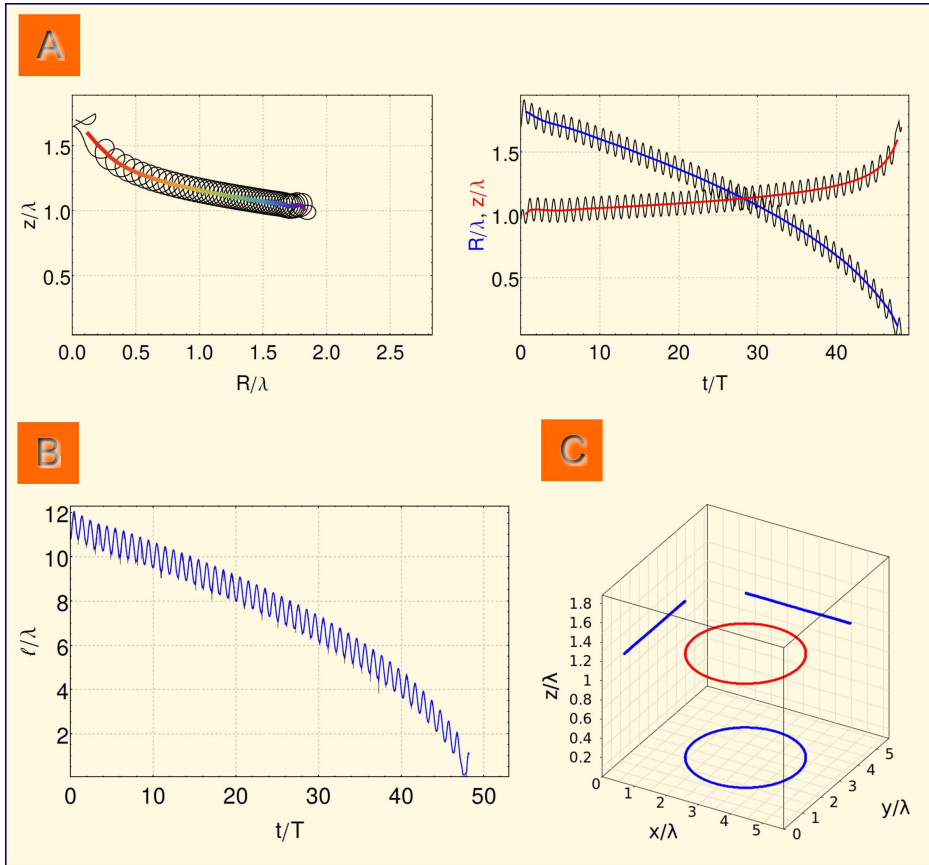


**Figure 29:** Analysis of scroll ring filaments. The space is scaled by the wavelength  $\lambda$  and the time by the rotation period  $T$  of the corresponding spiral wave. (A) Left: Phase plot showing the time evolution for the axial position of the filament plane  $z$  over the filament radius  $R$ . The thick rainbow-colored line denotes the mean trajectory of the filament's  $z$ - $R$ -evolution, with purple at the beginning and red at the end of the scroll ring life-time. Right: Evolution of  $z$  and  $R$  over time. The oscillations on the black curves are due to the rigid rotation of the spiral waves. The red and blue curves represent the moving central averages  $\bar{z}$  and  $\bar{R}$ , respectively. (B) Time evolution of the overall filament length. (D) One fixed state of the filament showing the filament in red and its projections to the walls in blue.

These plots are illustrated for a sample scroll ring in figure 29. The sample scroll ring was simulated in the framework of the MCO model. Panel A shows the evolution of  $z$  and  $R$  in time, while panel B displays the filament length over time. Additionally, pictures like shown in panel C will be found frequently throughout the following chapters of my thesis. These pictures shall illustrate the shape of the filaments in the course of time. Here, the filament is shown in red while its projections to the walls are drawn in blue.



### Part III

## STRAIGHT SCROLL WAVES UNDER SPATIAL CONFINEMENT



## NUMERICAL STUDY OF FILAMENT INSTABILITIES FOR STRAIGHT SCROLL WAVES UNDER CONFINEMENT

### 6.1 INTRODUCTION

In section 3.4, I presented a summary of the investigation for scroll waves in isotropic media by Henry and Hakim [87]. In the latter publication the authors reported on three types of instabilities for straight scroll waves in spatially extended media: translation-band instability, three-dimensional meander instability, and twist-induced sproing instability. These instabilities arise, even though corresponding spiral waves are stable in two-dimensional space.

The motivation for the present chapter is to study the influence of confinement on development of filament instabilities. I will examine the question if boundary-mediated restabilization of these unstable straight scroll waves can be achieved or not. Recently, Dierckx et al. reported on the suppression of the translation-band instability (e.g. the negative line-tension instability) by a vertical confinement of straight scroll wave filaments [167]. Above a certain critical thickness of the medium the latter filaments starts to buckle.

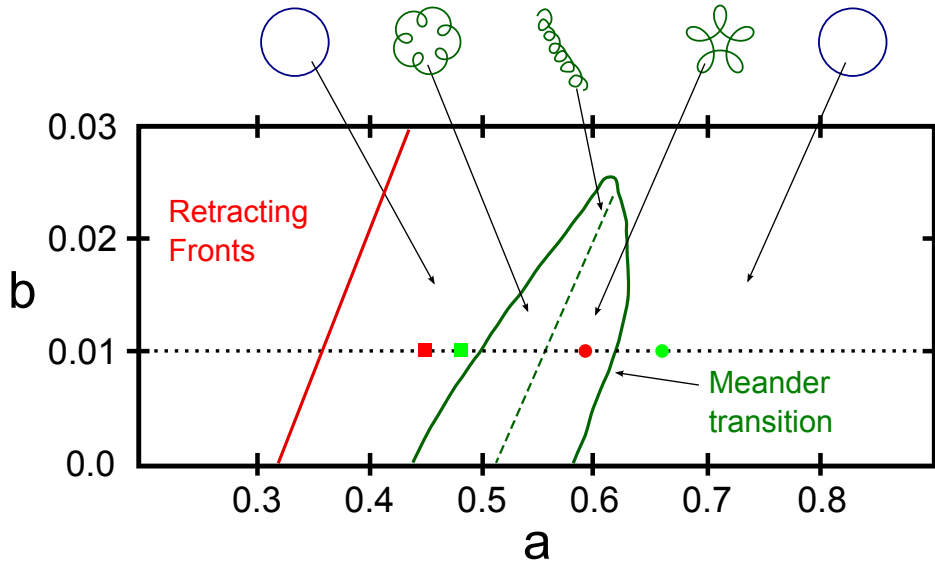


**Figure 30:** Schematic bifurcation diagram for spiral waves in the Barkley model. The bold green line depicts the meander transition line which separates spirals with rigidly rotating tips from spirals with meandering tip motion. Spirals retract left of the thick red line [131]. Along the dotted horizontal line through  $b = 0.01$  four different parameter points (green circle, red circle, green square, and red square) are chosen to investigate evolution of straight scroll waves under confinement. The remaining parameter is  $\epsilon = 0.025$ .

$a$	$\lambda$ [s.u.]	$T$ [s.u.]	Rotation	Indication in figure 30
0.44	19.8	5.5	rigid	red square
0.48	16.3	4.6	rigid	green square
0.58	11.0	4.0	meander	red circle
0.66	11.4	3.6	rigid	green circle

**Table 2:** Table shows results of the wave length and period determination for spiral waves simulated in the Barkley model for the parameters indicated in figure 30. The other parameters are fixed to  $b = 0.01$  and  $\epsilon = 0.025$ . The abbreviation s.u. depicts the term “simulation unit”.

Our objective was to examine the evolution of straight scroll waves which are rather horizontally than vertically confined numerically. In accordance with Henry and Hakim [87], we performed these investigations in the framework of the Barkley model for the four parameters which are shown in figure 30.

Some preliminary numerical investigations were accomplished for spiral waves in order to determine wave lengths  $\lambda$  and periods  $T$  for the chosen parameters. The results are presented in table 2. Note that apart from the parameter  $a = 0.58$ , which is supporting meandering spiral waves with outward petals, the other three parameters yield rigidly rotating spiral waves.

We consider two distinct setups for the numerical simulations. Both setups are sketched in figure 31. In both cases, periodic boundary conditions are chosen for the right and left walls (in direction of the filament). The upper and lower faces are no-flux boundaries, while at the two remaining faces (front and back) either no-flux or periodic boundary conditions are chosen. Furthermore, the size of the media are scaled in terms of the corresponding spiral wave length  $\lambda$ .

In the first setup (panel A), the influence of one no-flux boundary is investigated. Here, the scroll wave is initiated at a distance  $d \ll \lambda$  from the lower boundary. All other boundaries are always sufficiently far away ( $> \lambda$ ) from the filament, such that their influence on the filament evolution can be excluded. In terms of the second setup, displayed by panel B of figure 31, the scroll wave is initiated in the middle between all surrounding boundaries.

In the following two sections, I will present some of the results of numerical studies which were performed by Dirk Kulawiak within the scope of his Master thesis [168]. All simulations were achieved using the finite central difference method for the Laplacian with spatial discretizations  $dx = dy = dz = 0.2$ , and Euler forward stepping for time integration with discretization  $dt = 0.005$ . Diffusion coefficients for the two components in the Barkley model (see equations (81) - (84), and in the references [88, 87]) were chosen as  $D_u = 1$  and  $D_v = 0$ . In all numerical simulations, Gaussian white noise with zero mean value and variance  $\sigma = 0.1$  was applied to the unperturbed scroll wave as a spatio-temporal perturbation of model parameter  $a$ , and only during a short time after the initiation of the scroll wave, in order to examine the emergence of filament instabilities.

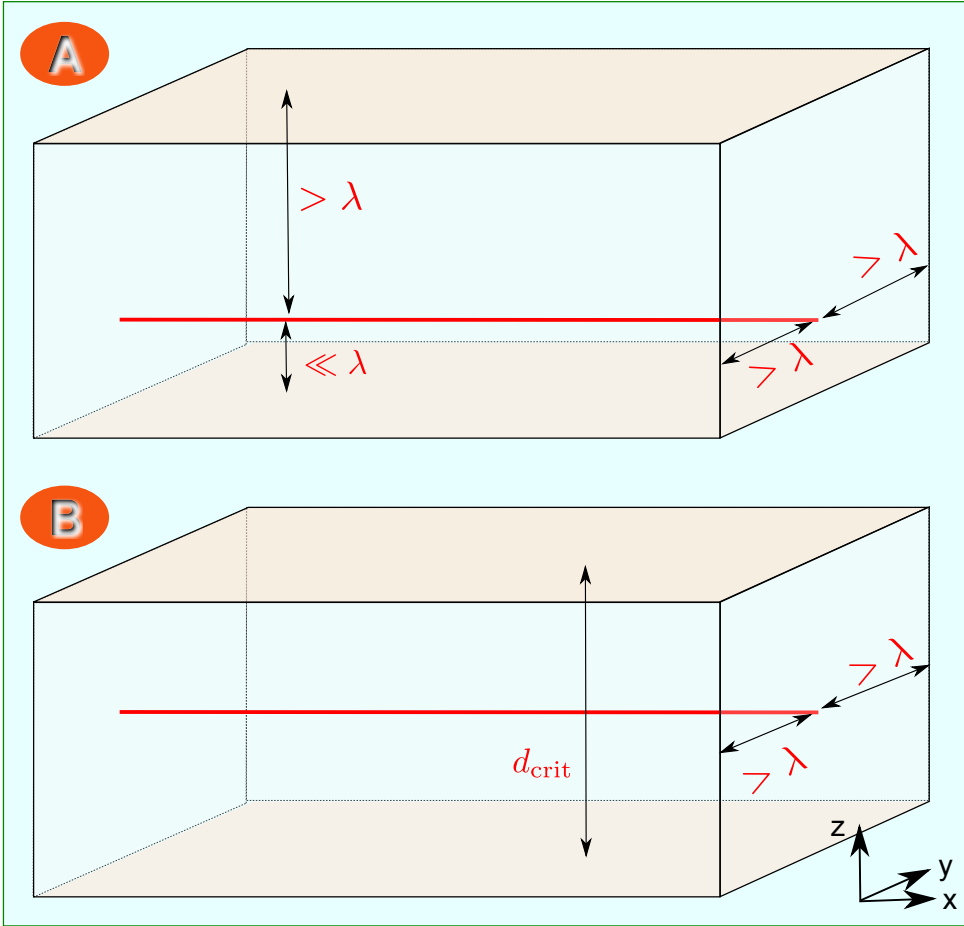


**Figure 31:** Two setups for numerical investigation of straight scroll waves under spatial confinement. The filament is displayed in red. Dimensionality of space is scaled in terms of spiral wave length  $\lambda$ . Panel A illustrates the first setup in which the evolution of the filament under the influence of the lower boundary is investigated. Panel B exposes the second setup in which the influence of media thickness on filament evolution is examined.

## 6.2 THREE-DIMENSIONAL MEANDER INSTABILITY

Let us primarily start with the parameter  $a = 0.66$  (green circle in figure 30). Numerical simulations were achieved first for an initially perturbed filament in an unbounded medium. This was done, in order to reproduce previously found results by Henry and Hakim [87]. Afterwards, we examined evolution of the filament at varying distances from one no-flux boundary. In both cases - free and confined scroll wave - the filament is restabilized to a helix. Our studies did not reveal a significant change to the restabilized state due to interaction with the no-flux boundary for this parameter.

Next, we studied evolution of filaments for the parameter  $a = 0.58$ . Henry and Hakim did not consider this parameter explicitly. Spiral waves meander with outward petals for this parameter (red circle in figure 30). Numerical simulations in an unbounded medium of size  $\sim 2.4 \times 7.3 \times 7.3 \lambda^3$  revealed a secondary three-dimensional meander instability.

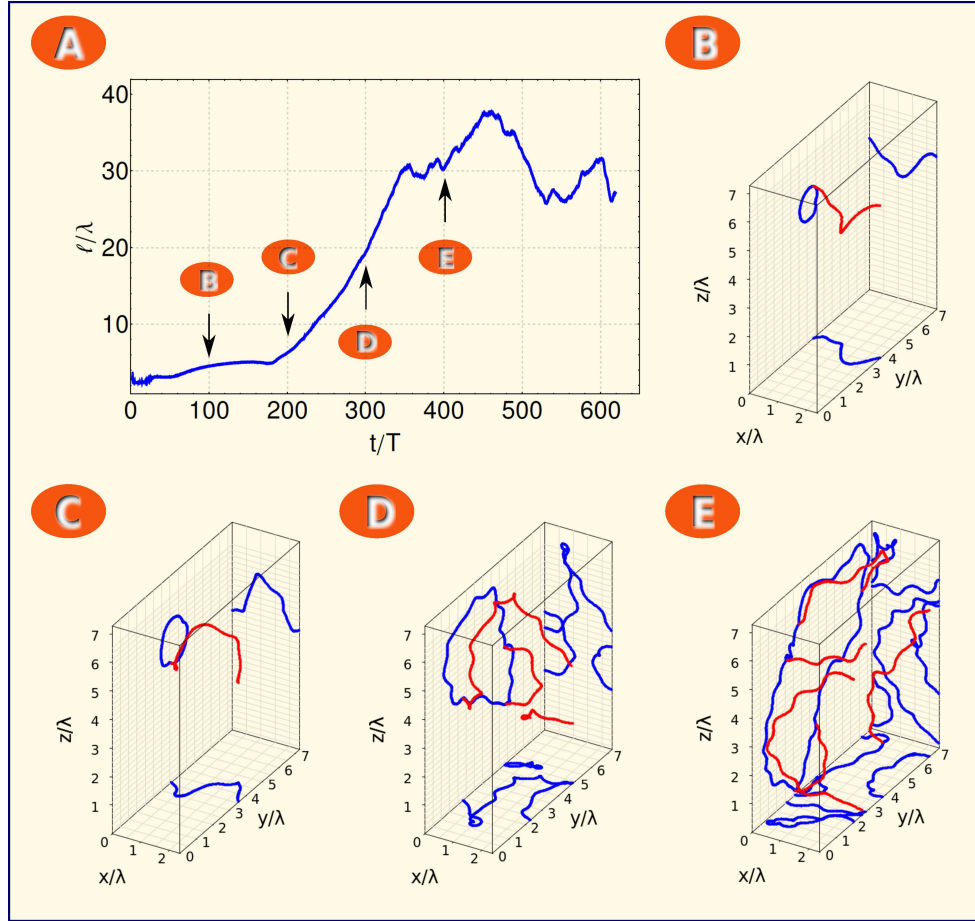


**Figure 32:** Secondary three-dimensional meander instability for parameter  $a = 0.58$ . (A) The mean filament length as a function of time is plotted in blue. Additionally, arrows are depicted to show location of the snapshots displayed by panels B to E. The snapshots are taken at (B)  $100 T$ , (C)  $200 T$ , (D)  $300 T$ , and (E)  $400 T$ . The filaments are shown in red and its projections in blue. Simulations were performed for the parameter set  $a = 0.58$ ,  $b = 0.01$ , and  $\epsilon = 0.025$ . Boundary conditions were chosen as periodic on the left, right, back, and front faces of the medium, while the upper and lower faces are no-flux boundaries. Medium size is  $2.4 \times 7.3 \times 7.3 \lambda^3$ .

This instability is qualitatively illustrated by figure 32. The panels in the figure demonstrate the emergence of the instability by the time evolution of the overall filament length (panel A) and four time snapshots (panels B to E). At the beginning, a straight filament is initiated in the center of the simulation domain. After a perturbation, the instability appears and is amplified (panels B and C). In comparison to the previously discussed parameter ( $a = 0.66$ ), here the filament does not restabilize to a helical shape, but further destabilizes (panels D and E). Finally, the overall filament length is grown enormously (panel A) and a breakup into several smaller filaments is reached (panel E).

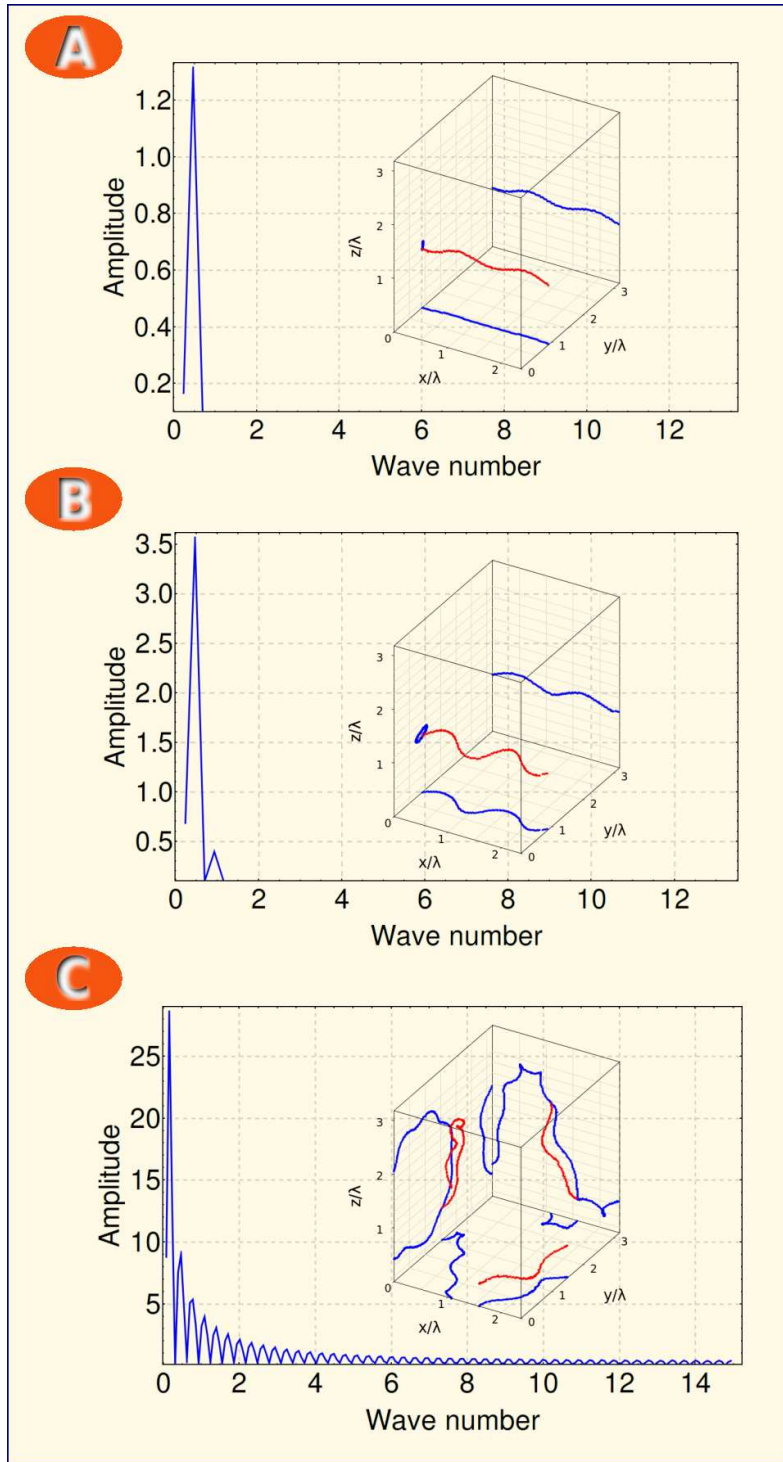


**Figure 33:** Fourier spectral analysis for a filament in an unbounded medium of size  $\sim 2.4 \times 3.2 \times 3.2 \lambda^3$  elucidating emergence of a secondary meander instability. In all three panels (A-C) the Fourier spectra for the  $y$ - coordinate data are shown (spectra for the  $z$ -coordinate data are analogous). The zeroth frequency mode, corresponding to the natural scroll wave rotation frequency, is dropped from the underlying spectral data. The inset figures display the filament states at the corresponding time points: (A) 12  $T$  (B) 22  $T$ , and (C) 225  $T$ . Parameters as in figure 32. Boundary conditions were chosen as periodic on the left, right, back, and front faces of the medium, while the upper and lower faces are no-flux boundaries.

In order to analyze the emergence of this secondary meander instability a bit more quantitatively, we applied a Fast Fourier Transformation (FFT) algorithm on the two spatial coordinates  $y$  and  $z$  along the filament (displayed by the projections of the filament on the medium walls, e.g. in figure 32), providing a power spectrum for each fixed time moment of filament evolution. Since periodic boundary conditions are set for the walls at both end points of the filament, only a discrete count of wave numbers can be observed. The results of the Fourier analysis for one sample simulation are depicted by figure 33. In early stages of filament evolution (panel A), small periodic modulations appear along the filament. The corresponding power spectrum shows the emergence of a peak at the wave number  $k_1 \approx 0.46$ . Note that this helix-shaped filament with the single wave number is the final restabilized state in case of parameter  $a = 0.66$ . In contrast, modulations are amplified further in case of  $a = 0.58$ , accompanied by the appearance of one more (smaller) peak at wave number  $k_2 = 0.94$  (after 22  $T$ , panel B). In the periods of the filament evolution following, further destabilization of the filament is accompanied by the amplification of continuously emerging modes (panel C). It has to be noted that this secondary instability solely could be observed in sufficiently large spatial domains (initially all surrounding boundaries more than  $2\lambda$  away from the filament). Moreover, the instability did not occur if no-flux boundary conditions are set for the walls at which the filament end points are attached.

Next, the influence of one planar no-flux boundary on the development of the secondary meander instability was studied. For that, numerical investigations in setup one (figure 31, A) and different distances from one no-flux boundary were achieved. Figure 34 displays one example simulation for a scroll wave which was initiated at  $\sim 0.2\lambda$  away from the upper no-flux boundary. Instead of the secondary meander instability observed in unbounded media, the filament now stays at the boundary, drifts along the boundary, and evolves into a non-stationary helical state.

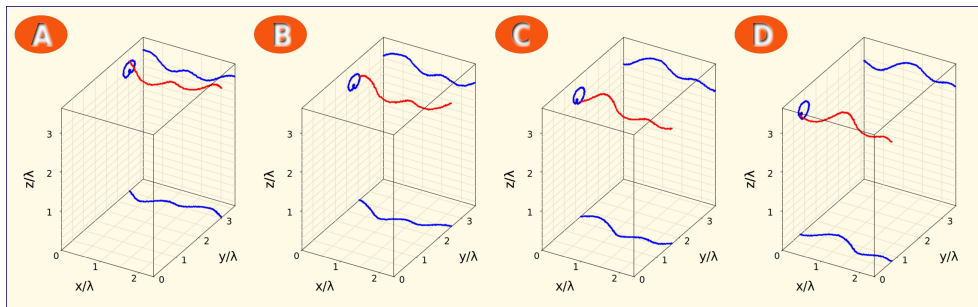


**Figure 34:** Suppression of the secondary meander instability in a medium of size  $\sim 2.4 \times 3.6 \times 3.6\lambda^3$ . The snapshots are taken at (A) 200  $T$ , (B) 250  $T$ , (C) 300  $T$ , and (D) 350  $T$ . The filaments are shown in red, and projections of the filaments in blue. Simulations were accomplished for the parameter set  $a = 0.58$ ,  $b = 0.01$ , and  $\epsilon = 0.025$ . Boundary conditions were chosen as periodic on the left, right, front, and back faces of the medium, while the upper and lower faces are no-flux boundaries.

Note that the size of the medium in  $x$ -direction is the same as in the case of the unbounded media. Hence, the filament is not restabilized due to a confinement in its length. In comparison to the helical state emerging for parameter  $a = 0.66$ , the restabilized state in case of  $a = 0.58$  is characterized by deformation waves which propagate along the filament, while the filament itself continuously drifts in parallel to the stabilizing boundary.

In order to investigate these deformation waves more quantitatively, we performed numerical simulations for scroll wave filaments with smaller initial lengths as we did above. Our focus was on finding a configuration in which only one wave peak may propagate along the filament. We found this situation in a spatial configuration  $1.8 \times 6.4 \times 1.3 \lambda^3$ . Due to the rather large length in  $y$ -direction, it was possible to study the wave propagating from the left to the right periodic boundary several times, before the filament itself was drifted from front to the back periodic boundary. This behavior is presented in figure 35, which is illustrating the evolution of the stabilized filament with the propagating wave along it by four distinct time snapshots. The shape of the deformation wave is well observable, both on the filament (shown in red) as well as in the projections onto the lower and back boundaries (displayed in blue).

Furthermore, we were able to show that the deformation wave does not change its form, even after several passes along the filament. The period of the deformation wave for this spatial configuration was determined as  $T_{\text{wave}} \approx 6.5 T$ , the corresponding propagation velocity as  $v_{\text{wave}} \approx 0.25 \frac{\lambda}{T}$ , and consequently the modulation wave length as  $\lambda_{\text{wave}} = v_{\text{wave}} \cdot T_{\text{wave}} \approx 1.6 \lambda$ . Additionally, we could show that the latter (wave propagation velocity) does not change over several passes through the filament.

Studies in setup two (figure 31, B) revealed a critical distance  $d_{\text{crit}}$ , below which a scroll wave filament initiated in the center of the medium drifts into

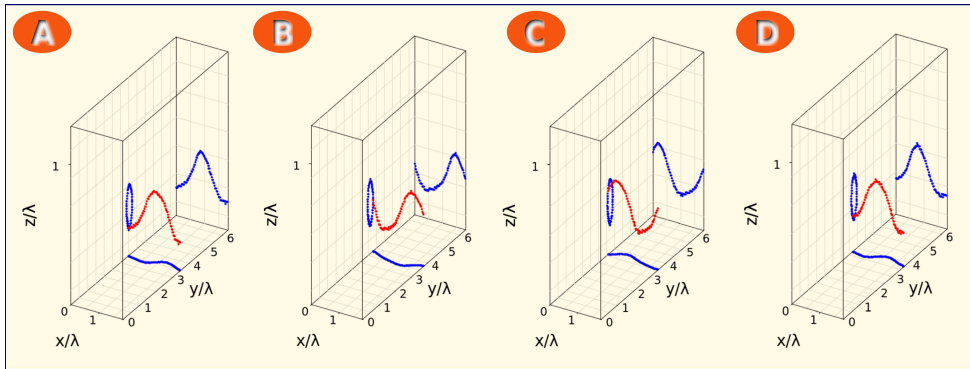


**Figure 35:** Deformation waves propagating along the secondary meander unstable filament at the upper no-flux boundary. The snapshots are taken at (A)  $60 T$ , (B)  $62 T$ , (C)  $64 T$ , and (D)  $66 T$ . The filaments are shown in red, and projections of the filaments in blue. Simulations were accomplished for the parameter set  $a = 0.58$ ,  $b = 0.01$ , and  $\epsilon = 0.025$ . The size of the medium was  $\sim 1.8 \times 6.4 \times 1.3 \lambda^3$ . Boundary conditions were chosen as periodic on the left, right, front, and back faces of the medium, while the upper and lower faces are no-flux boundaries.

the nearest wall. In the case that both the lower and the upper boundary are equally far away from the filament, the chirality of the scroll wave with respect to one of the boundaries (clockwise versus counter-clockwise) decides whether the filament drifts into one or the other boundary. Furthermore, the value of  $d_{\text{crit}}$  depends only slightly on the choice of boundary conditions for the four walls surrounding the filament. If solely two of these walls are chosen as no-flux boundaries, then we get  $d_{\text{crit}} = 3.1 \lambda$ . In case of no-flux boundary conditions for all the surrounding faces, the critical thickness shifts to  $d_{\text{crit}} = 3.2 \lambda$ . Below the critical thickness, the filament is restabilized. Above the critical thickness, the secondary meander instability emerges, but nevertheless the filament might be restabilized due to boundary effects at a later stage of filament evolution. In the latter case, the ongoing evolution of the filament depends on whether the whole filament is located near to one of the no-flux boundaries or partially at all four no-flux boundaries. The first case yields the previously discussed restabilized filament, while the second case yields a big helix. In the latter case, the growth of the instability is delayed leading to a lifetime enhancement of the scroll wave.

### 6.3 NEGATIVE LINE TENSION INSTABILITY

In this subsection, I will provide a summary of our numerical investigations for scroll waves which possess the negative line tension instability. The two parameters I consider here are those with  $a = 0.44$  and  $a = 0.48$  (green and red squares in figure 30 on page 81).

Primarily, we performed numerical simulations in unbounded media for both parameters. As an example case, the emergence of the negative line tension instability for  $a = 0.48$  is illustrated by figure 36. The scroll wave was initiated at the center of a medium with size  $1.6 \times 2.5 \times 2.5 \lambda^3$ . After a weak perturbation, an instability appears and is rapidly amplified until a breakup of the filament occurs. This highly turbulent state is known as scroll wave (Winfree) turbulence [93, 106].

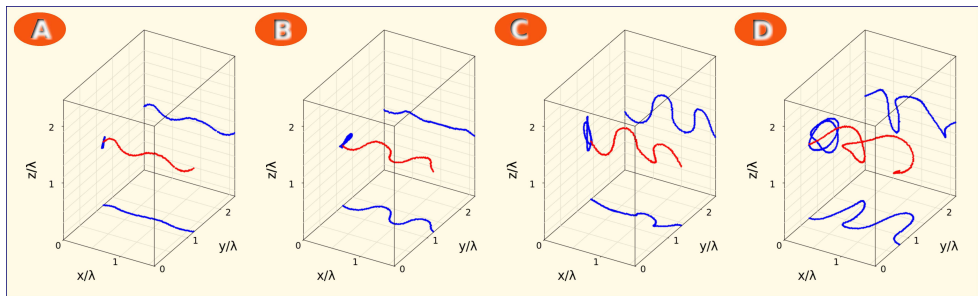


**Figure 36:** Development of the negative line tension instability. The snapshots are taken at (A)  $8 T$ , (B)  $10 T$ , (C)  $12 T$ , and (D)  $14 T$ . The filaments are shown in red, and projections of the filaments in blue. Simulations were achieved for the parameter set  $a = 0.48$ ,  $b = 0.01$ , and  $\epsilon = 0.025$  in a medium of size  $1.6 \times 2.5 \times 2.5 \lambda^3$ . Boundary conditions were chosen as periodic on the left and right faces of the medium while other walls were chosen as no-flux boundaries.

Numerical simulations for scroll waves at different initial distances to one boundary for parameter  $a = 0.44$  yields a complete suppression of the negative line tension instability at an initial distance of  $\sim 0.045 \lambda$  from the no-flux boundary. Even after 4500 periods of spiral rotation, the filament is stabilized at the boundary. In setup two (see figure 31 on page 83, panel B), stabilization of the scroll wave was achieved for media thickness in the interval between  $d_{\text{crit},1} = 0.45 \lambda$  and  $d_{\text{crit},2} = 0.75 \lambda$ . No scroll waves could be initiated in media thinner than  $d_{\text{crit},1}$  while scroll waves are unstable in media thicker than  $d_{\text{crit},2}$ .

In contrast, numerical investigations reveal the negative line tension instability to be delayed for  $a = 0.48$ , at least up to 500 rotation periods. We found out that at distances smaller than  $\sim 0.15 \lambda$  the instability is suppressed. The closer to the boundary one initiates the filament, the longer the suppression. Similar to the restabilized state for the meander unstable parameter  $a = 0.58$ , the boundary-stabilized filament drifts along the stabilizing boundary.

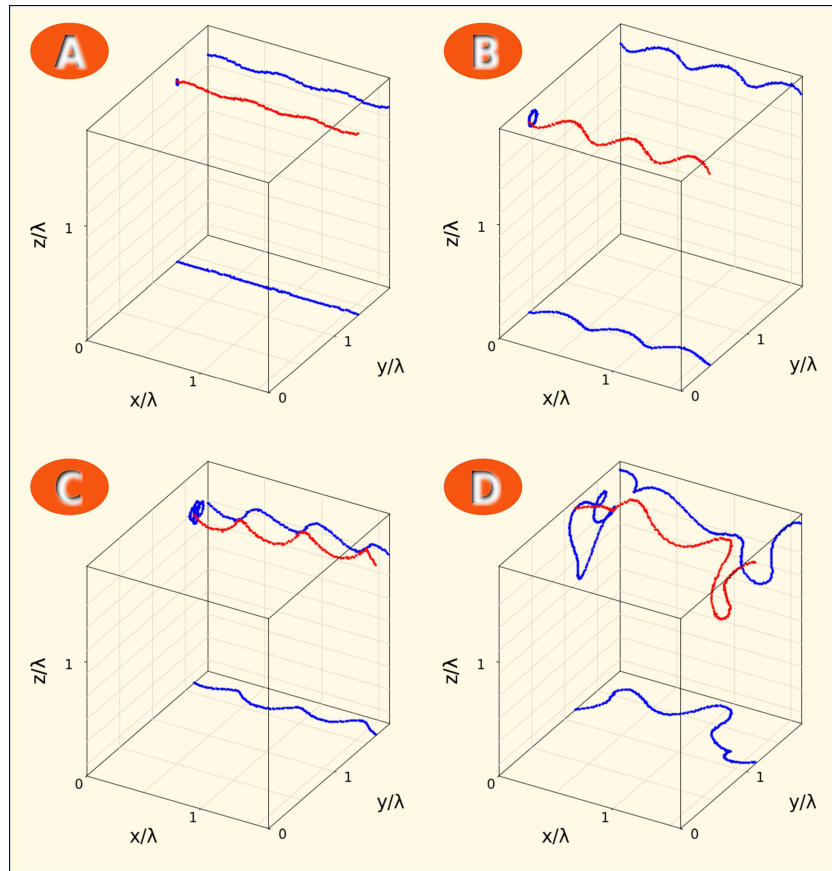


**Figure 37:** Delayed development of negative line tension instability. The snapshots are taken at (A) 270 T, (B) 320 T, (C) 505 T, and (D) 530 T. The filaments are shown in red and projections of the filaments in blue. Simulations were accomplished in a medium of size  $1.6 \times 1.8 \times 1.8 \lambda^3$ . Boundary conditions are chosen as periodic on the left, right, front, and back faces of the medium while the upper and lower faces are no-flux boundaries. Parameters as in figure 36.

Exemplarily, figure 37 demonstrates evolution of a scroll wave initiated at  $\sim 0.075\lambda$  below the upper no-flux boundary. Once the scroll wave is stabilized at the upper boundary, its filament remains nearly straight and drifts along the wall from the periodic boundary at the back to the one in front. Only after  $\sim 270T$  small modulations appear on the filament (panel A). Henceforth, these modulations are amplified and after  $\sim 320T$  (panel B), the twist along the filament exhibits a simple periodicity. This is indicated by the nearly perfect sinusoidal projections on the back and lower walls of the medium (once again panel B) and by the circular-shaped projection in direction of the filament (left wall of the medium in panel B). Hence, the filament is pushed away from the boundary and the negative line tension instability takes the lead again (panels C and D).

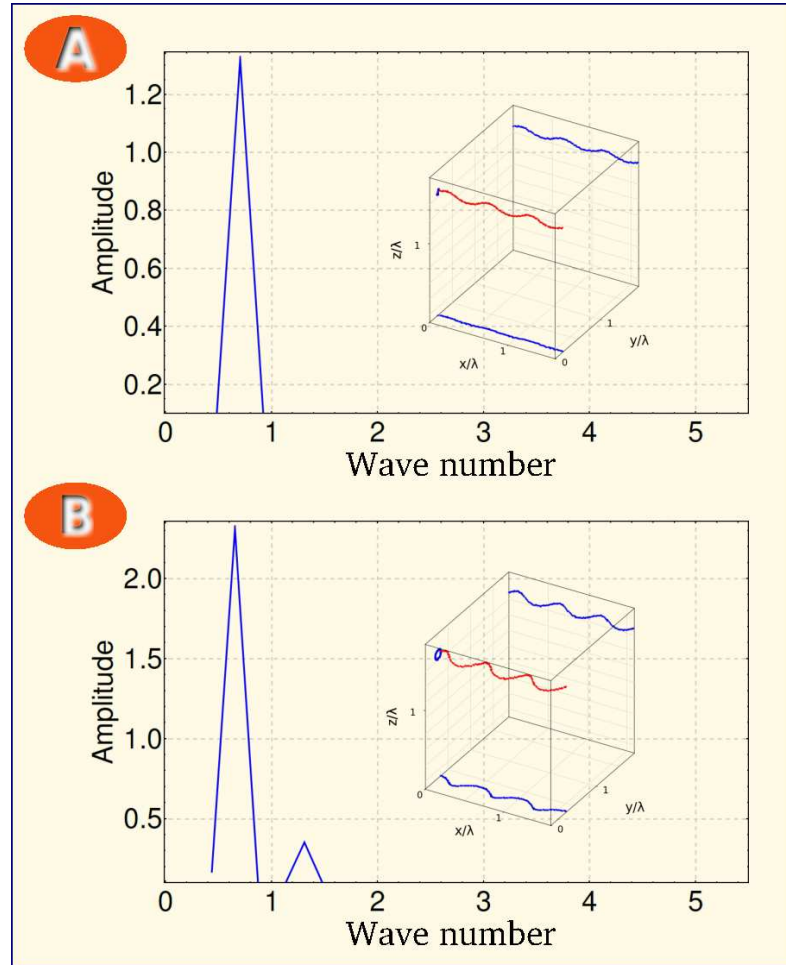


**Figure 38:** Fourier spectral analysis to explain delayed development of negative line tension instability for the parameter  $a = 0.48$ . In both panels the power spectra for the  $y$ - coordinate data are shown (spectra for the  $z$ -coordinate data are analogous). The zeroth frequency mode, corresponding to the natural scroll wave rotation frequency, is dropped from the underlying spectral data. The inset figures display the filament states at the corresponding time points: (A)  $282T$  and (B)  $370T$ . Parameters, medium size, and boundary conditions as in figure 37.

Qualitatively we shall interpret the delayed development of the negative line tension instability for  $a = 0.48$  as follows: In unbounded media, the evolution of the filament is dominated by the negative line tension instability. The latter is suppressed if the filament is located sufficiently near to one no-flux boundary. We propose that scroll waves also possess instability of the meander bands at this parameter, since it is located at the boundary to the parameter region with meandering spiral waves (see figure 30 on page 81). In unbounded media, the meander instability does not play a significant role in the evolution of the filament, compared to the instability of the translation bands. Yet, as the latter instability is suppressed by the no-flux boundary, the meander band instability comes into play. Consequently, some small perturbations along the filament are amplified continuously in the course of time. This yields a filament that possesses helical shape, being not completely in the interaction region with the boundary anymore. Hence, the previously suppressed instability of the translation bands takes over again, and leads itself to scroll wave turbulence.

The latter interpretation is quantified by a FFT analysis for parameter  $a = 0.48$ , results of which are illustrated by figure 38. After 282 periods, small modulations along the filament are accompanied by the appearance of one peak at the wave number  $k_1 \approx 0.7$  (Panel A). Later, an additional smaller peak becomes visible at the wave number  $k_2 \approx 1.3$  (panel B). Finally, the modulations along the filament are more and more amplified, leading to occurrence of additional modes in the Fourier spectrum (not shown here). Hence, the boundary is no more able to suppress the negative line tension instability and evolution of scroll wave turbulence is the consequence.



## THREE-DIMENSIONAL MEANDER UNSTABLE STRAIGHT SCROLL WAVES IN A CONFINED PBZ MEDIUM

---

### 7.1 INTRODUCTION

In the previous chapter we investigated evolution of straight scroll waves under confinement numerically. This was achieved in the framework of the Barkley model. It could be shown that scroll waves possessing both the meander as well as the negative line tension instability can be restabilized due to interaction with at least one no-flux boundary.

In this chapter, it is now my purpose to illustrate evolution of a straight scroll wave with meander instability in the photosensitive Belousov-Zhabotinsky (PBZ) medium. The scroll waves in the PBZ medium are initiated as illustrated in the experimental methods chapter (see section 4.5, in particular figure 23 on page 63). For the investigations herein, the recipe IV was used (see table 1 on page 64). Experiments were conducted at constant background light intensity of  $\Phi = 0.09 \text{ mW/cm}^2$ . A spiral wave performs a meandering tip motion with outward petals under the chosen chemical composition and the background illumination.

Experimental results are accompanied by numerical simulations within the modified complete Oregonator (MCO) model [169, 170], a three-variable reaction-diffusion model which is written in the following form:

$$\begin{aligned}\frac{\partial u}{\partial t} &= \frac{1}{\epsilon_u} [u - u^2 + w(q - u)] + D_u \nabla^2 u, \\ \frac{\partial v}{\partial t} &= u - v, \\ \frac{\partial w}{\partial t} &= \frac{1}{\epsilon_w} [\phi + fv - w(q + u)] + D_w \nabla^2 w.\end{aligned}\tag{98}$$

In this model, the variables  $u$ ,  $v$ , and  $w$  are proportional to concentrations of bromous acid [ $\text{HBrO}_2$ ], the oxidized catalyst ruthenium  $[\text{Ru}(\text{bpy})_3]^{3+}$ , and bromide  $[\text{Br}^-]$ , respectively. Moreover, the MCO is an activator-inhibitor system, with  $u$  being the activator,  $w$  the inhibitor, while the catalyst is given as  $v$ . Analogous to the experimental system, the catalyst is immobilized and does not diffuse. Contrary to that, the activator and inhibitor species are diffusing with slightly differing coefficients  $D_u = 1$  and  $D_w = 1.12$ , respectively. This model is a five-parameter system containing the recipe-dependent time scales  $\epsilon_u$  and  $\epsilon_w \ll \epsilon_u$ , the ratio of the rate constants  $q$ , the

stoichiometric parameter  $f$ , and the photochemically induced bromide flow  $\phi$ . The latter is assumed to be proportional to the applied light intensity and oxygen concentration [169].

The simulated scroll waves are initiated according to the setup shown in figure 39. Herein, panel A illustrates the situation for a scroll wave in unbounded media while panel B shows the setup for confined media. In both cases, a straight scroll wave with initial filament length of  $4\lambda$  is initiated.

A spatially periodic parametric perturbation is introduced along the filament, which is illustrated schematically by figure 39, panel C. The perturbation is achieved through the Oregonator parameter  $\phi$ , given by the function

$$\phi(y) = \phi_0 + 0.009 \cdot H \left[ \cos \left( \frac{6 \cdot \pi \cdot y}{15} \right) \right]. \quad (99)$$

The perturbation is turned on at time  $t_{\text{on}} = 0$  and turned off after one period of the corresponding spiral wave rotation ( $t_{\text{off}} = 1T$ ). Herein,  $\phi_0$  is fixed ( $\phi_0 = 0.022$ ) and  $H[\dots]$  is the Heaviside step function. The other parameters are  $\epsilon_u = 0.07$ ,  $\epsilon_w = \epsilon_u/90$ ,  $q = 0.002$ , and  $f = 1.16$ . The period of rotation  $T$  and wave length  $\lambda$  of a spiral wave together with the corresponding tip trajectory pattern are shown in figure 39, panel D.

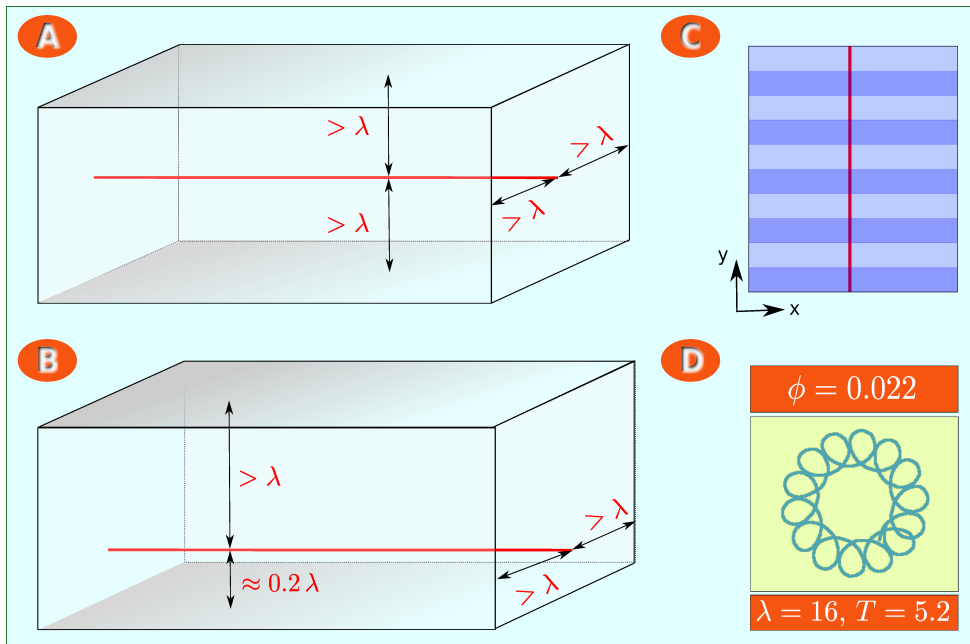


**Figure 39:** Simulation of scroll waves in the MCO model. (A) Setup of unbounded media. (B) Setup of bounded media. (C) Scheme of the spatially periodic parametric perturbation. The perturbation is applied with respect to the parameter  $\phi$  of the Oregonator model. The red line indicates the center line of the filament. (D) Tip pattern, wave length  $\lambda$ , and rotation period  $T$  of the corresponding spiral wave for the chosen parameters  $\phi = 0.022$ ,  $\epsilon_u = 0.07$ ,  $\epsilon_w = \epsilon_u/90$ ,  $q = 0.002$ , and  $f = 1.16$ .

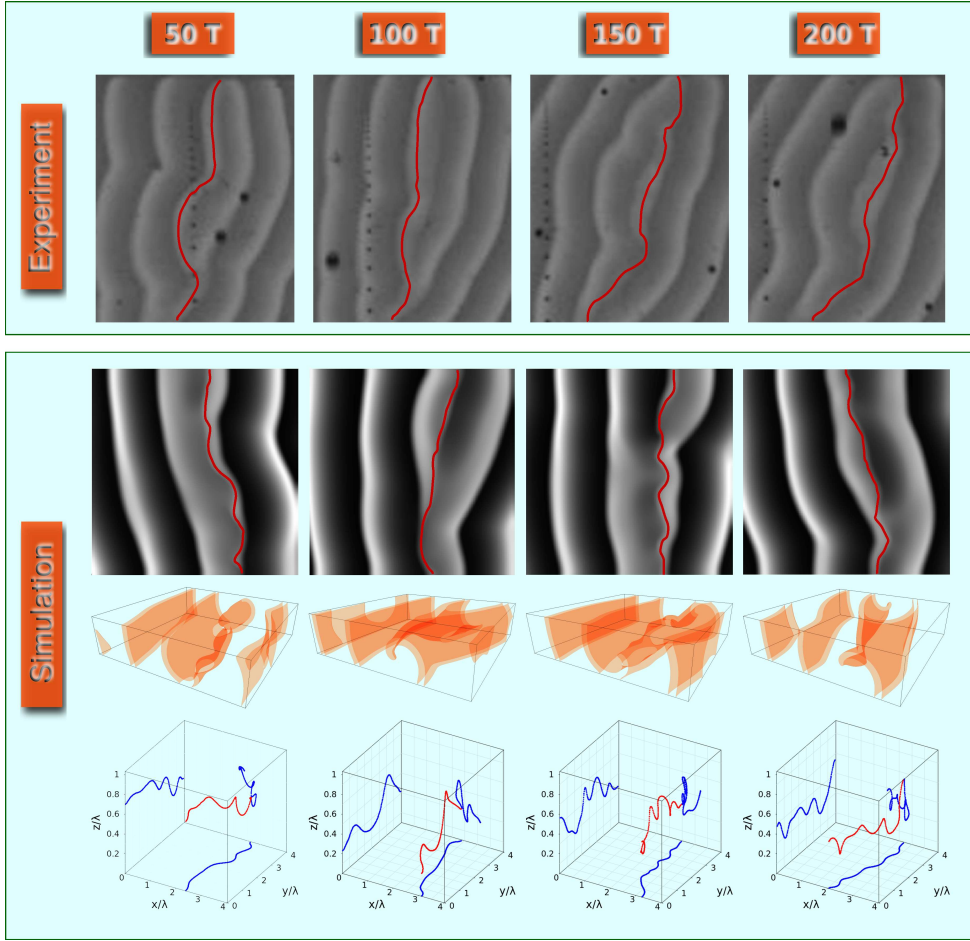


**Figure 4o:** Scroll waves at one no-flux boundary in the MCO model and in the PBZ medium. The experimental transmission image sequences, obtained in the PBZR, are shown on the top panel. Subsequently, top, perspective, and filament view of a scroll wave calculated numerically in the MCO (top, middle, and bottom of simulation panel, respectively) are presented. Snapshots of scroll wave evolution taken at: 50 T, 100 T, 150 T, and 200 T. The red curves on the numerical top view pictures and the experimental transmission image sequences indicate the filaments.

## 7.2 RESULTS

A qualitative comparison between a scroll wave initiated in the PBZ medium and a scroll wave in the numerical simulation is shown by figure 4o. The figure illustrates the time evolution of the scroll wave with four distinct time snapshots. While the experimentally investigated scroll wave is represented by top-view figures alone, the simulated scroll wave can be examined by more than one viewing mode. This allows a more detailed investigation of the scroll wave evolution. In addition to a top-view mode, we have the perspective view which shows the shape of waves emitted at the filament and a filament view that illustrates its shape. The top-view snapshots in figure 4o, both in the experiment and in the numerical simulation, show a qualitative similarity.

The curve-linear waves that are periodically emitted indicate a highly writhed filament of the scroll wave. What might be indicated by the experimental transmission image sequences, can be resolved in case of the numerical simulations. Here, in particular the filament view shows a highly chaotic and irregular filament shape evolution. Obviously, a single restabilized filament state can not be identified by the filament pictures. Instead, the modulations on the filament dynamically change over time.

Note that the filament dynamics presented here is not caused by the sproing instability. The latter instability was found by Pertsov and colleagues experimentally [81, 171, 83], who examined the evolution of scroll waves under parametric gradients (gradient of temperature). In contrast, the irregular modulation patterns on the filament presented here emerge under fully homogeneous conditions, apart from the time duration of one rotation period directly after scroll wave initiation when the spatially modulated parametric perturbation is turned on.

In the following, I will compare free and confined scroll waves exclusively in the numerical simulations, since free scroll waves can not be initiated in the thin layers of PBZR considered in our experimental setup (see chapter 4 on page 55). Figure 41 shall now exemplify the evolution of the free scroll wave obtained numerically. In this figure, panel A displays the evolution of the filament length within time. As we can see, the length of the perturbed filament grows until it has reached approximately twice its initial length after approximately 150 rotation periods. Afterwards, the scroll wave recontracts.

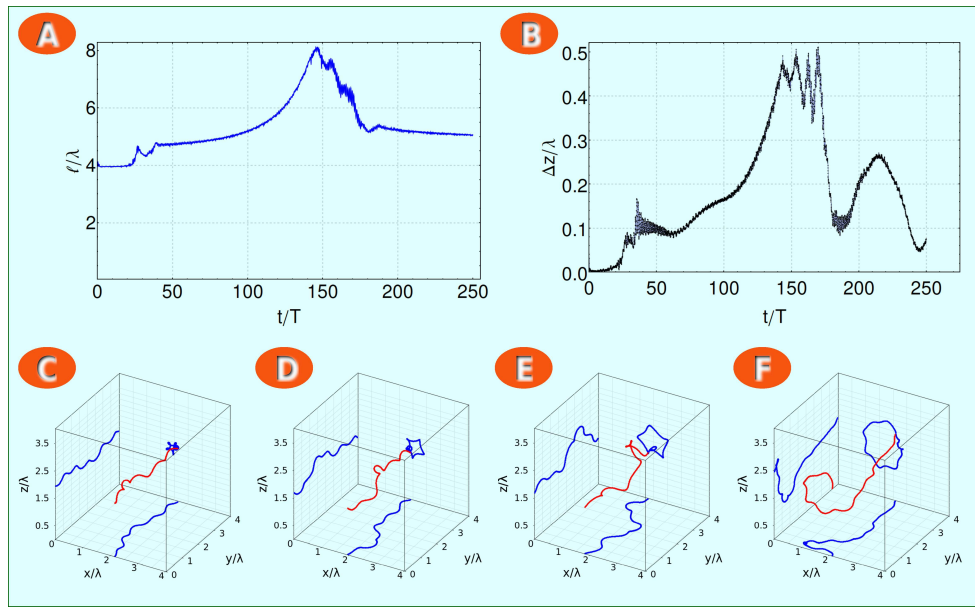


**Figure 41:** Time evolution of a free scroll wave in the MCO model. (A) Overall filament length plotted over time. (B) Mean variance of the height coordinate  $z$  along the filament over time. Filament snapshots taken after (C)  $50 T$ , (D)  $100 T$ , (E)  $125 T$ , and (F)  $150 T$ . Parameters chosen as in figure 40.

Panels C to F illustrate the considerable growth of the filament by four distinct time snapshots. In panel B, the mean variance of the height coordinate along the filament is shown.

The behavior of the free scroll wave filament presented here is similar to the case studied in the Barkley model in the previous chapter. The latter was illustrated by figure 32 on page 84. There the filament length growth was accompanied by highly irregular modulations along the filament until a breakup occurred. Note that the latter instability emerged only if for the medium walls in direction of the filament periodic boundary conditions were selected. In the case described here, all boundary conditions were chosen to be of no-flux type. This might be also the reason why the filament growth is stopped after  $150T$  and is turned back to a contraction. The recontraction sets in when major parts of the filament reach the vicinity of surrounding no-flux boundaries. In this sense, the no-flux boundaries suppress the secondary meander instability.

In comparison to the free scroll wave, figure 42 shall illustrate the evolution of filament length (panel A) and mean height variance along the filament (panel B) over time for a scroll wave under confinement. A clear restabilized state, as presented for some parameters with meander instability in the framework of the Barkley model, does not exist here. The restabilized states obtained in the last chapter were characterized by a stationary helix shape or a dynamical state in which one or more deformation waves propagate along the filament. Instead, the restabilized filament of the meander unstable scroll wave presented here, randomly oscillates around a mean overall length of approximately  $4.5\lambda$ . Furthermore, it is not possible to determine shape and number of propagating deformation waves along the filament. Moreover, deformation waves appear randomly at any position and time along the filament and propagate in both directions until two such deformation waves collide and annihilate.

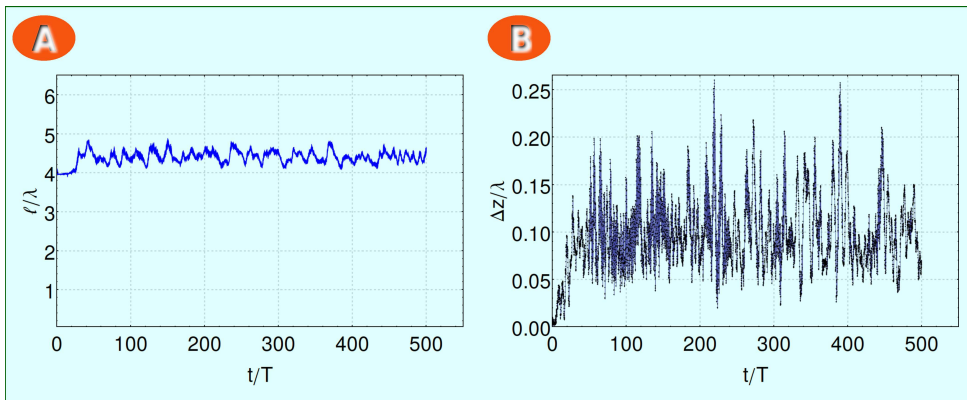


**Figure 42:** Time evolution for a confined scroll wave in the MCO model. (A) Overall filament length plotted over time. (B) Mean variance of the height coordinate  $z$  along the filament over time. Filament snapshots already shown in figure 40, bottom. Parameters as in figure 40.



## CONCLUSIONS

---

The focus of the latter two chapters was on the study of straight scroll waves under spatial confinement.

The work presented in chapter 6, is a numerical study in the framework of the Barkley model. Numerical studies of straight scroll waves under confinement revealed a complete suppression of the negative line tension instability (more than 4500 rotation periods). In contrast, development of the negative line tension instability was delayed for one parameter at the border to the meander regime, at least for 500 rotation periods.

With regard to the meander instability, at one parameter the scroll wave restabilizes into a helix. Another parameter, which is located within the outward meander regime, experiences a secondary three-dimensional meander instability in unbounded media. We were able to show that confinement suppresses the secondary meander instability, such that one pulselike deformation wave with constant shape and velocity propagates along the restabilized filament for evermore.

My experimental studies in the framework of the PBZ reaction (chapter 7) indicate the emergence of highly writhed filaments. Within time, the modulations along the filament occur irregularly, deformation waves propagate along the filament, and they annihilate each other upon collision. The observed filament state is characterized by a noisy evolution of its overall length.



## Part IV

### SCROLL RINGS UNDER SPATIAL CONFINEMENT



# 8

## A NUMERICAL STUDY OF SCROLL RINGS UNDER VARIATION OF EXCITABILITY - UNBOUNDEDNESS VERSUS CONFINEMENT

---

### 8.1 INTRODUCTION

In the present chapter, I will present results of numerically investigated scroll rings for two distinct parameter sets of the MCO model. I have introduced the MCO model already in chapter 7. The two parameter sets investigated herein are characterized by two different values of the time-scale parameter  $\epsilon_u$ : (1)  $\epsilon_u = 0.125$  and (2)  $\epsilon_u = 0.07$ . For each  $\epsilon_u$ -value, the parameter  $\phi$  will be specified in an interval ranging from  $\phi_1$  in the oscillatory regime to  $\phi_2$  at the border to the non-exitable regime. The variation step for  $\phi$  will be  $\Delta\phi = 1 \times 10^{-3}$  for both parameter sets. The remaining three parameters of the MCO model are  $\epsilon_w = \epsilon_u/90$ ,  $q = 0.002$ , and  $f = 1.16$ .

Before I discuss the numerical investigation for scroll rings, I shall present the results of spiral wave simulations for each element of the chosen parameter sets. These results are gathered in figure 43. As one can see, set (1) only possesses elements which support rigidly rotating spiral waves, while a transition from outward meander, over inward meander, to rigid rotation occurs in set (2). In all cases herein, a spiral wave was simulated by taking into account a half plane wave as initial condition in a square grid with  $500 \times 500$  elements. A forward Euler scheme for time integration and a nineteen point star discretization for the Laplacian were applied with the time and space discretizations being  $dt = 0.0005$  and  $dx = dy = 0.3$ , respectively. Each spiral wave was simulated up to 300 rotation periods before the tip trajectory patterns, wave lengths  $\lambda$  and rotation periods  $T$  were measured. This was performed in such a way, in order to preclude transient effects that might be present at the beginning. The rotation periods and wave lengths which were determined for spiral waves will serve as scaling factors of time and space in the three-dimensional simulations, respectively.

For each element of the two parameter sets given in figure 43, I performed numerical simulations for scroll rings in unbounded and confined media. The scroll rings were initialized in a similar manner like in the chemical experiment (see figure 24 on page 65). An outwardly propagating cylindrical wave front (cylinder axis in  $z$ -direction) was exposed to inhibiting illumination by increasing the parameter  $\phi$  for a certain time interval  $\Delta t_{\text{ini}}$  to a value  $\phi_{\text{ini}} \gg \phi_2$  in the complete spatial region from  $z = a$  to  $z = z_{\text{top}}$  ( $\phi_2$  being the border to the non-exitable parameter regime and  $z_{\text{top}}$  the top boundary of the medium).

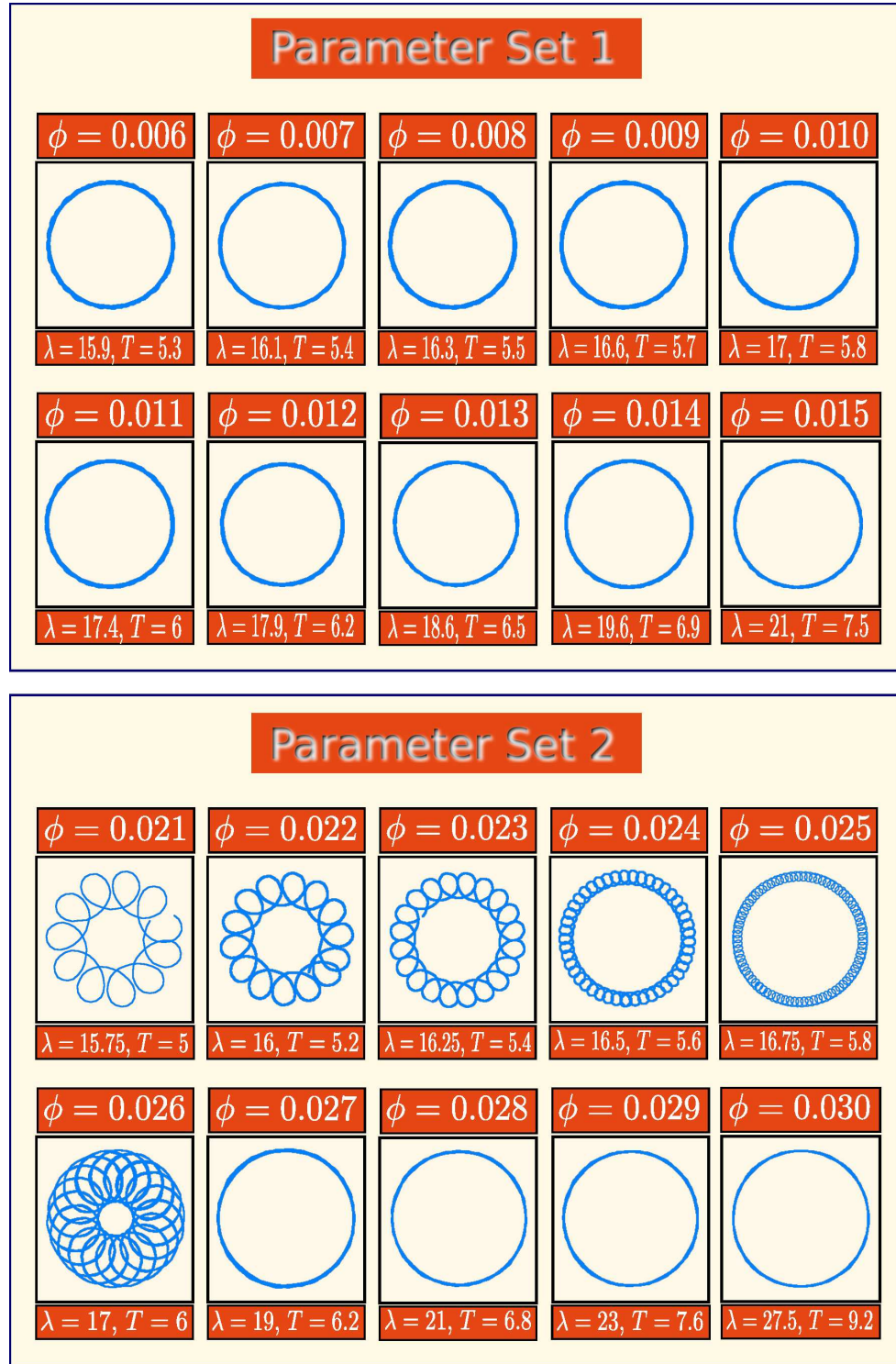


**Figure 43:** Tip trajectory patterns, rotation periods  $T$  and wave lengths  $\lambda$  for spirals under variation of photoexcitability parameter  $\phi$  of the MCO. Two parameter sets, characterized by two different values of time-scale parameter  $\epsilon_u$ , are shown. Set (1) with  $\epsilon_u = 0.125$  and Set (2) with  $\epsilon_u = 0.07$ . The other parameters are  $\epsilon_w = \epsilon/90$ ,  $q = 0.002$ , and  $f = 1.16$ .

The filaments' initial distance  $z_0$  from the bottom of the layer and the initial filament radius  $R_0$  can be controlled choosing appropriate values of the parameters  $\Delta t_{\text{ini}}$  and  $a$ . This procedure annihilates the wave in the illuminated region and leads to the formation of an untwisted scroll ring with the filament plane exactly in parallel to the  $x$ - $y$  plane, after the medium has recovered to the  $\phi$  level before inhibition.

The initial position of the emerging ring-shaped filament is shown in figure 44. In case of the unbounded medium the filament plane is located in the middle of the medium (panel A), while the confined scroll ring filament resides at a position  $0.2 - 0.3 \lambda$  away from the lower no-flux boundary (panel B). In the former case (free scroll ring), simulations were achieved in a cuboidal space with  $4 \times 4 \times 2 \lambda^3$  and in case of confined scroll rings in a cuboidal space with  $4 \times 4 \times 1 \lambda^3$ . In both cases, no-flux boundary condition was chosen for all medium walls.

Note that the position of the forming scroll ring excludes interaction with the lateral no-flux boundaries which are at least  $2\lambda$  away from the filament. The instantaneous position of the filament was defined from the crossing of the two iso-concentration surfaces  $u_f = 0.3$  and  $v_f = 0.1$  (index  $f$  denoting filament). This definition yields graphs for the filament radius  $R$ , for the axial position  $z$  of the filament, and for the filament length  $l$  with superimposed oscillations. This is due to the rigid, respectively meandering, tip trajectory patterns of the spiral waves rotating around the filament.

The structure of this chapter is as follows. In the next section, I will discuss results of simulations in unbounded media for both parameter sets. In particular, the focus will be on the transition from contracting scroll rings (positive filament tension,  $\alpha > 0$ ) to expanding scroll rings (negative filament tension,  $\alpha < 0$ ). Afterwards, the effect of one no-flux boundary on the life time of intrinsically contracting scroll rings will be discussed. Finally, it will be tested if a no-flux boundary might reverse the expansion of negative filament tension rings.

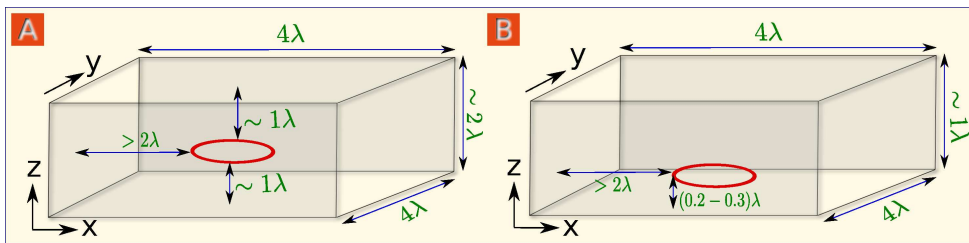


**Figure 44:** Initial placement of scroll ring filaments in numerical simulations which were achieved (A) in unbounded media, and (B) in confined media.

## 8.2 FREE SCROLL RINGS

The asymptotic theory of scroll wave filaments in the form derived by Keener, Biktashev and others yields a set of two ordinary differential equations (ODEs) for the time evolution of the radius  $R$  and the axial drift along the symmetry axis  $z$  for a free untwisted scroll ring [99, 89] (see also in section 3.2 on page 36):

$$\begin{aligned}\frac{dR}{dt} &= -\frac{\alpha}{R}, \\ \frac{dz}{dt} &= \frac{\beta}{R},\end{aligned}\quad (100)$$

Here, the sign of filament tension parameter  $\alpha$  determines whether the ring contracts ( $\alpha > 0$ ) or expands ( $\alpha < 0$ ) with time, and the vertical drift coefficient  $\beta$  determines the degree and direction for the drift of the whole filament plane.

Solving the two ODEs yields

$$\begin{aligned}R(t) &= \sqrt{R_0^2 - 2\alpha t}, \\ z(t) &= z_0 - \frac{\beta}{\alpha}R(t),\end{aligned}\quad (101)$$

with arbitrary initial conditions  $R_0$  and  $z_0$ .

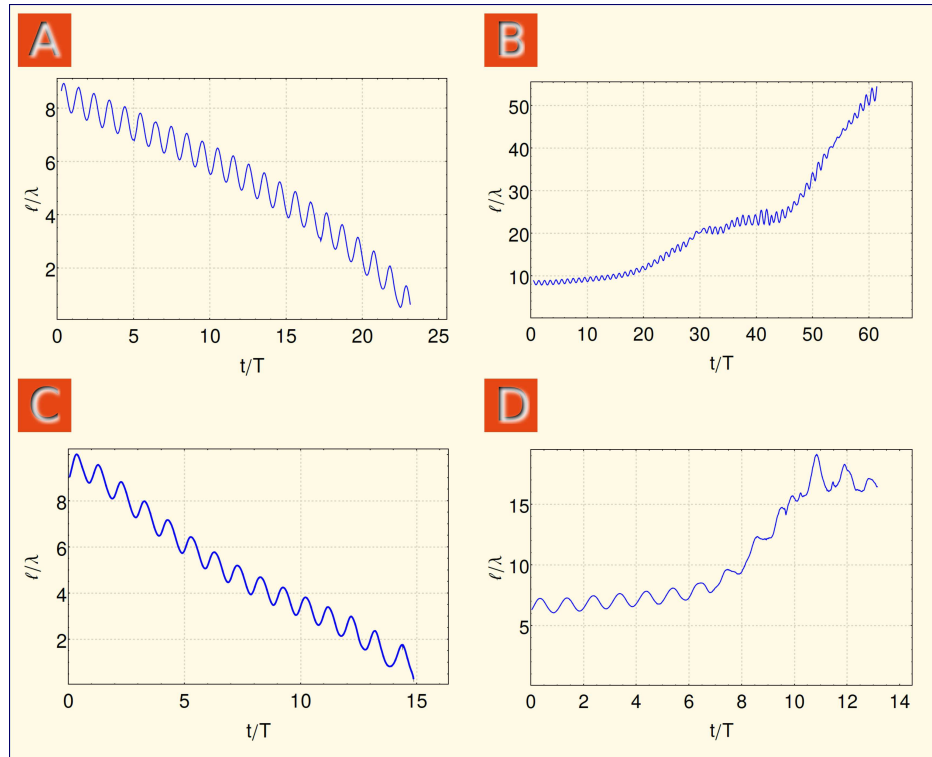


**Figure 45:** Time evolution of the overall filament length for contracting and expanding scroll rings in unbounded media. (A) Parameter set (1) with  $\phi = 0.008$ , (B) set (1) with  $\phi = 0.013$ , (C) set (2) with  $\phi = 0.022$ , and (D) set (2) with  $\phi = 0.029$ .

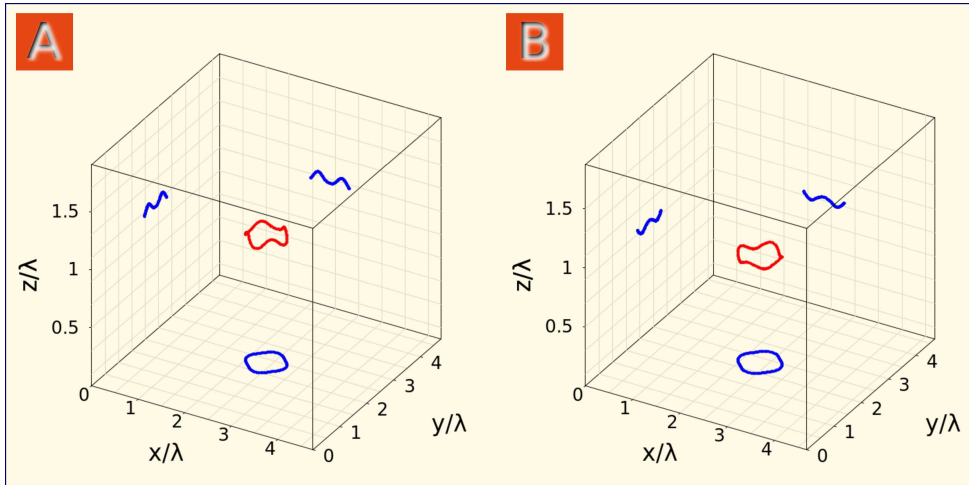


**Figure 46:** Modulations along the filaments of contracting free scroll rings in parameter set (2). (A)  $\phi = 0.021$  after  $t = 20 T$  and (B)  $\phi = 0.022$  after  $t = 12 T$ .

A set of four sample simulations illustrating the contraction and the expansion of free scroll rings in both parameter sets is given in figure 45. In this figure, the time evolution of the overall filament length is shown for each sample simulation. Panels A and C display contraction while panels B and D show expansion of the corresponding filaments.

In order to determine the filament tension  $\alpha$  and drift coefficient  $\beta$  for each element of the two chosen parameter sets, the solution equations (101) have been fitted to the numerical filament data from the corresponding simulations in unbounded media. The latter fitting procedure yields a transition from positive to negative filament tension at  $\phi = 0.012$  in parameter set (1) and at  $\phi = 0.026$  in set (2). Note that the fitting was only applied to those parts of the data that are linear in time.

The mean life time for the free scroll rings with positive filament tension in parameter set (1) is  $\bar{t}_{\text{life}} = 26.0 \pm 2.2 T$ , while for set (2) this is  $\bar{t}_{\text{life}} = 15.2 \pm 3.1 T$ . Hence, the contracting free scroll rings in set (2) possess a significantly shorter life time compared to the rings in set (1). However, at some parameters in set (2) filament modulations emerge before the final collapse of the ring. The two cases in set (2), where modulations of the filament are visible before collapse, are shown in figure 46. Panel A of this figure shows the case with  $\phi = 0.021$  at time  $t = 20 T$  and panel B the case with  $\phi = 0.022$  at time  $t = 12 T$ . In both cases, the filament is square-shaped.

With regard to free scroll rings with negative filament tension, Bikashev was the first to show that negative filament tension yields a turbulent behavior after a first phase of expansion. He termed this turbulent behavior as scroll wave turbulence [93].

The evolution of expanding free scroll rings is exemplified in figure 47, illustrating results of numerical simulations obtained in parameter set (1) with  $\phi = 0.014$ . Four distinct time snapshots during the early life time of the scroll ring is shown in the figure. Already after 10 rotation periods bumps

are observable (e.g. in top view mode) along the emitted waves. These bumps grow ( $15 T$  and  $20 T$ ) and breakup occurs at  $25 T$ . Note that all four steps of the destabilization presented in this figure are characterized by very symmetric emergence of modulations along the ring. One might pose the assumption that this may be due to the geometry of the space on the one hand and due to the small distance of the surrounding boundaries on the other hand.

In order to preclude any possible influence of the surrounding boundaries, numerical simulations were performed additionally in larger spaces, e.g. in spaces with dimensionalities  $4 \times 4 \times 4 \lambda^3$  and  $8 \times 8 \times 2 \lambda^3$ . The latter simulations support the symmetric nature of the instability at the first stages of the scroll wave turbulence. Only later, after the primary breakup of the scroll ring filament, the symmetry disappears and the further evolution of the filaments is more and more characterized by a chaotic and turbulent state.

To better illustrate all stages of the turbulence, including the more chaotic later stages, figure 48 is presented. In this figure, the evolution of the filament itself is illustrated at four time moments. At  $t = 20 T$  one can still see the large bumps that are symmetrically distributed along the ring filament (panel A). After  $t = 30 T$ , the breakup already has been occurred (panel B). Finally, the chaotic late stages are observable (panels C and D).

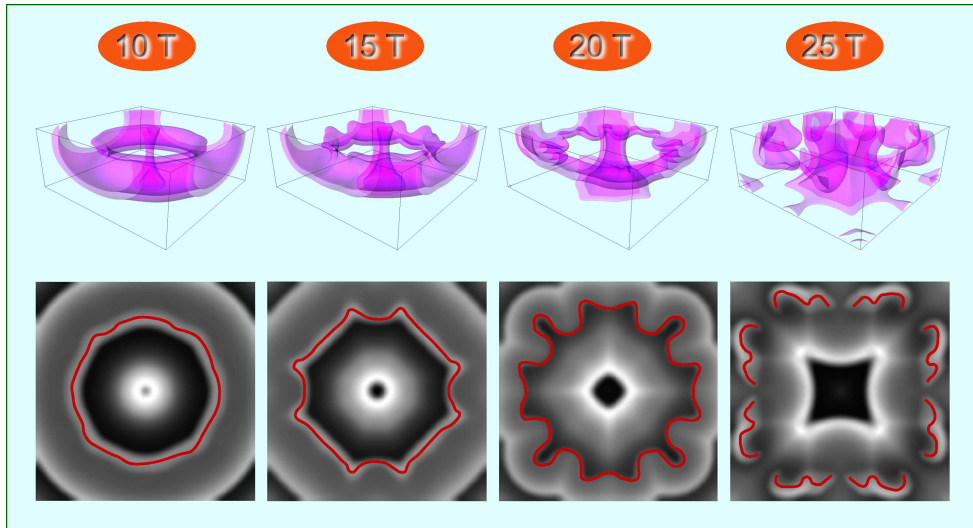


**Figure 47:** First stages of an expanding free scroll ring. Two different viewing modes: Perspective view and top view. The red curves on the top view pictures depict the filament location. Simulation performed for parameter set (1) with  $\phi = 0.014$ .

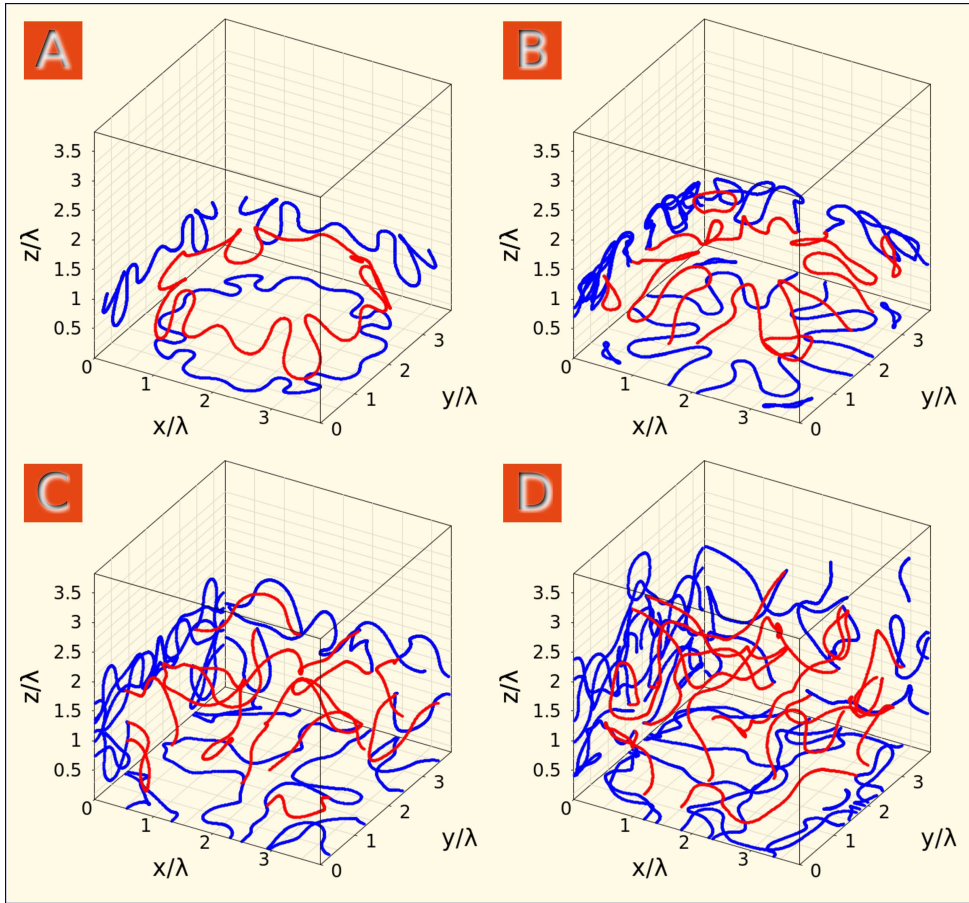


**Figure 48:** Development of scroll wave turbulence. (A)  $20 T$ , (B)  $30 T$ , (C)  $40 T$ , and (D)  $50 T$ . The filament is shown in red and its projections to the walls of the medium in blue. Simulation performed for parameter set (1) with  $\phi = 0.014$  and medium size is  $\sim 4 \times 4 \times 4 \lambda^3$ .

### 8.3 MOTIVATION FOR STUDYING CONFINED SCROLL RINGS

Now that we have examined the evolution of free scroll rings in the two chosen parameter sets, it is time to discuss the influence of no-flux boundaries on this evolution. Though scroll rings are non-stationary objects (either they contract or they expand), it is of great importance to investigate the influence of confining boundaries on the evolution of scroll rings.

It has to be emphasized that the effect of boundary interaction depends on the chirality of the scroll ring in relation to the boundary. At best, one can illustrate this by one cross-section through the ring center, showing two symmetric counter-rotating spiral waves. Schematically, this is done by figure 49, both for a scroll ring with positive and for a scroll ring with negative filament tension. Certainly, it depends additionally on the chosen parameters in numerical simulations or the chosen recipe in the BZ reaction whether one or the other chirality leads to one or the other change of filament evolution.

Herein, I shall distinguish two cases of boundary interaction that were introduced by F. Paul within the scope of his diploma thesis [172].

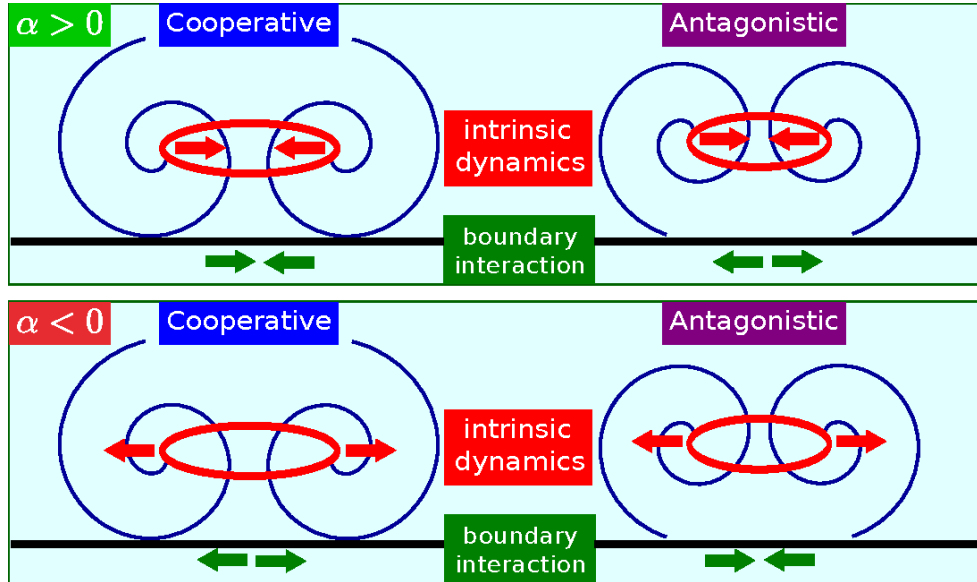


**Figure 49:** Sketch to illustrate cooperative and antagonistic boundary interactions for scroll rings with positive ( $\alpha > 0$ ) and negative ( $\alpha < 0$ ) filament tension.

These two effective changes of the filament dynamics will be denoted cooperative and antagonistic, respectively. The cooperative boundary interaction yields an amplification of the intrinsic filament dynamics: A contracting scroll ring will collapse faster while an expanding ring will reach the turbulent state earlier. In contrast, the antagonistic interaction might slow down or even reverse the intrinsic evolution of the scroll ring.

The latter, namely the antagonistic boundary interaction shall benefit us in seeking stationary scroll rings. This will lead us the way through the now following sections and chapters. We will discuss the possible adjustments to the known free scroll ring evolution, once confinement comes into play. The following section focuses on intrinsically contracting scroll rings. subsequently, the next section will report on the modifications that confinement introduces to the evolution of scroll rings with negative filament tension.

#### 8.4 CONTRACTING SCROLL RINGS

In this section, I will report on the numerical study of intrinsically contracting scroll rings in the vicinity of one no-flux boundary. The numerical setup is shown in figure 44, panel B (see on page 105). The rings are initiated such that they interact in the antagonistic sense with the lower no-flux boundary, with their filament plane located  $0.2 - 0.3 \lambda$  above the boundary.

The results of the numerical simulations for parameter set (1) and (2) are shown in figure 50. As we can see, the life time enhancement in set (2) is ten times higher than it is the case for the scroll rings in set (1). Additionally, in both cases a rapid decrease of life time enhancement is observed when approaching the border to negative filament tension parameter region.

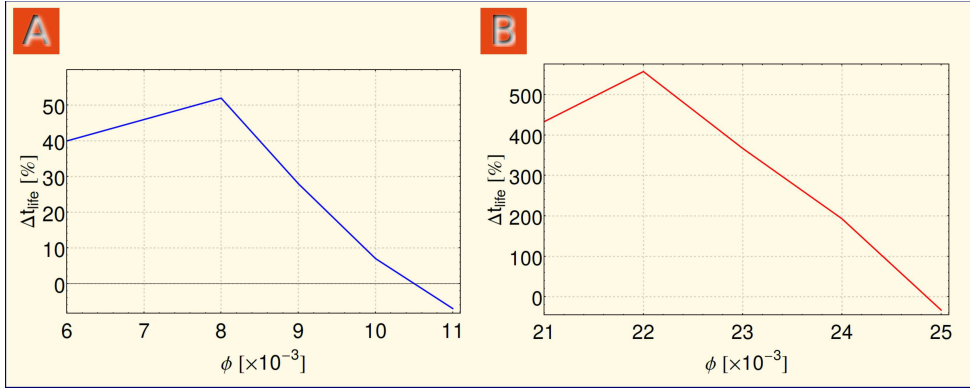


**Figure 50:** Life time enhancement for contracting scroll rings at one planar no-flux boundary, plotted in percent relative to the total life time of the corresponding free scroll rings regarding the (A) parameter set (1) and (B) parameter set (2).

Directly before this border, the life time enhancement even turns to a life time shortening (negative values for  $\Delta t_{\text{life}}$  at  $\phi = 0.011$  for parameter set (1) and at  $\phi = 0.025$  in set (2)).

As an example, figure 51 illustrates the significant life time enhancement in the case of  $\phi = 0.022$  in parameter set (2). Panel A shows the time evolution for the filament radius  $R(t)$  and the axial drift  $z(t)$  in direction of the symmetry axis for a scroll ring simulated in an unbounded medium. Analogously, panel B exemplifies  $R(t)$  and  $z(t)$  for the ring in the confined case.

A substantial increase in the life time of scroll rings with positive filament tension was already found experimentally in the framework of the BZ reaction system [154]. The authors report on their experimental results with accompanying numerical simulations within the scope of the Rovinsky model [173]. Furthermore, a kinematical model was proposed that takes into account the interaction of the scroll ring with a no-flux boundary.

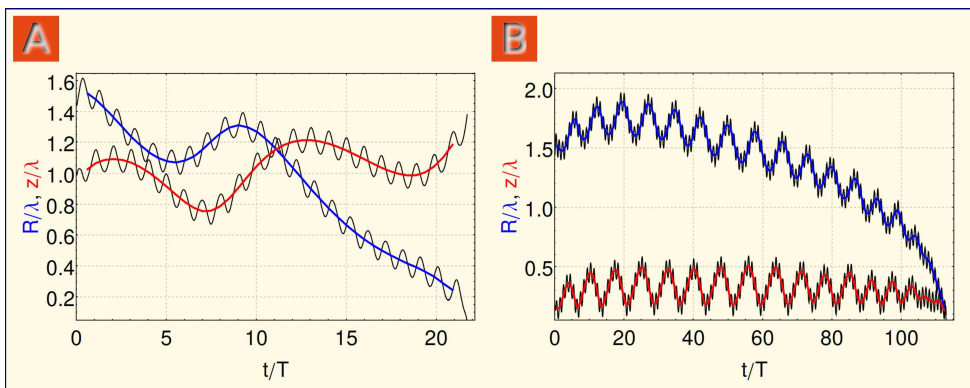


**Figure 51:** Free versus confined scroll rings for parameter set (2) and  $\phi = 0.022$ . (A) for a free scroll ring, and (B) for the scroll ring at one no-flux boundary. Plotted are the filament radius  $R$  and the axial position  $z$  of the filament plane over time. Additionally, mean radius  $\bar{R}$  and the mean axial position  $\bar{z}$  are plotted in blue and red, respectively.

The proposed model, being a superposition of the intrinsic free scroll ring evolution and the assumed boundary interaction, successfully reproduces both the experimental as well the numerical results.

In general, one can write down the extended kinematical model by Totz et al. as follows [154]:

$$\frac{dR}{dt} = -\frac{\alpha}{R} + c_{\parallel}^{2D}(z) + c_{\perp}^{2D}(R), \quad (102)$$

$$\frac{dz}{dt} = \frac{\beta}{R} + c_{\perp}^{2D}(z) - c_{\parallel}^{2D}(R). \quad (103)$$

The first right-hand side terms in the above two equations account for the well-known intrinsic scroll ring dynamics. The assumed boundary interaction enters through the functions  $c_{\parallel}^{2D}(x)$  and  $c_{\perp}^{2D}(x)$  with  $x$  being either  $z$  or  $R$ . In particular, the function  $c_{\parallel}^{2D}(z)$  might strengthen the intrinsic time evolution of the filament (cooperative boundary interaction) or weaken it (antagonistic interaction).

Note that Totz et al. considered the above model with the assumption of  $\beta = 0$  since the scroll rings reported by them in the experiments and in the numerical simulations do not drift vertically. In contrast, the unbounded scroll rings which were investigated in this chapter possess a non-vanishing vertical drift coefficient  $\beta$  for both parameter sets, with the vector of their vertical drift pointing in direction of the antagonistic boundary.

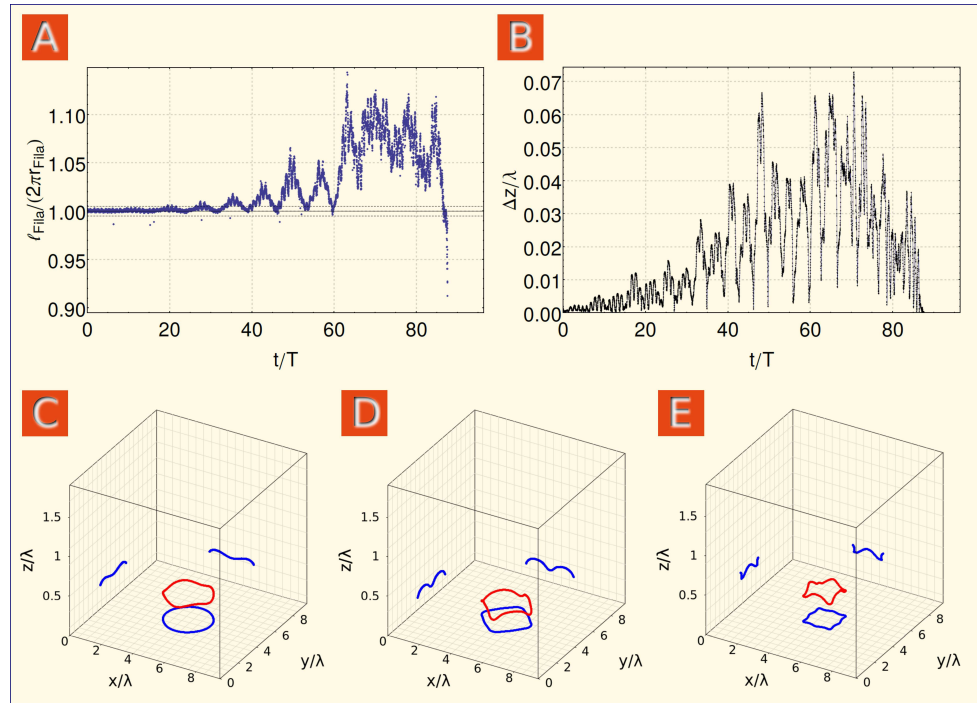


**Figure 52:** Emergence of filament modulations for parameter set (2) and  $\phi = 0.021$ . (A) Deviation from a perfect ring. (B) Mean variation of the height coordinate  $z$  along the filament. (C) Filament snapshot after  $30 T$ , (D) after  $50 T$ , and (E) after  $70 T$ .

In section 8.2 (e.g. figure 46 on page 107) another peculiarity for contracting scroll rings in parameter set (2) was discussed, namely the emergence of modulations on the filament. The modulations appear shortly before the collapse of the scroll rings, only for two sample values ( $\phi = 0.021$  and  $\phi = 0.022$ ), and the filaments possess the same square shape (observable on the  $x$ - $y$ -projections).

We can now take the substantial life time enhancement in case of the corresponding confined rings as an advantage for a better examination of the emerging filament modulations. Primarily, scroll rings with different initial radii were simulated near the lower no-flux boundary for  $\phi = 0.021$ . Simulations were performed in cuboidal spaces with dimensionality  $\sim 9 \times 9 \times 2\lambda^3$ . Such a big space was chosen, in order to preclude influences by the surrounding no-flux boundaries. The filaments are located at the center of the medium (with respect to  $x$ - and  $y$ -coordinates), thus at all times at least  $2\lambda$  away from the surrounding boundaries.

The evolution of the filament modulations in that case is illustrated by figure 52. Panel A shows the degree of deviation from a perfect ring over time. The latter is calculated through the formula  $l_{\text{Fila}}(t) / (2\pi r_{\text{Fila}}(t))$  where  $l_{\text{Fila}}(t)$  denotes the filament length and  $r_{\text{Fila}}(t)$  the filament radius at time  $t$ . A perfect ring yields a value of 1. As we can see in this graph, small deviations emerge after  $\sim 20 T$ , are amplified, and the peaks display a periodic behavior. After  $60 T$ , the periodicity disappears and the ring deviation shows a noisy behavior in the region between the values 1.05 and 1.15. The continuous change in the filament shape is further supported by the evolution of the mean variance in the height coordinate  $z$  along the filament, shown in panel B. Finally, panels C to E display the shape of the filament for three distinct moments in time, namely after 30, 50, and 70 periods of rotation. The latter show the preservation of the square shape (projections on the  $x$ - $y$ -plane).

Analogously, evolution of the filament shapes were studied for the cases  $\phi = 0.022$  and  $\phi = 0.023$ . This is illustrated by figure 53, showing snapshots of the filament in steps of  $1 T$  from  $50 T$  to  $53 T$ . In case of  $\phi = 0.022$ , the filament shape slightly changes ( $t = 52$  and  $t = 53$ ) as the filament drifts slightly away from the lower boundary. The instability mode is doubled compared to  $\phi = 0.021$  (eight compared to four). In case of  $\phi = 0.023$ , the filament shape is no more preserved, but changes continuously in form and instability mode.

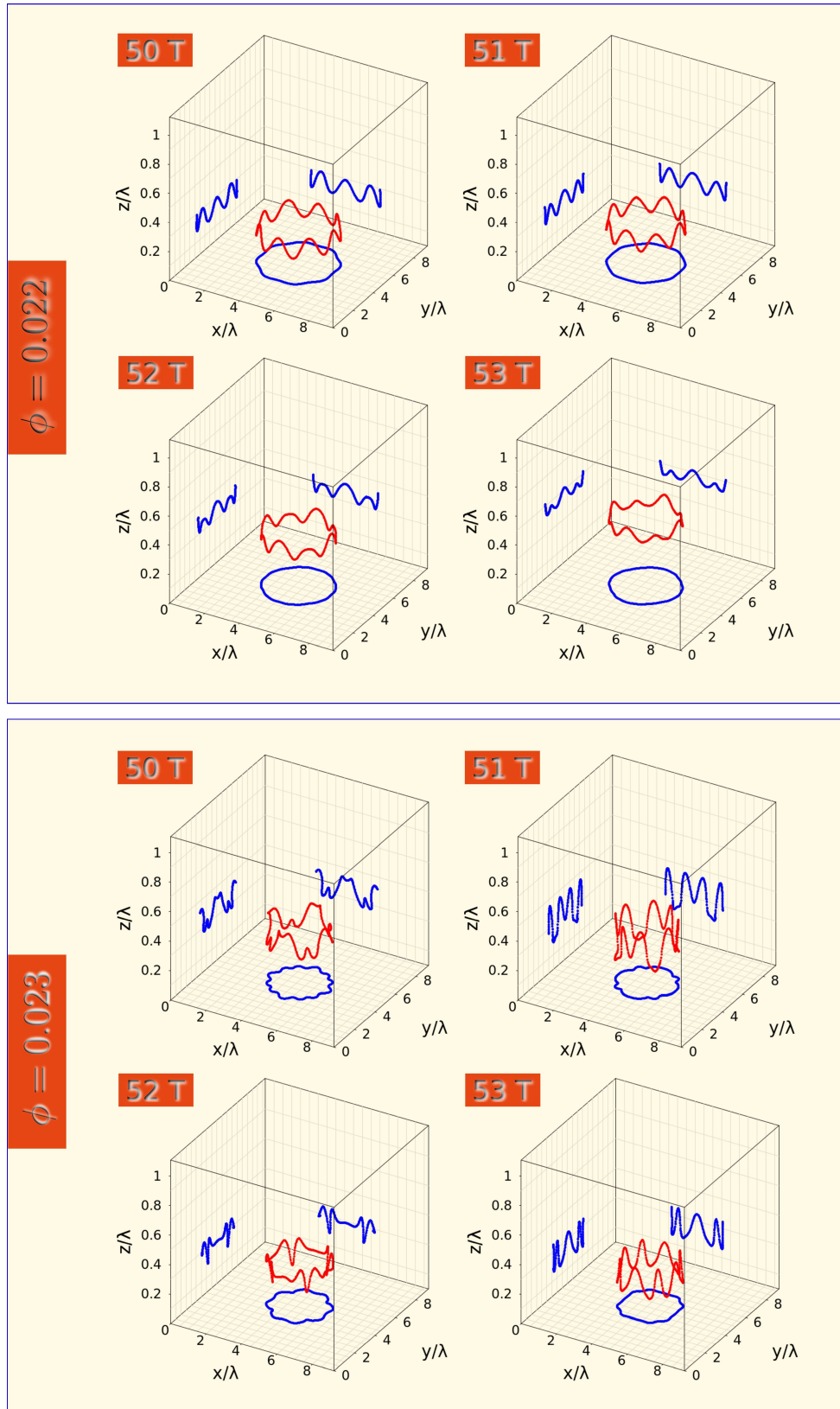


**Figure 53:** Filament shape evolution for  $\phi = 0.022$  and  $\phi = 0.023$  in parameter set (2).

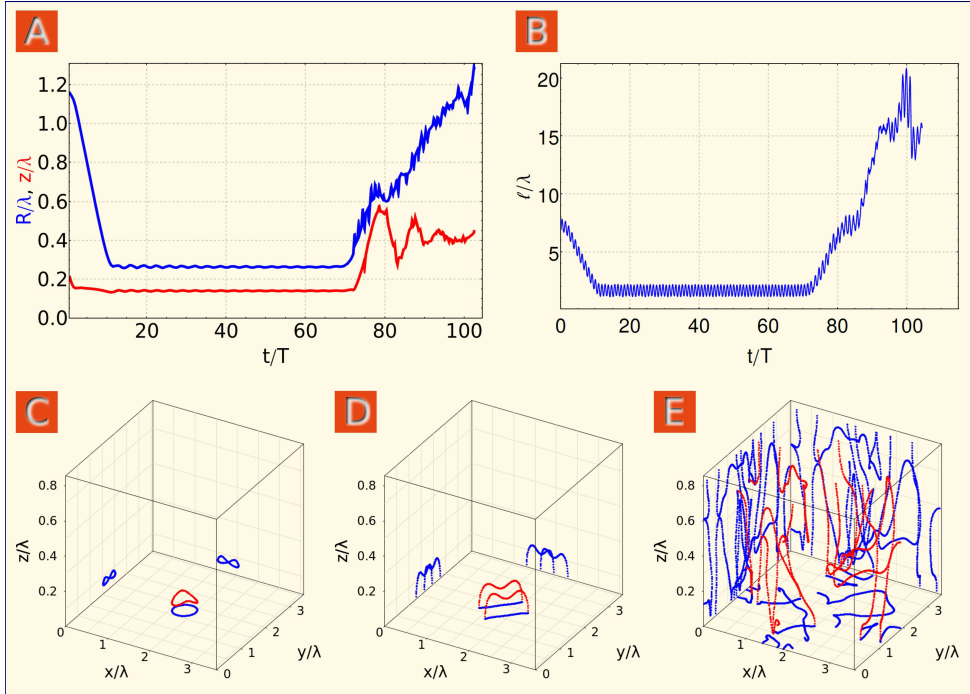


**Figure 54:** Delayed development of negative filament tension for  $\phi = 0.028$  in set (2). (A) Plot of mean filament radius  $\bar{R}(t)$  in blue and the mean axial position of the filament plane  $\bar{z}(t)$  in red. (B) Plot of the filament length  $l(t)$ . (C) Snapshot of the filament after  $t = 72 T$ , (D) after  $t = 74 T$ , and (E) after  $t = 100 T$ .

### 8.5 EXPANDING SCROLL RINGS

In this section, I will discuss the influence of one no-flux boundary on the evolution of scroll rings which expand over time in unbounded media. Simulations that were performed in parameter set (2) yield a significantly delayed development of the negative line tension instability at a planar no-flux boundary. Exemplarily, this is illustrated for  $\phi = 0.028$  in figure 54. One can see that the mean radius  $\bar{R}$  and the mean axial position  $\bar{z}$  show small periodic modulations after the boundary-induced stabilization (panel A). This indicates the presence of the three-dimensional meander instability, though corresponding spiral waves perform rigid tip motion in 2D.

Apparently, the negative line tension instability is suppressed by the boundary. In contrast, the meander instability, being negligible in comparison to the stronger negative line tension instability in unbounded media, plays now a role in the time evolution of the boundary-stabilized scroll ring. The meander instability leads to emergence of modulations on the filament (panel C). In this case, the filament possesses an oval shape (projection onto the  $x$ - $y$ -plane). At the two elongated sides of the filament which are located next to the lower boundary, the filament touches the boundary and splits up (panel D). From this moment on, the further evolution is governed by the previously suppressed negative line tension instability and yields scroll wave turbulence.

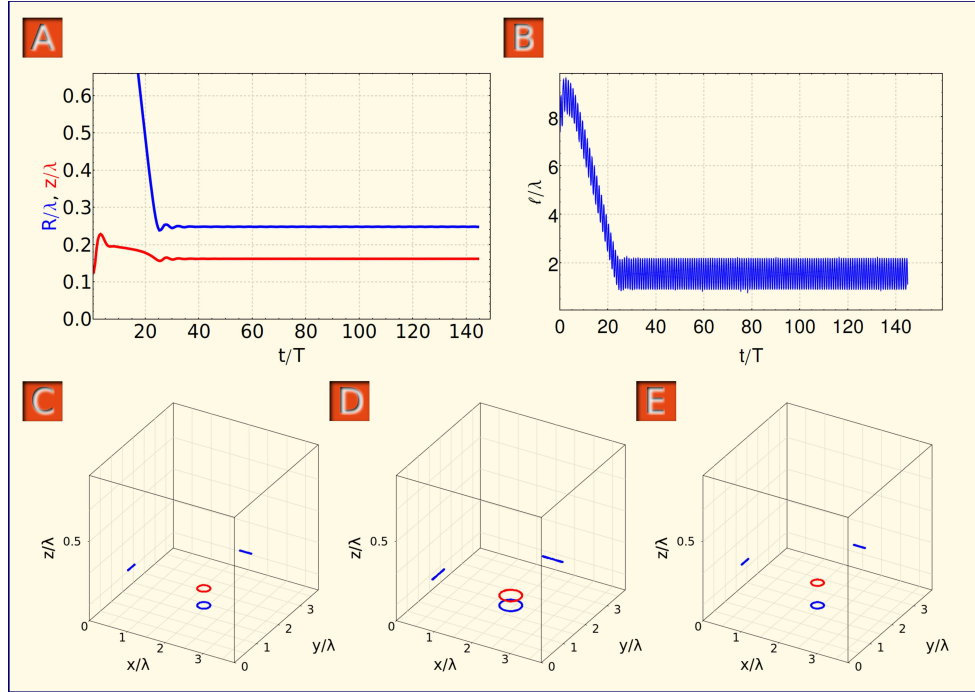


**Figure 55:** Complete stabilization of scroll ring for  $\phi = 0.014$  in set (1). (A) Mean filament radius  $\bar{R}(t)$  in blue and the mean axial position of filament plane  $\bar{z}(t)$  in red. (B) Plot of the filament length  $l(t)$ . (C) Snapshot of the filament after  $t = 50 T$ , (D) after  $t = 150 T$ , and (E) after  $t = 450 T$ .

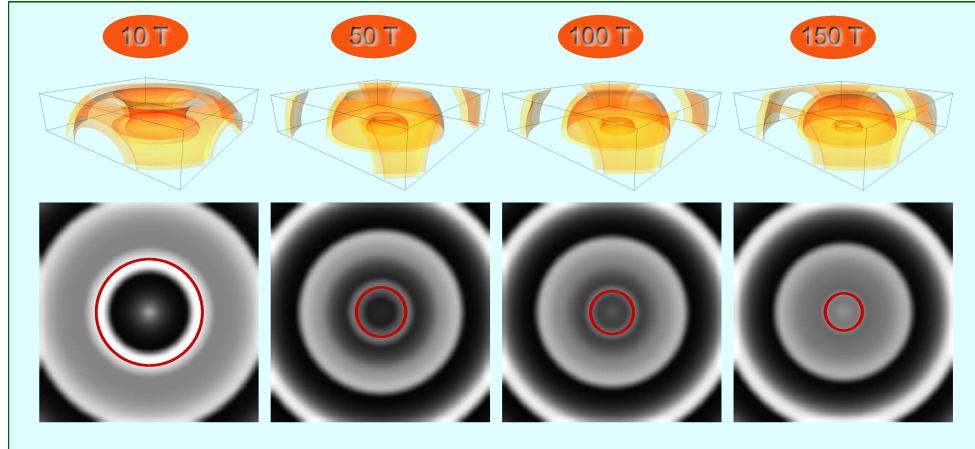


**Figure 56:** Complete stabilization of scroll ring for  $\phi = 0.014$  in set (1) illustrated by two viewing modes: perspective view and top view. The red curves on the top view pictures depict the filament location.

Complete stabilization of scroll rings at planar no-flux boundaries could be achieved for several  $\phi$ -values with negative filament tension in set (1). As an example, the evolution of a boundary-stabilized scroll ring at one planar no-flux boundary is shown for  $\phi = 0.014$  in figure 55. In this figure, the mean filament radius  $\bar{R}(t)$ , the mean axial position  $\bar{z}(t)$ , and the overall filament length  $l(t)$  are plotted only for the first 140 rotation periods (average values are calculated over one corresponding rotation period).

Nevertheless, the scroll ring is stable for more than  $450 T$  without any change in the shape of the corresponding filament. The preservation of filament shape is illustrated by the single time snapshots in panels C to E. Additionally one can illustrate the propagating waves that are periodically emitted from the filament of the corresponding scroll ring. This is done in figure 56 through different viewing modes for distinct time moments.

Compared to the simulations for  $\phi = 0.014$  in unbounded media, illustrated by figure 47 (on page 108) showing the consequence of expansion and scroll wave turbulence on the shape of the waves, the confined counterpart presented here is stabilized while preserving both the clean and regular shapes of the propagating waves as well as the perfectly ring-shaped filament in time. For the reason of comprehensibility, the evolution up to 150 rotation periods is shown. Moreover, all important information is already included, and no significant change in the shape of the propagating waves will be observable in the remaining 350 periods.

Such boundary-stabilized scroll rings can be seen as a novel type of autonomous pacemakers (APMs) in three-dimensional media. Formation of these APMs can be understood qualitatively if we again consider the kinematical model represented by the equations (102) and (103) (on page 112). In order to apply this kinematical model to the numerically observed scroll ring stabilization, the drift velocity functions were determined numerically [174]. This was achieved by initiating a spiral wave at different distances to the boundary within the same parameter set and  $\phi$ -value allowing the formation of boundary-stabilized scroll rings.

In case of  $\phi = 0.014$ , the latter procedure delivers the following qualitative result: The absolute value of both drift velocity components are negligible as long as the distance between spiral core center and the boundary is larger than approximately  $0.3 \lambda$ . At a distance in the region between  $(0.2 - 0.3) \lambda$ , the absolute values significantly increase. Particularly, the parallel component attains a maximum absolute value of  $|c_{\parallel}^{2D}| \approx 0.03 \lambda/T$ . The latter represents the magnitude of drift in parallel to the boundary. The direction of that parallel drift has the opposite sign in comparison to the intrinsically provided filament expansion. Hence, the latter is suppressed and even reversed until the ring is stabilized at a mean filament radius  $\bar{R} \approx 0.25 \lambda$  and a mean distance  $\bar{z} \approx 0.16 \lambda$  of the filament plane to the lower boundary.

Additionally, a linear stability analysis approach for the extended kinematical model delivered some more quantitative results [175]. Major suggestions of this approach are the existence of both stationary as well as limit cycle solutions in the  $R$ - $z$  phase space, while transition from the stationary to the limit cycle solution occurs in the form of a supercritical Hopf bifurcation. The stationary solution represents the stationary APM found at  $\phi = 0.014$ . The limit cycle solution, which is emerging in the linear stability analysis, indicates another very interesting type of APM. I shall term the latter as a “breathing” APM.

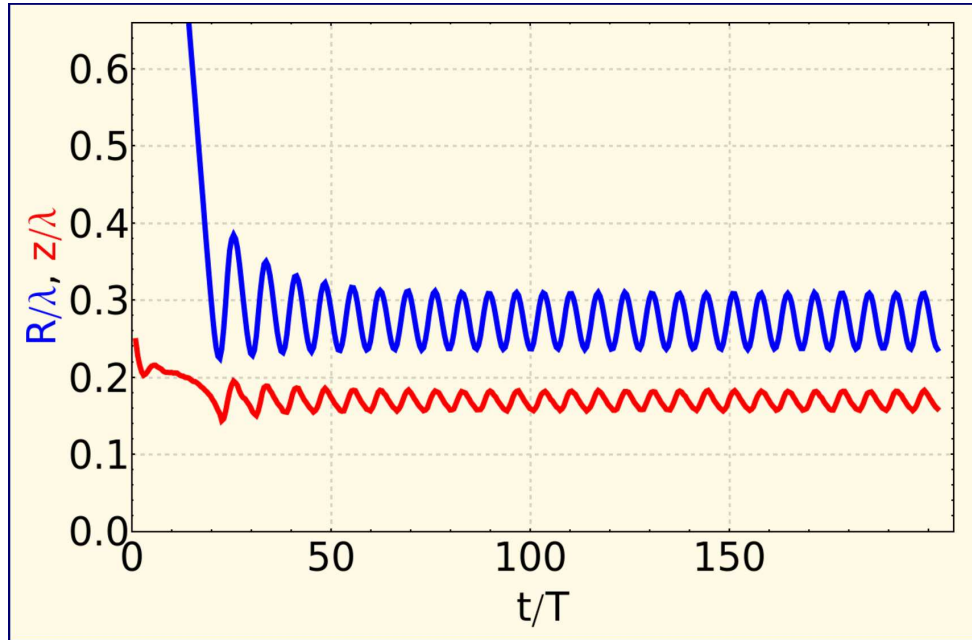


**Figure 57:** Breathing autonomous pacemaker for  $\phi = 0.0125$  in parameter set (1). Plot of the mean radius  $\bar{R}$  (in blue) and the mean axial position  $\bar{z}$  (in red).

If observable, a breathing APM will be characterized by periodic oscillations both in its mean filament radius  $\bar{R}(t)$  as well as in the mean axial position  $\bar{z}(t)$  of its filament plane. Indeed, I was able to find breathing APMs in the numerical simulations within the parameter set (1). The stationary APM goes over to the breathing APM at  $\phi_{\text{Hopf}}$  in between 0.0125 and 0.013, if starting from  $\phi = 0.014$ , and continuously lowering the value for  $\phi$ . Hence, the value for  $\phi_{\text{Hopf}}$  marks the supercritical Hopf bifurcation in the parameter set (1).

Exemplarily, the mentioned periodic oscillations in both the mean radius as well as in the mean axial position for  $\phi = 0.0125$  are shown in figure 57. Furthermore, in case of  $\phi = 0.012$ , the breathing of the filament during one corresponding period is illustrated by single filament snapshots in figure 58. It has to be emphasized that the breathing periods vary strongly in these two exposed examples, namely  $T_B \approx 7T$  for  $\phi = 0.0125$  and  $T_B \approx 17T$  for  $\phi = 0.012$ .

The region of existence for breathing APMs spans all values in the interval between  $\phi_{\text{NLTI}} = 0.012$  and  $\phi_{\text{Hopf}}$ . Note that  $\phi_{\text{NLTI}}$  marks the transition to the parameter region where scroll wave filaments possess negative tension, hence denoted with NLTI.

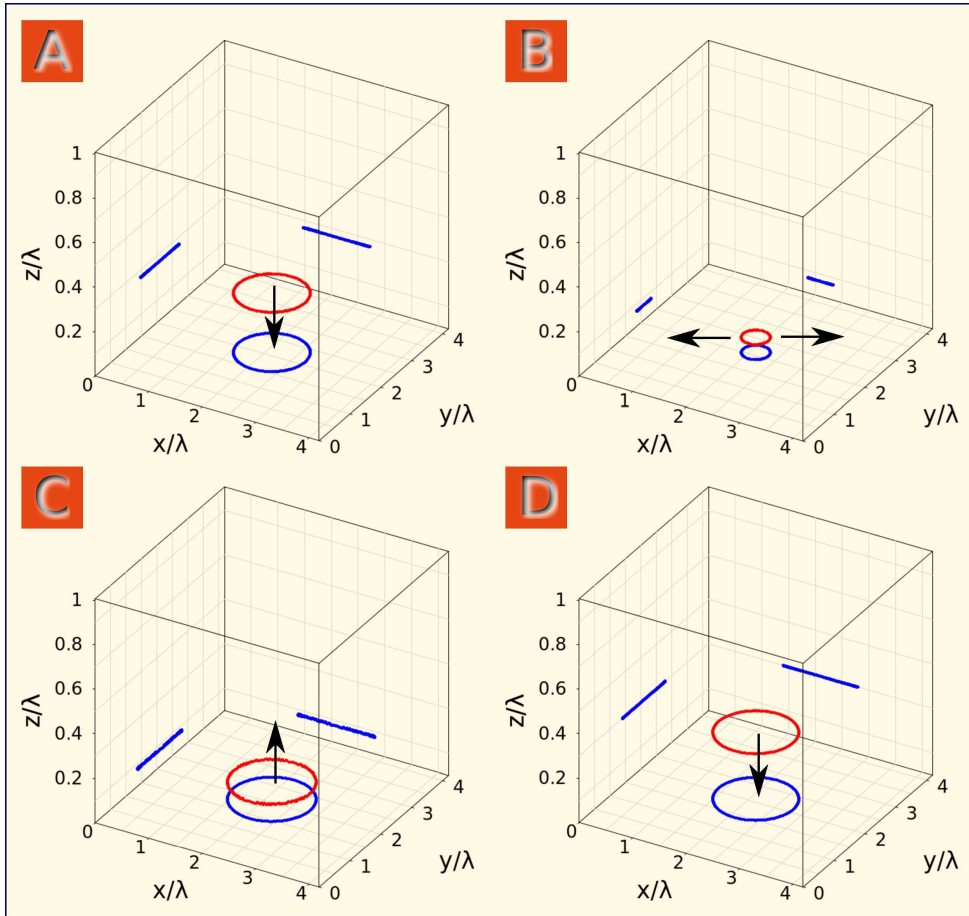


**Figure 58:** Breathing APM in parameter set (1) with  $\phi = 0.012$ . Filaments are plotted in red while its projections to the walls are drawn in blue. The black arrows denote the direction of motion for the filament. (A)  $t = 30 T$ , (B)  $t = 38 T$ , (C)  $t = 43 T$ , and (D)  $t = 47 T$ .

### 8.6 NUMERICAL TESTS FOR OBSERVING AN APM IN THE PBZR

In this section, I will discuss some conditions under which one might be able to observe boundary-mediated formation of three-dimensional APMs in the PBZR. I have decided to focus on the specific case of  $\phi = 0.014$  in the parameter set (1), where a stationary APM forms at one no-flux boundary. Figures 55 and 56 (see on the pages 116 and 116, respectively) illustrate the formation and evolution of such a stationary APM very well.

The first to be investigated here is the question for combinations of minimum medium height and intensity of photoinhibition at which stable scroll rings can form. The latter, namely the intensity of photoinhibition, will be considered for the primary initiation of scroll rings from outwardly propagating cylindric waves that reach from top to bottom of the media. The question about the minimum medium height is important here, since layers of excitable PBZ media taken into account in our lab are very thin. Very thin here means heights between  $0.5 \lambda$  to  $1 \lambda$  (in most chemical recipes and background illuminations considered in my thesis).

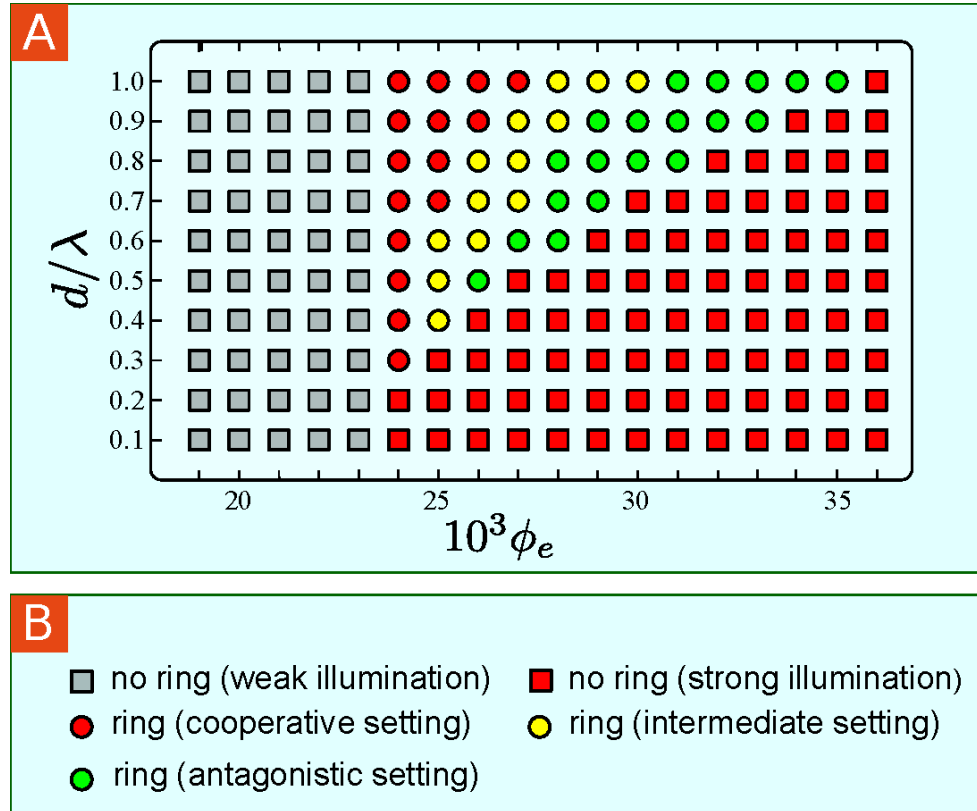


**Figure 59:** Numerical results of the investigation for the layer thickness  $d$  versus intensity of photoinhibition  $\phi_e$ . (A) Initiation of scroll rings under usage of the Lambert-Beer relation (104) with  $\mu = 0.05$ . The total medium thickness  $d$  is varied against the illumination intensity parameter  $\phi_e$ . (B) The legend for panel A.

Scroll rings are initiated in the PBZ medium by illuminating the medium from above or below. The incident light is attenuated due to absorption in the medium. Thus, an illumination gradient in  $z$ -direction will be the consequence. This will yield a gradient of the inhibitor  $Br^-$  concentration in  $z$ -direction. Mathematically the light attenuation can be represented by the Lambert-Beer relation [151, 85]:

$$\phi(z) = \phi_e \exp(-\mu z), \quad (104)$$

if illumination from below is considered. Parameter  $\mu$  and the amplitude variable  $\phi_e$  can be identified by the absorption coefficient and the quantum efficiency for the photochemical production of bromide, respectively [151].

Now, I choose  $\mu = 0.05$  while systematically varying the total height of the media  $d$  for chosen values of the illumination intensity parameter  $\phi_e$ . The high-intensity illumination represented by the Lambert-Beer relation (104) will be turned on at time  $t_{\text{start}} = 0$  and turned off at time  $t_{\text{end}} = 2$ .

Results are shown in figure 59. In the complete region below  $\phi_e = 24 \cdot 10^{-3}$ , the overall illumination is too weak for initiating stably rotating scroll rings. This is indicated by grey squares in the figure. For media with height values below  $0.3 \lambda$ , the total height is too small to support formation of scroll rings.

This is because illumination intensity values higher than  $\phi_e = 24 \cdot 10^{-3}$  lead to complete inhibition of waves (indicated by red squares). Red circles represent formation of rings interacting with one of the walls in the cooperative sense. Yellow circles denote the rings initiated such that their filament plane is located in the middle between the two boundaries. Finally, by green circles the truly boundary-stabilized scroll rings are represented. In the latter cases, both the layer thickness as well as the illumination intensity are appropriate for initiating rings in the interaction regime of the stabilizing boundary.

Under some circumstances, the illumination in experiments with PBZR might also be non-homogeneous in horizontal direction. Hence, scroll rings may be initiated such that the initial filament plane is inclined. Now, I will address this issue by initiating the scroll ring through the following function:

$$\phi(x, z) = \phi_0 + \phi_e \exp(-\mu z) + \frac{\phi_i}{L} x, \quad (105)$$

turned on at time  $t_{\text{start}} = 0$  and turned off at time  $t_{\text{end}} = 0.5$ . In the above function, the second term with parameters  $\phi_e$  and  $\mu$  is the previously introduced Lambert-Beer relation (104). Yet, it shall be assumed that  $\phi_e = 0.05$  and  $\mu = 0.1$ . The actual inclination of the initial filament plane emerges due to the last term. Degree and strength of the inclination can be controlled by parameters  $\phi_i$  and  $L$ .

The simulations for inclined scroll rings are achieved at the upper no-flux boundary in the antagonistic setting with  $\phi_i = 0.01$  and two different values for parameter  $L$ : (1)  $L = 125$  and (2)  $L = 100$ . Selected results of the numerical simulation in the first case ( $L = 125$ ) are illustrated by figure 6o, showing three time snapshots of the filament. As is observable, the filament plane aligns parallel to the boundary already after  $5 T$  and the ring is stabilized at the upper no-flux boundary.

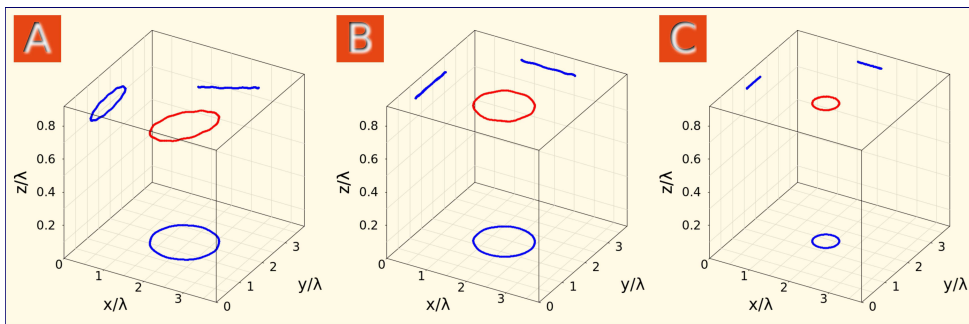


**Figure 6o:** Inclined initiation of a scroll ring at the upper no-flux boundary for  $\phi = 0.014$  in parameter set (1). (A)  $t = 1 T$ , (B)  $t = 5 T$ , and (C)  $t = 100 T$ . Initiation was achieved through application of equation (105) with  $\phi_e = 0.05$ ,  $\mu = 0.1$ ,  $\phi_i = 0.01$ , and  $L = 125$ .

The last condition to be investigated is the following: How stable is a boundary-mediated APM, once formed at the no-flux boundary, under the presence of a permanent gradient of the background illumination in  $z$ -direction?

Numerically, this is investigated by taking a very early state (after 2 rotation periods) of the stabilized scroll ring for  $\phi = 0.014$  as initial state for each new simulation run. Henceforth, a permanent gradient in the background illumination is achieved by setting the light parameter  $\phi$  equal to the Lambert-Beer relation (104) from below and turned on during the whole simulation time. It is  $\phi_e = \phi_0 = 0.014$  and three different absorption parameters are considered: (1)  $\mu_1 = 0.0033$ , (2)  $\mu_2 = 0.01$ , and (3)  $\mu_3 = 0.25$ . For all three gradient strengths, the scroll ring proved to be stable for more than 400 rotation periods of the corresponding spiral wave.

## A THREE-DIMENSIONAL AUTONOMOUS PACEMAKER IN THE PBZ MEDIUM

---

In general, an autonomous pacemaker (APM) features a particular example for the more generic class of pacemakers (PMs) in excitable or oscillatory media. A prominent example for such PMs is represented by target patterns which were among the first patterns observed in the BZ reaction [14], and are characterized by a source in the center of the pattern periodically emitting outwardly propagating waves. In addition, target patterns were also described in a variety of systems in chemistry, physics and biology [27, 28, 29, 30, 176]. Theoretically, Kuramoto was able to explain formation of target patterns as a consequence of localized frequency defects [26].

One can differentiate two types of PMs: One type is emerging due to local heterogeneities in the medium, and another one results from intrinsically present dynamical processes in otherwise spatially uniform media, thus being denoted as self-organized. In that sense, the latter type of PMs are autonomous.

While target patterns by definition refer to two-dimensional media, my focus herein will be on formation of three-dimensional APMs. As mentioned previously in section 8.4 (on page 110), formation of these specific APMs are due to boundary-mediated stabilization of scroll rings, otherwise expanding in unbounded media. At the end of the last chapter, I have shown numerically that initiation and observation of such boundary-mediated APMs shall be achievable in the experiments within the PBZR. Now, I will present and discuss the first successful experimental observation of a truly three-dimensional APM and compare it with the APMs previously predicted by numerical simulations in the framework of the MCO model.

The experiments reported here were conducted within the recipe V (see table 1 on page 64). The photosensitive catalytic complex Ruthenium-4,4'-dimethyl-2,2'-bipyridyl was fixed in a thin ( $1.0 - 1.5\text{ mm}$ ) layer of silica hydrogel. Circulating water from a thermostat kept the temperature fixed at  $22.0 \pm 0.5^\circ\text{C}$ .

Scroll rings have been initiated through the procedure that is well described in section 4.5 (e.g. figure 24 on page 65). The evolution of such initiated scroll rings were studied at constant background illumination in the range of the interval  $0.12\text{ mW/cm}^2 < \Phi < 0.16\text{ mW/cm}^2$  under otherwise fixed conditions (e.g. the composition of BZ mixture, layer height).

An example for a boundary-stabilized scroll ring is shown in figure 61. This experiment was performed at constant light intensity  $\Phi = 0.14\text{ mW/cm}^2$ . At the same intensity regime a rigidly rotating spiral wave with a wavelength

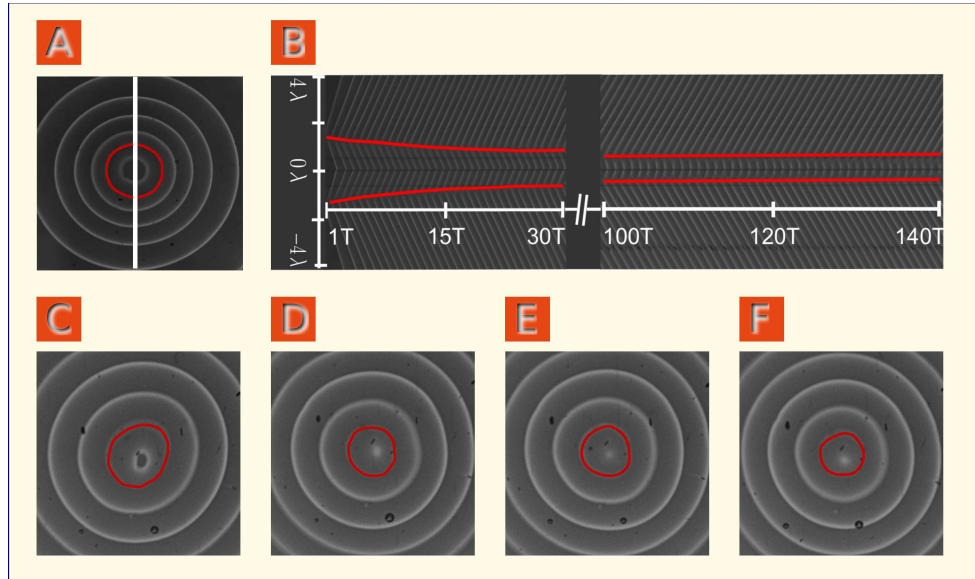


**Figure 61:** Primary experimental observation of a stationary APM in the PBZR. (A) A transmission image sequence obtained 15 periods of spiral wave rotation after the initiation of the scroll ring. (B) Spacetime plot obtained along the white vertical line in panel A. The red lines in panel B indicate the location of the scroll ring filament. The lower panels display four more transmission image sequences, namely at (C)  $t = 40 T$ , (D)  $t = 60 T$ , (E)  $t = 80 T$ , and (F)  $100 T$ . The red ring-shaped curves in the transmission image sequences indicate the location of the filament.

$\lambda \approx 2.3 \text{ mm}$ , a core diameter  $d \approx 0.5 \text{ mm}$ , and a rotation period  $T \approx 60 \text{ s}$  can be observed [177]. These values correspond to very low excitability and negative filament tension (see for example [91, 92]).

The overall thickness of the gel layer was approximately  $1.4 \text{ mm} \approx 0.6 \lambda$ . As a consequence, the studied scroll ring was located within interaction distance to the upper and lower layer boundary and therefore definitely confined. Because in our experiments the gel layers are placed on top of a glass plate, the lower boundary can be seen as a no-flux boundary. The diameter of the gel layer  $5 \text{ cm} \approx 22 \lambda$  was large enough to exclude interaction of the centrally placed scroll ring with the lateral layer boundaries.

The above described boundary-stabilized scroll ring represents the first experimental verification of a stable three-dimensional self-organized pacemaker that Nandapurkar and Winfree predicted already in 1989 by numerical simulations of the FitzHugh-Nagumo equations [73]. Numerical simulations of the MCO model, being one of the models to describe emerging nonlinear wave patterns in the PBZ media qualitatively very well, confirmed the existence of such stable three-dimensional APMs in a wide range of the chosen parameter set. Formation of these stationary APMs were discussed in section 8.5 (on page 115), indicating their existence under application of the photoinhibitory parameter  $\phi$  out of the interval  $0.013 < \phi < \phi_{\text{non-excit}}$ . Herein,  $\phi_{\text{non-excit}}$  denotes the transition to the non-excitable regime. Particularly, the case of  $\phi = 0.014$  was examined and discussed widely in my thesis (see sections 8.5 and 8.6).

Simulations within the  $\phi$ -regime that I mentioned in the above paragraph yield a reversal of the intrinsically present filament expansion. Instead of the expansion and the emergence of the scroll wave turbulence, the filament shrinks until it reaches a stable radius. Once the stable radius is reached, the filament maintains both a stable distance  $z(t) = \text{const.}$  from the stabilizing boundary as well as a constant filament radius,  $R(t) = \text{const.}$

The latter behavior indicates the presence of a stable fixed point in the  $R$ - $z$ -phase space which now was proven to exist also in the PBZ medium. My numerical simulations within the parameter set (1) have shown also the existence of a Hopf bifurcation giving rise to limit cycle oscillations in the  $R$ - $z$ -phase space. The evolution of scroll rings at  $\phi$ -values located in the limit-cycle regime were presented in section 8.5. I have named that specific type of self-organized pacemaker as a breathing APM. Illustration of the breathing APMs were presented in the figures 57 and 58 (on the pages 118 and 119, respectively). So far, the breathing APM was not found in the PBZR.



## EXPERIMENTAL EVIDENCE FOR MODULATED RING FILAMENTS IN THE PBZ MEDIUM

---

The emergence of modulations along the filaments of scroll waves have been studied within the scope of my thesis primarily in chapter 6 (see on page 81). The main cause for such modulations stems from the three-dimensional meander instability being present in a distinct parameter region as was shown by Henry and Hakim [87].

In succession, our numerical simulations of the Barkley model under confinement have shown novel types of filament states. In the subsequent chapter (see chapter 7 on page 93), evidence for the existence of meander-unstable scroll waves in the PBZ reaction was delivered.

The pure numerical study of both contracting as well as the expanding scroll rings were performed for two distinct parameter sets of the MCO model under variation of the photoexcitability parameter  $\phi$  in chapter 8 (on page 103). The advantage of large life-time enhancement for contracting scroll rings at one no-flux boundary allowed a better examination of the different filament shapes which emerge: square, triangle, oval, and even more complicated filament shapes.

In the present chapter, I will deliver experimental evidence for existence of these filament geometries in the PBZR. Depending on the choice of recipes and varying background illumination intensities, both the square-shaped filament as well as more complicated filament morphologies are observed at conditions that yield qualitatively the same spiral tip patterns as in the numerical simulations.

Initiation of scroll rings has been achieved in the manner as was described in section 4.5 (see on page 64). Gel layers containing the photosensitive catalyst Ruthenium-4,4'-dimethyl-2,2'-bipyridyl with (5 – 6) cm in diameter and (1.2 – 1.5) mm in height were used. The chemical conditions maintained by the used recipes and the constant background illumination intensities yield gel heights in the region of (0.6 – 0.8)  $\lambda$ , in relation to the corresponding spiral wave lengths  $\lambda$ . Unless not stated otherwise, the reaction chamber is maintained at a temperature of 22°C. Numerical simulations in confined media were performed in the framework of the MCO model (introduced in section 7.1 on page 93) under conditions described in section 8.1 on page 103.

In order to seek for experimental evidence with regard to the square-shaped filament, at first I examined spiral wave tip patterns under variation of the illumination intensity for several BZ recipes. In this survey, some conditions could be picked out that yield similar spiral tip patterns which we also find in the  $\phi$ -interval of parameter set (2) possessing the three-dimensional meander instability.

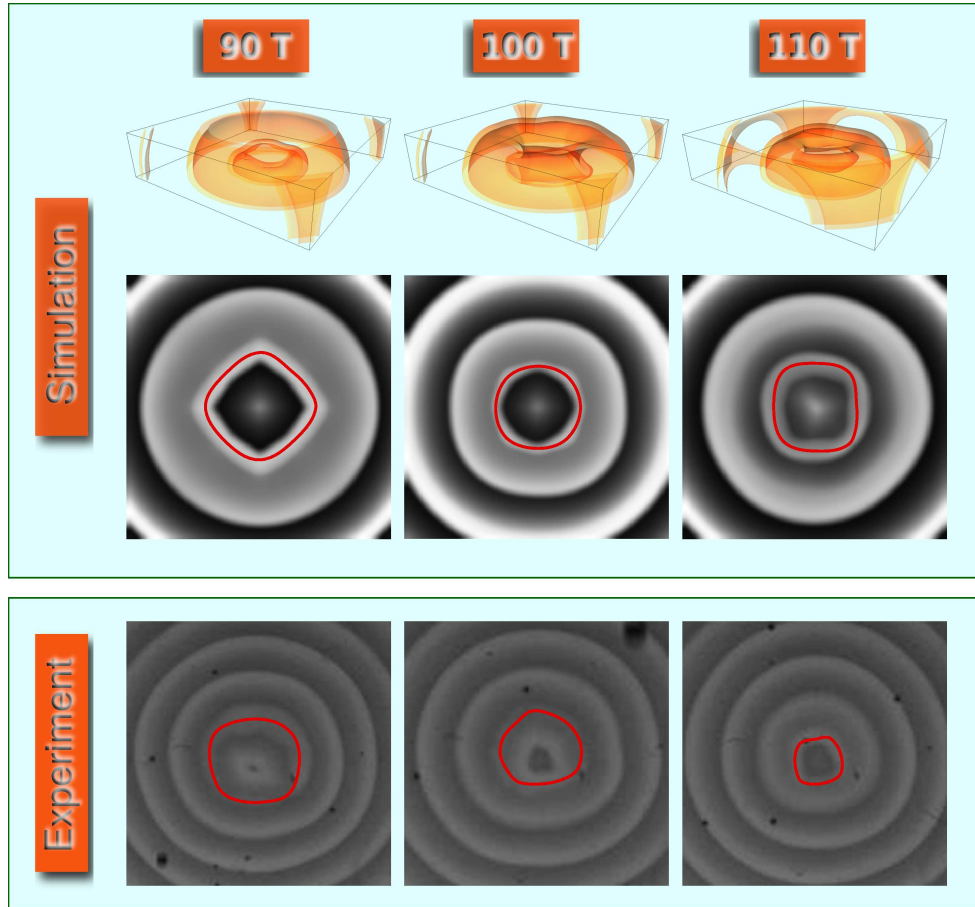


**Figure 62:** Experimental verification of a scroll ring with square-shaped filament in the PBZR (recipe VI with  $\Phi = 0.09 \text{ W/cm}^2$ ), compared to the results of numerical simulations based on the MCO model ( $\phi = 0.021$  in parameter set (2)). Top view mode in case of the experiment and two viewing modes for the numerical simulation (perspective view and top view) are presented. The closed red curves on the top view images (simulation and experiment) shall indicate the filaments.

Next, I have conducted experiments in which scroll rings were initiated at the lower no-flux boundary (the glass plate holding the gel layer) in thin layers of BZ media ( $0.6 - 0.8 \lambda$  in height). Indeed, the emergence of the square-shaped filament could be observed in several recipes. Exemplarily, one such experiment is illustrated and compared to the results of numerical simulations in figure 62. This experiment was achieved with the BZ recipe IV (see in table 1 on page 64 for the concentration values). The intensity for the background illumination, being fixed during the complete experimental run, was  $\Phi = 0.09 \text{ mW/cm}^2$ . The experimental images are cropped areas from a bigger ( $\sim 0.5 \text{ cm}$ ) gel diameter to better illustrate the results.

The accompanying numerical simulation was performed for  $\phi = 0.021$  in parameter set (2) (see figure 43 on page 104). The images are taken from a numerical simulation which was conducted in a  $4 \times 4 \times 1 \lambda^3$  cube. It has to be emphasized that the arising square-shaped filament is not caused by the geometry of the underlying simulation cube. Even though the surrounding

boundaries might be less than  $1 \lambda$  away from the filament at some moments in the evolution of the ring, the emerging filament shape is appearing also in simulations that were achieved in much bigger domains. This was already shown for a simulation in a cube with the volume  $9 \times 9 \times 2 \lambda^3$  (see figure 52 on page 112).

On the transmission image sequences showing the time evolution of the ring from top, the filament is indicated by closed red curves. As we can see, the shape of the filament possesses nearly a square geometry in the experimental case. Compared to the top view mode in the numerical simulation, the square shape is not perfect. This might be explained by the fact that numerical simulations are performed under completely homogeneous conditions while in the experiments, despite the very good homogenization of the control light source, a perfect homogeneous situation can not be maintained in horizontal direction of the layer. Moreover, illumination is additionally attenuated in the bulk of the reacting layer. Thus, an exponential gradient of the intensity will always be the case in the experiment. The consequence is that even very small horizontal gradients will be amplified additionally by the present vertical gradient. This will serve as a continuous source for twist along the filament and tend to further destabilize the filament.

Besides the experiments which support the emergence of the square-shaped filament, some other experimental conditions (e.g. the chosen recipe and the intensity of the background illumination) yield formation of filaments with other geometries. This includes an oval-shaped filament, a triangle-shaped filament, and so on. The filaments with triangle and oval shapes are presented in figure 63.

Further experimental studies in numerous BZ recipes also confirmed the existence of more complicated filament shapes. The complexity of the latter filament structures can not be assigned uniquely to one specific geometry

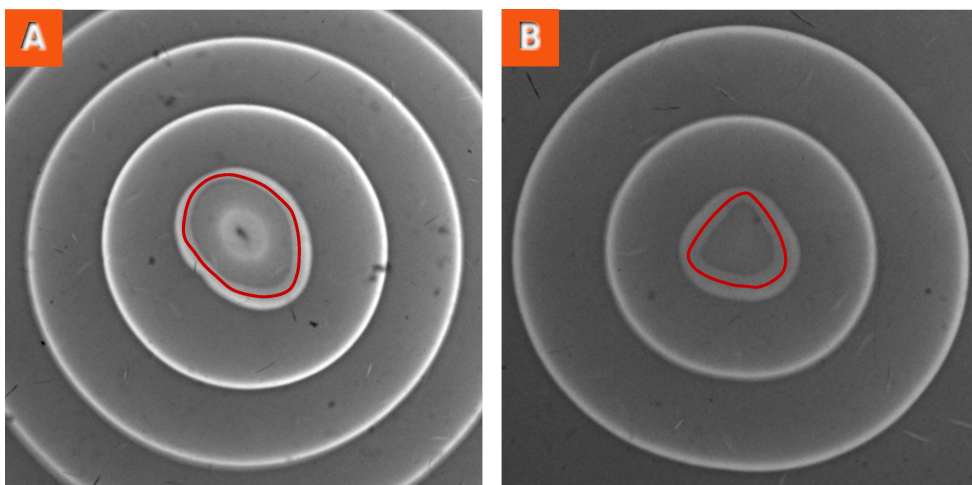


**Figure 63:** Examples for triangle- and oval-shaped filaments in the PBZR. (A) Oval-shaped filament measured in an experiment with recipe I at  $T = 22^\circ\text{C}$ . (B) Triangle-shaped filament measured in an experiment with recipe I at  $T = 25^\circ\text{C}$ . In both cases the background illumination intensity was  $\Phi = 0.09 \text{ mW/cm}^2$ .

(e.g. a square, a triangle, an oval, and so on). Instead, the emerging filament shape is irregular.

One example case showing formation of more complex filament shapes for scroll rings in the PBZ medium is illustrated in figure 64. In this figure, the experimental result, obtained in the BZ recipe VI under the constant intensity of illumination  $\Phi = 0.1 \text{ mW/cm}^2$ , is illustrated by two snapshots during the life-time of the ring. This experimental finding compares well with the numerical simulation obtained in the framework of the MCO model for  $\phi = 0.023$  in parameter set (2). The numerical findings are depicted by two snapshots at the same evolution times as in the experimental case. The projection of the filament into the  $x$ - $y$ -plane shows a very good qualitative agreement with the filament shapes observed in the experiment.

Furthermore, the projections onto the surrounding walls illustrate the highly complex deviations along the filament. Some of these deviations almost span the whole height of the medium as can be seen at  $t = 140 T$ .

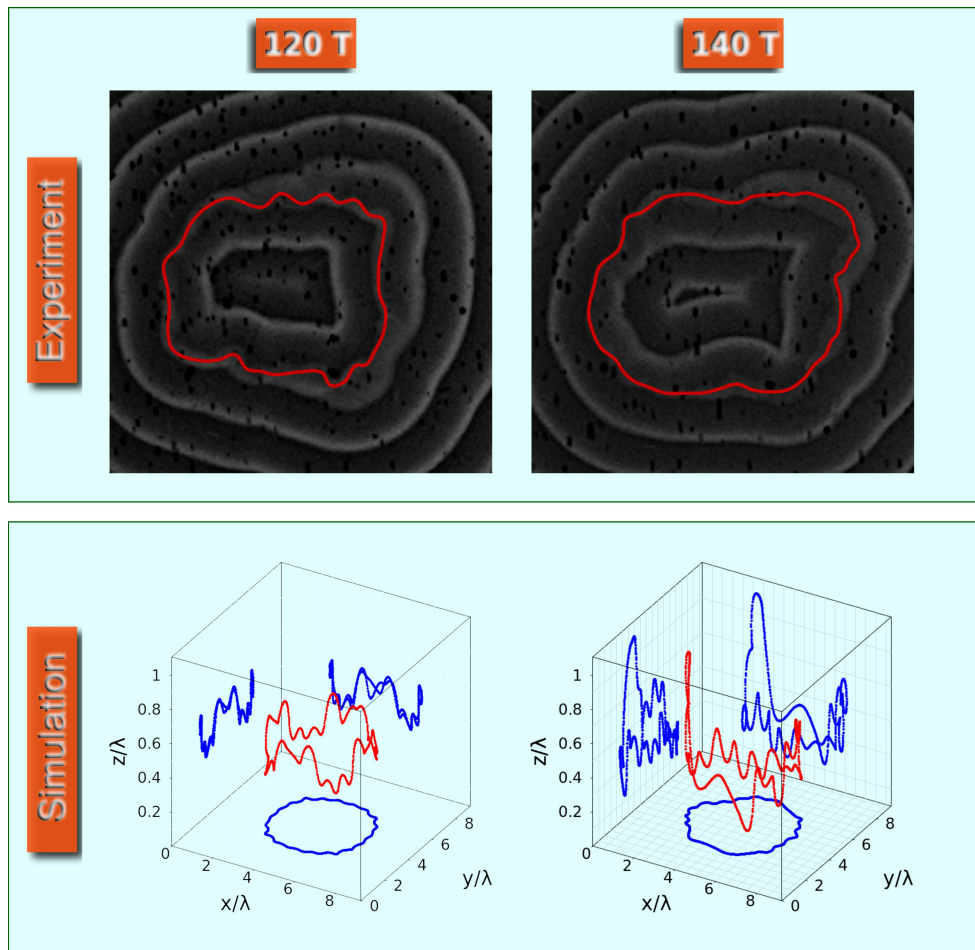


**Figure 64:** Emergence of an highly modulated ring filament in the PBZR compared with the filament shapes arising for a numerically simulated scroll ring in the MCO model. The experiment was achieved in recipe VI with  $\Phi = 0.1 \text{ mW/cm}^2$  while the numerical simulation was performed for  $\phi = 0.023$  in parameter set (2).

As a consequence, the filament might touch one of the boundaries if the medium is confined, particularly in case of our experiments, where the gel layers possess heights ranging between  $0.6\lambda$  and  $0.8\lambda$ . Hence, most of the experimentally obtained scroll rings (and also scroll waves) tend to depart after some time at one or even more points along the filament.



## CONCLUSIONS

---

The focus of this part was on the study of scroll rings under spatial confinement.

Numerical simulations of contracting scroll rings at one no-flux boundary revealed a substantial life time enhancement (section 8.4). In particular, this is the case for a parameter region supporting meandering spiral waves, with the life time enhancement reaching up to more than 500 % in relation to the corresponding free scroll rings. Moreover, the latter confined scroll rings in the meander regime show filament modulations with distinct geometries. I reported on the observation of ellipse-shaped, triangle-shaped, and square-shaped filaments, both in the experiment (chapter 10) as well as in the numerical simulations (section 8.4).

With regard to the scroll rings possessing the negative filament tension, development of the scroll wave turbulence was shown to be delayed significantly at the boundary, if in addition to the negative line tension instability also the three-dimensional meander instability is present. In contrast, expanding scroll rings are fully stabilized at the planar no-flux boundary, if no meander instability is present (section 8.5). These fully stabilized scroll rings resemble a novel type of stationary autonomous pacemakers (APMs), characterized by fixed values for both the ring radius  $R$  as well as for the axial position of the filament plane  $z$ . Additionally, “breathing” autonomous pacemakers were observed in numerical simulations. The latter are characterized by perfect sinusoidal oscillations in  $R$  and  $z$ . The transition from stationary to breathing APMs was shown to be a supercritical Hopf bifurcation. Experimental evidence for the stationary APM was delivered within the PBZR (chapter 9), while so far the breathing APM was not found in the experiment.



## Part V

### DYNAMICS OF FILAMENTS WITHIN A NONLINEAR ELASTICITY THEORY



# 12

## DYNAMICS OF FILAMENTS WITHIN A NONLINEAR ELASTICITY THEORY

---

In this chapter, it is my purpose to convince you that a nonlinear theory for elastic rods developed by A. Goriely and colleagues [178, 179, 180, 181, 182] is well-suited to predict emergence and dynamics of some filament instabilities that I observed both in the experiment and in numerical simulations.

The nonlinear theory for elastic rods is derived on the basis of the Kirchhoff model. The latter model links the forces and moments acting on the filament to the intrinsic stresses (tension, curvature, and twist). As such, the nonlinear elasticity theory unifies effects that emerge due to not only twist, but also to the other potential stresses like curvature and tension within one consistent theory. Moreover, scroll waves as particular representatives for the class of nonlinear three-dimensional waves can now be described in their evolution within time on the basis of a theory which also describes systems of such different kind as for example proteins like the DNA and bacterial fibers [183, 184, 185, 186, 187, 188]; polymers and liquid crystals [189, 190]; vortex tubes in hydrodynamics [191]; sun spots and the heating dynamics in the solar corona [192, 193].

In the next section, I shall first summarize the approach by Goriely and colleagues. I will focus on the most important basics and results of the theory, while omitting the rather lengthy derivations. Subsequently, I will present some of the intriguing predictions for straight and ring filaments and compare these predictions with the matching results that I have obtained in the experiments and in numerical simulations.

### 12.1 THE BASIC ELEMENTS OF THE APPROACH BY GORIELY AND COLLEAGUES

The approach by Goriely and colleagues can be split in two parts, the first of which is a kinematic description of a filament by a local frame of reference what they denote as the director basis. The second part is a dynamical description of filament evolution within the Kirchhoff equations for “thin” elastic rods in the limit of linear elasticity theory [178]. In the following, I will adhere mostly to the reference [178].

The kinematical description of the filament within the director basis is shown in figure 65. The thin red curve shall depict the center line of our filament. This curve can now be parametrized by the arc length  $s$ , such that its position be given by a function  $x(s, t)$ , depending on the arc length  $s$  and time  $t$ . The director basis as a local orthonormal frame of reference is now constructed as follows: The tangent vector is given by  $d_3 = \partial_s x(s, t)$ . Then, the two other unit vectors  $d_1$  and  $d_2$  can be chosen arbitrarily in the plane normal to  $d_3$ , with the only condition that  $\{d_1(s, t), d_2(s, t), d_3(s, t)\}$  must form a right-handed orthonormal basis for each value of  $s$  and  $t$ .

The spatio-temporal evolution along the curve is governed by the so-called spin and twist equations:

$$\frac{\partial}{\partial s} d_i = \kappa \times d_i, \quad (106)$$

$$\frac{\partial}{\partial t} d_i = \omega \times d_i, \quad (107)$$

with  $i = 1, 2, 3$ . In these two equations we have the twist vector

$$\kappa = \kappa_1 d_1 + \kappa_2 d_2 + \kappa_3 d_3$$

and the spin vector

$$\omega = \omega_1 d_1 + \omega_2 d_2 + \omega_3 d_3.$$

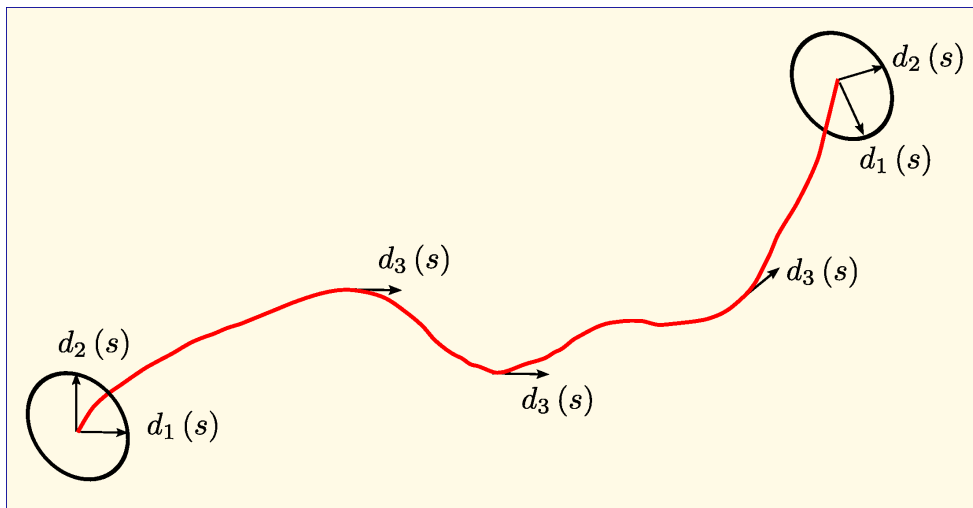


**Figure 65:** Sketch of a filament (in red) that is described by the director basis  $\{d_1(s, t), d_2(s, t), d_3(s, t)\}$ .

To determine the position of the curve at each moment in time  $t$ , we seek knowledge of  $\kappa = \kappa(s, t)$  and  $\omega = \omega(s, t)$ , since the twist and spin equations have to be solved to get  $d_3$ , and the latter shall be integrated once to get  $x = x(s, t)$ .

Note that the director frame can be reduced to the Frenet-Serret frame [135], if we consider  $d_1$  being the normal vector and  $d_2$  being the bi-normal vector. But, the director basis is general by construction, and this generality will show up as the power of the director basis. Particularly, the local choice of the vectors  $d_1$  and  $d_2$  along the filament aids us in capturing certain material properties.

The dynamics of the filament curve is now governed by the Kirchhoff model for elastic rods. The validity of the Kirchhoff model is ensured by the condition stating that the length of the filament is much greater than the cross-sectional radius. Two other conditions that can be taken into account, but are not mandatory, are: (1) The curve shall be inextensible and (2) the cross-section shall be circular. A one-dimensional theory can now be derived, which links the total force  $F = F(s, t)$  and moment  $M = M(s, t)$  exerted on the filament with the intrinsic stresses like twisting and bending. This derivation yields the following scaled Kirchhoff model expressed locally in terms of the director basis [194, 195]:

$$F'' = \ddot{d}_3, \quad (108)$$

$$M' + d_3 \times F = d_1 \times \ddot{d}_1 + d_2 \times \ddot{d}_2, \quad (109)$$

$$M = \kappa_1 d_1 + \kappa_2 d_2 + \Gamma \kappa_3 d_3. \quad (110)$$

Here, the abbreviations  $(\cdot)' = \partial_s$  and  $(\cdot) = \partial_t$  were introduced. Within this system of coupled equations, the third equation represents the constitutive relationship of linear elasticity theory. The parameter

$$\Gamma = \frac{1}{1 + \sigma}$$

with the Poisson ratio  $\sigma$  resembles a measure for the ratio between the bending and twisting coefficients of the rod. In most cases  $\Gamma$  varies in a range between  $2/3$  (incompressible) and  $1$  (hyperelastic).

Provided that a stationary solution of the Kirchhoff model is given, the stability of this solution is studied within the framework of a perturbation analysis that is achieved in terms of the director basis directly. The condition which must be fulfilled is that at each order of perturbation the approximated local basis

$$d_i = d_i^{(0)} + \epsilon d_i^{(1)} + \epsilon^2 d_i^{(2)} + \dots$$

remains orthonormal. Generally defined, the condition

$$d_i \cdot d_j = \delta_{ij} + \mathcal{O}(\epsilon^{m+1})$$

has to be satisfied at order  $\mathcal{O}(\epsilon^m)$ . By this condition three arbitrary parameters arise at each order and allows us to express the perturbed basis with

respect to the unperturbed basis. The parameters at the order  $\mathcal{O}(\epsilon^m)$  are  $\{\alpha_1^{(m)}, \alpha_2^{(m)}, \alpha_3^{(m)}\}$  and the perturbed basis is expressed as

$$d_i^{(m)} = \alpha^{(m)} \times d_i^{(0)} + \sum_j \beta_{ij} d_j^{(0)}, \quad i = 1, 2, 3. \quad (111)$$

Herein, the symmetric tensor  $\beta^{(m)}$  contains entries that only depend on  $\alpha^{(k)}$  with  $k < m$ .

Subsequently, all intriguing entities of the theory can be expressed in terms of the parameters  $\alpha$  and the corresponding unperturbed entities. In particular, the perturbed twist and spin vectors at first order are:

$$\kappa = \kappa^{(0)} + (\alpha^{(0)})' + \kappa^{(0)} \times \alpha^{(1)} + \mathcal{O}(\epsilon^2), \quad (112)$$

$$\omega = \dot{\alpha}^{(1)} + \mathcal{O}(\epsilon^2). \quad (113)$$

Analogously, the perturbed force at first order becomes

$$F = \sum_i \left\{ f_i^{(0)} + \epsilon \left[ f_i^{(1)} + (\alpha \times f^{(0)})_i \right] \right\} d_i^{(0)} + \mathcal{O}(\epsilon^2).$$

Given the stationary filament configuration  $(f^{(0)}, \kappa^{(0)})$  together with the introduced perturbation scheme yields the variational equations

$$\mathcal{L}_E (\kappa^{(0)}, f^{(0)}) \cdot \mu^{(1)} = 0. \quad (114)$$

Herein, we have a linear, second-order differential operator  $\mathcal{L}_E$  in  $s$  and  $t$  and the six-dimensional vector  $\mu^{(1)} = \{\alpha^{(1)}, f^{(1)}\}$ . The explicit form of this linear system is provided in [182].

## 12.2 THE STRAIGHT FILAMENT

Within this section, I will discuss the implications of the above described theory for a straight rod under twist. The two unit vectors  $d_1$  and  $d_2$  now follow the twist  $\gamma$ . The stationary solution is expressed by

$$\kappa^{(0)} = (0, 0, \gamma), \quad (115)$$

$$f^{(0)} = (0, 0, P^2). \quad (116)$$

The rod is considered to be under tension, meaning that  $f_3^{(0)} = P^2 > 0$ . The linear solutions to the variational equations (114) can be expressed as

$$\mu_j^{(1)} = e^{\sigma t} \left( Ax_j e^{ins} + A^* x_j^* e^{-ins} \right), \quad j = 1, \dots, 6. \quad (117)$$

Substituting these linear solutions into the variational equations (114) yields dispersion relations  $\Delta(\sigma, n) = 0$ , from which then the growth rate  $\sigma$  can be determined. The dispersion relation in this case is:

$$(\gamma^2 - n^2) \left\{ [\gamma^2 (\Gamma - 1) - P^2 - n^2]^2 - \gamma^2 (\Gamma - 2)^2 n^2 \right\} = 0. \quad (118)$$

There are two neutral curves as solutions to this dispersion relation: (1) A trivial solution  $\kappa^{(1)} = \omega^{(1)} = 0$  for the mode  $n = \gamma$  and (2) a parabolic solution that corresponds to an unstable helix with the following critical parameters:

$$n_c = \frac{P(2 - \Gamma)}{\Gamma}, \quad (119)$$

$$\gamma_c = \pm \frac{2P}{\Gamma}. \quad (120)$$

The second solution to the dispersion relation is intriguing, since it states that the twisted rod transforms to a helix above the critical twist  $\gamma_c$ . The calculated shape of the rod is

$$x = \left( s, -\frac{2A}{P} \sin(sP), \frac{2A}{P} \cos(sP) \right). \quad (121)$$

In order to study the nonlinear behavior of the unstable modes, a nonlinear analysis is conducted (described in detail in the references [180, 182]). To achieve the analysis, the perturbation parameter is specified as

$$\epsilon^2 = \gamma - \gamma_c. \quad (122)$$

In addition, the stretched time and space scales  $t_1 = \epsilon t$  and  $s_1 = \epsilon s$  are introduced. Then, the linear solution at order  $\mathcal{O}(\epsilon)$  follows as a superposition of the neutral modes:

$$\mu^{(1)} = Y\xi_0 + X\xi_n e^{ins} + X^* \xi_n^* e^{-ins}. \quad (123)$$

Here, we have the slowly varying amplitude of the axial twist,  $Y = Y(s_1, t_1)$ , and the unstable helical mode  $X = X(s_1, t_1)$ . Furthermore, it is  $n = n_c$  and

$$\begin{aligned} \xi_0 &= (0, 0, 1, 0, 0, 1), \\ \xi_n &= (1, i, 0, -iP^2, P^2, 0). \end{aligned}$$

Through the application of the multiple scales analysis two amplitude equations are derived to third order in  $\epsilon$ . For the details of the derivation see in [180, 182]. The resulting equations resemble two coupled nonlinear Klein-Gordon equations for the amplitudes  $X$  and  $Y$ :

$$\left( \frac{P^2 + 1}{P^2} \right) \frac{\partial^2 X}{\partial t_1^2} - \frac{\partial^2 X}{\partial s_1^2} = P\Gamma X \left( 1 - 2P|X|^2 + \frac{\partial Y}{\partial s_1} \right), \quad (124)$$

$$\frac{2}{\Gamma} \frac{\partial^2 Y}{\partial t_1^2} - \frac{\partial^2 Y}{\partial s_1^2} = -2P \frac{\partial |X|^2}{\partial s_1}. \quad (125)$$

We may discuss two interesting special solutions for these equations:

(1) HOMOGENEOUS SOLUTION: Considering homogeneous twist along the filament, decouples the twist density  $Y$  from the deformation  $X$  and yields the following time evolution equation for the deformation:

$$\frac{\partial^2 X}{\partial t_1^2} = \frac{P^3 \Gamma}{P^2 + 1} X \left( 1 - 2P|X|^2 \right). \quad (126)$$

Integration yields the shape of the filament solution as a helix that is described by the equation (121) with  $A = \epsilon X(\epsilon t)$ .

The homogeneous case corresponds particularly to the helicoidal filaments that arise for three-dimensional meander unstable scroll waves. One example was already found for one parameter in the Barkley model by Henry and Hakim (see section 6.2 on page 83).

(2) TRAVELLING WAVE SOLUTIONS: If one considers  $z = s_1 - ct_1$ , the amplitude equations are reduced to

$$\frac{\partial^2 X}{\partial z^2} = \frac{P^3 \Gamma}{P^2(c^2 - 1) + c^2} X \left( K + 1 + \frac{4Pc^2}{\Gamma - 2c^2} |X|^2 \right), \quad (127)$$

with the constant  $K$  chosen such that the derivative of the twist density  $Y$  tends to zero at infinity. From here on, two separate solutions emerge:

If  $c^2 > \max \left\{ \frac{\Gamma}{2}, \frac{P^2}{P^2+1} \right\}$ , a homoclinic orbit occurs:

$$X(z) = \rho_1 \operatorname{sech}(\rho_2 z). \quad (128)$$

with

$$\begin{aligned} K &= 0, \\ \rho_1^2 &= \frac{2c^2 - \Gamma}{2Pc^2}, \\ \rho_2^2 &= \frac{P^3 \Gamma}{P^2 c^2 - P^2 + c^2}. \end{aligned}$$

The solution (128) corresponds to a pulselike solitary wave propagating with constant velocity along the filament. This state was found for a straight scroll

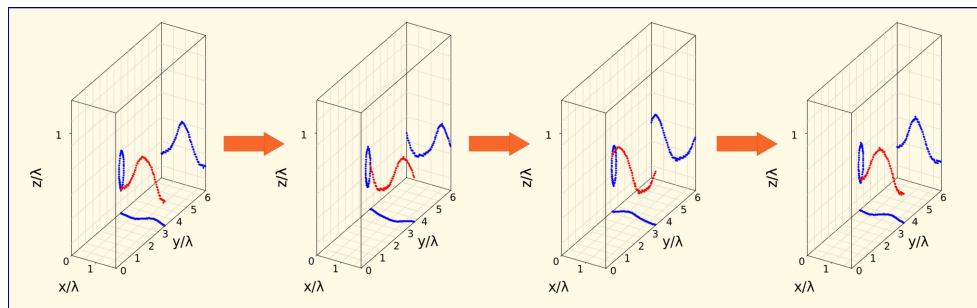


**Figure 66:** Travelling pulselike deformation wave observed in the Barkley model. The filament shown in red and its projections to the walls in blue.

wave under spatial confinement in numerical simulations within the Barkley model. It was shown that these scroll waves experience a secondary meander instability in unbounded media. The specific case is illustrated by figure 66.

In contrast, for the condition  $\frac{P^2}{P^2+1} > c^2 > \frac{\Gamma}{2}$  one gets a heteroclinic function

$$X(z) = \rho_1 \tanh(\rho_2 z), \quad (129)$$

with

$$\begin{aligned} K &= \frac{\Gamma}{\Gamma - 2c^2}, \\ \rho_1^2 &= \frac{1}{2P}, \\ \rho_2^2 &= \frac{c^2 P^3 \Gamma}{(P^2 c^2 - P^2 + c^2)(\Gamma - 2c^2)}. \end{aligned}$$

This solution describes a frontlike solitary wave and corresponds to the meander unstable filament observed in the modified complete Oregonator (MCO) model and in the experiment within the PBZR (see chapter 7 on page 93). Figure 67 shall illustrate the travelling front along the filament in case of the numerical simulation within the MCO model.

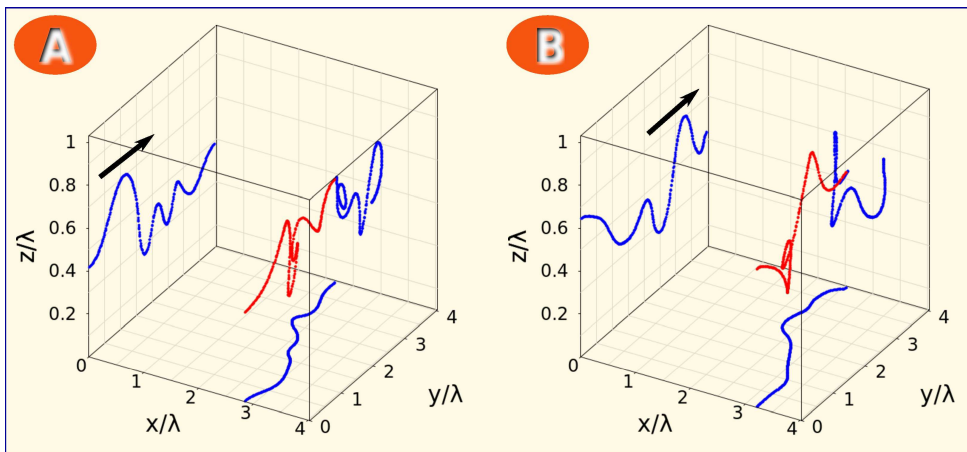


**Figure 67:** Travelling frontlike deformation wave in the MCO model. The filament shown in red and its projections to the walls in blue. The black arrows shall depict the direction of the propagation for the wave. Numerical simulation was achieved for  $\phi = 0.022$  in parameter set (2) of the MCO model (same parameter as in figure 40 on page 95) (A)  $t = 125 T$  and (B)  $t = 132 T$ .

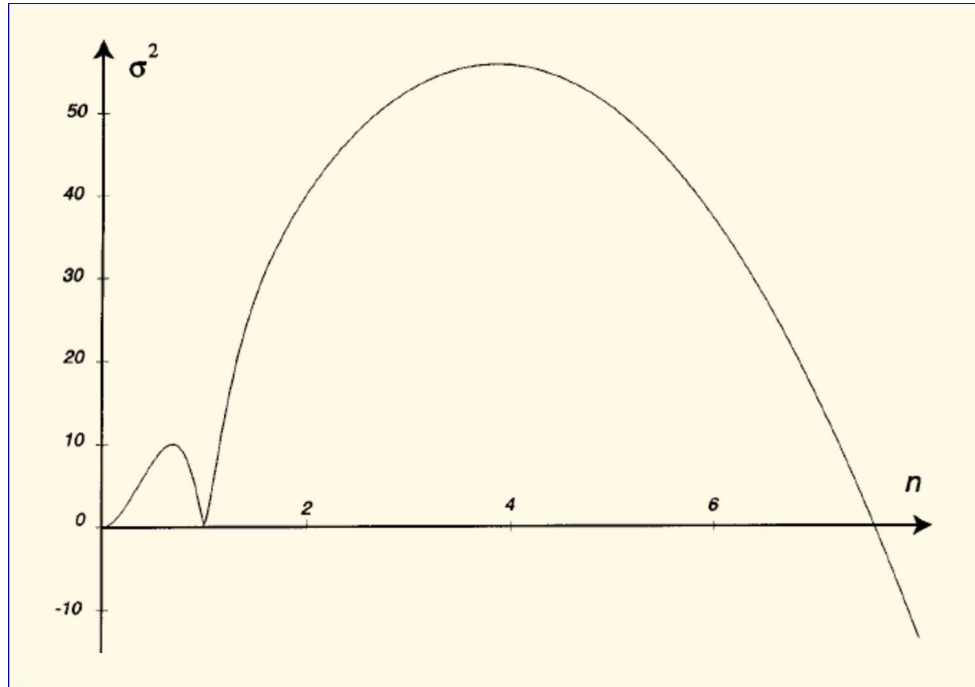


**Figure 68:** Dispersion relation for a ring filament. Graph shows the plot of  $\sigma^2$  as a function of  $n$  for the total twist  $\tau = 30 \gg \tau_c$ . Graph reprinted with permission from [182], copyright by Springer.

### 12.3 THE RING-SHAPED FILAMENT

In an analogous way as illustrated in the previous section, one can study the evolution of a ring-shaped filament within the nonlinear elasticity approach. First, the linear stability of a stationary solution is examined. The stationary solution is chosen to be

$$\kappa^{(0)} = (k \sin(\gamma s), k \cos(\gamma s), \gamma), \quad (130)$$

$$f^{(0)} = (\Gamma \gamma k \sin(\gamma s), \Gamma \gamma k \cos(\gamma s), 0). \quad (131)$$

Herein, we have the curvature of the ring filament  $k = \frac{1}{R}$  ( $R$  being the radius of the ring),  $\gamma = k\tau$  is the twist density, and  $\tau$  the total twist.

Without going too much into details of the actual derivations, the approach is again such that the linear solutions (117) are inserted into the variational equations (114), but now with the stationary ring setup (130) and (131) as the unperturbed solution. This yields a dispersion relation that is now much more complicated (polynomial of degree 6 in the growth rate  $\sigma$  and degree 12 in the unstable mode  $n$ ) than the one in case of the straight filament. Hence, I omit to write it down here. Nevertheless, it can be found in the reference [182].

One sample dispersion relation is plotted in figure 68. Obviously, the unstable mode  $n = 4$  dominates, a fact that explains why in case of the meander-unstable free scroll rings within the MCO model, the emerging filament shape is always observed to be square-shaped (see figure 46).

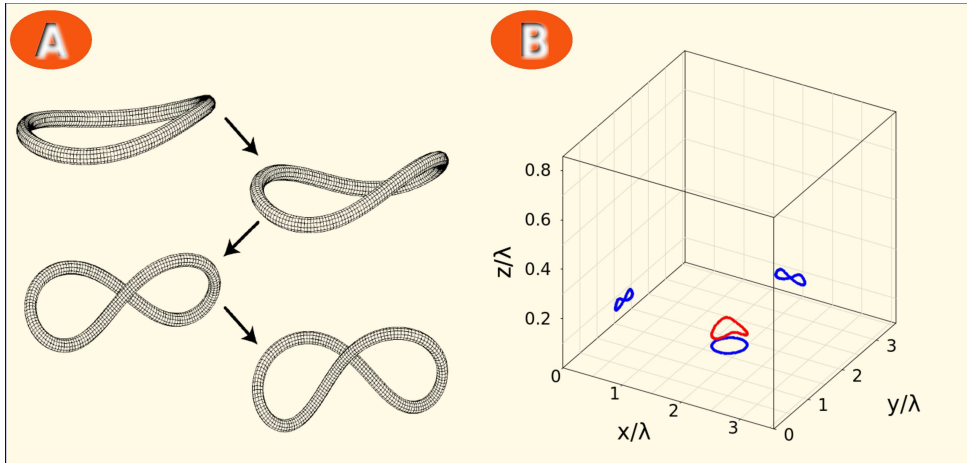


**Figure 69:** Evolution of the mode  $n = 2$ . (A) Within the nonlinear elasticity theory for growing amplitude and for  $k = 1/16$ ,  $\Gamma = 3/4$  (reprinted with permission from [182], copyright by Springer). (B) Obtained snapshot after  $t = 72 T$  within the MCO model for  $\phi = 0.028$  in parameter set (2).

Moreover, the dispersion relations determine the critical value of twist above which the stationary ring filament gets unstable, namely as

$$\tau = \pm \frac{\sqrt{n^2 - 1}}{\Gamma}. \quad (132)$$

The primary mode that is getting unstable, is the mode  $n = 2$  for a critical twist of  $\tau_c = \sqrt{3}/\Gamma$ . Once again, a counterpart for the evolution of this mode was already observed and discussed in my thesis. In figure 69, the evolution of mode  $n = 2$  (panel A) in the elasticity theory is compared with the evolution of a temporarily stabilized scroll ring at a planar no-flux boundary (panel B). We discussed the latter as an example for delayed development of the negative line tension instability. All four stages that are shown in panel A are also observed for the scroll ring, although solely the last illustrated stage in panel A is depicted here in case of the scroll ring.



Part VI

CONCLUSIONS AND OUTLOOK



## CONCLUSIONS AND OUTLOOK

---

The evolution of free scroll waves in several types of excitable media have been studied extensively during the last three to four decades. However, the evolution of scroll waves under spatial confinement has been studied not as systematically as it is the case for the free scroll waves. The lack of a systematic study in this direction was the motivation for my thesis.

The primary task to accomplish at the beginning of my studies was to develop well-suited experimental and numerical methods. The experiments were conducted in thin layers of excitable and oscillatory photosensitive Belousov-Zhabotinsky (PBZ) media. In order to maintain these media at stationary non-equilibrium conditions, a continuously stirred tank reactor (CSTR) was used. The aim to initiate straight scroll waves and scroll rings in a reproducible manner, demanded to develop a novel experimental setup. Me and my colleagues achieved this task.

Inspired by the capabilities maintained in our experimental laboratory, we developed a general reaction-diffusion (RD) simulation program. This program, which is termed Virtual Lab, allows us to study nonlinear waves in one to three dimensions. The program incorporates different RD models, boundary conditions, numerical algorithms, and is constructed such that it mimics parameter variation strategies that already enabled to reproducibly initiate various types of three-dimensional (3D) waves in our experimental laboratory.

In part three of my thesis, I reported on the numerical and experimental study of straight scroll waves under spatial confinement. First, an extensive numerical survey within the framework of the Barkley RD model was presented. The latter studies revealed a complete suppression of the negative line tension instability (more than 4500 rotation periods), and a delayed development of the negative line tension instability for one parameter at the border to the meander regime (up to 500 rotation periods). For the case of straight scroll waves possessing the 3D meander instability, at one parameter the scroll wave restabilizes into a helix. Another parameter, which is located within the outward meander regime, experiences a secondary 3D meander instability in unbounded media. We were able to show that confinement suppresses the secondary meander instability, such that one pulselike deformation wave with constant shape and velocity propagates along the restabilized filament. My experimental studies within the PBZ reaction showed the emergence of highly writhed filaments. Within time, the deviations on the filament occur irregularly and deformation waves of varying shapes propagate along the filament. The observed filament state is characterized by a noisy evolution of its overall length.

In part four, I presented results of my studies regarding scroll rings under spatial confinement. Primarily, I achieved a thorough numerical study of scroll rings in the framework of the modified complete Oregonator (MCO) model. The numerical studies for contracting scroll rings revealed a substantial life time enhancement due to boundary interaction, more than 500 % in relation to the corresponding free scroll rings. Additionally, modulated ring filaments of distinct geometries emerge for scroll rings in the meander regime, for example ellipse-shaped, triangle-shaped, and square-shaped filaments. The latter filament geometries were also obtained in the experiment. Development of the scroll wave turbulence was shown to be delayed significantly in case of scroll rings possessing the meander instability in addition to the negative line tension instability. If the meander instability is not present, expanding scroll rings are fully stabilized at the planar no-flux boundary. The fully stabilized scroll rings resemble a novel type of stationary autonomous pacemakers (APMs) in 3D excitable media. They are characterized by constant values for both the ring filament radius  $R$  and the  $z$  axis position of the filament plane. In addition, I also found “breathing” APMs in numerical simulations. These breathing APMs show perfect sinusoidal oscillations in  $R$  and  $z$ . The transition from stationary to breathing APMs within the examined parameter regime was shown to be a supercritical Hopf bifurcation. As the highlight of my studies on confined scroll rings, I reported on the first experimental evidence for a stationary APM within the PBZ reaction.

Finally, a bunch of publications by Goriely and colleagues arrested my attention [178, 179, 180, 181, 182]. The approach by them resembles a reconsideration and extension of the classical elasticity theory for thin rods [135, 136]. This nonlinear elasticity theory is well suited for explaining emergence and evolution of almost all effects that were reported on with respect to straight scroll waves and scroll rings in my thesis. Amplitude equations (two coupled nonlinear Klein-Gordon equations) that are derived for straight scroll wave filaments reproduce the transition to helix-shaped filaments due to a critical homogeneous twist along the filament, whereas pulses and waves are shown to propagate along the filament as an effect of non-homogeneous, time-depending twist. With regard to ring-shaped filaments, the emergence of different modulation geometries are explained while the theory by Goriely and colleagues shows the mode  $n = 4$ -instability (square-shaped filament) to dominate.

Albeit, the study of scroll waves has reached a matured state within the last decades, my thesis might have shown that it is still worth to study the evolution of these mesmerizing structures under varying spatial, temporal, and any other conditions. I am convinced that this will be the case also in the next decades to come. To examine the evolution of scroll waves at planar no-flux boundaries was my purpose herein. But, planar boundaries can only be the starting point. In a next step, one can investigate scroll wave evolution at various types of uneven walls. Just recently, the dynamics of straight scroll waves at a step was studied analytically [196] and experimentally in the BZ

reaction [197]. Martens et al. investigated the properties of propagating fronts in channels with spatially modulated cross-sections [198]. It would be intriguing to study effects which may arise when a straight scroll wave or a scroll ring is placed in a 3D version of these channels, particularly for the propagation of the emitted waves. What would for example happen, if the chosen modulation of the medium boundaries cause a propagation failure for the emitted waves, as it was reported by Martens and colleagues in case of the propagating fronts? Would it cause a “bunching” of waves at the site where a wave is trapped by a bottleneck? And if so, how would the relapse effects on the organizing filament look like?

It is needless to pursue in the intention to string together more ideas. Any good scientific work also yields new questions and traces for novel directions to investigate. With this in mind, I hope that my thesis provoked enthusiasm for the study of scroll waves, and I concede to you the joy of thinking through own ideas and questions that might be intriguing to investigate.



Part VII  
**BIBLIOGRAPHY**



## BIBLIOGRAPHY

---

- [1] G. Nicolis and I. Prigogine. *Self-Organization in Nonequilibrium Systems*. Interscience Publishers, John Wiley & Sons, 1977. (Cited on pages 1, 2, and 3.)
- [2] A. M. Turing. The chemical basis of morphogenesis. *Philosophical Transactions of the Royal Society of London*, 237(641):37–72, 1952. (Cited on page 1.)
- [3] I. Prigogine. *Introduction to Thermodynamics of Irreversible Processes*. Interscience Publishers, John Wiley & Sons, 3rd edition, 1967. (Cited on pages 1 and 3.)
- [4] I. Prigogine and G. Nicolis. On symmetry-breaking instabilities in dissipative systems. *Journal of Chemical Physics*, 46(9):3542–3550, 1967. (Cited on page 1.)
- [5] I. Prigogine, R. Lefever, A. Goldbeter, and M. Herschkowitz-Kaufman. Symmetry breaking instabilities in biological systems. *Nature*, 223:913–916, 1969. (Cited on page 1.)
- [6] W. Ebeling. *Strukturbildung bei irreversiblen Prozessen. Eine Einführung in die Theorie dissipativer Strukturen*. B. G. Teubner, Leipzig, 1976. (Cited on page 1.)
- [7] L. Onsager. Reciprocal relations in irreversible processes. II. *Physical Review*, 38(405):2265–2279, 1931. (Cited on page 2.)
- [8] E. L. Koschmieder. Bénard convection. *Adv. Chem. Phys.*, 26:177–212, 1974. (Cited on page 3.)
- [9] S. Chandrasekhar. *Hydrodynamic and Hydromagnetic Stability*. Oxford University Press, London, 1961. (Cited on page 3.)
- [10] B. P. Belousov. A periodic reaction and its mechanism. In *Collection of short papers on radiation medicine for 1958*, page 145. Medical Publications, Moscow, 1959. (Cited on pages 3 and 55.)
- [11] B. P. Belousov. A periodic reaction and its mechanism. In R. J. Field and M. Burger, editors, *Oscillations and Traveling Waves in Chemical Systems*. Wiley, New York, 1985. (Cited on page 3.)
- [12] O. Steinbock. *Untersuchung chemischer Wellen in der Belousov-Zhabotinsky-Reaktion mittels externer Beeinflussung und Kontrolle photosensitiver Systemeigenschaften*. PhD thesis, Georg-August-Universität Göttingen, Göttingen, Germany, 1993. (Cited on pages 3 and 55.)
- [13] A. M. Zhabotinsky. *Investigations of homogeneous chemical auto-oscillating systems (in Russian)*. PhD thesis, Institute of Biological Physics of the Academy of Sciences, Pushino, USSR, 1970. (Cited on pages 4 and 7.)

- [14] A. N. Zaikin and A. M. Zhabotinsky. Concentration wave propagation in two-dimensional liquid-phase self-oscillating system. *Nature*, 225(5232):535–537, 1970. (Cited on pages 4 and 123.)
- [15] A. T. Winfree. Two kinds of wave in an oscillating chemical solution. *Faraday Symposia of the Chemical Society*, 9:38–46, 1974. (Cited on pages 5, 10, and 56.)
- [16] G. Bordiougov and H. Engel. From trigger to phase waves and back again. *Physica D*, 215(1):25–37, 2006. (Cited on page 5.)
- [17] M.-L. Smoes and J. Dreitlein. Dissipative structures in chemical oscillations with concentrations-dependent frequency. *The Journal of Chemical Physics*, 59(12):6277–6285, 1973. (Cited on page 5.)
- [18] D. Thoenes. "Spatial oscillations" in the zhabotinskii reactionorto. *Nature Physical Science*, 243:18–20, 1973. (Cited on page 5.)
- [19] P. Ortoleva and J. Ross. Phase waves in oscillatory chemical reactions. *The Journal of Chemical Physics*, 58(12):5673–5680, 1973. (Cited on page 5.)
- [20] P. Ortoleva and J. Ross. On a variety of wave phenomena in chemical reactions. *The Journal of Chemical Physics*, 60(12):5090–5107, 1974. (Cited on page 5.)
- [21] A. T. Winfree. Wavelike activity in biological and chemical media. In P. van den Driessche, editor, *Mathematical Problems in Biology, Lecture Notes in Biomathematics*, volume 2, pages 241–260. Springer-Verlag, 1974. (Cited on page 5.)
- [22] A. T. Winfree. Spiral waves of chemical activity. *Science*, 175(4022):634–636, 1972. (Cited on pages 5, 6, and 7.)
- [23] N. Kopell and L. N. Howard. Horizontal bands in the Belousov reaction. *Science*, 180(4091):1173–1175, 1973. (Cited on page 5.)
- [24] J. A. DeSimone, D. L. Beil, and L. E. Scriven. Ferroin-collodion membranes: Dynamic concentration patterns in planar membranes. *Science*, 180(4089):946–948, 1973. (Cited on page 5.)
- [25] A. T. Winfree. Spatial and temporal organization in the Zhabotinsky reaction. *Advances in Biological and Medical Physics*, 16:115–136, 1977. (Cited on page 5.)
- [26] Y. Kuramoto. *Chemical Oscillations, Waves, and Turbulence*. Springer-Verlag, 1984. (Cited on pages 5 and 123.)
- [27] S. Jakubith, H.-H. Rotermund, W. Engel, A. von Oertzen, and G. Ertl. Spatiotemporal concentration patterns in a surface reaction: Propagating and standing waves, rotating spirals, and turbulence. *Physical Review Letters*, 65(24):3013–3016, 1990. (Cited on pages 6, 7, and 123.)
- [28] M. Assenheimer and V. Steinberg. Rayleigh-Bénard convection near the gas-liquid critical point. *Physical Review Letters*, 70(25):3888–3891, 1993. (Cited on pages 6 and 123.)

- [29] Y. A. Astrov, I. Müller, E. Ammelt, and H.-G. Purwins. Zigzag destabilized spirals and targets. *Physical Review Letters*, 80(24):5341–5344, 1998. (Cited on pages 6, 7, and 123.)
- [30] J. Christoph, R. D. Otterstedt, M. Eiswirth, N. I. Jaeger, and J. L. Hudson. Negative coupling during oscillatory pattern formation on a ring electrode. *The Journal of Chemical Physics*, 110(17):8614–8621, 1999. (Cited on pages 6 and 123.)
- [31] A. S. Mikhailov. Stable autonomous pacemakers in the enlarged Ginzburg-Landau model. *Physica D*, 55:99–112, 1992. (Cited on page 6.)
- [32] M. Stich, M. Ipsen, and A. S. Mikhailov. Self-organized stable pacemakers near the onset of birhythmicity. *Physical Review Letters*, 86(19):4406–4409, 2001. (Cited on page 6.)
- [33] M. Stich, M. Ipsen, and A. S. Mikhailov. Self-organized pacemakers in birhythmic media. *Physica D*, 171:19–40, 2002. (Cited on page 6.)
- [34] M. Stich. *Target patterns and pacemakers in reaction-diffusion systems*. PhD thesis, Technische Universität Berlin, Berlin, Germany, 2003. (Cited on page 6.)
- [35] M. Stich, A. S. Mikhailov, and Y. Kuramoto. Self-organized pacemakers and bistability of pulses in an excitable medium. *Physical Review E*, 79:026110, 2009. (Cited on page 6.)
- [36] N. A. Gorelova and J. Bureš. Spiral waves of spreading depression in the isolated chicken retina. *Journal of Neurobiology*, 14(5):353–363, 1983. (Cited on page 7.)
- [37] S. C. Müller, T. Plessner, and B. Hess. The structure of the core of the spiral wave in the Belousov-Zhabotinskii reaction. *Science*, 230:661–663, 1985. (Cited on pages 7, 59, 60, and 74.)
- [38] F. Siegert and C. Weijer. Digital image processing of optical density wave propagation in *Dictyostelium discoideum* and analysis of the effects of caffeine and ammonia. *Journal of Cell Science*, 93:325–335, 1989. (Cited on page 7.)
- [39] T. Frisch, S. Rica, P. Coullet, and J. M. Gilli. Spiral waves in liquid crystal. *Physical Review Letters*, 72(10):1471–1474, 1994. (Cited on page 7.)
- [40] M. Falcke, J. L. Hudson, P. Camacho, and J. D. Lechleiter. Impact of mitochondrial  $\text{Ca}^{2+}$  cycling on pattern formation and stability. *Biochemical Journal*, 77:37–44, 1999. (Cited on page 7.)
- [41] M.R. Tinsley, D. Collison, and K. Showalter. Propagating precipitation waves: experiments and modeling. *The Journal of Physical Chemistry A*, 117(48):12719–12725, 2013. (Cited on page 7.)
- [42] N. Hartmann, M. Bär, I. G. Kevrekidis, K. Krischer, and R. Imbihl. Rotating chemical waves in small circular domains. *Physical Review Letters*, 76(8):1384–1387, 1996. (Cited on page 8.)

- [43] N. Hartmann, Y. Kevrekidis, and R. Imbihl. Pattern formation in restricted geometries: The NO + CO reaction on Pt(100). *The Journal of Chemical Physics*, 112(15):6795–6803, 2000. (Cited on page 8.)
- [44] H. Brandstädter, M. Braune, I. Schebesch, and H. Engel. Experimental study of the dynamics of spiral pairs in light-sensitive Belousov-Zhabotinskii media using an open-gel reactor. *Chemical Physics Letters*, 323:145–154, 2000. (Cited on pages 8, 24, 58, 59, and 60.)
- [45] M. Gómez-Gesteira, A. P. Muñuzuri, V. Pérez-Muñuzuri, and V. Pérez-Villar. Boundary-imposed spiral drift. *Physical Review E*, 53(5):5480–5483, 1996. (Cited on page 8.)
- [46] M. Ruiz-Villareal, M. Gómez-Gesteira, C. Souto, A. P. Muñuzuri, and V. Pérez-Villar. Long term vortex interaction in active media. *Physical Review E*, 54(3):2999–3002, 1996. (Cited on page 8.)
- [47] D. Kupitz and M. J. B. Hauser. Interaction of a pair of parallel scroll waves. *The Journal of Physical Chemistry A*, 117:12711–12718, 2013. (Cited on pages 8 and 24.)
- [48] I. V. Biktasheva and V. N. Biktashev. Wave-particle dualism of spiral wave dynamics. *Physical Review E*, 67:026221, 2003. (Cited on pages 8, 9, 21, 24, 27, 28, and 30.)
- [49] S. Rica and E. Tirapegui. Interaction of defects in two-dimensional systems. *Physical Review Letters*, 64(8):878–881, 1990. (Cited on page 8.)
- [50] C. Elphick and E. Meron. Dynamics of phase singularities in two-dimensional oscillating systems. *Physica D*, 53:385–399, 1991. (Cited on page 8.)
- [51] I. Aranson, L. Kamer, and A. Weber. On the interaction of spiral waves in non-equilibrium media. *Physica D*, 53:376–384, 1991. (Cited on page 8.)
- [52] I. Aranson, D. Kessler, and I. Mitkov. Boundary-induced drift of spirals in excitable media. *Physical Review E*, 50(4):2395–2398, 1994. (Cited on page 8.)
- [53] M. Bär, A. K. Bangia, and I. G. Kevrekidis. Bifurcation and stability analysis of rotating chemical spirals in circular domains: Boundary-induced meandering and stabilization. *Physical Review E*, 67:056126, 2003. (Cited on page 8.)
- [54] J. Goldstone. Field theories with "superconductor" solutions. *Il Nuovo Cimento*, 19(1):154–164, 1961. (Cited on page 8.)
- [55] D. Barkley. Linear stability analysis of rotating spiral waves in excitable media. *Physical Review Letters*, 68(13):2090–2093, 1992. (Cited on pages 8 and 45.)
- [56] V. N. Biktashev and A. V. Holden. Resonant drift of autowave vortices in two dimensions and the effects of boundaries and inhomogeneities. *Chaos, Solitons & Fractals*, 5(3/4):575–622, 1995. (Cited on pages 8, 21, 22, 24, 26, 29, and 50.)

- [57] I. V. Biktasheva, D. Barkley, V. N. Biktashev, G. V. Bordyugov, and A. J. Foulkes. Computation of the response functions of spiral waves in active media. *Physical Review E*, 79:056702, 2009. (Cited on pages 9, 21, 22, 27, 28, 30, and 33.)
- [58] I. V. Biktasheva, D. Barkley, V. N. Biktashev, and A. J. Foulkes. Computation of the drift of spiral waves using response functions. *Physical Review E*, 81:066202, 2010. (Cited on pages 9, 21, 22, 27, 30, 32, and 33.)
- [59] J. J. Tyson and L. Glass. Arthur T. Winfree (1942-2002). *Journal of Theoretical Biology*, 230:433–439, 2004. (Cited on page 10.)
- [60] A. T. Winfree. Scroll-shaped waves of chemical activity in three dimensions. *Science*, 181:937–939, 1973. (Cited on pages 10 and 56.)
- [61] A. T. Winfree. Rotating chemical reactions. *Scientific American*, 230(6):82–95, 1974. (Cited on pages 10, 11, and 56.)
- [62] B. J. Welsh, J. Gomatam, and A. E. Burgess. Three-dimensional chemical waves in the Belousov-Zhabotinskii reaction. *Nature*, 304:611–614, 1983. (Cited on page 12.)
- [63] A. V. Panfilov and A. M. Pertsov. Vortex ring in a 3-dimensional active medium described by reaction-diffusion equations. *Doklady Akademii Nauk SSSR*, 274(6):1500–1503, 1984. (Cited on pages 12, 57, and 64.)
- [64] A. T. Winfree, E. M. Winfree, and H. Seifert. Organizing centers in a cellular excitable medium. *Physica D*, 17:109–115, 1985. (Cited on page 12.)
- [65] A. T. Winfree and S. H. Strogatz. Singular filaments organize chemical waves in three dimensions. I. Geometrically simple waves. *Physica D*, 8:35–49, 1983. (Cited on page 12.)
- [66] A. T. Winfree and S. H. Strogatz. Singular filaments organize chemical waves in three dimensions. II. Twisted waves. *Physica D*, 9:65–80, 1983. (Cited on page 12.)
- [67] A. T. Winfree and S. H. Strogatz. Singular filaments organize chemical waves in three dimensions. III. Knotted waves. *Physica D*, 9:333–345, 1983. (Cited on page 12.)
- [68] A. T. Winfree and S. H. Strogatz. Singular filaments organize chemical waves in three dimensions. IV. Wave taxonomy. *Physica D*, 13:221–233, 1984. (Cited on page 12.)
- [69] A. T. Winfree and S. H. Strogatz. Organizing centres for three-dimensional chemical waves. *Nature*, 311:611–615, 1984. (Cited on page 12.)
- [70] A. V. Panfilov and A. T. Winfree. Dynamical simulations of twisted scroll rings in three-dimensional excitable media. *Physica D*, 17:323–330, 1985. (Cited on page 12.)
- [71] W. Jahnke, C. Henze, and A. T. Winfree. Chemical vortex dynamics in three-dimensional excitable media. *Nature*, 336:662–665, 1988. (Cited on page 12.)

- [72] A. V. Panfilov and A. N. Rudenko. Two regimes of the scroll ring drift in the three-dimensional active media. *Physica D*, 28:215–218, 1987. (Cited on page 12.)
- [73] P. J. Nandapurkar and A. T. Winfree. Dynamical stability of untwisted scroll rings in excitable media. *Physica D*, 35:277–288, 1989. (Cited on pages 12 and 124.)
- [74] J. P. Keener and J. J. Tyson. The motion of untwisted untorced scroll waves in Belousov-Zhabotinsky reagent. *Science*, 239:1284–1286, 1988. (Cited on pages 12 and 40.)
- [75] P. J. Nandapurkar and A. T. Winfree. A computational study of twisted linked scroll waves in excitable media. *Physica D*, 29:68–83, 1987. (Cited on page 12.)
- [76] V. N. Biktashev. Evolution of twist of an autowave vortex. *Physica D*, 36:167–172, 1989. (Cited on page 12.)
- [77] C. Henze, E. Lugosi, and A. T. Winfree. Helical organizing centers in excitable media. *Canadian Journal of Physics*, 68:683–710, 1990. (Cited on pages 13, 36, 49, and 50.)
- [78] J. P. Keener and J. J. Tyson. The dynamics of helical scroll scroll waves in excitable media. *Physica D*, 53:151–161, 1991. (Cited on page 13.)
- [79] I. Aranson and I. Mitkov. Helicoidal instability of a scroll vortex in three-dimensional reaction-diffusion systems. *Physical Review E*, 58(4):4556–4559, 1998. (Cited on pages 13 and 49.)
- [80] D. Margerit and D. Barkley. Selection of twisted scroll waves in three-dimensional excitable media. *Physical Review Letters*, 86(1):175–178, 2001. (Cited on page 13.)
- [81] A. Pertsov, R. R. Aliev, and V. I. Krinsky. Three-dimensional twisted vortices in an excitable chemical medium. *Nature*, 345:419–421, 1990. (Cited on pages 13, 49, 50, and 96.)
- [82] S. Mironov, M. Vinson, S. Mulvey, and A. Pertsov. Destabilization of three-dimensional rotating chemical waves in an inhomogeneous BZ reaction. *The Journal of Physical Chemistry*, 100:1975–1983, 1996. (Cited on pages 13, 49, and 50.)
- [83] M. Vinson, S. Mironov, S. Mulvey, and A. Pertsov. Control of spatial orientation and lifetime of scroll rings in excitable media. *Nature*, 386:477–480, 1997. (Cited on pages 13 and 96.)
- [84] M. Vinson and A. Pertsov. Dynamics of scroll rings in a parameter gradient. *Physical Review E*, 59(3):2764–2771, 1999. (Cited on page 13.)
- [85] T. Amemiya, P. Kettunen, S. Kádár, T. Yamaguchi, and K. Showalter. Formation and evolution of scroll waves in photosensitive excitable media. *Chaos*, 8(4):872–878, 1998. (Cited on pages 13, 56, and 120.)
- [86] H. Henry and V. Hakim. Linear stability of scroll waves. *Physical Review Letters*, 85(25):5328–5331, 2000. (Cited on pages 13, 36, and 43.)

- [87] H. Henry and V. Hakim. Scroll waves in isotropic excitable media: Linear instabilities, bifurcations, and restabilized states. *Physical Review E*, 65:046235, 2002. (Cited on pages 13, 36, 43, 47, 48, 49, 50, 81, 82, 83, and 127.)
- [88] D. Barkley. A model for fast computer simulation of waves in excitable media. *Physica D*, 49:61–70, 1991. (Cited on pages 13, 43, and 82.)
- [89] V. N. Biktashev, A. V. Holden, and H. Zhang. Tension of organizing filaments of scroll waves. *Philosophical Transactions of the Royal Society of London A*, 347:611–630, 1994. (Cited on pages 13, 14, 26, 35, 36, 40, 41, 42, 46, 47, and 106.)
- [90] S. Alonso, R. Kähler, A. S. Mikhailov, and F. Sagués. Expanding scroll rings and negative tension turbulence in a model of excitable media. *Physical Review E*, 70:056201, 2004. (Cited on pages 13 and 36.)
- [91] S. Alonso, F. Sagués, and A. S. Mikhailov. Negative-tension instability of scroll waves and Winfree turbulence in the Oregonator model. *The Journal of Physical Chemistry A*, 110:12063–12071, 2006. (Cited on pages 13, 36, and 124.)
- [92] S. Alonso and A. V. Panfilov. Negative filament tension at high excitability in a model of cardiac tissue. *Physical Review Letters*, 100:218101, 2008. (Cited on pages 13, 36, and 124.)
- [93] V. N. Biktashev. A three-dimensional autowave turbulence. *International Journal of Bifurcation and Chaos*, 8(4):677–684, 1998. (Cited on pages 13, 36, 88, and 107.)
- [94] R. M. Zaritski, S. F. Mironov, and A. M. Pertsov. Intermittent self-organization of scroll wave turbulence in three-dimensional excitable media. *Physical Review Letters*, 92(16):168302, 2004. (Cited on pages 13 and 36.)
- [95] J. E. Marsden and M. McCracken. *The Hopf bifurcation and its applications*, volume 19. Springer-Verlag, 1976. (Cited on page 13.)
- [96] T. Bánsági Jr. and O. Steinbock. Negative filament tension of scroll rings in an excitable system. *Physical Review E*, 76:045202(R), 2007. (Cited on page 14.)
- [97] C. Luengviriya, U. Storb, G. Lindner, S. C. Müller, M. Bär, and M. J. B. Hauser. Scroll wave instabilities in an excitable chemical medium. *Physical Review Letters*, 100:148302, 2008. (Cited on page 14.)
- [98] L. V. Yakushevich. Vortex filament elasticity in active medium. *Studia biophysica*, 100(3):195–200, 1984. (Cited on pages 14 and 35.)
- [99] James P. Keener. The dynamics of three-dimensional scroll waves in excitable media. *Physica D*, 31:269–276, 1988. (Cited on pages 14, 35, 36, 39, and 106.)
- [100] H. Dierckx and H. Verschelde. Effective dynamics of twisted and curved scroll waves using virtual filaments. *Physical Review E*, 88:062907, 2013. (Cited on pages 14, 36, and 51.)

- [101] P. K. Brazhnik, V. A. Davydov, and A. S. Mikhailov. Kinematic approach to the description of autowave processes in active media. *Teoreticheskaya i Matematicheskaya Fizika*, 74(3):440–447, 1988. (Cited on page 14.)
- [102] A. S. Mikhailov and V. S. Zykov. Kinematical theory of spiral waves in excitable media: Comparison with numerical simulations. *Physica D*, 52:379–397, 1991. (Cited on page 14.)
- [103] A. S. Mikhailov, V. A. Davydov, and V. S. Zykov. Complex dynamics of spiral waves and motion of curves. *Physica D*, 70:1–39, 1994. (Cited on page 14.)
- [104] P. K. Brazhnik, V. A. Davydov, V. S. Zykov, and A. S. Mikhailov. Vortex rings in excitable media. *JETP*, 66(5):984–990, 1987. (Cited on page 14.)
- [105] A. S. Mikhailov. Three-dimensional kinematics. *Chaos, Solitons & Fractals*, 5(3):673–679, 1995. (Cited on page 14.)
- [106] S. Alonso, F. Sagués, and A. S. Mikhailov. Taming Winfree turbulence of scroll waves in excitable media. *Science*, 299:1722–1725, 2003. (Cited on pages 14 and 88.)
- [107] S. Alonso, F. Sagués, and A. S. Mikhailov. Periodic forcing of scroll rings and control of Winfree turbulence in excitable media. *Chaos*, 16:023124, 2006. (Cited on page 14.)
- [108] H. Zhang, Z. Cao, N.-J. Wu, H.-P. Ying, and G. Hu. Suppress Winfree turbulence by local forcing excitable systems. *Physical Review Letters*, 94:188301, 2005. (Cited on page 14.)
- [109] N.-J. Wu, H. Zhang, H.-P. Ying, Z. Cao, and G. Hu. Suppression of Winfree turbulence under weak spatiotemporal perturbation. *Physical Review E*, 73:060901(R), 2006. (Cited on page 14.)
- [110] V. Pérez-Muñuzuri, F. Sagués, and J. M. Sancho. Lifetime enhancement of scroll rings by spatiotemporal fluctuations. *Physical Review E*, 62(1):94–99, 2000. (Cited on page 14.)
- [111] C. Zhang, H. Liao, and Q. Ouyang. Chemical turbulence and line defects induced by gradient effects in a three-dimensional reaction-diffusion system. *The Journal of Physical Chemistry B*, 110:7508–7512, 2006. (Cited on page 14.)
- [112] C. Qiao, Y. Wu, X. Lu, C. Wang, Q. Ouyang, and H. Wang. Control of scroll wave turbulence in a three-dimensional reaction-diffusion system with gradient. *Chaos*, 18:026109, 2008. (Cited on page 14.)
- [113] B. Echebarria, V. Hakim, and H. Henry. Nonequilibrium ribbon model of twisted scroll waves. *Physical Review Letters*, 96:098301, 2006. (Cited on pages 14 and 51.)
- [114] B. Marts, T. Bánsági Jr., and O. Steinbock. Evidence for Burgers' equation describing the untwisting of scroll rings. *Europhysics Letters*, 83:30010, 2008. (Cited on page 14.)

- [115] T. Bánsági Jr., K. J. Meyer, and O. Steinbock. Wave-pinned filaments of scroll waves. *The Journal of Chemical Physics*, 128:094503, 2008. (Cited on page 14.)
- [116] Z. A. Jiménez, B. Marts, and O. Steinbock. Pinned scroll rings in an excitable system. *Physical Review Letters*, 102:244101, 2009. (Cited on pages 14 and 58.)
- [117] E. Nakouzi, Z. A. Jiménez, V. N. Biktashev, and O. Steinbock. Analysis of anchor-size effects on pinned scroll waves and measurement of filament rigidity. *Physical Review E*, 89:042902, 2014. (Cited on page 14.)
- [118] S. Dutta and O. Steinbock. Steady motion of hairpin-shaped vortex filaments in excitable systems. *Physical Review E*, 81:055202(R), 2010. (Cited on pages 14 and 58.)
- [119] C. Luengviriya, S. C. Müller, and M. J. B. Hauser. Reorientation of scroll rings in an advective field. *Physical Review E*, 77:015201(R), 2008. (Cited on page 14.)
- [120] C. Luengviriya and M. J. B. Hauser. Stability of scroll ring orientation in an advective field. *Physical Review E*, 77:056214, 2008. (Cited on page 14.)
- [121] P. Dähmlow, S. Alonso, M. Bär, and M. J. B. Hauser. Twists of Opposite Handedness on a Scroll Wave. *Physical Review Letters*, 110:234102, 2013. (Cited on page 14.)
- [122] P. A. Kolski. Dreidimensionale Effekte bei der Ausbreitung nichtlinearer Erregungswellen in dünnen Schichten. Diploma thesis, Technische Universität Berlin, Berlin, Germany, 2009. (Cited on pages 15 and 60.)
- [123] V.S. Zykov and H. Engel. Feedback-mediated control of spiral waves. *Physica D*, 199(1-2):243–263, December 2004. (Cited on page 21.)
- [124] V. N. Biktashev, D. Barkley, I. V. Biktasheva, G. V. Bordyugov, H. Dierckx, A. J. Foulkes, S. W. Morgan, G. Plank, N. A. Saravazyan, O. Selsil, and H. Verschelde. Asymptotic dynamics and control of spiral and scroll waves. In K. Agaladze and G. Guria, editors, *Instabilities and Control of Excitable Networks: from macro- to nano-systems*, pages 8–18, 2012. (Cited on page 21.)
- [125] V. N. Biktashev. *Evolution of vortices in active media*. PhD thesis, Moscow Institute of Physics and Technology, Moscow, USSR, 1989. (Cited on page 21.)
- [126] J. Kevorkian and J. D. Cole. *Multiple Scale and Singular Perturbation Methods*. Springer-Verlag, 1996. (Cited on page 25.)
- [127] C. M. Bender and S. A. Orszag. *Advanced Mathematical Methods for Scientists and Engineers I - Asymptotic Methods and Perturbation Theory*. Springer-Verlag, 1999. (Cited on page 25.)
- [128] E. A. Ermakova and A. M. Pertsov. Interaction of rotating spiral waves with a boundary. *Biofizika*, 31:855–861, 1986. (Cited on page 29.)

- [129] R. B. Lehoucq, D. C. Sorensen, and C. Yang. *ARPACK User's Guide: Solution of Large Scale Eigenvalue Problems with Implicitly Restarted Arnoldi Methods*. SIAM, 1998. (Cited on page 31.)
- [130] A. V. Panfilov, A. N. Rudenko, and V. I. Krinsky. Vortex rings in three-dimensional active media with diffusion in two components. *Biophysics*, 31:926–931, 1986. (Cited on page 40.)
- [131] V. Hakim and A. Karma. Theory of spiral wave dynamics in weakly excitable media: Asymptotic reduction to a kinematic model and applications. *Physical Review E*, 60(5):5073–5105, 1999. (Cited on pages 44, 47, and 81.)
- [132] I. Goldhirsch, S. A. Orszag, and B. K. Maulik. An efficient method for computing leading eigenvalues and eigenvectors of large asymmetric matrices. *Journal of Scientific Computing*, 2(1):33–58, 1987. (Cited on page 45.)
- [133] D. Barkley. Euclidean symmetry and the dynamics of rotating spiral waves. *Physical Review Letters*, 72(1):164–168, 1994. (Cited on page 45.)
- [134] A. T. Winfree. Electrical turbulence in three-dimensional heart muscle. *Science*, 266:1003–1006, 1994. (Cited on page 49.)
- [135] A. E. H. Love. *A Treatise on the Mathematical Theory of Elasticity*. Cambridge University Press, 1892. (Cited on pages 50, 139, and 150.)
- [136] L. D. Landau and E. M. Lifshitz. *Theory of Elasticity*. Pergamon Press, Oxford, 1959. (Cited on pages 50 and 150.)
- [137] A. T. Winfree. The prehistory of the Belousov-Zhabotinsky oscillator. *Journal of Chemical Education*, 61(8):661–663, 1984. (Cited on page 55.)
- [138] R. J. Field, E. Körös, and R. M. Noyes. Oscillations in chemical systems. II. Thorough analysis of temporal oscillation in the bromate-cerium-malonic acid system. *Journal of the American Chemical Society*, 94(25):8649–8664, 1972. (Cited on page 55.)
- [139] I. Schebesch. *Wellenausbreitung unter Variation der Anregungsschwelle des Mediums*. Phd thesis, Technische Universität Berlin, Berlin, Germany, 1999. (Cited on page 55.)
- [140] V. Gáspár, G. Basza, and M. T. Beck. The Influence of Visible Light on the Belousov-Zhabotinskii Oscillating Reactions applying Different Catalysts. *Zeitschrift für Physikalische Chemie*, 264(1):43–48, 1983. (Cited on page 55.)
- [141] L. Kuhnert. Photochemische Manipulation von chemischen Wellen. *Naturwissenschaften*, 73:96–97, 1986. (Cited on page 55.)
- [142] L. Kuhnert. A new optical photochemical memory device in a light-sensitive chemical active medium. *Nature*, 319:393–394, 1986. (Cited on page 55.)

- [143] L. Kuhnert and H.-J. Krug. Kinetics of chemical waves in the acidic Bromate-Malonic Acid-Ru(bpy)<sub>3</sub><sup>2+</sup> system in comparison with the Ferooin systems. *The Journal of Physical Chemistry*, 91:730–733, 1987. (Cited on page 55.)
- [144] L. Kuhnert, K. I. Agladze, and V. I. Krinsky. Image processing using light-sensitive chemical waves. *Nature*, 337:244–247, 1989. (Cited on page 55.)
- [145] M. Jinguji, M. Ishihara, and T. Nakazawa. Photoinduced formation of spatial patterns in the Belousov-Zhabotinskii reaction. *The Journal of Physical Chemistry*, 94(4):1226–1229, 1990. (Cited on page 55.)
- [146] M. Jinguji, M. Ishihara, and T. Nakazawa. Primary process of illumination effect on the Ru(bpy)<sub>3</sub><sup>2+</sup>-Catalyzed Belousov-Zhabotinskii reaction. *The Journal of Physical Chemistry*, 96(11):4279–4281, 1992. (Cited on page 55.)
- [147] M. Schröder and T. A. Stephenson. Ruthenium. In G. Wilkinson, R. D. Gillard, and J. A. McCleverty, editors, *Comprehensive Coordination Chemistry - The Synthesis, Reactions, Properties & Applications of Coordination Compounds*, volume 4. Pergamon Press, Oxford, 1987. (Cited on page 55.)
- [148] M. Braune and H. Engel. Compound rotation of spiral waves in a light-sensitive Belousov-Zhabotinsky medium. *Chemical Physics Letters*, 204(3,4):257–264, 1993. (Cited on pages 55 and 60.)
- [149] M. Braune and H. Engel. Compound rotation of spiral waves in active media with periodically modulated excitability. *Chemical Physics Letters*, 211(6):534–540, 1993. (Cited on pages 55 and 60.)
- [150] O. Steinbock, V. S. Zykov, and S. C. Müller. Control of spiral-wave dynamics in active media by periodic modulation of excitability. *Nature*, 366:322–324, 1993. (Cited on page 55.)
- [151] T. Amemiya, S. Kádár, P. Kettunen, and K. Showalter. Spiral wave formation in three-dimensional excitable media. *Physical Review Letters*, 77(15):3244–3247, 1996. (Cited on pages 56, 58, 64, and 120.)
- [152] K. I. Agladze, V. I. Krinsky, A. V. Panfilov, H. Linde, and L. Kuhnert. Three-dimensional vortex with spiral filament in a chemically active medium. *Physica D*, 39:38–42, 1989. (Cited on pages 57 and 64.)
- [153] H. Linde and H. Engel. Autowave propagation in heterogeneous active media. *Physica D*, 49:13–20, 1991. (Cited on pages 57 and 64.)
- [154] J. F. Totz, H. Engel, and O. Steinbock. Spatial confinement causes lifetime enhancement and expansion of vortex rings with positive filament tension. *ArXiv*, 1401:6550, 2014. (Cited on pages 58, 111, and 112.)
- [155] M. Braune, A. Schrader, and H. Engel. Entrainment and resonance of spiral waves in active media with periodically modulated excitability. *Chemical Physics Letters*, 222:358–362, 1994. (Cited on pages 58 and 60.)

- [156] M. Braune and H. Engel. Feedback-controlled forcing of meandering spiral waves in an open gel reactor. *Physical Review E*, 62(5):5986–5988, 2000. (Cited on pages 59 and 60.)
- [157] V. S. Zykov, G. Bordiougov, H. Brandstädter, I. Gerdes, and H. Engel. Global Control of Spiral Wave Dynamics in an Excitable Domain of Circular and Elliptical Shape. *Physical Review Letters*, 92(1):018304, 2004. (Cited on pages 59 and 60.)
- [158] V. Beato, I. Sendiña-Nadal, I. Gerdes, and H. Engel. Noise-induced wave nucleations in an excitable chemical reaction. *Physical Review E*, 71:035204(R), 2005. (Cited on pages 59 and 60.)
- [159] V. Beato, I. Sendiña-Nadal, I. Gerdes, and H. Engel. Coherence resonance in a chemical excitable system driven by coloured noise. *Philosophical Transactions of the Royal Society London A*, 366:381–395, 2008. (Cited on pages 59 and 60.)
- [160] J. Schlesner, V. S. Zykov, H. Brandstädter, I. Gerdes, and H. Engel. Efficient control of spiral wave location in an excitable medium with localized heterogeneities. *New Journal of Physics*, 10:015003, 2008. (Cited on pages 59 and 60.)
- [161] T. Plessner, S. C. Müller, and B. Hess. Spiral wave dynamics as a function of proton concentration in the ferroin-catalyzed Belousov-Zhabotinskii reaction. *The Journal of Physical Chemistry*, 94:7501–7507, 1990. (Cited on pages 59, 60, and 74.)
- [162] S. C. Müller, T. Plessner, and B. Hess. Two-dimensional spectrophotometry of spiral wave propagation in the Belousov-Zhabotinskii reaction i. Experiments and digital data representation. *Physica D*, 24:71–86, 1987. (Cited on pages 59, 60, and 74.)
- [163] H. Engel and M. Braune. Dynamics of nonlinear waves in chemical active media. *Physica Scripta*, T49B:685–690, 1993. (Cited on page 60.)
- [164] J. Schlesner. *Control of spiral wave dynamics in active media*. PhD thesis, Technische Universität Berlin, Berlin, Germany, 2015. (Cited on pages 60, 61, and 62.)
- [165] S. Fruhner. *Realistic Models of the Electrical Excitation in the Human Heart and the Determination of the Cardiac Magnetic Field*. PhD thesis, Technische Universität Berlin, Berlin, Germany, 2014. (Cited on page 68.)
- [166] W. H. Press, S. A. Teukolsky, W. T. Vetterling, and B. P. Flannery. *Numerical Recipes - The Art of Scientific Computing*. Cambridge University Press, 3rd edition, 2007. (Cited on page 70.)
- [167] H. Dierckx, H. Verschelde, Ö. Selsil, and V. N. Biktashev. Buckling of scroll waves. *Physical Review Letters*, 109:174102, 2012. (Cited on page 81.)
- [168] D. A. Kulawiak. Über die Wechselwirkung rotierender dreidimensionaler Erregungswellen mit begrenzenden Neumann-Rändern. Master

- thesis, Technische Universität Berlin, Berlin, Germany, 2014. (Cited on page 82.)
- [169] H.-J. Krug, L. Pohlmann, and L. Kuhnert. Analysis of the Modified Complete Oregonator accounting for oxygen sensitivity and photosensitivity of Belousov-Zhabotinsky systems. *The Journal of Physical Chemistry*, 94:4862–4866, 1990. (Cited on pages 93 and 94.)
- [170] S. Kádár, T. Amemiya, and K. Showalter. Reaction mechanism for light sensitivity of the Ru (bpy)<sub>3</sub><sup>2+</sup>-catalyzed Belousov-Zhabotinsky reaction. *Journal of Physical Chemistry A*, 101(44):8200–8206, 1997. (Cited on page 93.)
- [171] A. Pertsov and M. Vinson. Dynamics of scroll waves in inhomogeneous excitable media. *Philosophical Transactions of the Royal Society of London A*, 347:687–700, 1994. (Cited on page 96.)
- [172] F. Paul. Dreidimensionale Erregungswellen in oszillatorischen Medien. Diploma thesis, Technische Universität Berlin, Berlin, Germany, 2011. (Cited on page 109.)
- [173] A. B. Rovinsky and A. M. Zhabotinsky. Mechanisms and mathematical model of the oscillating bromate-ferroin-bromomalonic acid reaction. *The Journal of Physical Chemistry*, 88(25):6081–6084, 1984. (Cited on page 111.)
- [174] F. Buchholz. Spiral Drift at a No-Flux Boundary under Variation of Excitability. Bachelor thesis, Technische Universität Berlin, Berlin, Germany, 2013. (Cited on page 117.)
- [175] G. Zimmermann. Bifurkationsanalyse des Phasenraums eines Scrollrings in Wechselwirkung mit einem Neumann-Rand. Bachelor thesis, Technische Universität Berlin, Berlin, Germany, 2014. (Cited on page 117.)
- [176] B. Blasius, A. Huppert, and L. Stone. Complex dynamics and phase synchronization in spatially extended ecological systems. *Nature*, 399:354–359, 1999. (Cited on page 123.)
- [177] O.-U. Kheowan, V. Gáspár, V. S. Zykov, and S. C. Müller. Measurements of kinematic parameters of spiral waves in media of low excitability. *Physical Chemistry Chemical Physics*, 3:4747–4752, 2001. (Cited on page 124.)
- [178] A. Goriely and M. Tabor. New amplitude equations for thin elastic rods. *Physical Review Letters*, 77(17):3537–3540, 1996. (Cited on pages 137, 138, and 150.)
- [179] A. Goriely and M. Tabor. Nonlinear dynamics of filaments I. Dynamical instabilities. *Physica D*, 105:20–44, 1997. (Cited on pages 137 and 150.)
- [180] A. Goriely and M. Tabor. Nonlinear dynamics of filaments II. Nonlinear analysis. *Physica D*, 105:45–61, 1997. (Cited on pages 137, 141, and 150.)

- [181] A. Goriely and M. Tabor. Nonlinear dynamics of filaments III. Instabilities of helical rods. *Proceedings of the Royal Society of London A*, 453(1967):2583–2601, 1997. (Cited on pages 137 and 150.)
- [182] A. Goriely and M. Tabor. The Nonlinear Dynamics of Filaments. *Non-linear Dynamics*, 21:101–133, 2000. (Cited on pages 137, 140, 141, 144, 145, and 150.)
- [183] M. D. Barkley and B. H. Zimm. Theory of twisting and bending of chain macromolecules; analysis of the fluorescence depolarization of DNA. *The Journal of Chemical Physics*, 70(6):2991–3007, 1979. (Cited on page 137.)
- [184] C. J. Benham. Theoretical analysis of conformational equilibria in superhelical DNA. *Annual Review of Biophysics and Biophysical Chemistry*, 14:23–45, 1985. (Cited on page 137.)
- [185] N. H. Mendelson. Bacterial macrofibers: The morphogenesis of complex multicellular bacterial forms. *Scientific Progress Oxford*, 74:425–441, 1990. (Cited on page 137.)
- [186] N. G. Hunt and J. E. Hearst. Elastic model of DNA supercoiling in the infinite-length limit. *The Journal of chemical physics*, 95(12):9329–9336, 1991. (Cited on page 137.)
- [187] W. R. Bauer, R. A. Lund, and J. H. White. Twist and writhe of a DNA loop containing intrinsic bends. *Proceedings of the National Academy of Sciences*, 90(3):833–837, 1993. (Cited on page 137.)
- [188] Y. Shi and J. E. Hearst. The Kirchhoff elastic rod, the nonlinear Schrödinger equation, and DNA supercoiling. *The Journal of chemical physics*, 101(6):5186–5200, 1994. (Cited on page 137.)
- [189] R. E. Goldstein and S. A. Langer. Nonlinear dynamics of stiff polymers. *Physical Review Letters*, 75(6):1094–1097, 1995. (Cited on page 137.)
- [190] M. J. Shelley and T. Ueda. The nonlocal dynamics of stretching, buckling filaments. In *Advances in multi-fluid flows*, pages 415–425. SIAM, 1996. (Cited on page 137.)
- [191] J. P. Keener. Knotted vortex filaments in an ideal fluid. *Journal of Fluid Mechanics*, 211:629–651, 1990. (Cited on page 137.)
- [192] H. C. Spruit. Motion of magnetic flux tubes in the solar convection zone and chromosphere. *Astronomy and Astrophysics*, 98:155–160, 1981. (Cited on page 137.)
- [193] S. D’silva and A. R. Choudhuri. A theoretical model for tilts of bipolar magnetic regions. *Astronomy and Astrophysics*, 272:621–633, 1993. (Cited on page 137.)
- [194] E. H. Dill. Kirchhoff’s theory of rods. *Archives of the History of Exact Science*, 44:2–23, 1992. (Cited on page 139.)
- [195] B. D. Coleman, E. H. Dill, M. Lembo, Z. Lu, and I. Tobias. On the dynamics of rods in the theory of Kirchhoff and Clebsch. *Archive for rational mechanics and analysis*, 121(4):339–359, 1993. (Cited on page 139.)

- [196] I. V. Biktasheva, H. Dierckx, and V. N. Biktashev. Drift of waves in thin layers caused by thickness features: Asymptotic theory and numerical simulations. *Physical Review Letters*, 114:068302, 2015. (Cited on page 150.)
- [197] H. Ke, Z. Zhang, and O. Steinbock. Scroll wave drift along steps, troughs, and corners. *Chaos*, 25(6):064303, 2015. (Cited on page 151.)
- [198] S. Martens, J. Löber, and H. Engel. Front propagation in channels with spatially modulated cross section. *Physical Review E*, 91(2):022902, 2015. (Cited on page 151.)



## ACKNOWLEDGMENTS

---

First of all I would like to thank my supervisor, Prof. Dr. Harald Engel, for giving me the opportunity to study these mesmerizing patterns called scroll waves. Furthermore, he always tried to provide precise suggestions for scientific directions to investigate and demanded to achieve always better. Moreover, I would like to thank Prof. Dr. Markus Bär for agreeing to referee my thesis, but also for some very useful scientific suggestions. I would also like to thank Prof. Dr. Oliver Steinbock for agreeing to referee my thesis and for his contagious enthusiasm in doing and thinking science.

The work that I achieved and presented here would not be possible without the admirable work of many colleagues. My thanks go to Jan Totz, Sonja Molnos, Teresa Reinhard, Enrico Diez, and Helmar Dittrich for huge help in the development of the experimental setup. In this connection, I would like to thank also Ulrike Künkel for essential help in the lab. The Virtual Lab is something that I am very proud of, and I am very happy to have worked on its development with a bunch of nice and enthusiastic people. In this connection, I am very grateful for the work of Stefan Fruhner. His conviction and persistence made it all possible. Furthermore, I would like to thank Rico Buchholz for whom any emerging programming problem appeared to be solvable. Many thanks go also to the several people who participated in the process of development: Fabian Paul, Martin Marmulla, Philipp Gast, Jan Totz, Sonja Molnos, and Dirk Kulawiak, and all those I forgot unintentionally.

During the process of finishing my thesis, I was happy to know so much nice people who agreed to read my manuscript and suggested very helpful comments and corrections. In this connection, I am very grateful to Dayton Syme for his admirable and extremely useful suggestions regarding the English language and Steffen Martens for a lot of essential hints. Moreover, I also would like to thank Elias Nakouzi, Martin Marmulla, Markus Radzsuweit, Stefan Fruhner, Martin Senne and Margit Schlottmann for careful reading of different parts of my manuscript. Very special thank goes to Martin Senne who provided a lot of moral support, starting with the time of my diploma thesis up to now, making him a very special friend of mine. Furthermore, I would like to thank some of the folks from other working groups that joined us at lunch and coffee times: David Strehober, Carlos Alvarez, and Peter Zurek.

I am very grateful for the everlasting support of my family: my parents Laila and Najib; my brothers Passun and Yama; and my sister Mariam. Finally, and most importantly, my biggest gratitude goes to my beloved girlfriend, Elli Schlottmann. Her moral support was indispensable for finishing my thesis and a lot more. Almost everything what I have achieved here is dedicated to her.



## DECLARATION

---

Hiermit erkläre ich an Eides statt, dass ich die vorliegende Arbeit selbständig verfasst und alle Quellen und Hilfsmittel korrekt und vollständig angegeben habe.

*Berlin, 25. Juni 2015*

---

Dipl. Phys. Arash Azhand